Marquette University
e-Publications@Marquette

Dissertations (2009 -) | Dissertations, Theses, and Professional Projects

MATRIX-ISOLATION AND COMPUTATIONAL STUDIES OF TRANSIENT POLYHALOGENATED INTERMEDIATES AND WEAKLY-BOUND COMPLEXES.

AIMABLE KALUME
Marquette University

Recommended Citation
KALUME, AIMABLE, "MATRIX-ISOLATION AND COMPUTATIONAL STUDIES OF TRANSIENT POLYHALOGENATED INTERMEDIATES AND WEAKLY-BOUND COMPLEXES." (2013). *Dissertations (2009 -)*. Paper 274.
http://epublications.marquette.edu/dissertations_mu/274

MATRIX-ISOLATION AND COMPUTATIONAL STUDIES OF TRANSIENT POLYHALOGENATED INTERMEDIATES AND WEAKLY-BOUND COMPLEXES.

by

Aimable KALUME

A Dissertation submitted to the Faculty of the Graduate School,
Marquette University,
in Partial Fulfillment of the Requirements for
the Degree of Doctor of Philosophy.

Milwaukee, Wisconsin

May 2013

ABSTRACT

MATRIX-ISOLATION AND COMPUTATIONAL STUDIES OF TRANSIENT POLYHALOGENATED INTERMEDIATES AND WEAKLY-BOUND COMPLEXES.

Aimable KALUME

Marquette University, 2013

As time goes by and new innovations are brought up to improve living conditions, the human impact on the environment becomes more significant. It has been shown that man-made halogenated compounds play a key role in many real-world chemical processes. For example, in combustion, these compounds are used as fire retardant agents, and in atmospheric chemistry, they initiate ozone depletion reactions.[1-4] However little is known about the mechanisms governing these processes and many intermediates involved in these processes have been elusive to researchers for diverse reasons such as short lifetime and difficulty in distinguishing products from parents molecules. The studies compiled in this work are focused on exploring the photochemical behavior of various intermediates derived from polyhalogenated compounds. These intermediates are trapped in inert rigid matrix and characterized by using IR, UV/Vis spectroscopy supported by computational methods. The photochemistry is explored using selected wavelength appropriate to each species. In this work, the photolysis products of CF_2I_2, CF_2Br_2, $CXBr_3$ (X=H, D, F), $C_2H_4Br_2$, $C_2F_4Br_2$ have been generated and trapped in Argon or Neon matrices and most of them were characterized for the first time. We have also studied weakly bound complexes ($C_2H_4\cdots Br_2$, $C_2H_4\cdots I_2$), formed in matrix by co-deposition of monomers or by trapping fragments resulting from high voltage discharge ($H_2CXBr\cdots Br$; X=H, Cl, Br). We hope that our results will contribute to better understand the photochemical behavior of polyhalogenated species, and to some extent help to understand mechanism in different phenomena involving these species.

ACKNOWLEDGMENTS

Aimable KALUME

Marquette University, 2013

I am and will always be grateful to the Almighty God, for having led me on this path, protected and surrounded me with wonderful people. I couldn't ask more.

It is my honor to express my deepest gratitude to my advisor and committee chair, Professor Scott A. Reid, who has the attitude and substance of a genius. You gave me the unique opportunity to join your lab, introduced me to molecular spectroscopy and guided me through this challenging project. But most of all you set me a role model in every sense of the word: whether scientific analysis, practical and technical skills.

I extend my sincere gratitude, to my committee members, Dr. Rajendra Rathore and Dr. Qadir Timerghazin; I am really thankful for your time in reading, correcting and guiding my work.

My appreciation also goes to Professor Yuan-Pern Lee at the National Chiao Tung University in Taiwan: inviting and hosting me in your lab was such a great and enriching technical experience.

I share the credit of my work with people that I had the chance to work with. Special thanks to Dr. Lisa George for guiding my first steps in Matrix-solation field, and providing your experience and skills. Special thanks to my colleague students, Lloyd Muzangwa, Silver Nyambo, Brandon Uhler, for providing the exciting, pleasant and funniest workplace.

My great pleasure to acknowledge the most important people in my life: my family and friends. It was your omnipresent support and encouragements that kept me moving in the right direction. Thanks for believing in me and understanding when I was physically and/or mentally absent.

I am sincerely indebted to Marquette University, for the scholarship, financial support and Fellowship awards (ACS, Bournique and Eisch fellowships).

Finally, I don’t have words to thank my best friend and sister, Solange, for this lifetime opportunity of being where I stand today.

DEDICATION

To the loving memory of my Mother, Salomé M.

To my Father, Henri T.

For their immeasurable sacrifices and courage

I, humbly, dedicate this work.

PUBLICATIONS

1. Lisa George, Aimable Kalume and Scott A. Reid, Pulsed Jet Discharge and Computational Study of CX_2Br^+ (X=H, F), Chemical Physics Letters (**2010**) 484 214-218

2. Patrick Z. El-Khoury, Lisa George, Aimable Kalume ,Scott A. Reid, Bruce S. Ault, Alexander Tarnovsky, Characterization of iso-CF_2I_2 in frequency and ultrafast time domains, The Journal of Chemical Physics, (**2010**) 132, 124501

3. Patrick Z. El-Khoury, Lisa George, Aimable Kalume, Igor Schapiro, Massimo Olivucci Alexander N. Tarnovsky, Scott A. Reid, Matrix Isolation and Computational Study of CF_2I radical, Chemical Physics Letters, (**2010**) 496, 68-73

4. Lisa George, Aimable Kalume, Patrick El-Khoury, Alexander Tarnovsky and Scott A. Reid, Matrix isolation and computational study of isodifluorodibromomethane, $F_2CBr–Br…$: A route to Br_2 formation in CF_2Br_2 photolysis, The Journal of Chemical Physics, (**2010**) 132, 084503

5. Lisa George, Aimable Kalume, Brian Esselman, James Wagner and Scott A. Reid, Spectroscopic and Computational Studies of matrix isolated iso-$CHBr_3$: Structures, properties and photochemistry of *iso*-bromoform, The Journal of Chemical Physics, (**2011**) 135, 124503

6. Thomas J. Preston, Maitreya Dutta, Brian Esselman, Aimable Kalume, Lisa George, Robert J. McMahon, Scott A. Reid and Fleming Crim, Formation and relaxation dynamics of iso-CH2Cl-I in cryogenic matrices, The Journal of Chemical Physics, (**2011**) 135, 114503

7. Aimable Kalume, Lisa George and Scott A. Reid, Isomerization as a key path to molecular products in the gas-phase decomposition of halons, The Journal of Physical Chemistry Letters, (**2010**) 1 ,3090-3095

8. Aimable Kalume, Lisa George, Patrick El-Khoury, Alexander N. Tarnovsky and Scott A. Reid, Spectroscopic and Computational Studies of the Laser Photolysis of Matrix Isolated 1,2-Dibromoethanes: Formation and Fate of the Bromoethyl radicals, The Journal of Physical Chemistry A., (**2010**) 114, 9919-9926

9. Lisa George, Laura Wittmann, Aimable Kalume, and Scott A. Reid, Photoinduced Electron Transfer in a Prototypical Mulliken Donor-Acceptor Complex: $C_2H_4\cdots Br_2$, Journal of Physical Chemistry Letters, (**2010**), 1, 2618-2621

10. Lisa George, Aimable Kalume, Brian Esselman, Robert J. McMahon and Scott A. Reid, Pulsed-Jet Discharge and Computational Study of Bromine Atom Complexes:

Br•••BrCH$_2$X (X=H, Cl, Br), The Journal of Physical Chemistry A., (**2011**) 115, 9820-9827.

11. L. George, A. Kalume, B. Esselman, J. Wagner, R. J. McMahon, and S. A. Reid, "Spectroscopic and computational studies of matrix-isolated iso-CHBr$_3$: Structure, properties, and photochemistry of iso-bromoform", *J. Chem. Phys.*, **2011**, Vol. 135, 124503/1-124503/8.

12. Lisa George, Aimable Kalume, Scott A. Reid, Brian Esselman, Robert J. McMahon, Spectroscopic and Computational Studies of Matrix-Isolated of *iso*-CXBr$_3$ (X = F, Cl, Br): Structure, properties, and photochemistry of substituted iso-tribromomethanes, The Journal of Molecular structure, (**2012**), 1025, 61-68.

13. Aimable Kalume, Lisa George, Scott A. Reid, On the Electronic Spectroscopy of the *iso*-polyhalomethanes, Chemical Physics Letters, (**2012**), 551, 64-67.

14. Lisa George, Aimable Kalume, Scott A. Reid, Probing Radical Pathways in Electrophilic Addition of Halogens: Classical vs. Bridged Intermediates, Chemical Physics Letters (**2012**), 554, 86-89.

15. Aimable Kalume, Lisa George, Nicole Cunningham, Scott A. Reid, A New View of proton-Coupled Electron Transfer: Concerted vs. Sequential Pathways in Hydrogen Halide Elimination, Chemical Physics Letters (**2013**), 556, 35-38

LIST OF CONTENTS

ABSTRACT ii
ACKNOWLEDGMENTS iii
DEDICATION v
PUBLICATIONS vi
LIST OF CONTENTS viii
LIST OF TABLES xii
LIST OF FIGURES xiv
LIST OF SYMBOLS AND ACRONYMS xxi
Chapter 1. INTRODUCTION 1
Chapter 2. EXPERIMENTAL AND COMPUTATIONAL METHODS 7
2.1 Experimental methods 7
2.1.1 Matrix-isolation spectroscopy. 7
2.1.2 Matrix-isolation apparatus 8
2.1.3 Sample preparation techniques 10
2.1.3.1 Making matrix-gas mixture 10
2.1.3.2 Matrix-gas deposition 12
2.1.3.3 Pulsed-jet high voltage discharge matrix-isolation 15
2.1.4 Irradiation light sources 18
2.1.5 Detection and data collection 19
2.2 Computational methods used 19
2.2.1 Hartree-Fock method 20
2.2.2 Møller-Plesset Perturbation Theory (MP*n*) 21
2.2.3 Coupled Cluster methods 22
2.2.4 Density functional methods 24
2.2.5 Basis sets 25
2.2.5.1 Gaussian-type basis sets 25
2.2.5.2 Basis set superposition error and Counterpoise correction 28
2.2.6 Correlation between IR and UV-Vis spectra 29
ISO-POLYHALOMETHANES 30

Chapter 3. FORMATION AND CHARACTERIZATION OF *iso*-CF_2X_2 (X=I, Br) IN SOLID MATRIX 33
3.1 Experimental set up 36
3.2 Computational methods 36
3.2.1 Results and discussion 37
3.2.2 Characterization of iso-CF_2I_2 in solid Ar matrix 37
3.2.3 Characterization of *iso*-CF_2Br_2 in solid Ar matrix 52
3.3 Summary 68
Chapter 4. FORMATION AND CHARACTERIZATION OF *iso*-TRIBROMOMETHANES (*iso*-$CXBr_3$, X=H, D, F, Cl, Br) IN SOLID MATRIX 69
4.1 Experimental methods 72
4.2 Computational methods 72
4.3 Results and Discussion 73
4.3.1 Formation and characterization of *iso*-bromoform 73
4.3.2 Extending the study to the characterization of iso-$CXBr_3$ (X=F, Cl and Br) 90
4.3.3 Structure and bonding in *iso*-$CXBr_3$ and the $CXBr_3$ Potential Energy Surface 105
4.3.4 The photochemistry of the *iso*-$CXBr_3$. 117
4.3.5 Modeling the electronic absorption signature of *iso*-halons 120
4.4 Summary 127
Chapter 5. PHOTOCHEMISTRY OF 1,2-DIBROMOETHANE AND 1,2-DIBROMOTETRAFLUOROETHANE IN SOLID MATRIX. 128
5.1 Experimental methods 130
5.2 Computational methods 130
5.3 Results and discussion 131
5.3.1 Conformational distribution in the matrix 131
5.3.2 Photolysis of matrix isolated 1,2-$C_2H_4Br_2$ 135
5.3.3 Photolysis of matrix isolated TFEDB 141
5.3.4 Photolysis mechanism(s): comparison with the gas-phase 146
5.4 Summary 156
Chapter 6. PHOTOLYSIS OF 1,1-DIBROMOETHANE: A NEW VIEW OF PROTON-COUPLED ELECTRON TRANSFER. 157
6.1 Experimental set-up 159

6.2 Computational methods 159
6.3 Results and Discussion 160
6.3.1 HBr elimination pathways 166
6.3.2 Elimination of Br_2 from 1,1EDB 170
6.3.3 Role of the missing *iso*-1,1-dibromoethane 171
6.3.4 HBr···Vinyl bromide complexes. 179
6.4 Summary 183
Chapter 7. PRODUCTION AND PHOTOCHEMISTRY OF $C_2H_4\cdots Br_2$ CHARGE TRANSFER COMPLEX IN SOLID MATRIX. 184
7.1 Experimental methods 187
7.2 Computational methods 187
7.3 Results and discussion 188
7.4 Summary 195
Chapter 8. PRODUCTION AND PHOTOCHEMISTRY OF $C_2H_2\cdots I_2$ CHARGE TRANSFER COMPLEX: PROBING RADICAL PATHWAYS IN ELECTROPHILIC ADDITION OF HALOGENS. 196
8.1 Experimental set-up 197
8.2 Computational methods 198
8.3 Results and Discussion 200
8.3.1 Formation and characterization of $C_2H_4\cdots I_2$ complex 200
8.3.2 Excitation of the CT versus I_2 chromophore band 203
8.3.3 Photochemistry of $C_2H_4\cdots I\bullet$ complex 206
Chapter 9. FORMATION AND CHARACTERIZATION OF BROMINE ATOM COMPLEXES: $Br\cdots BrXCH_2$ (X= H, Cl, Br) 216
9.1 Experimental methods 217
9.2 Results and Discussion 217
9.2.1 Spectroscopy and Structure of Br atom complexes 217
9.2.2 Binding Energy of Br atom complexes 232
9.2.3 Charge Transfer photochemistry of Br atom complexes 236
9.3 Summary 240
Chapter 10. PULSED-JET DISCHARGE MATRIX-ISOLATION AND COMPUTATIONAL STUDY OF CX_2Br^+ (X=H, F). 241
10.1 Experimental set up 244

10.2 Computational Methods 244
10.3 Results and Discussion 244
10.4 Summary 252
CONCLUSION 253
BIBLIOGRAPHY 257

LIST OF TABLES

Table 3-1: Calculated vibrational frequencies in cm^{-1} (intensities in km/mol) for CF_2I_2 at various levels of theory.....46

Table 3-2 : Optimized structural parameters for *iso*-CF_2I_2 at various levels of theory. ...47

Table 3-3 Calculated vibrational frequencies (cm^{-1}) for *iso*-CF_2I_2 at various levels of theory 50

Table 3-4: Fully optimized geometrical parameters for the *iso*-CF_2Br_2 (angles are given in degrees, bondlength in angstroms) 56

Table 3-5: Vibrational frequencies of *iso*-CF_2Br_2 (B3LYP/aug-cc-pVTZ).....58

Table 4-1: Vibrational frequencies of *iso*-$CHBr_3$ determined at the B3LYP/aug-cc-pVTZ level of theory. 76

Table 4-3.**Table 4-2:** Predicted (TDB3LYP/aug-cc-pVTZ) and observed electronic absorptions for *iso*- $CXBr_3$ (X = H, F).....78

Table 4-3: Fully optimized geometrical parameters for the *iso*-$CXBr_3$ (X = H, F) species and the first-order saddle point connecting this species to the normal isomer. Angles are given in degrees and bond lengths in Ångstrøms. 79

Table 4-4 Observed and calculated electronic absorptions (in nm) of *iso*-$CXBr_3$. Calculations were performed using TDDFT with the noted functionals and an aug-cc-pVTZ basis set. Oscillator strengths are given in parentheses.....93

Table 4-5 Observed and calculated vibrational frequencies (in cm^{-1}) of *iso*-$CClBr_3$. Calculations were performed with the methods shown and an aug-cc-pVTZ basis-set. Calculated intensities in km/mol are given in parentheses. 98

Table 4-6 Observed and calculated vibrational frequencies (in cm^{-1}) of *iso*-CBr_4. Calculations were performed with the methods shown and an aug-cc-pVTZ basis set. Calculated intensities in km/mol are given in parentheses. 104

Table 4-7: Resonance contributions in the *iso*-$CXBr_3$ species derived from NRT analysis.113

Table 4-8. Natural bond order analysis for *iso*–$CFBr_2$–Br (MP2/aug-cc-pVTZ in Gaussian 09, with NBO 5.9).....114

Table 4-9 Natural bond order analysis for *iso*–$CClBr_2$–Br (MP2/aug-cc-pVTZ in Gaussian 09, with NBO 5.9).....115

Table 4-10 Natural bond order analysis for *iso*–CBr_3–Br (MP2/aug-cc-pVTZ in Gaussian 09, with NBO 5.9).....116

Table 5-1: Calculated harmonic vibrational frequencies in cm^{-1} (intensities in km/mol) of the $C_2H_4\cdots Br_2$ complex. 137

Table 5-2: Calculated wavelengths (oscillator strengths) of the vertical electronic transitions of the $C_2H_4\cdots Br_2$ complex. 139

Table 5-3: Calculated harmonic vibrational frequencies in cm^{-1} (intensities in km/mol) of the anti- and gauche conformers of the C_2F_4Br radical. 143

Table 5-4: Energies (in kcal mol^{-1}) of the fully optimized transition state (TS) and bridged structures of C_2H_4Br relative to the energies of the classical radical. 154

Table 6-1 Observed and calculated vibrational frequencies (cm^{-1}) and their intensities (km/mol) 162

Table 6-2 Calculated and Observed Electronic absorptions with their oscillator strength165

Table 6-3 Predicted Binding Energies (in kJ/mol).....182

Table 8-1 Observed and predicted electronic absorptions with their oscillator strengths.202

Table 8-2: Observed and calculated vibrational frequencies of species relevant to this work. 211

Table 9-1 Calculated and Observed Vibrational Frequencies, Intensities of the $Br\cdots BrCH_2X$ (X=H,Cl,Br) 223

Table 9-2 Optimized geometrical parameters of the $Br\cdots BrCH_2X$ (X=H,Cl,Br) complexes. Bond lengths are in Å and angles in degrees. 225

Table 9-3 Observed (Ne matrix) and predicted electronic absorptions (in nm) and oscillator strengths (*f*) of the $Br\cdots BrCH_2X$ (X=H,Cl,Br) complexes. 226

Table 9-4 Predicted binding energies (in kcal/mol, including zero-point energy) of the $Br\cdots BrCH_2X$ (X=H,Cl,Br) complexes. 234

Table 9-5 Natural Bond Orders, Charges and Natural Spin Densities in Doublet $Br\cdots BrCH_3$.....235

Table 10-1 Comparison of experiment and theory for vibrational spectra of CX_2Br^+ (X=H,F).....250

LIST OF FIGURES

Figure 2.1 Schematic of a dual stage closed-cycle helium cryostat.....9

Figure 2.2 Diagram of the vacuum system and manifold used to prepare matrix-gas mixture. 11

Figure 2.3 Schematic of various pulsed-valve adaptors 14

Figure 2.4 Electrical diagram for the high voltage discharge unit. 17

Figure 4.1: Lower panel: IR spectrum of a CF_2I_2:Ar matrix (1:1500) at 8.5 K in the C–F stretching region. **Middle panel:** Difference spectrum obtained following irradiation of an as-deposited matrix at 266 nm. **Upper panel:** Difference spectrum obtained after annealing to 33 K 38

Figure 4.2 Infrared spectrum of a CF_2I_2:Ar matrix (1:1500) at 8.5 K in the C-F stretching region before and after annealing at 35 K. **Lower panel:** Difference spectrum. 39

Figure 4.3: Infrared spectrum of *iso*-CF_2I_2 in the C-F stretching region obtained in **(a)** Ar and **(b)** Ne matrices at ~ 5 K. These spectra are difference spectra following annealing, as described in the main text. 41

Figure 4.4: UV/Vis spectra of CF_2I_2 in Neon matrix. **(a):** as deposited at 5 K, **(b):** after irradiation at 266 nm, **(c):** after annealing to 9 K. 43

Figure 4.5 Calculated (MP2/Sadlej-pVTZ) potential energy surface of CF_2I_2 in the region of the *iso*-CF_2I_2 minimum. This surface represents a relaxed 2-D scan along the C-I-I angle and C-I bond distance. 51

Figure 4.6: (a) IR spectrum of a CF_2Br_2:Ar matrix (1:5000) at 5 K. **(b)** Difference spectrum obtained following irradiation of an as-deposited matrix at 240 nm. **(c)** Difference spectrum obtained following annealing of a CF_2Br_2:Ar matrix that was first irradiated at 240 nm.**(d)** B3LYP/aug-cc-pVTZ predicted IR spectrum of *iso*-CF_2Br_2. 53

Figure 4.7: **Upper panel:** Infrared spectrum of a CF_2Br_2:Ar matrix (1:5000) at 8.5 K in the C-Br and C-F stretching region. **Middle panel:** Difference spectrum obtained after annealing at 35 K. **Lower panel:** Difference spectrum obtained following the annealing of a CF_2Br_2:Ar matrix that was first irradiated at 266 nm. 54

Figure 4.8: (a) Relaxed PES of *iso*-CF_2Br_2 calculated at the B3LYP/cc-pVDZ level of theory. **(b)** Relaxed PES of $CF_2\cdots Br_2$ complex calculated at the B3LYP/cc-pVDZ (the Br-Br distance was fixed at the equilibrium separation of Br_2.) 57

Figure 4.9: Calculated stationary points on the CF_2Br_2 potential energy surface, in gas-phase. The energies were calculated with CCSD(T)/aug-cc-pVTZ using structures optimized at the B3LYP/aug-cc-pVTZ level. 60

Figure 4.10 : Upper panel: Infrared spectrum of a CF_2Br_2:Ar matrix (1:5000) at 8.5 K in the C-Br and C-F stretching region. **Middle panel:** Difference spectrum obtained following irradiation of an as-deposited matrix at 266. **Lower panel:** Difference spectrum obtained following the second irradiation at 266 nm. 62

Figure 4.11: Calculated Mulliken charge on *iso*-CF_2Br_2 (MP2/aug-cc-pVTZ).....63

Figure 4.12(a) IR and UV/Visible spectra of a CF_2Br_2:Ar matrix at 5 K. **(b)** Spectra following irradiation at 240 nm. **(c)** Spectra following annealing to 35 K and re-cooling to 5 K. The bars in these spectra are predictions at the TD-B3LYP/aug-cc-pVTZ level ..65

Figure 4.13 Difference IR spectrum obtained following 355 nm irradiation of matrix isolated *iso*-CF_2Br_2. The IR absorptions (1188, 1240 cm^{-1}) of the isomer decrease, while the parent CF_2Br_2 bands increase. 66

Figure 5.1: Upper panel: Infrared spectrum of a $CHBr_3$:Ar matrix (~1:500) at ~ 5 K following laser irradiation at 220 nm, and the predicted (B3LYP/aug-cc-pVTZ) infrared spectrum of *iso*-$CHBr_3$. **Lower panel:** The corresponding UV/Visible spectrum, compared with the predicted (TDB3LYP/aug-cc-pVTZ) spectrum of *iso*-$CHBr_3$. 74

Figure 5.2: Upper panel: Infrared spectrum of a $CHBr_3$:Ne matrix (~1:500) at ~ 5 K following laser irradiation at 220 nm and annealing to 9 K. **Lower panel:** The corresponding UV/Visible spectrum.....75

Figure 5.3 Relaxed potential energy surface scan of *iso*-$CHBr_3$ along ∠C-Br-Br and R_{Br-Br}, calculated at the M06/6-311++G(2df,2p) level of theory. 83

Figure 5.4 Calculated stationary points on the $CHBr_3$ potential energy surfaces at various levels of theory. 85

Figure 5.5 Upper panel: Infrared spectrum of a $CDBr_3$:Ne matrix (~1:1500) at ~ 5 K following laser irradiation at 220 nm and annealing to 9 K. **Lower panel:** Infrared spectrum of a $CHBr_3$:Ne matrix (~1:500) at ~ 5 K following laser irradiation at 220 nm and annealing to 9 K. 87

Figure 5.6: (a)Relaxed redundant scan along the C-Br-Br angle for $CHBr_3$, and (b)IRC path calculated at the B3LYP/cc-pVTZ level of theory. This illustrates that the normal and *iso*-forms of $CHBr_3$ are connected by a first order saddle point. 89

Figure 5.7 Upper panel: Infrared spectrum of a $CFBr_3$:Ar matrix (~1:500) at ~ 5 K following laser irradiation at 220 nm, and the predicted (B3LYP/aug-cc-pVTZ) infrared

spectrum of *iso*-$CFBr_3$. **Lower panel:** The corresponding UV/Visible spectrum, compared with the predicted (TD-B3LYP/aug-cc-pVTZ) spectrum of *iso*-$CFBr_3$. 91

Figure 5.8 Calculated stationary points on the $CFBr_3$ potential energy surfaces at various levels of theory.....92

Figure 5.10 Observed difference IR spectrum following 220 nm laser photolysis of a CClBr3 sample held at 5 K and calculated (B3LYP/aug-cc-pVTZ) infrared spectra of the three possible isomers. Calculated intensities are arbitrary scaled; quantitative information is given in Table 4-5.....96

Figure 5.11 UV-Vis spectrum following 220 nm laser photolysis of a $CClBr_3$:Ar sample held at 5 K and calculated (TD-M06/aug-cc-pVTZ) electronic spectra of the three possible isomers. Calculated intensities are arbitrary scaled; quantitative information is given in Table 4-4 97

Figure 5.12 (a) Infrared spectrum of a CBr_4:Ar sample at 5 K. **(b)** Difference spectrum following photolysis of the sample at 266 nm. The calculated (M06/aug-cc-pVTZ) spectrum of *iso*-CBr_4 is shown as stick spectrum and the intensities are arbitrarily scaled; quantitative information is given in Table 4-6. **(c)** Difference spectrum following photolysis at 266 nm and subsequent annealing to 30 K, followed by re-cooling to 5 K.102

Figure 5.13 UV-Vis spectrum of a CBr_4:Ar sample following photolysis at 266 nm. The calculated (TD-M06/aug-cc-pVTZ) spectrum of *iso*-CBr_4 is shown as a stick spectrum with arbitrarily scaled intensity.....103

Figure 5.14 Potential resonance structures for *iso*-$CXBr_3$ species. **(b)** Comparison of calculated (B3LYP/aug-cc-pVTZ) structural parameters with those of the corresponding halomethyl cation and radical. **(c)** Calculated Mulliken charges for *iso*-$CHBr_3$ and *iso*-$CFBr_3$ at the B3LYP/aug-cc-pVTZ and (in brackets) MP2/cc-pVTZ levels of theory. ..106

Figure 5.15 Calculated structures of *iso*-$CXBr_3$ (X=F, Cl, Br) species at the B3LYP/aug-cc-pVTZ level. Selected geometrical parameters are given. Bond angles are in degrees and bond lengths are in Angstroms.....107

Figure 5.16 Calculated resonance structure weights along the IRC path in the isomerization of $CFBr_3$, using Natural Resonance Theory analysis at the MP2/aug-cc-pVTZ level. The transition state located near point 40, represents a cross-over from covalent to ion-pair binding. The five resonances structures with the largest weights are identified. 110

Figure 5.17 Calculated resonance structure weights along the IRC path in the isomerization of $CClBr_3$, using Natural Resonance Theory analysis at the MP2/aug-cc-pVTZ level. 111

Figure 5.18 Calculated resonance structure weights along the IRC path in the isomerization of CBr_4, using Natural Resonance Theory analysis at the MP2/aug-cc-pVTZ level. 112

Figure 5.19 Difference IR spectra obtained following 440 nm laser irradiation of matrix isolated **(a)** *iso*-$CHBr_3$ and **(b)** *iso*-$CFBr_3$. In each case the IR absorptions of the *iso*-species decrease and the bands of the parent increase, illustrating a facile back photoisomerization. 118

Figure 5.20 Difference spectrum following 440 nm excitation of matrix-isolated CBr_4. Laser irradiation of the isomer leads to the loss of the isomer IR bands and reformation of the parent halon. 119

Figure 5.21 Example UV-Visible spectra of iso-polyhalomethanes trapped in rare gas cryogenic matrices at 5 K. From upper left: *iso*-CF_2Br_2 (Ar), *iso*-$CHBr_3$ (Ne), *iso*-$CFBr_3$ (Ne), *iso*-CH_2I_2 (Ar). All species show weak $S_0 \rightarrow S_1$, S_2 absorptions peaking in the visible, and a stronger ($S_0 \rightarrow S_3$) absorption in the near-UV/blue region. 121

Figure 5.21 Optimized structures of the S_0 and S_3 states of iso-$CHBr_3$. The prominent Franck–Condon active modes are shown at right. 123

Figure 5.23 Isosurfaces (isovalue of 0.03) of the HOMO and LUMO of iso-$CHBr_3$.....124

Figure 5.24 Experimental (top) and Franck–Condon simulation of the $S_0 \rightarrow S_3$ transition of iso-$CHBr_3$. The simulation included three modes, as described in the text, and is shown as a stick spectrum to illustrate the density of transitions. 126

Figure 6.1:(a) Infrared spectrum of EDB in an Ar matrix at 5 K, with the calculated spectra for the anti- and gauche-conformers. The calculated spectrum indicates a 30:1 anti:gauche ratio. **(b)** Experimental and calculated spectra of matrix isolated TFEDB, indicating a 3:1 anti:gauche ratio. 133

Figure 6.2: Calculated (B3LYP/aug-cc-pVDZ) relaxed energy profiles for C-C bond rotation in EDB and TFEDB. 134

Figure 6.3: IR difference spectrum following 220 nm laser photolysis of an EDB:Ar (1:560) sample at 5 K. The calculated spectrum of the gauche-conformer of EDB [B3LYP/6-311++G(2df,2p)] and $C_2H_4 \cdots Br_2$ complex [MP2/cc-pVTZ] are shown. 136

Figure 6.4: UV/Visible spectrum of: **(a)** an EDB:Ar (1:560) sample at 5 K, **(b)** the same sample following laser photolysis at 220 nm, and **(c)** the irradiated sample following annealing 140

Figure 6.5: IR spectrum recorded after photolysis of TFEDB with 220 nm laser light, in comparison with predicted spectra of photoproducts: anti and gauche C_2F_4Br radicals. (B3LYP/aug-cc-pVTZ). 142

Figure 6.6: UV/Visible spectrum following laser photolysis (220 nm) of a TFEDB:Ar (1:2000) sample at 5 K. Shown as a stick spectrum are the predicted transitions at the TD-B3LYP/aug-cc-pVTZ level. 144

Figure 6.7: IR difference spectrum following sequential 220 and 266 nm photolysis of a TFEDB:Ar (1:2000) sample at 5 K. The disappearance of bands assigned to the gauche- and anti-conformers of the C_2F_4Br radical and growth of bands assigned to C_2F_4 is observed. 145

Figure 6.8: Schematic mechanism for the photolysis of matrix isolated EDB. 148

Figure 6.9: A color map surface representing the **(a)** UB3LYP/aug-cc-pVDZ and **(b)** UMP2/aug-cc-pVDZ relaxed redundant coordinate scans along the C-C-Br angle and H-C-C-Br dihedral in the classical (non-bridged) C_2H_4Br radical. Energies are given in kcal/mol.....150

Figure 6.10: Relaxed redundant coordinate scans along the C-C-Br angle of the C_2H_4Br radical using different DFT and *ab initio* methods and the aug-cc-pVDZ basis set. The critical points extracted from this Figure were used as guess structures for full geometry optimization 152

Figure 7.1: (a) Calculated infrared spectrum of 1,1-EDB, **(b)** experimental difference spectrum following photolysis of matrix isolated 1,1-dibromoethane at 5 K in comparison with calculated unscaled spectra of various photoproducts: **(c)** C_2H_4-Br_2**, (d)** C_2H_2-Br_2 and **(e)**HBr-CH_2CHBr Complex calculated at M06-2X/aug-cc-pVTZ level. 161

Figure 7.2: UV-Visible spectrum **(a)** matrix isolated 1,1-dibromoethane as deposited at 5 K, **(b)** difference spectrum recorded after photolysis at 220 nm, **(c)** spectrum recorded after annealing to 32K following irradiation and **(d)** theoretical spectrum of C_2H_4-Br_2 calculated at the TD-M06-2X/aug-cc-pVTZ level of theory. 164

Figure 7.3 Calculated Stationary points on the 1,1-dibromoethane Potential Energy Surface (PES) at the CCSD(T)//M06-2X/aug-cc-pVTZ level of theory. 168

Figure 7.4: Calculated partial potential energy surface (PES) for HX (X=Br, Cl) elimination from 1,1-dihaloethane, at the CCSD(T)//M06-2X/aug-cc-pVTZ.....169

Figure 7.5: Difference spectrum following 240 nm irradiation of 1,1dibromo2,2,2-trifluoroethane in a Ne matrix at 5 K, in comparison with calculated spectra of parent and photoproduct, calculated at the M06-2X/aug-cc-pVTZ level. 173

Figure 7.6: Partial Potential Energy Surface (PES) of 1,1-EDB showing the sequential pathway of the molecular elimination involving the *iso*-halon intermediate (CCSD(T)//M06-2X/aug-cc-pVTZ level). 175

Figure 7.7 Intrinsic Reaction Coordinate calculations of the reaction paths linking 1,1-dibromoethane and *iso*-1,1-dibromoethane to the elimination of molecular products HBr and Br_2, performed at M06-2X/aug-cc-pVTZ 176

Figure 7.8: Relaxed scans along C-Br-Br bond angle, in both singlet and triplet PES (M06-2X/aug-cc-pVDZ).....177

Figure 7.9: Prediction of microscopic rates as function of energy (kcal/mol), using input values from MP2/aug-cc-pVTZ results. 178

Figure 7.10 Optimized structures for various stationary points calculated on the PES of 1,1-Dibromoethane 180

Figure 7.11: Electrostatic potential surface maps showing intermolecular interactions for various HBr···Vinyil bromide complexes, calculated at the MP2/aug-cc-pVTZ (isovalue=0.0004) 181

Figure 8.1: Orientation of bromine in its complex with acetone as determined from X-Ray crystallographic studies.[206].....186

Figure 8.2: Radical mechanisms for reaction of the C_2H_4…Br_2 complex. 189

Figure 8.3 charge transfer mechanisms for reaction of the C_2H_4…Br_2 complex. 190

Figure 8.4 Spectra for three different experiments. (detail in in the text) The calculated (MP2/aug-cc-pVTZ) spectra of C_2H_4 and the C_2H_4···Br_2 complex are shown. 192

Figure 8.5: Difference IR spectrum obtained following photolysis of the C_2H_4—Br_2 complex at 266 nm. A single photoproduct is observed, *anti*-1,2-dibromoethane. The calculated (unscaled MP2/aug-cc-pVTZ) spectrum of the product is shown.....194

Figure 9.1 Structural motifs for haloalkyl radicals (X=Cl, Br, I) 199

Figure 9.2: UV/visible spectrum of (a) Ethylene−I2 complex, as deposited in Ar matrix. (b) Difference spectrum after photolysis at 355 nm laser light. 201

Figure 9.3: Difference infrared spectrum after photolysis of Ethylene-I_2 complex with 240 nm laser light. In comparison spectra of photoproducts calculated at the M06-2X-aug-cc-pVTZ-PP level. 205

Figure 9.4 UV-Vis spectrum obtained after irradiation of C_2H_4···I complex with 355 nm laser light. In comparison with calculated spectra of C_2H_4···I_2 and C_2H_4···I. 207

Figure 9.5 Difference IR spectrum obtained following 355 nm irradiation of an ethylene:I2:Ne (~1:2:500) matrix that was pre-irradiated at 240 nm 208

Figure 9.6 Photoinitiated the reaction mechanisms of (a) Br_2 and (b) I_2 with ethylene. 212

Figure 9.7 Intrinsic reaction coordinate scan from symmetric bridged transition state, illustrating concerted stereospecific addition.....213

Figure 9.8 Selected geometrical parameters of the optimized structures of the ethylene complexes with atomic and molecular iodine, calculated at the M06/aug-cc-pVTZ-pp level.....214

Figure 9.9 IR spectra obtained before and after photolysis of the $C_2H_4\cdots I_2$ complex ...215

Figure 10.1: Infrared spectrum of a CH_3Br/Ar (1:220) matrix following pulsed deposition on a KBr window at 23 K and subsequent cooling to 5 K, with (red, upper) and without (black, lower) discharge.....219

Figure 10.2: (a) The difference spectrum of the scans shown in Figure 6.1, compared with the predicted IR spectrum of the $Br\bullet\bullet\bullet BrCH_3$ complex. **(b)** the corresponding UV-Visible spectrum of the complex, with the predicted spectrum at the TD-CAM-B3LYP/aug-cc-pVTZ level.....220

Figure 10.3: Mulliken plot of the CT band energy (in cm^{-1}) versus the donor ionization energy for a range of Br atom complexes with various donors, as described in the text.231

Figure 10.4: photochemistry of the CT of $Br\cdots BrCH_2Br$ complex. **Upper panel:** UV-Vis spectrum of $BrCH_2Br$ in Ar without discharge. **Middle panel:** UV-Vis spectrum of $BrCH_2Br$ in Ar with discharge. **Lower panel:** UV-Vis spectrum after photolysis with 355 nm laser light.....238

Figure 10.5: difference spectrum illustrating the formation and destruction of the $Br\bullet\bullet\bullet BrCH_3$ complex. **Upper trace:** the difference spectrum of discharge on and off is shown. The loss of the parent absorption near $1200cm^{-1}$ and growth of the complex band at slightly lower cm^{-1} is apparent. Upon photolysis of the complex at 355 nm (**blue, lower trace**), the complex bands decrease, and the parent band increases. 239

Figure 11.1: Dependence on discharge voltage of the integrated infrared absorbance of three species (CH_2Br, CH_2Br^+ and $CHBr_2^+$) formed in CH_2Br_2:Ar discharge and subsequently trapped using the pulsed-jet discharge matrix isolation technique. 243

Figure 11.2: (a) Infrared spectrum of a CF_2Br_2:Ar matrix (~1:5000) at 8.5 . **(b)** Spectrum obtained following irradiation of an as-deposited matrix at 240 nm. **(c)** Spectrum obtained following trapping of the discharge products of a CF_2Br_2:Ar sample (~1-5000) using pulsed-jet matrix isolation technique: the strongest absorptions are assigned.....248

Figure 11.3: Experimental (line) and calculated (Bars) infrared spectra of the CH_2Br^+ ion. The calculated frequencies and intensities of the ion are given in Table 10-1.....249

LIST OF SYMBOLS AND ACRONYMS

aug-	augmented
B3LYP	Becke 3-Parameter (Exchange), Lee, Yang and Parr (correlation; density functional theory)
BLYP	Becke-Lee-Yang-Parr (Density functional)
CBS	Complete Basis Set
CC(S,D,T)	Coupled Cluster (single, double, triple excitations)
cm^{-1}	wavenumber
CT	Charge transfer
$\angle$	Angle
DFT	Density Functional Theory
EDB	Ethylene Dibromide
ET	Electron Transfer
FTIR	Fourier Transform Infrared
GC	Gradient Corrected
h	Planck's constant
HF	Hartree-Fock
HOMO	Highest Occupied Molecular Orbital
Hz	Hertz
IR	Infrared
IRC	Intrinsic Reaction Coordinate
K	Kelvin degrees
kJ/mol	Kilojoules per mol
kPa	KiloPascal
L/min	Litter per minute
LDA	Local Density Approximation
LUMO	Lowest Unoccupied Molecular Orbital
mJ	Millijoule
MPn	Møller-Plesset methods
ms	Millisecond
Nd:YAG	Neodymium Yttrium Aluminum Garnet
nm	Nanometer
NRT	Natural resonance theory
PCET	Proton coupled electron transfer
PES	Potential Energy Surface
PT	Proton transfer
REMPI	Resonance Enhanced Multi Photons Ionization

TD-DFT	Time Dependent Density Functional Theory
TFEDB	Tetrafluoro Ethylene Dibromide
TS	Transition State
UV/Vis	Ultraviolet and Visible
λ	wavelength

Chapter 1. INTRODUCTION

Our research program is mainly focused on studying transient intermediate species (free radical, ions, carbenes and weakly bound species). Transient chemical intermediates have a very short life-time and their characterization has always been a challenge to physical chemistry. However two complementary approaches have proven to satisfy this ambitious goal. The first one uses fast detection techniques such as ultrafast transient absorbance spectroscopy [5] to take a snapshot of these fleeting intermediates in real time. In the second approach, one can lengthen the lifetime of these intermediates by studying them at low temperature. In this document we discuss about one technique in the latter category, which is called "Matrix Isolation Technique".

Matrix isolation was introduced for the first time by George Pimentel, in 1945.[6],[7] This technique is based on a simple idea, whereby the transient target species are trapped and frozen in an inert rare gas (generally Ar, Ne and N_2) but more recently extended to quantum solids such as para-hydrogen (p-H_2). The sample is deposited on a cold transparent window and can be subject to various spectroscopic measurements (IR, UV/Vis and Raman). For chemists, the most common reasons for wanting to do matrix experiments are to observe directly and characterize reaction intermediates, to generate and study novel reactive species, to determine the structures of reactive species, to characterize molecular complexes and study weak interactions between species, and finally to freeze and study particular molecular conformations.[6, 7] For instance, Räsänen and co-workers isolated three conformers of chloroacetic acid, two differ from

Cl-C-C-O dihedral angle with 5 kcal mol^{-1} interconversion barrier, and the third isomer presenting an intramolecular H-bonding.[8]

Once the sample deposited onto the cold transparent window, it can be subject to various spectroscopic and analytical methods, mostly the infrared and UV/Vis spectroscopy and occasionally the analysis is supplemented with less common techniques such as Raman spectroscopy, laser-induced emission and electron spin resonance (ESR).[6]

In comparison with other spectroscopic techniques, the matrix-isolation offers several advantages and the purely physical effect is the most evident. The matrix host acts not only as a cage but also as a clamp that prevent rotation and diffusion of the guest, this effect is reflected by fairy narrow IR bands. One may think about the host-guest interactions and the effect that would have on the spectrum, but fortunately, these interactions are weak in the solidified matrix and the frequency shifts tend to be small. However, the perturbation is more significant in the electronic spectrum due to the interaction between valence electrons of the guest molecule and rare-gas lattice.[7] Another great advantage of Matrix Isolation experiments is the “cage effect” and this property can be exploited to influence reaction pathways. For instance the cage effect will minimize the probability of two radicals to diffuse away from each other, but will rather allow them to get closer, react and form a product, generally unstable at room temperature, which is at its turn also trapped in matrix and can be subject to subsequent analysis. In photochemical research, compared with flash photolysis, the matrix isolation has brought the benefit of accessing the IR range and providing more structural information.[6]

The main inconvenience of carrying Matrix-isolation experiments is that the guest compound must be volatile at a temperature below its decomposition point, since the sample is highly diluted and the dilution is achieved in gas phase prior to deposition onto the cold window.

The studies compiled in this work are more specifically focused on halogenated compounds (halomethanes, haloethanes, polyhalogenated complexes and various isomers). Some of these compounds are naturally formed (especially in marine environment) other are man-made, where they have been used as refrigerants, solvents, propellants, fumigating agents, fire retardants and most of them are known as “halons” and CFC’s (chlorofluorocarbons). [9, 10]

Halons comprise a class of halogenated compounds containing bromine that have been widely used as gaseous fire retardants in a wide range of fire and explosion protection applications.[11] The production and use of halogenated compounds was mainly motivated by their chemical inertness and stability. Unfortunately, this property is the one leading to their harmful effect on the environment: the long tropospheric lifetime plays in favor of their transport to the stratosphere, where they can dissociate upon solar radiation and produce highly reactive species involved in ozone depletion. The ozone layer constitutes a thin shield protecting all life on Earth from the Sun’s harmful ultraviolet radiation. This radiation has the potential to damage DNA in living cells, inhibit plan growth, damage animal and human skin, be at the origin of skin cancer, affect the immune system or damage the eye cornea.[12-14]

Scientists believed that the ozone concentration has been constant over the history of earth; however it has been recently observed that this concentration is declining fast. The first shocking discoveries about the ozone depletion took place in the 1980's.

In 1985, the revelation of rapid ozone depletion in Antarctic, known as "Ozone Hole", by the British Antarctic Survey caught the scientific community by surprise and without explanation. It was reported that the springtime Antarctic ozone layer has decreased by almost half in comparison with measurements taken in 1960 and late 1970's[15] Since then, divergent theories were developed and after three decades of extensive research the most accepted is the one showing the relation between ozone depletion and man-made chlorine and bromine compounds.

For instance halons 1211, 1301 and 2402 (CF_2ClBr, $CBrF_3$, $C_2F_4Br_2$) which are fully halogenated chemicals that have very long lifetimes in the atmosphere are decomposed in stratosphere releasing reactive bromine atom that is extremely damaging to ozone.[16] These halogen radicals are known to initiate catalytical ozone cycles such as [16]:

$$Cl + O_3 \rightarrow ClO + O_2$$
$$ClO + H_2O \rightarrow HClO + O_2$$
$$HOCl + h\nu \rightarrow OH + Cl$$
$$OH + O_3 \rightarrow HO_2 + O_2$$
$$\textbf{Net: } \mathbf{2\ O_3 + \rightarrow 3\ O_2}$$

$$Br + O_3 \rightarrow BrO + O_2$$
$$BrO + H_2O \rightarrow HBrO + O_2$$
$$HOBr + h\nu \rightarrow OH + Br$$
$$OH + O_3 \rightarrow HO_2 + O_2$$
$$\textbf{Net: } \mathbf{2\ O_3 + \rightarrow 3\ O_2}$$

Because no significant reservoir species exists for iodine, (HI, HOI and $IONO_2$ would all be rapidly photolyzed), and almost all inorganic iodine would exist as active IO or I atom.[17]

Coupling the chemistry of iodine to that of bromine and chlorine

$IO + ClO \rightarrow I + Cl + O_2$

$IO + BrO \rightarrow I + Br + O_2$

followed by reaction of free halogen atoms could lead to ozone depletion.

In 1986 Bottenheim and co-workers [18] and later Hausmann and Platt [3], in 1992, have shown that the low ozone concentration regions in stratosphere were well correlated to the high concentration in bromine (especially in BrO). Since then, several studies have confirmed these observations not only in the Arctic [1, 19-21], but also in Antarctic.[22],[23] Satellite observations show that regions with elevated BrO frequently extend over several million square kilometers.[24, 25]

The international scientific community, as represented by the Scientific Assessment of Stratospheric Ozone: 1994, believed that current scientific findings strengthened the conclusion that "anthropogenic chlorine and bromine compounds, coupled with surface chemistry on natural polar stratospheric particles, are cause of polar ozone depletion". [26]

In order to face this alarming discovery, as the International Community, in September 1987, 47 countries agreed on the "Montreal Protocol" [26] on substances that deplete the Ozone Layer which first required controls on consumption of ozone depleting chemicals. This protocol was amended in 1990 (London) and 1992 (Copenhagen) to accelerate the phase-out required by the original protocol. Some additional adjustments

were made to this protocol in 1995 (Vienna), 1997 (Montreal) and 1999 (Beijing). Halons production in U.S. ended on December 31st, 1993.

Although it has been shown that ozone depletion is associated with the high concentrations in halogenated reactive species, the so complicated mechanisms governing this destruction are not fully understood. In this work we are more focused on the photochemical behavior of various halogenated compounds, especially their degradation upon ultraviolet radiation and the photochemical distribution.

In our experiments we are studying different intermediates derived from polyhalogenated compounds, and half of the document discuss about a special class of iso-halon species, which exhibit a typical C-X-Y bonding scheme, where X and Y are halogen atoms. To our knowledge, the first iso-species were observed in UV irradiated glasses containing halomethanes, which exhibited "color centres" that were assigned first to trapped electrons [27], and later to trapped ions[28] The iso-halons play a key-role in atmospheric and solution phase photochemistry, where there are thought to be plausible precursor to molecular halogen products and monocarbenes involved in addition reactions such as cyclopropanation of olefins.[29]

This document compiles studies on various polyhalogenated intermediates trapped in inert rigid matrix, interrogated spectrospically and computationally. We hope that our results will contribute to better understand the photochemical behavior of polyhalogenated species, and to some extent help to understand mechanism in different phenomena observed in atmospheric chemistry.

Chapter 2. EXPERIMENTAL AND COMPUTATIONAL METHODS

2.1 Experimental methods

2.1.1 Matrix-isolation spectroscopy.

Matrix-isolation spectroscopy includes a range of experimental techniques in which the reactives *guest* molecules are trapped in rigid *host* material.

The benefits of isolating the sample from contaminant evironment were known before the matrix-isolation technique. At the end of the nineteen century, scientists have noticed that some organic compounds emitted light when immersed in liquid nitrogen at 77 K. This enhancement of phosphorescence process was partially due to the absence of triplet quenchers such as oxygen. However this approach was not universal, since most of solutions tend to form cloudy solid with highly light-scattering properties, making absorption spectroscopy more difficult.

In 1930, Gilbert N. Lewis and co-workers studied various solvent mixtures in search of a clear glass with good optical properties.[30] They found that EPA, a mixture made of ether, isopentane and alcohol (ethanol), typically in the ratio 5:5:2 was the best candidate for that purpose. This mixture formed a clear glass transparent throughout the UV-Visible region.

The efforts to conduct chemical reaction in a clean environment continued until 1954, when George Pimentel proposed for the first time, the idea of isolating reactive species in a frozen and inert noble gas.[31] The lowest temperature achieved at that time was about 66 K, cold enough for Xe matrix, but too warm to solidify Ne, Ar or Kr.

Nowadays, modern cryostats, commercially available, can achieve lower temperatures, generally in the range of 12 to 3K. Special cryostats, using mixture of ^{3}He and ^{4}He isotopes as a cryogenic fluid can reach temperatures down to few mK.[6]

2.1.2 Matrix-isolation apparatus

The matrix isolation used in our experiments utilizes a cryostat based upon a closed cycle two-stage He displex (ARS Displex DE-204S). On the cold tip is mounted an optical sample holder containing a 25.4 mm diameter CaF_2 or KBr window. A loop of 1.0 mm diameter Indium wire is placed between window and sample holder to ensure good thermal contact, while a thin layer of cryogenic grease (Apiezon N) and an Indium washer are placed between the cold tip and sample mount for the same purpose. A nickel-plated copper radiation shield with two circular ports encloses the cold tip. The displex and attached radiation shield are inserted into a clamped vacuum shroud and sealed with a double O-ring seal that allows the sample assembly to be rotated under vacuum.

The vacuum shroud is equipped with four orthogonal window mounts. On two opposing mounts are attached 50.8 mm diameter polished KBr windows. A 10 mm thick custom-made flange that couples to a commercial pulsed valve is attached to a third mount (Figure 2.1). The pumping station consists of a liquid-nitrogen trapped diffusion pump (Varian H-4) backed by a scroll pump (Edwards XDS-10), connected to the cryostat via a NW-40 port welded onto the vacuum shroud. An ionization gauge (Edwards WRG-S-NW25) mounted at this port monitors the vacuum inside the cryostat. The temperature at the cold tip and sample window are monitored simultaneously using two Si diodes that are interfaced to a temperature controller (Lakeshore 330).

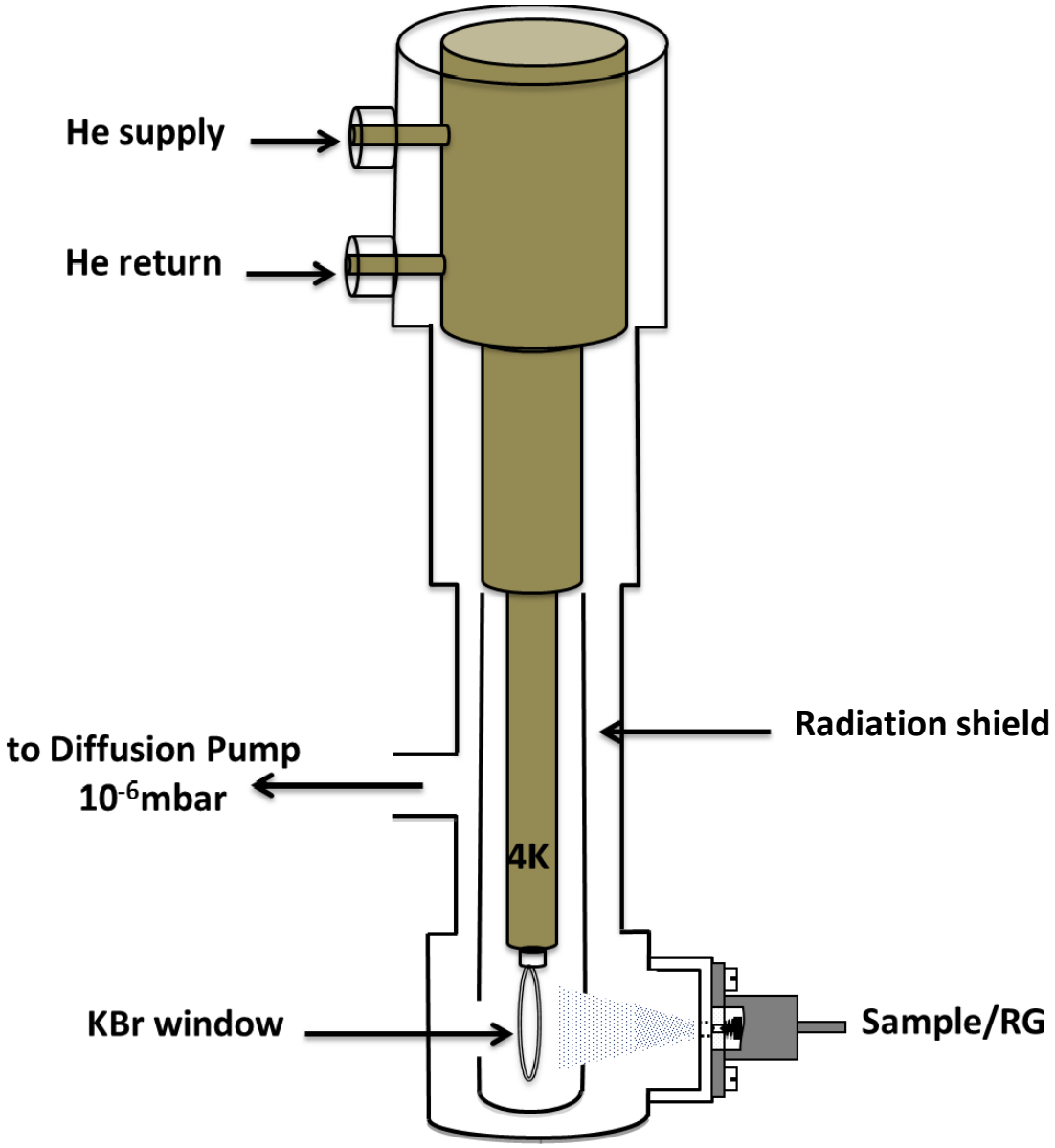


Figure 2.1 Schematic of a dual stage closed-cycle helium cryostat

2.1.3 Sample preparation techniques

2.1.3.1 Making matrix-gas mixture

While the basic idea of matrix-isolation technique seems straightforward, one of the big challenges is the generation of reactive species. This can be achieved in different ways such as deposition of a matrix containing a stable precursor followed by irradiation, external generation of the reactive species in gas the phase, co-condensation of two streams of chemicals onto the cold window or by allowing reactive species, generated by one of the methods stated above, to undergo a thermal reaction within the matrix.

In our experiments, the matrix-gas mixture is typically made up as follow: a fresh precursor sample is placed into a small stainless steel tank connected to the manifold and vacuum system is mixed with high purity Ar or Ne gas. Prior to mixing with the rare gas, the precursor is purified by few freeze-pump-thaw cycles. The mixture is prepared on a manifold (Figure 2.2) using standard manometric techniques, to achieve a typical precursor:rare-gas ratio in the range of 1:500 to 1:2000, depending on the signal intensity of the compound or its tendency to cluster.

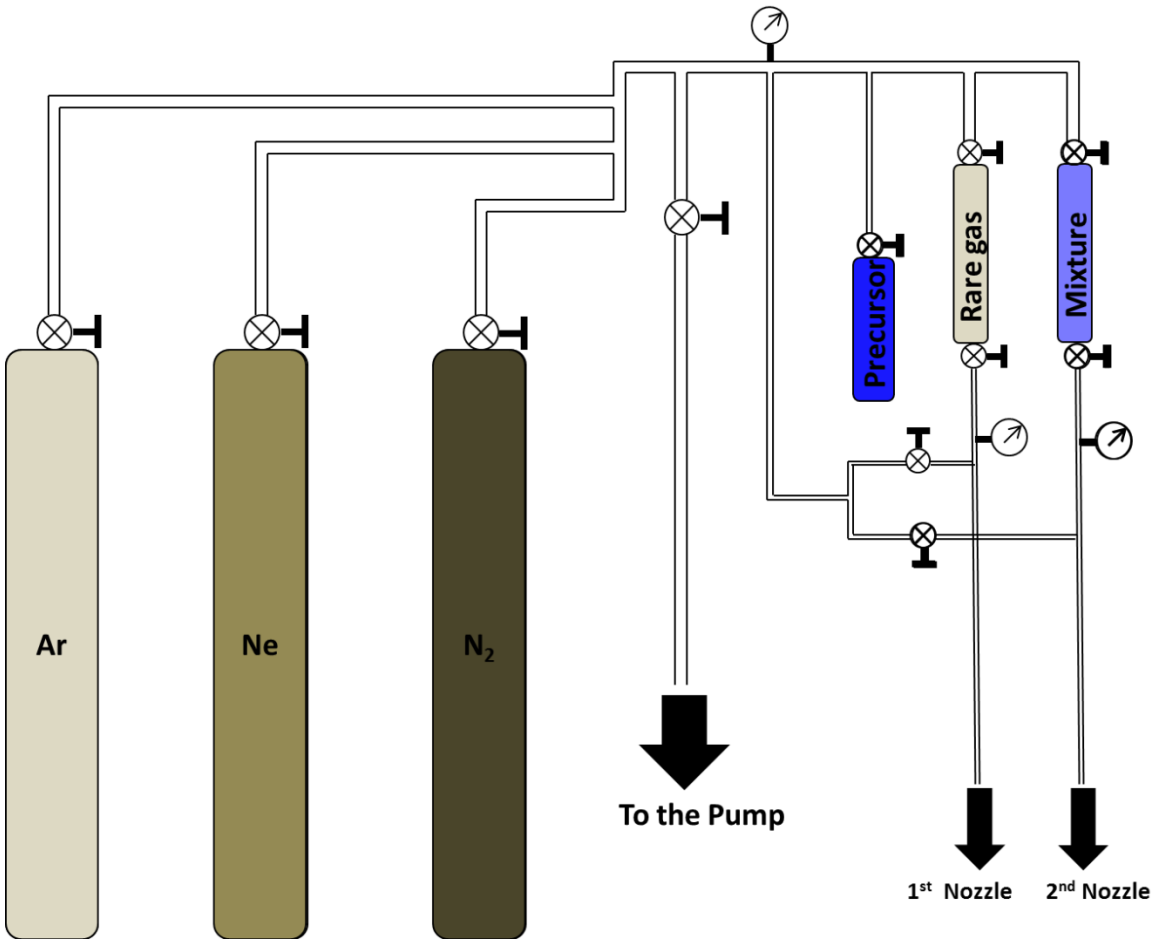


Figure 2.2 Diagram of the vacuum system and manifold used to prepare matrix-gas mixture.

2.1.3.2 Matrix-gas deposition

The pre-mixed sample can be applied to the cold window by either pulsed or continuous deposition and both techniques are used in our laboratory. The slow spray-on continuous deposition is the most widely used. The sample flow is controlled by a needle valve at a typical rate of 1 torr min^{-1}. In the pulsed deposition, a premixed matrix-gas is deposited onto the cold KBr window held at ~ 5 K using a solenoid actuated pulsed valve (Parker-Hannifan, General Valve Division, Iota-1). Typical deposition conditions are: 1ms pulse duration, 5 Hz repetition rate, 1-2h deposition time, about 1 bar backing pressure. A schematic diagram of a pulsed valve coupled to the cryostat is shown in Figure 2.3

A primary advantage of the pulsed deposition method over continuous deposition is that the short (ms) pulses produce a self-annealing effect due to the instantaneous temperature rise in the surface layers during deposition, which gives rise to clear, highly transparent matrices. Pulsed deposition also minimizes the effect of trapping residual gases such as air and water vapor.

For the experiments that require the co-deposition, such as the formation of charge-transfer complex, we have developed a new method using a dual nozzle late mixing source (Figure 2.3) where the two chemicals are deposited on the cold window from two different nozzles. Note that the entire matrix isolation system is still based on a "pulsed deposition" and the timing of pulses can be adjusted to overlap, be slightly delayed, or operate in a difference of phase.

We have also found another advantage, in that the dependence of the absorption intensity on discharge current varies dramatically for different species, which provides a convenient diagnostic for identification.

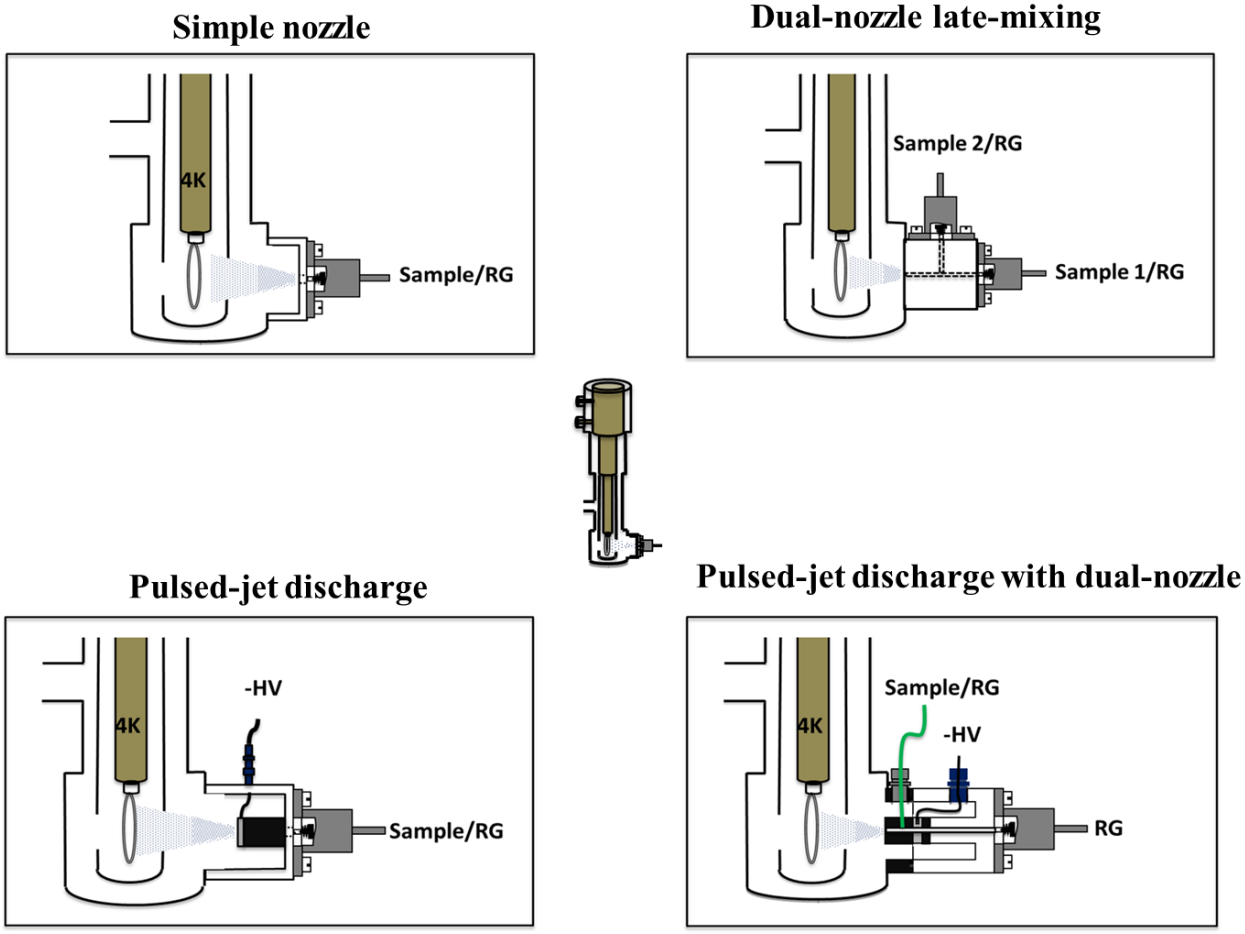


Figure 2.3 Schematic of various pulsed-valve adaptors

2.1.3.3 Pulsed-jet high voltage discharge matrix-isolation

In some of our experiments, where we were looking for various reactive carbocations we used another alternative way to produce transient species, called high voltage discharge. This method was initially demonstrated by Bondybey and co-workers [32, 33], who combined a pulsed discharge source with matrix isolation and demonstrated that a variety of transient species (radicals, carbocations, and carbanions) could be studied.

A schematic of the pulsed-jet discharge matrix isolation apparatus shown in Figure 2.3 consists of two parts: a solenoid actuated pulsed nozzle and a discharge adapter connecting the nozzle to the cryostat. The adapter is made of two aluminum electrodes separated by an electrical insulator (Teflon block).

A custom-made aluminum discharge assembly that coupled to a commercial pulsed valve (Parker-Hannifan, Series 9) was attached at right angle to the cryostat. Discharge was initiated by applying a negative DC high voltage (typically -600 V) through a 15 kΩ current limiting ballast resistor to a stainless steel ring electrode, which was separated from the wall of the assembly by a 3 mm Delrin spacer. The body of the assembly, connected to the power supply ground, served as the second electrode. The discharge current and stability was monitored using the voltage drop across a small (100 Ω) resistor placed in the discharge circuit, as shown in Figure 2.4.

Based on this design, we have improved our experimental set-up by incorporating the idea of discharging the pure rare gas prior to meeting with the sample gas. We have designed and built a dual-nozzle late-mixing adapter coupled to the discharge unit, as

depicted in Figure 2.3. This design was found to be very efficient without producing extensive fragmentation at higher voltages.

From our experience we have found that the dependence of absorption intensity on discharge current varies dramatically for different species and this provides a convenient diagnostic for identification.

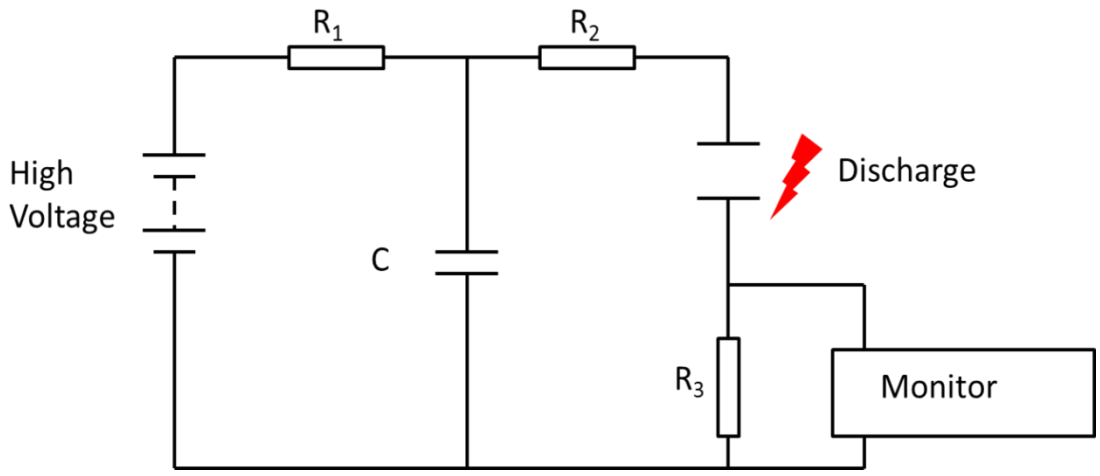


Figure 2.4 Electrical diagram for the high voltage discharge unit.

2.1.4 Irradiation light sources

In order to investigate the photochemistry behavior of various polyhalogenated compounds, appropriate light sources are needed to photolyzed precursor molecules or intermediates species trapped in solid matrix. In our experiments we mainly use a monochromatic light from a Nd:YAG laser [34] or a dye laser [35].

Nd:YAG laser is based on the light emitted from a neodymium-doped yttrium aluminum garnet ($Nd:Y_3Al_5O_{12}$) rod. The YAG crystal is doped with about 1% of Nd^{3+}, and these neodymium cations emit light, with photon energy of 1064 nm, when they relax from $^4F_{3/2}$ to $^4I_{11/2}$ excited states. The Nd:YAG output frequency can be multiplied by non-linear optical methods to higher harmonics: 532, 355 and 266 nm.[34]

In our experiments the sample on the cold window is irradiated with the third (355 nm) or fourth harmonic (266 nm) of a Nd:YAG laser (Continuum Minilite). However, it often happens that the molecules being studied do not absorb at any of wavelengths provided by a Nd:YAG laser. In such case, the appropriate wavelength is be obtained by using a dye laser system (Lambda-Physik Scanmate 2E) pumped by a third (355 nm) or second harmonic (532 nm) of Nd:YAG laser (Continuum NY-61). Despite its low power output, the dye laser system has advantage of flexibility to tune the output wavelength anywhere in the range of ~370 to 900 nm, and this selectivity can be very helpful in case there are more than one species, with different absorption bands, in the matrix-sample.

Typical irradiation times are 1-2 h and in order to fill the cold window and avoid damage to the KBr window, the photolysis beam is expanded using a 4:1 beam expander.

2.1.5 Detection and data collection

Infrared absorption spectra are obtained with Fourier transform infrared spectrometers (Mattson, Galaxy series equipped with a deuterated triglycine sulfate detector or Nicolet 6700 model, equipped with a DTGS detector), which are purged at a flow rate of 20 L/min using a purge gas generator (Parker-Balston 75–52A). The IR spectra are recorded at typically 1 cm^{-1} resolution and averaged over 128 scans. Ultraviolet/visible (UV/VIS) absorption spectra are obtained with an Agilent 8453 diode array spectrophotometer. The reference spectra for both IR and UV/VIS are recorded for the cold sample holder immediately prior to matrix deposition, and the entire cryostat is mounted on a home-built rail system that allows quick interchange between spectrometers.

All spectra were referenced to the cold sample window, and subsequently transferred to a spreadsheet and analysis program (Origin 8.0) for workup.[36]

2.2 Computational methods used

In modern chemical research, the experimental is aided by an extensive theoretical support, due to increase in computational power. Computational chemistry is a very powerful tool to predict and understand in detail many properties such as structure (i.e. the expected positions of the constituent atoms), absolute and relative (interaction) energies, electronic charge distributions, dipoles and higher multipole moments, vibrational frequencies, vertical transitions and oscillator strengths, reactivity or other spectroscopic quantities, and cross sections for collision with other particles.

In spectroscopy in general and particularly in the matrix-isolation field computational chemistry is very useful in order to compare the experimental data and aid in the assignment of different spectral bands. The routine calculations include the geometry optimization, vibrational frequencies to compare with IR or Raman spectra, vertical excitations and oscillator strengths for the UV/Vis spectrum.

In our research, we use various computational methods, always trying to get as much accurate results as possible, however depending on the cost of the calculations, the need and the nature of the system to be studied. The next section describes briefly the commonly encountered methods in this work.

2.2.1 Hartree-Fock method

Hartree-Fock theory is the basis on which all of the electronic structure calculations rest and is one of the simplest approximate theories for solving the many-body Hamiltonian. It is based on a simple approximation to the true many-body wavefunction: that the wavefunction is given by a single Slater determinant of N spin-orbitals.

$$\psi(N) = \frac{1}{\sqrt{N!}}\begin{bmatrix} \psi_1(x_1) & \psi_2(x_1) & \cdots & \psi_n(x_1) \\ \vdots & & \ddots & \vdots \\ \psi_1(x_n) & \psi_2(x_n) & \cdots & \psi_n(x_n) \end{bmatrix} \qquad \text{(Equation 2.1)}$$

The variables x_1 indicates a function that depends on the space and spin coordinates of the electron labeled “1”.

The wavefunction is antisymmetric with respect to an interchange of any two electron positions (Pauli Exclusion Principle). The fundamental assumption of the

Hartree-Fock self-consistent field theory is that each electron sees all others as an average field.

In general, the energy is given by this expression:

$$E_{HF} = \frac{\langle \psi_{HF} | \hat{H} | \psi_{HF} \rangle}{\langle \psi_{HF} | \psi_{HF} \rangle} \quad \text{(Equation 2.2)}$$

Where $\hat{H}$ is the Hamiltonian.

In spite of its fairly significant fundamental assumption, an enormous amount of effort was provided on developing mathematical and computational techniques to reach the HF limit, which is to say to solve the HF equations with the equivalent of an infinite basis set, with no additional approximations. If the HF limit is achieved, then the energy error associated with the HF approximation is defined as the electron correlation energy $E_{corr.}$[37] Beside the electron-correlation issue (which limits the best calculation to 99% of the total energy), the HF theory is known to be simple, fast and inexpensive, with favorable scaling into the number of basis functions (N^4) [38]

2.2.2 Møller-Plesset Perturbation Theory (MP*n*)

In general, perturbation theory can be thought as a set of mathematical methods, used to find an approximate solution of a complicated system, which cannot be exactly solved, starting from the exact solution of a small and related system.[39] In quantum mechanics, the perturbation theory comprises approximation schemes used to describe a complicated quantum system in terms of simpler ones, generally HF.

Introduced by Christian Møller and Milton S. Plesset in 1934 [38, 40], these methods improve on the HF method by adding electron correlation effects by means of

Rayleigh-Schrodinger perturbation theory. Within the Perturbation theory, the Hamiltonian is partitioned as $\hat{H} = \hat{H}_0 + \lambda\hat{V}$ where $\hat{H}_0$ is the unperturbed HF Hamiltonian, λ a real parameter and $\hat{V}$ is the external perturbation (correlation potential). The Møller-plesset methods are typically referred to by the acronym MP*n*, where the letter *n* indicates the order at which the perturbation theory is truncated (MP2, MP3, MP4). Since the HF is the energy correct through first-order in Møller-Plesset perturbation theory, the MP2 method is the most commonly used to correct the electron-correlation. However is not clear how to reach the exact result with this approach. In fact, the perturbation expansion has been shown not to converge as N becomes larger in some cases.

The MP formalism should be used carefully, because on one side the PT works best when the perturbation is small and on the other side in the MP the perturbation is the full electron-electron repulsion energy, which is a rather large contributor to the total energy. MP*n* approach has another drawback of being not variational and the calculated energy can be less than the true energy. However the MP*n* provide a good treatment of the electronic structure, and the MP4 has empirically proven to count for ~95% of the correlation energy.[38]

2.2.3 Coupled Cluster methods

Introduced by Coester and Kümmel in 1958 [41], the Coupled Cluster is a numerical technique used for describing many electron systems. The main feature of the CC method, common with other correlated *ab initio* methods, is the extension from a one to a multi determinant function.

While the CI methods use a linear excitation operator, the Coupled Cluster methods use an exponential excitation operator and the wavefunction is usually written as [41] :

$$\psi = e^{\hat{T}}\Phi_0 \qquad \text{(Equation 2.3)}$$

Where $$\hat{T} = \hat{T}_1 + \hat{T}_2 + \hat{T}_3 + \cdots + \hat{T}_n \qquad \text{(Equation 2.4)}$$

Within the Coupled Cluster approach, the operator $\hat{T}_i$ acts on a HF single determinant Φ_0 to generate all excited Slater determinants.

$$\hat{T}_1\Phi_0 = \sum_i^{occ}\sum_a^{vir} t_i^a \Phi_i^a \qquad \text{(Equation 2.5)}$$

$$\hat{T}_2\Phi_0 = \sum_{i<j}^{occ}\sum_{a<b}^{vir} t_i^{ab} \Phi_i^{ab} \qquad \text{(Equation 2.6)}$$

Including all cluster operators up to $\hat{T}_n$ will generate all possible excited determinants and the resulting wavefunction will be equivalent to the full CI. However, this is impossible for all but smallest systems. So, here comes the advantage of using the exponential operator, because it can be expanded as Taylor series and truncated at some excitation level. Unfortunately the energy derived from this truncation will no longer be exact, and the accuracy of the approximation will depend on how many terms are included in $\hat{T}$. Since the $\hat{T}_1$, does not improve over the HF, the lowest level of approximation is $\hat{T} = \hat{T}_2$, referred to as *Coupled Cluster Doubles* (CCD) including the doubly excited states. A more complete model is provided by CCSD, which includes singly and doubly excited states at slightly more demanding cost (scaling as N^6). The next higher level is given by CCSDT which adds the triply excited states, but this method is more expensive than the CISDT (scaling as N^8), and can only be applied to small systems. This problem can be fixed by treating singly and doubly excited states

analytically while the triply excitations are treated perturbatively, which leads to the CCSD(T) method often used in this work. [38, 41, 42]

2.2.4 Density functional methods

Although the modern density functional theory was developed in early 1960s with the Hohenberg-Kohn Theorems, the first idea of DFT was introduced in 1926.[38, 43, 44] The basic philosophy of this method is that energy is obtained from electron density instead of a "wave function" (the Hamiltonian depends on the total number of electrons). The DFT methods replace the HF, rather than being an additional step as in MP*n* methods. They offer many advantages such as adding some degree of electron correlation, providing good results at lower price, being more robust than HF for open shell system treatment, etc. In general, in density functional theory, the energy of a system is computed as a sum of six components:

$$E_{DFT} = E_{NN} + E_T + E_V + E_{coul} + E_{exch} + E_{corr}$$

where E_{exch} term represents the electron-electron exchange energies, however different from those used in HF. The last term, E_{corr}, describes the correlated movement of electrons and it is not included in Hartree-Fock scheme. However the DFT methods encounter some difficulties like the poor treatment of long range interactions and the need of knowing the dependence of a chemical property on the density.[38]

There are roughly three types, or categories, of density functional methods. *Local density approximation (LDA)* methods assume that the density of the molecule is uniform throughout the molecule, and is typically not a very popular or useful method. *Gradient corrected (GC)* methods look to account for the non-uniformity of the electron density.

Hybrid methods, as the name suggests, attempt to incorporate some of the more useful features from *ab initio* methods with some of the improvements of DFT mathematics, such as the use of exact exchange functional from Hartree-Fock. In this work we used various DFT methods such as BLYP, B3LYP, M06 and M06-2X, taking the advantage of their good performance at relatively lower cost in comparison with *ab initio* methods.

BLYP method is a gradient corrected method combining Becke's 1988 exchange functional with the correlation functional by Lee, Yang and Parr. The widely used B3LYP is a hybrid DFT method mixing different parameters in a following scheme [38, 45]:

$E_{XC} = 0.2\ E_X^{(HF)} + 0.8\ E_X^{(LSDA)} + 0.72\ DE_X^{(B88)} + 0.81\ E_C^{(LYP)} + 0.19\ E_C^{(VWN).}$

Although, these methods have shown a good performance in predicting many chemical properties, such as geometry optimization and frequency calculation, they are known to poorly perform in energy calculation, especially in case of long range interactions. Truhlar and co-workers have developed M06 and M06-2X DFT methods, which are more reliable at long range interactions, in a sense they correct the self-consistent error found in local DFT exchange functionals.[46]

2.2.5 Basis sets

2.2.5.1 Gaussian-type basis sets

By definition, a basis set is a mathematical description of orbitals of a system, which is used for approximate theoretical calculation or modeling. Different basis sets are

used in computational chemistry, in order to derive chemical information by solving Schrodinger equation.

Commonly, in electronic structure calculations, there are two types of basis functions: *Slater Type Orbitals* (STO) and *Gaussian Type Orbitals* (GTO) and within the frame of this document we will only discuss about the latter class.

A *Gaussian Type Orbital* can be written in terms of polar or Cartesian coordinates with a subtle difference: for instance, a d-type GTO has five components in spherical coordinates ($Y_{2,2}$, $Y_{2,1}$, $Y_{2,0}$, $Y_{2,-1}$, $Y_{2,-2}$) but there appear to be six components in the Cartesian coordinates (x^2, y^2, z^2, xy, xz, yz). The latter six functions, however, may be transformed to the five spherical d-functions and one additional s-function ($x^2+y^2+z^2$)

Generally in electronic structure modeling, the most important factor is the number of basis functions to be used and the smallest number of basis function possible is called the minimum basis set. In this case the hydrogen and helium atoms would require only one s-function to contain all the electrons. There are different types of basis sets, but in this work we will discuss about two main types: Pople's and Dunning's basis sets.

The most known Pople's basis sets are typically *split valence double-zeta* basis sets and this class includes basis sets such as 3-21G, 6-21G, 4-31G, 6-31G… Using a generic formula X-YZG, the first number x represents the number of primitives Gaussians assigned to each core atomic orbital. The valence orbitals are split between outer and inner orbitals and they are represented by two basis functions each: Y and Z. Triple-zeta (Z-YZWG) or quadruple-zeta can also be used. In this work we generally used Pople's basis sets ranging from 6-31G to 6-311++G**. In early 1990's, Dunning

and co-workers [38, 47-50] developed another type of basis set called "*correlation consistent and polarization valence split basis sets"* with the generic acronym cc-pVnZ (n=D: double, T: triple, Q: quadruple…) The advantage of using these basis sets is that they include shells of polarization functions (d, f, g etc.) and as their size increases, the calculated energy tend to converge to the complete basis set limit (CBS). As indicated by their name, these basis sets work only for valence orbitals.

In order to treat anions, highly excited states, or supermolecular complexes which are more spatially diffused, the basis set has to be more flexible to allow a weakly bound electron to localize far from the remaining density. In this case, the basis set is augmented with a diffuse function, symbolized by "aug" prefix for the Dunning's basis sets and "+" sign for Pople's family. For instance, aug-cc-pVTZ basis set has f, d, p and s diffuse functions on the heavy atoms and d, p and s function on H and He atoms.

With bond formation in molecules, the atomic orbitals get distorted from their original shape. This phenomenon can be treated by adding "*polarization functions*" to the standard basis sets. Polarization functions help to describe electron away from the nucleus and they correspond to one unit of angular momentum higher than the valence orbitals. Within the People's family, the polarization function are represented by the "*" sign.

Electron correlation treatment becomes more difficult as the number of electrons involved increase and regular Dunning's basis sets are not available for molecules including large atoms. Fortunately, most of chemical properties depend mainly on valence electrons and this problem can be solved by considering only valence electrons and replacing core electron by an approximate pseudopotential. Effective core

pseudopotential basis sets have been developed in the past [51-53] and within this approach, the computation time no longer depends on Z, but on the screened nuclear charge, $Z^{eff} = Z - N_{core}$ which remains a small number of electrons. In our calculations, iodine atom is treated with an aug-cc-pVTZ-PP basis set, developed by Peterson and co-workers in 2003.[54] Similarly to their counterparts from the Dunning's family, these small-core pseudopotential and correlation consistent basis sets (cc-pVnZ-PP) exhibit a systematic convergence and accuracy as their size increases. In some other cases, calculations on molecules including iodine atom were performed using the Sadlej-pVTZ basis set, which has proven to provide an aug-cc-pVTZ output quality.[55]

2.2.5.2 Basis set superposition error and Counterpoise correction

As two molecules approach each other, their basis functions integrals can overlap. In such case, one monomer can borrow functions from nearby components resulting in significant increase in its basis set, artificial stabilization and improvement in calculations. The main problem is not the overlap itself but, the inconsistent treatment of the monomers, since the overlap directly depends on the distance between monomers. For example, if the total energy is minimized as function of geometry, there is a mismatch between the short-range interaction energy in the dimer and the long-range interaction energy when the overlap is too small.

There are different methods to fix this problem, and in this work we have used the counterpoise method [41, 56] to correct the energy of weakly bound complexes. The typical uncorrected interaction energy between two monomers A and B would be calculated as following:

$$\Delta E_{int}(AB) = E_{AB}^{AB}(AB) - E_{A}^{A}(A) - E_{B}^{B}(B) \quad \text{(Equation 2.7)}$$

Where the superscript indicates the basis used and the number in parenthesis corresponds to the system studied. This can be corrected by estimating the amount of artificial stabilization for each monomer:

$$E_{BSSE}(A) = E_{A}^{AB}(A) - E_{A}^{A}(A) \quad \text{(Equation 2.8)}$$

$$E_{BSSE}(B) = E_{B}^{AB}(B) - E_{B}^{B}(B) \quad \text{(Equation 2.9)}$$

After substitution, the CP corrected interaction energy will be given by:

$$\Delta E_{int}^{CP}(AB) = E_{AB}^{AB}(AB) - E_{A}^{AB}(A) - E_{B}^{AB}(B) \quad \text{(Equation 2.10)}$$

2.2.6 Correlation between IR and UV-Vis spectra

In order to ensure the correlation between IR and UV/Vis spectra, and assuming that the IR and UV/Vis were sampling the same spot of the matrix, we were able to estimate the oscillator strength of the UV/Vis transitions. First, the integrated IR absorption was divided by the calculated intensity (in km/mol) to give the column density in the matrix. The oscillator strength was then obtained by dividing the Integrated UV/Vis absorption by the column density utilizing the following formula [57]:

$$f = \frac{\int A_{UV}(\tilde{\nu})d(\tilde{\nu})}{N_{IR}} \times (1.87 \times 10^{-7} mol/km)$$

Chapter 3. *ISO*-POLYHALOMETHANES

The following chapters discuss studies we conducted on polyhalomethane molecules. Polyhalomethanes constitute an important class of polyhalogenated compounds that undergo photoinduced bond breaking and structural rearrangement reactions that have long been of interest to atmospheric and environmental chemistry, photosynthetic chemistry, and chemical reaction dynamics[58, 59]. Different types of polyhalomethane molecules have been observed in the atmosphere and they are believed to be significant sources of reactive halogens released into the atmosphere.[2, 4]

Many studies, theoretical and experimental, referenced in this work, have been carried out on polyhalomethane molecules and the major issue encountered was the controversial photodecomposition pathways. Two major channels have been identified, the first one leads to the formation of halogen atom and a reactive radical, the second channel is the one leading to molecular products.

Studying water catalyzed dehalogenation reactions, in 2004, Phillips and co-workers showed that photolysis of bromoform, at 240 nm in pure water as solvent, led to production of HBr (H^+ and Br^- in solution)[60].

$$CHBr_3 + nH_2O \xrightarrow{h\nu} CO + 3HBr + (n-1)H_2O \qquad \text{(major products)}$$

$$CHBr_3 + nH_2O \xrightarrow{h\nu} HCOOH + 3HBr + (n-2)H_2O \qquad \text{(minor products)}$$

Supported by *ab initio* calculations, they suggested a five-step mechanism for this reaction, where the first step consisted of homolytic C-Br bond cleavage. In this study, it was confirmed that the Br- was derived directly from the parent bromoform.

It was previously demonstrated that condensed phase environments promote a new photochemical path leading to the formation of metastable *iso*-polyhalomethane species. [29, 61-70] The known functions of these reaction intermediates include the production of ions in the ocean [33] and photocyclopropanation reactions of olefins in solution.[58, 59, 71]

In 2005, Carpenter and co-workers[72], investigated the solar photolysis of different polyhalomethanes (CH_2I_2, CH_2ICl, and CH_2IBr) in water, seawater and saltwater. The excitation in the gas phase produced mainly iodine atom and a halomethane radical. In aqueous solution, the cage effect pushed the reaction to the formation of a dihalomethane isomer (CH_2X-I, X=I, Br, Cl). These results are in agreement with the photolysis of CH_2I_2 in 0.5M NaCl study, done by Guan and co-workers, where the *iso*-CH_2I-Cl species was observed.[73] Different mechanisms have been proposed for this reaction, and they are all thought to occur following the first step in which the C-I bond is homolytically cleaved, producing iodine atom and CH_2I radical.

Phillips and co-workers [74] studied photochemistry of CH_2I_2, CH_2IBr, and CH_2ICl in the UV range and at low concentration in water. They observed a transient CH_2X-I intermediate, which reacted further with water to give almost complete conversion into $CH_2(OH)_2$, along with HX and HI products.

In 2000, Cameron and Bacskay [75] studied computationally the thermal decomposition of CF_2X_2 (X=Cl, Br, I), using G2/ID and G3/ID methods. It was suggested that CF_2X_2 will decompose following different channels:

$$CF_2X_2 \rightarrow CF_2X + X \qquad (1)$$

$$CF_2X \rightarrow CF_2 + X \qquad (2)$$

$CF_2X_2 \rightarrow CF_2 + 2X$ (3)

$CF_2X_2 \rightarrow CF_2 + X_2$ (4)

The energy calculations showed that the molecular elimination is favored by ~10 to 12 kcal/mol in case of Cl and Br, but they could not find a multicenter transition state that would relate products to parent molecule. In the same study, the calculations showed that in case of CF_2H_2, the molecular elimination channel is favored by ~ 40 kcal/mol, and an associated transition state was localized on the ground state surface.

The molecular elimination has been also observed experimentally in various studies [76, 77] and this led us to investigate computationally and experimentally the possibilities to produce the molecular photoproducts.

While it is difficult to visualize the photochemical release of dihalogen from polyhalomethanes, in this work we show the dependence of molecular elimination channel on isomerization pathway.

Chapter 4. FORMATION AND CHARACTERIZATION OF *iso*-CF_2X_2 (X=I, Br) IN SOLID MATRIX

In expansion of earlier studies highlighted in previous section, this chapter discusses the photochemistry of two dihalogenomethane molecules CF_2I_2 and CF_2Br_2 and photochemical formation of their homologue isomers.

In a study conducted by Huber and co-workers in gas phase, using REMPI technique [78] , they found that excitation of CF_2I_2 into the first excited singlet S_1 state at 350 nm, produces 98% of I($^2P_{3/2}$) and 2% of I($^2P_{1/2}$) atoms while the excitation at $\lambda \geq 266$ nm leads to a concerted three-body decay: $CF_2I_2 \rightarrow CF_2 + I + I$. In different but related studies, it has been shown that photolysis of CF_2I_2 at shorter wavelength (193 nm) produces molecular iodine.[79-82] In contrast to the gas-phase photochemistry, Tarnovsky and co-workers [83] observed that excitation of CF_2I_2 in *n*-hexane at 350 nm, leads to the ultrafast formation of molecular iodine in a 32% quantum yield. Excitation of related CH_2XI (X=Cl,Br and I) molecules, in solution, has led to formation of molecular halogen products, and the typical UV-Vis band associated to *iso*-CH_2XI intermediates have been observed. However no such intermediate was observed in case of CF_2I_2 and this may raise a question of whether or not the photochemical reaction path of CF_2I_2, in solution is entirely different. Note that, theoretical studies [84, 85] have characterized *iso*-CF_2I_2 as a minimum on the on ground state of CF_2I_2 molecule.

The dibromodifluoromethane (CF_2Br_2), also called halon-1202, is one of the bromine containing halocarbons molecules which have been of particular interest in few past years. Halons are used as fire extinguishing agents, both in built-in systems and in

handheld portable fire extinguishers. These molecules have received extensive investigation due to their high ozone depletion potential. They can dissociate upon solar radiation and produce the bromine atom which is many times more efficient at destroying ozone than chlorine. Their production in U.S. ended on December 31st, 1993. Many recent works were exploring the wavelength mechanisms of the photochemical reactions that occur upon UV excitation.[86]

Although their ozone depleting potential is well known, the photochemistry of halons is not well understood. For instance, the dibromodifluoromethane (CF_2Br_2) is a prototypical halon, exhibiting a rich photochemistry with many pending questions such as the branching between two nearly isoenergetic dissociation channels :(i) a radical channel yielding $CF_2Br + Br$ and (ii) a molecular elimination channel yielding $CF_2 + Br_2$.

Normally the CF_2Br_2 molecule shows two bands at ~188 nm and ~226 nm in the UV absorption spectrum recorded at room temperature. In 1960, Mann and Thrush[87] reported formation of CF_2 following flash photolysis of CF_2Br_2. In 1972, a gas-phase photolysis study at 260 nm proved the formation of both CF_2Br radical and Br atoms.[88] Later, prompt fluorescence from CF_2 was observed in the 248 nm photolysis of CF_2Br_2 and emission from Br_2 and Br was also observed.[89] These results suggested the possibility of both channels at this wavelength. The photodissociation of CF_2Br_2 at 248 nm, using photofragment translational energy spectroscopy, has shown only one channel: C-Br fission; however it was found that CF_2 was formed under collision free conditions. This was claimed to be due to the secondary photolysis of the CF_2Br radical. More recent studies [90-92] interrogated the wavelength dependence of the photolysis and most of them showed a consistent picture of the UV photodissociation of CF_2Br_2 as involving the

C-Br fission in an initial step followed by a second C-Br fission as result of intramolecular vibrational energy redistribution, which leads to CF_2 formation for wavelength below 260 nm. On the other side, Huber et al.[93] , Park et al.[94], Lin and co-workers[95] and other recent studies, have shown the possibility of the Br_2 elimination channel.

In this study, we investigated the photolysis of CF_2Br_2 in Ar matrix at ~5 K at wavelength of 240 nm and 266 nm, above and below the threshold for CF_2 formation reported by Kable and co-workers[90].

Our experiments were carried out in much dilute matrices (CF_2Br_2:Ar=1:5000) in attempt to avoid aggregation. In 1977, Jacox [96] carried out a similar study on photolysis of CF_2Br_2 using a more concentrated sample (CF_2Br_2:Ar=1:270) and various polymerization products such as C_2F_4 (1129, 1180, 1330 cm^{-1}), $(CF_2Br)_2$ (769, 877, 1014, 1173, 1244 cm^{-1}) were observed. The high concentration in matrix increases the probability of having guest molecules in close proximity and the photoproducts from different parent molecules may undergo a recombination reaction to form polymer species. In contrast, for much diluted matrices, there is less probability to polymerize and the recombination reactions are most likely to occur among photoproducts derived from the same parent molecule.

This work complements the earlier studies of isoforms of CH_2X_2 (X=Cl, Br, I), which were isolated and characterized under matrix conditions by Maier and co-workers.[64, 65] and our primary goal is to produce, trap and spectroscopically characterize *iso*-CF_2I_2 and *iso*-CF_2Br_2 molecules in solid argon.

4.1 Experimental set up

The detail on the matrix-isolation set-up used in these experiments was given in Chapter 2. The CF_2I_2 sample (Synquest Laboratories, 98.5% purity), used without further purification was mixed with high purity Ar gas to produce a mixture of typically 1500:1 Ar:CF_2I_2 ratio. This mixture was deposited onto the cold window held at 8 K using the pulsed deposition technique.[32, 97-99] Following deposition, the cold window was irradiated with 355 nm and 266 nm, in separate experiments. Typical irradiation times were 30 min at 355 nm (6.2 mJ/pulse) and 10 min at 266 nm (2.3 mJ/pulse). Note that the gas-phase absorption cross-section of the parent is around three times larger at 266 nm than at 355 nm.[68]

The CF_2Br_2 sample (Synquest Laboratories, 99% stated purity, used without further purification) was premixed in a 0.5 L stainless steel mixing tank with high purity Argon (CF_2Br_2:Ar = 1:1500). The photolysis was done using a laser light at 266 nm or at 240 nm, as described in Chapter 2. The gas-phase absorption cross section of CF_2Br_2 at 210K is ~30 times larger at 240 nm than at 266 nm[68]; and therefore typical irradiation times were 1 ½ h at 240 nm (10 ns pulses, 1 mJ/pulse and 10Hz) and 5h at 266 nm (5 ns pulses, 2.3mJ/pulse, and 5Hz).

4.2 Computational methods

All calculations were performed using Gaussian 03 suite.[100] Geometry optimization was performed using the B3LYP and the M06–2X density functional[101, 102] on one hand, and the MP2 and the coupled-cluster singles and doubles (CCSD)

wavefunctions on the other hand. Two triple zeta quality basis sets are used for the purpose of this study, (i) a small-core relativistic correlation consistent triple zeta valence basis in combination with a pseudopotential to describe iodine atoms (aug-cc-pVTZ-PP),[103] and (ii) the Sadlej-pVTZ [104] full atomic basis set with polarization on all atoms. All angles are reported in degrees and bond lengths in Ångstrøms.

4.2.1 Results and discussion

4.2.2 Characterization of iso-CF_2I_2 in solid Ar matrix

The sample was deposited in a ratio of ~1:1500 Ar:CF_2I_2. The irradiation was done at 266 nm and 355 nm for different experiments, and in both cases the sample was annealed at 33K.

The IR spectrum recorded after deposition shows two main features, assigned to the parent CF_2I_2 C-F stretching modes, at 1058 and 1105 cm^{-1}.(Figure 4.1) These frequencies are in very good agreement with the computational predictions: B3LYP/Sadlej-pVTZ (1059, 1102 cm^{-1}), MP2/Sadlej-pVTZ (1058, 1104 cm^{-1}). The photolysis either at 266 nm or at 355 nm produced new species identified to be CF_2 (1143, 1151, 1241 cm^{-1})[89], and CF_2I (626, 1123, 1172 cm^{-1}). Note that the 1172 cm^{-1} band of CF_2I radical has not been previously reported!

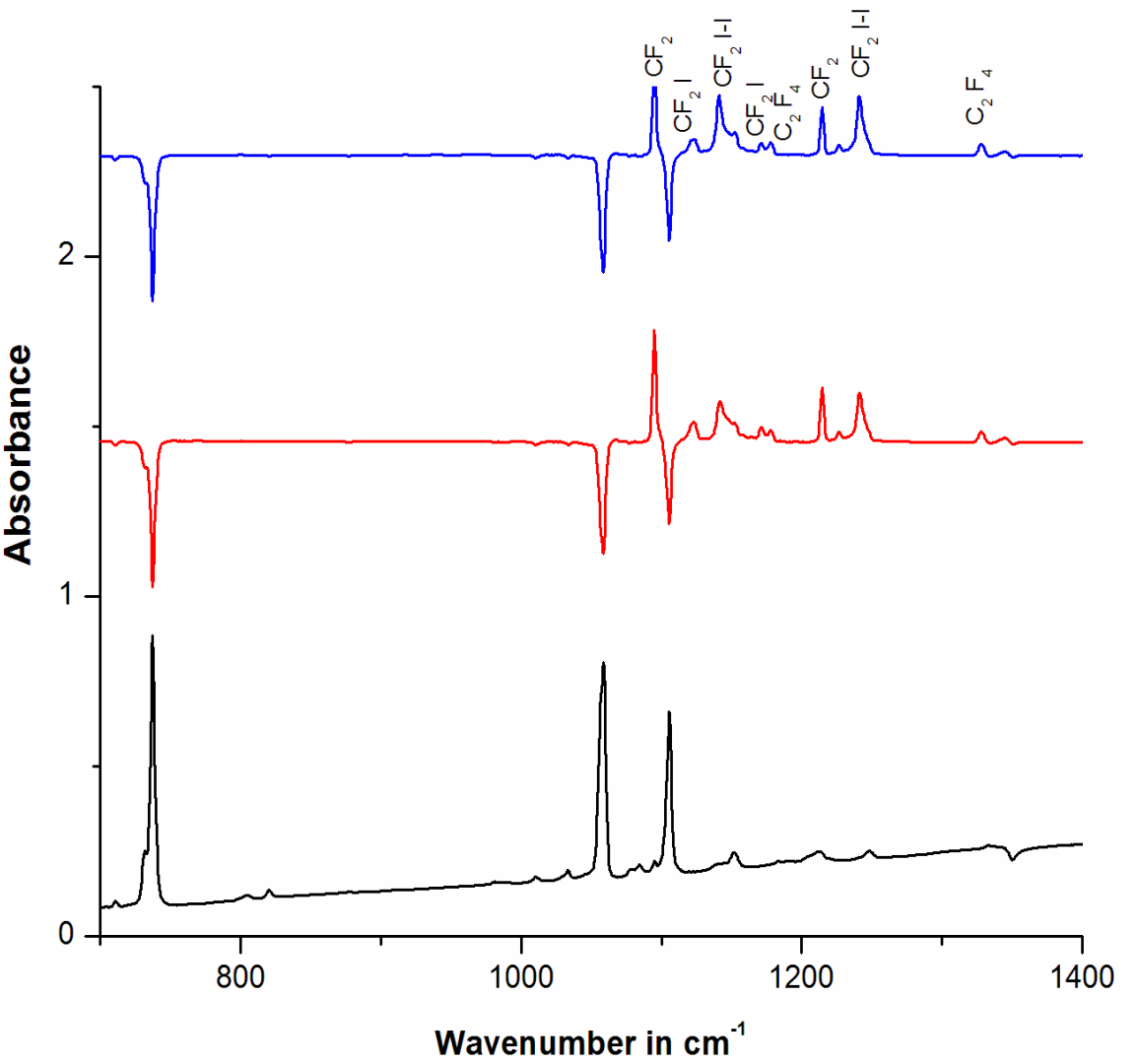


Figure 4.1: Lower panel: IR spectrum of a CF_2I_2:Ar matrix (1:1500) at 8.5 K in the C–F stretching region. **Middle panel:** Difference spectrum obtained following irradiation of an as-deposited matrix at 266 nm. **Upper panel:** Difference spectrum obtained after annealing to 33 K

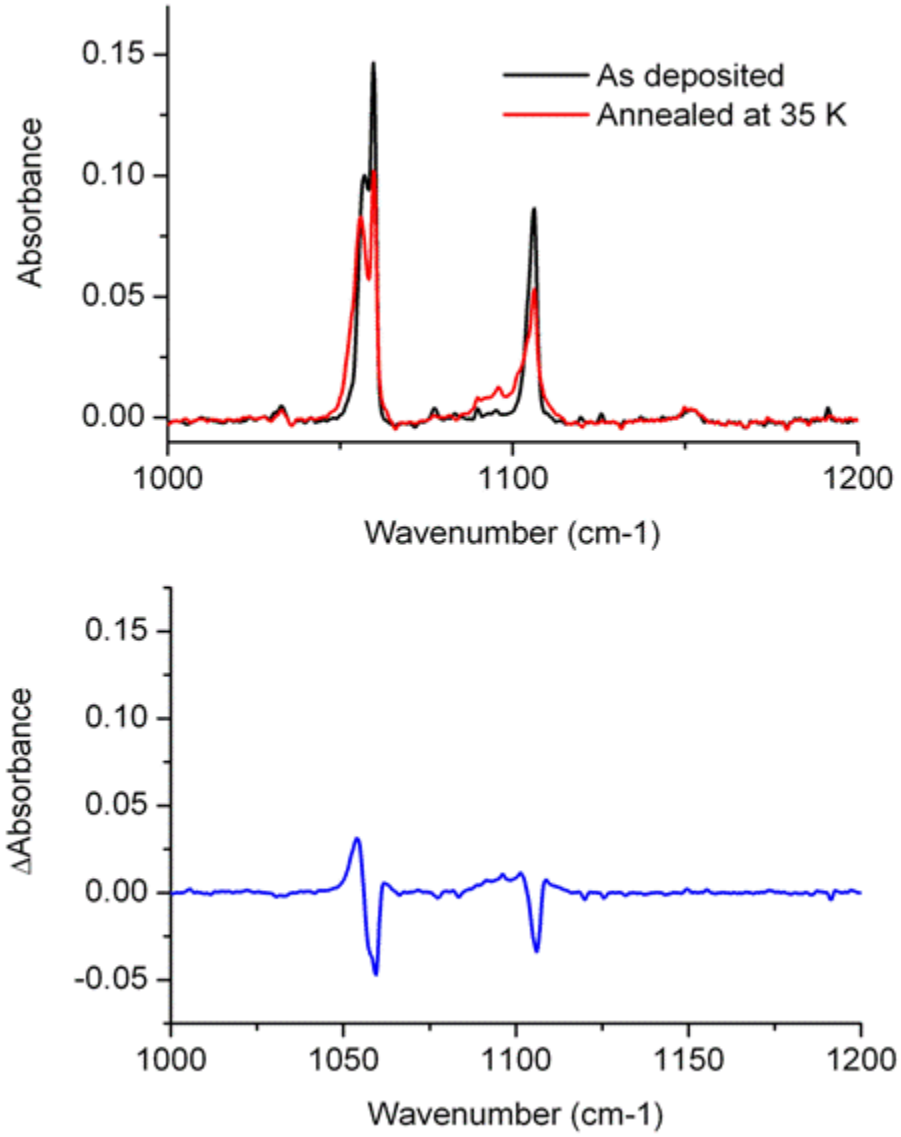


Figure 4.2 Infrared spectrum of a CF_2I_2:Ar matrix (1:1500) at 8.5 K in the C-F stretching region before and after annealing at 35 K. **Lower panel:** Difference spectrum.

Upon annealing at 33K, only the intensity of the unassigned bands at 1143 and 1241 cm^{-1} significantly increased all other bands decreased (Figure 4.1). A band close to 1058 cm^{-1} also increased a bit, however this reflects changes in the spectrum of the unphotolysed parent upon annealing (Figure 4.2). This change may be attributed to the trapping of the molecule in different types of site in the rare gas lattice. The annealing experiments show that the 1143 and 1241 cm^{-1} bands belong to the same species, and the growth upon annealing shows that this is not a radical intermediate. The band assigned to C_2F_4 did not increase upon annealing, suggesting that the CF_2 did not form a dimer, it rather recombined with I_2 or I. The recombination to the parent CF_2I_2 molecule would require inserting the CF_2 into I-I bond and such process needs to overcome an 18.8 kcal/mol barrier. Conversely the attachment of I-I onto the CF_2 is an exothermic barrierless process and, therefore, it would be easier to form *iso*-CF_2I-I in matrix. Based on that, three bands were assigned to the *iso*-CF_2I_2 species: C-F asymmetric (1143cm^{-1}) and C-F symmetric stretching modes, the third one (1151cm^{-1}) was due to the site splitting. This was confirmed by the experiments in Ne matrix, as shown in Figure 3.3. Such splitting frequently occur for molecules isolated in rare-gas matrices and may be attributed to the trapping of the molecule in different types of sites in the rare-gas lattice.[96]. As we expected, the IR spectrum in Ne matrix shows a blue shift of ~ 5 - 11 cm^{-1}, with respect to the Ar matrix results.

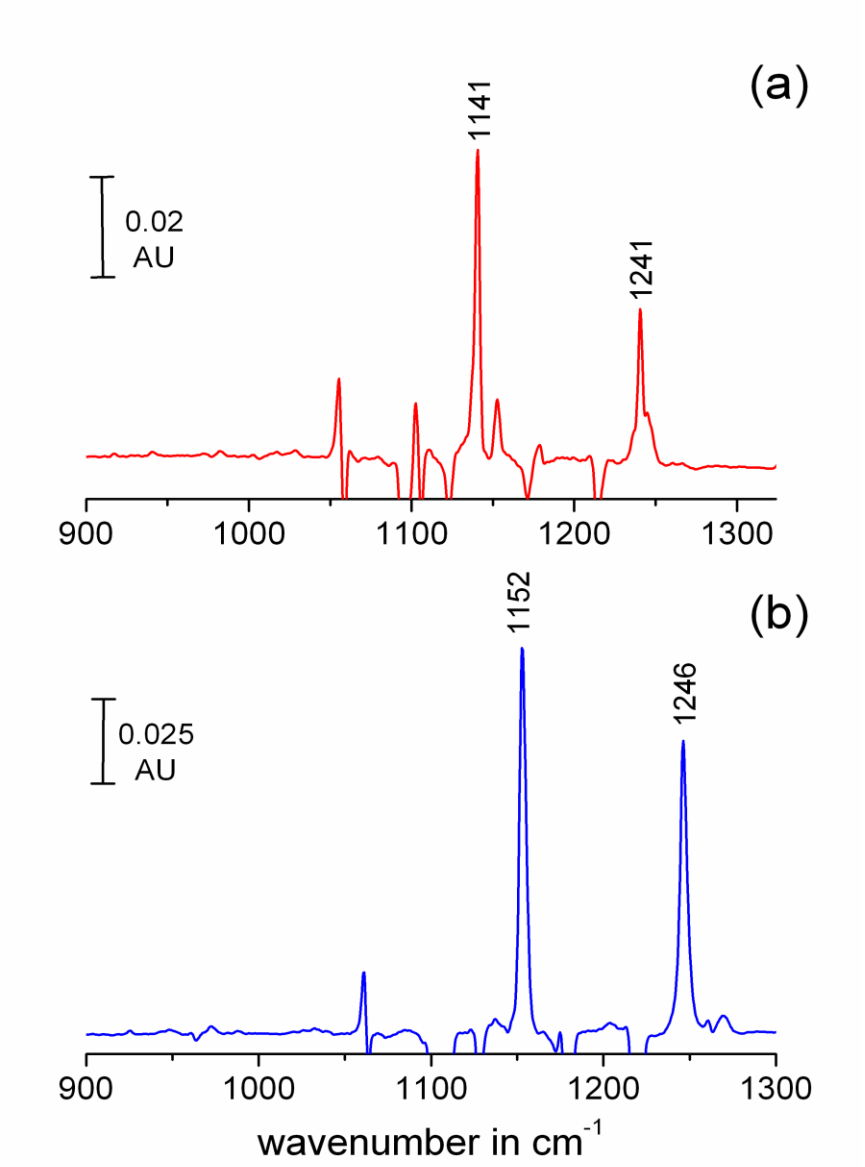


Figure 4.3: Infrared spectrum of *iso*-CF_2I_2 in the C-F stretching region obtained in **(a)** Ar and **(b)** Ne matrices at ~ 5 K. These spectra are difference spectra following annealing, as described in the main text.

The *iso*-CF_2I_2 absorption has also been observed in UV/Vis range. Figure 4.4 shows the UV/Vis spectrum of CF_2I_2:Ar sample. As deposited the parent spectrum shows two strong bands at ~270 and 296 nm. The broadness of these bands allowed the photolysis at either 266 nm or 355 nm. However, due to the difference in absorption cross-sections at the wavelength considered, the irradiation at 266 nm was much more efficient than at 355 nm (Figure 4.4 a). Upon irradiation at 266 nm laser light, the bands due to the parent molecule significantly decreased, and new bands appeared: one at ~250 nm due to the CF_2 photoproduct and a broad band at ~ 468 nm assigned to the *iso*-CF_2I_2. This band increased in intensity when the sample was annealed by heating the window to 10 K and re-cooling back down. This suggests that this band was due to a molecule stabilized in matrix and not a radical species. (Figure 4.4 c)

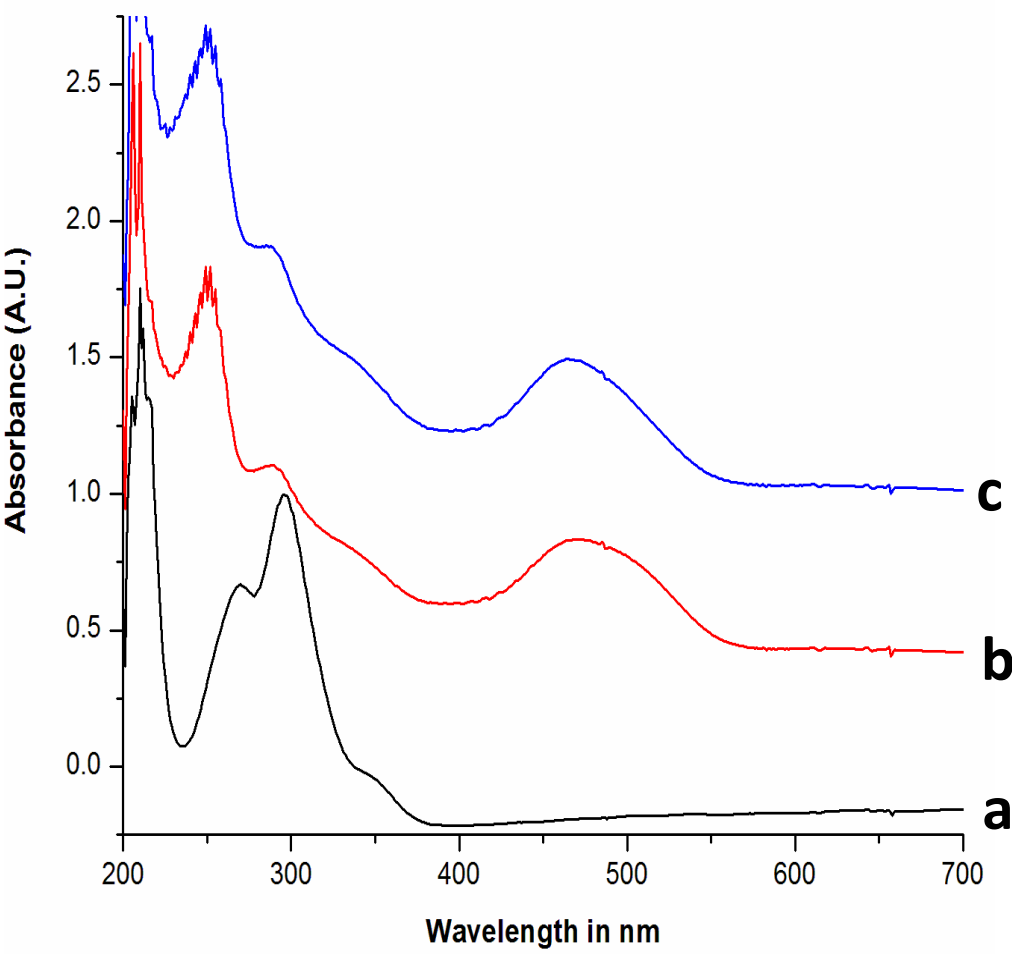


Figure 4.4: UV/Vis spectra of CF_2I_2 in Neon matrix. **(a):** as deposited at 5 K, **(b):** after irradiation at 266 nm, **(c):** after annealing to 9 K.

In order to verify the validity of our assignments, an extensive *ab initio* study was carried out on different species encountered in these experiments. The CF_2I_2 parent molecule was optimized at different levels of theory and the vibrational frequencies, calculated using the aug-cc-pVTZ and Sadlej-pVTZ basis sets, are provided in Table 3.1: the geometry optimization of the parent CF_2I_2 was found to be non-depending on the choice of the basis set used or on the fundamentally different wave functions and density functional used.

There are two main fundamental vibrations: ν_8 and ν_9, corresponding to the C-F stretching modes. The B3LYP/aug-cc-pVTZ-PP, B3LYP/Sadlej-pVTZ, and MP2/Sadlej-pVTZ calculated frequencies are consistent, and agree well with experiment (Table 2.1). However, the MP2/aug-cc-pVTZ-PP frequencies are slightly overestimated by factors of 1.02 for both ν8 and ν9. The M06-2X/aug-cc-pVTZ-PP and M06–2x/Sadlej-pVTZ on the other hand are significantly overestimated: factors of 1.06/1.07 for ν_8 / ν_9 using the correlation consistent basis set, and factors of 1.05/1.07 for ν_8 / ν_9 when the Sadlej-pVTZ basis set is used.

We also investigated the other isomer (*iso*-CF_2I_2 or F_2C-I-I) using various different levels of theory combined with aug-cc-pVTZ-PP and Sadlej-pVTZ basis sets. The fully optimized geometrical parameters are summarized in Table 3.2. Unlike for the parent CF_2I_2, the geometry optimization has shown dependence on the method used, and the B3LYP functional always tended to underestimate the values of C-I bond and C-I-I angle, compared to other methods used in this work. With reference to the most accurate CCSD method, the B3LYP seemed to be in error and this might be rationalized by the

poor performance of B3LYP functional in describing weakly bound F_2C-I-I structure! The B3LYP predicted a bent angle of about 166 to 168°, while the structure was nearly-linear for more accurate methods (180.0 ° at CCSD).

Table 4-1: Calculated vibrational frequencies in cm^{-1} (intensities in km/mol) for CF_2I_2 at various levels of theory

	B3LYP		**M06-2X**		**MP2**	
	aug-cc-pVTZ-PP	**Sadlej-pVTZ**	**aug-cc-pVTZ-PP**	**Sadlej-pVTZ**	**aug-cc-pVTZ-PP**	**Sadlej-pVTZ**
ν_1	109(0)	111(0)	118(0)	119(0)	117(0)	119(0)
ν_2	245(0)	249(0)	252(0)	257(0)	253(0)	255(0)
ν_3	267(0)	268(0)	281(0)	283(0)	286(0)	283(0)
ν_4	270(0)	270(0)	272(0)	283(0)	289(0)	285(0)
ν_5	304(0)	308(0)	319(0)	321(0)	316(0)	315(0)
ν_6	603(5)	600(5)	617(5)	615(5)	605(4)	595(4)
ν_7	725(345)	726(338)	764(3)	762(329)	779(299)	759(317)
ν_8	1064(279)	1060(270)	1118(279)	1111(267)	1081(250)	1059(251)
ν_9	1106(141)	1104(141)	1179(140)	1177(139)	1124(128)	1104(132)

Table 4-2 : Optimized structural parameters for *iso*-CF_2I_2 at various levels of theory.

Method		**C-F**	**C-I**	**I-I**	**F-C-F**	**F-C-I**	**C-I-I**
B3LYP/	aug-cc-pVTZ-PP	1.295	2.570	2.780	106.9	121.7	166.9
	Sadlej-pVTZ	1.298	2.678	2.785	106.6	122.0	168.3
M06-2X/	aug-cc-pVTZ-PP	1.287	3.043	2.678	105.6	127.0	176.4
	Sadlej-pVTZ	1.291	3.127	2.676	105.4	126.9	176.3
MP2/	aug-cc-pVTZ-PP	1.291	2.835	2.695	106.2	126.9	180.0
	Sadlej-pVTZ	1.303	3/046	2.702	105.6	127.2	180.0
CCSD/	aug-cc-pVTZ-PP	1.290	3.054	2.697	105.6	127.2	180.0
	Sadlej-pVTZ	1.306	2.954	2.779	106.1	127.1	180.0

In order to assign the experimentally observed IR bands, we have computed vibrational frequencies for the *iso*-CF_2I_2, and the results are shown in Table 4-3. Given the poor performance of B3LYP in optimization of the F_2C-I-I structure, its vibrational frequencies were not used for assignment. The two fundamental vibrations in the IR spectrum are ν_8 and ν_9, and they were assigned to the C-F stretching mode in the *iso*-CF_2I_2. Using the scaling factors derived from the parent molecule using the M06-2X and MP2/aug-cc-pVTZ results, the calculated frequencies would be self-consistent within an acceptable error bar. However this approach would not be reflecting reality since it's assumed that the electronic environment around the two C-F anharmonic oscillators was the same for the parent and *iso*-analogue! Without applying any scaling factors, the MP2/sadlej-pVTZ frequencies could be directly assigned to the observed 1143/1151 and 1241 cm^{-1} IR bands due to the *iso*-CF_2I_2 in matrix.

Figure 4.5 depicts a two-dimensional (2D) relaxed redundant coordinate scan around the isomer minimum at the MP2/sadlej-pVTZ level of theory along C-I bond and C-I-I angle. This figure tells about the need of a highly correlated electronic structure method to optimize the *iso*-CF_2I_2 structure. The MP2 and CCSD methods predict a linear form for the *iso*-minimum. However the potential geometry in the vicinity of MP2/CCSD global minimum is shallow enough for the constrained parameters corresponding to the optimized B3LYP geometry to lie within a barrierless 3 kcal/mol from the critical point. The shallowness of this part of the isomer ground state potential energy surface indicates that multiple conformations are accessible within few kcal/mol, the calculated ZPE of the MP2 fully optimized being about 5 kcal/mol.

In parallel with this study, the dynamics of the *iso*-CF_2I_2 formation in liquid solutions at room temperature was investigated by means of ultrafast spectroscopy and the results are very consistent for both studies, however the detail will not be discussed in this document.

	B3LYP		M06-2X		MP2			
	aug-cc-pVTZ-PP	**Sadlej-pVTZ**	**aug-cc-pVTZ-PP**	**Sadlej-pVTZ**	**aug-cc-pVTZ-PP**	**Sadlej-p-VTZ**	**Sym.**	**Assignments [a]**
v1	26(0)	24(0)	12(0)	12(0)	22(0)	19(0)	A’	C-I-I bend oop
v2	57(0)	51(0)	24(0)	27(0)	27(0)	20(0)	A”	C-I-I bend i.p
v3	77(16)	71(13)	64(6)	60(5)	67(14)	55(7)	A’	C-I stretch
v4	152(0)	136(0)	78(0)	74(0)	105(0)	81(0)	A”	CF_2 rock
v5	172(13)	175(13)	187(2)	185(3)	202(0)	160(0)	A’	CF_2 wag
v6	325(51)	290(44)	223(7)	223(5)	212(10)	216(5)	A’	I-I stretch
v7	668(5)	667(5)	695(5)	693(5)	682(2)	670(2)	A’	CF_2 scissor
v8	1183(303)	1181(307)	1220(246)	1215(348)	1199(348)	1154(362)	A”	CF_2asym. Str
v 9	1218(709)	1223(636)	1303(323)	1300(301)	1282(291)	1252(260)	A’	CF_2 sym.str

Table 4-3 Calculated vibrational frequencies (cm^{-1}) for *iso*-CF_2I_2 at various levels of theory

a: Tentative assignments based on the calculated MP2/Sadlej-pVTZ vibrational frequencies

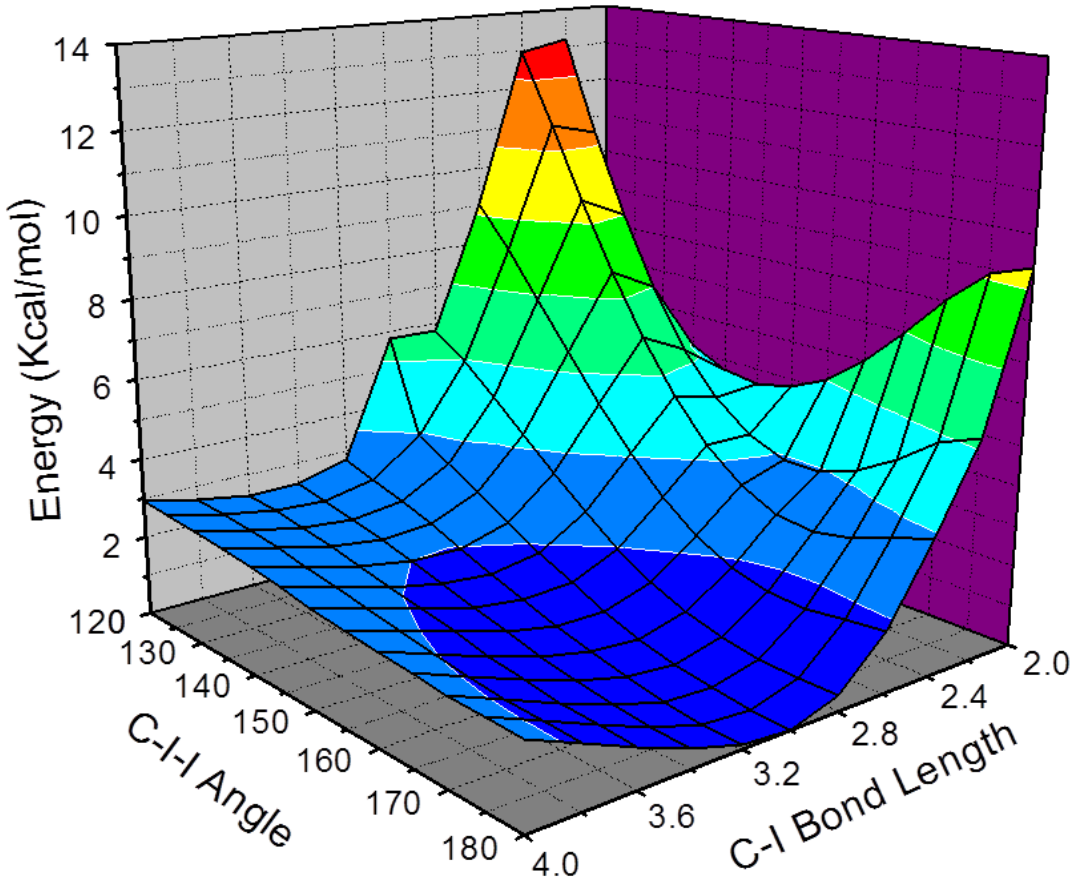


Figure 4.5 Calculated (MP2/Sadlej-pVTZ) potential energy surface of CF_2I_2 in the region of the *iso*-CF_2I_2 minimum. This surface represents a relaxed 2-D scan along the C-I-I angle and C-I bond distance.

4.2.3 Characterization of *iso*-CF_2Br_2 in solid Ar matrix

After deposition on a cold KBr window, the sample (CF_2Br_2:Ar 1:1500) was irradiated with 240 nm laser light then annealed to 35 K, and the results are shown in Figure 4.6. In the IR spectrum recorded after deposition, there are three CF_2Br_2 absorption bands at 820, 1080 and 1142 cm^{-1} well consistent with previous studies.[93] Upon irradiation at 240 nm, new bands came out: a strong peaks at 1098 and 1217 cm^{-1} assigned to CF_2, and other 2 bands due to the isomer of the parent molecule (*iso*-CF_2Br_2). The 1188 cm-1 band was assigned to the symmetric (ν_1) and the band at 1240 cm^{-1} was assigned to the antisymmetric (ν_2) C-F stretching mode of *iso*-CF_2Br_2. This assignment is supported by annealing experiments, whereby the KBr window was heated up to 35 K then re-cooled back down to 5 K: the bands assigned to the *iso*-CF_2Br_2 grew in at the expenses of those assigned to the CF_2 molecule. In the same spectrum at lower frequency (509 cm^{-1}) there is a band that was not observed in the parent spectrum. This band was assigned to the C-Br stretching mode of the *iso*-CF_2Br_2. Figure 4.6 is also showing the good agreement with calculated (B3LYP/aug-cc-pVTZ) IR spectrum of *iso*-CF_2Br_2. In panel (c) there is a strong band near the parent absorption at 1142 cm-1, due to the annealing effect on the parent molecule. In order to verify this, a freshly deposited sample was annealed without irradiation, and the same shift was observed (Figure 4.7). Note that the increase of the *iso*-CF_2Br_2 bands upon annealing was logically consistent with our observations in the *iso*-CF_2I_2 experiments.

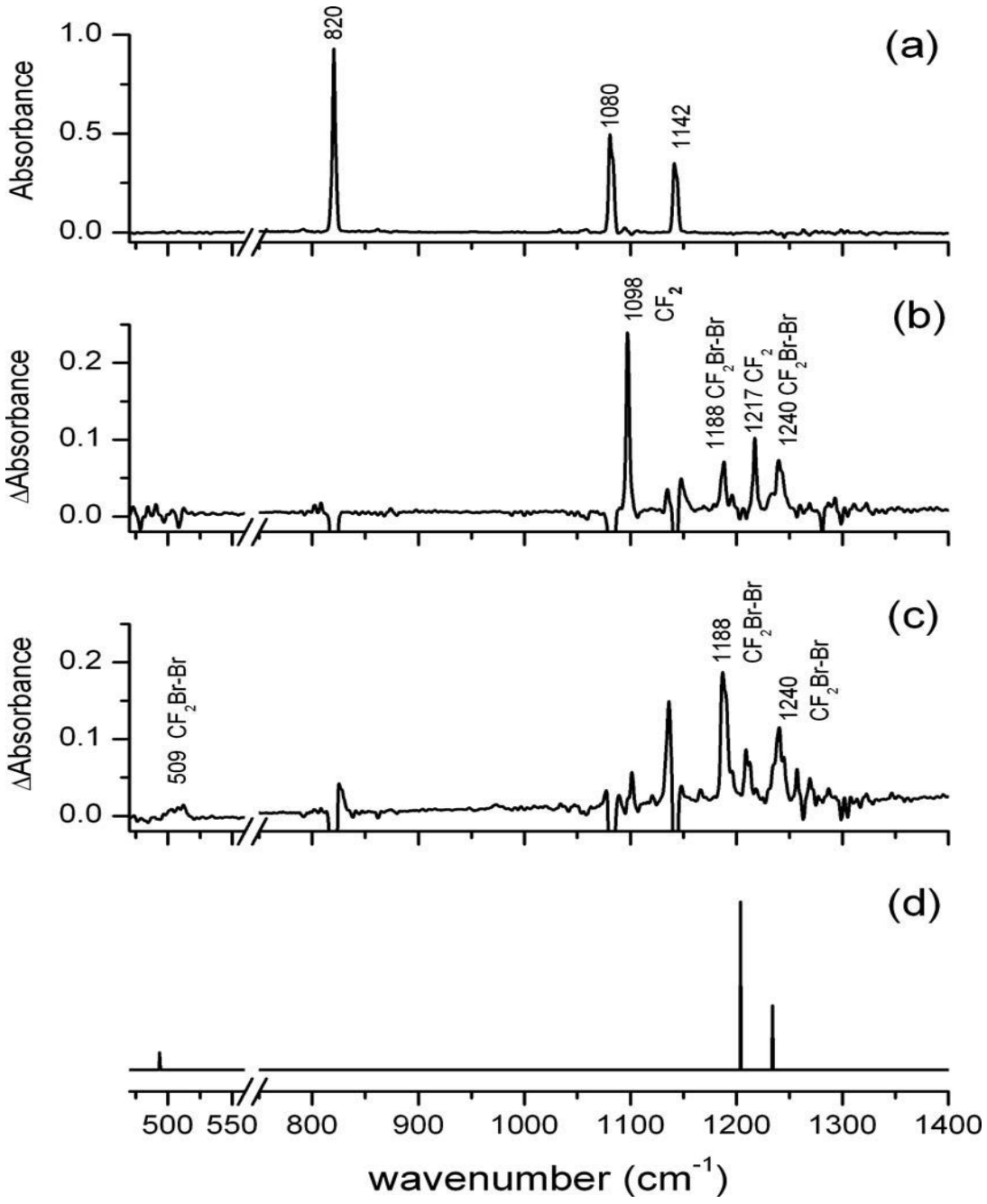


Figure 4.6: (a) IR spectrum of a CF_2Br_2:Ar matrix (1:5000) at 5 K. **(b)** Difference spectrum obtained following irradiation of an as-deposited matrix at 240 nm. **(c)** Difference spectrum obtained following annealing of a CF_2Br_2:Ar matrix that was first irradiated at 240 nm.**(d)** B3LYP/aug-cc-pVTZ predicted IR spectrum of *iso*-CF_2Br_2.

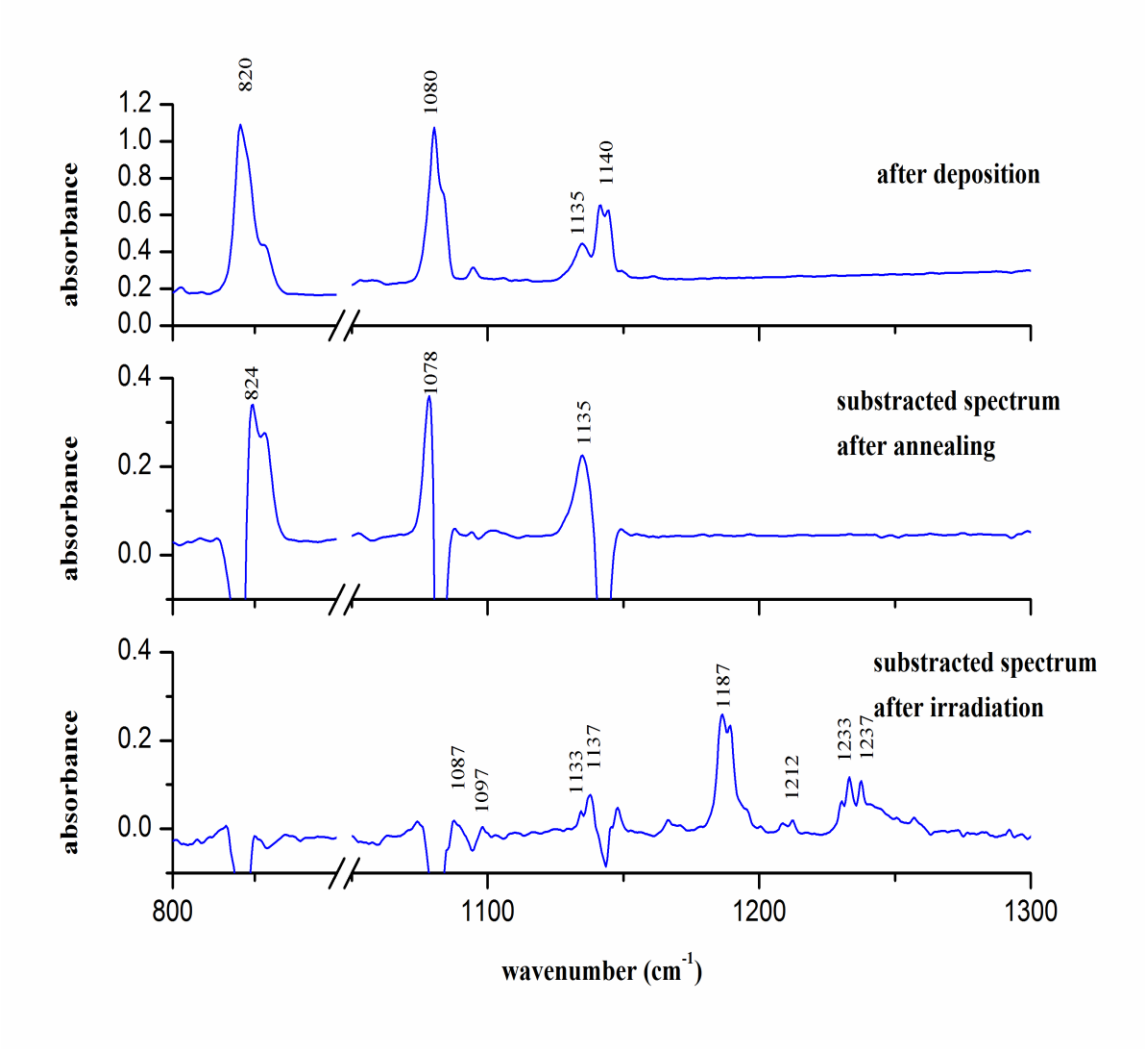


Figure 4.7: **Upper panel:** Infrared spectrum of a CF_2Br_2:Ar matrix (1:5000) at 8.5 K in the C-Br and C-F stretching region. **Middle panel:** Difference spectrum obtained after annealing at 35 K. **Lower panel:** Difference spectrum obtained following the annealing of a CF_2Br_2:Ar matrix that was first irradiated at 266 nm.

In parallel with the experimental, we carried out an extensive computational study on molecules involved in this work, especially the *iso*-CF_2Br_2. This isomer was fully optimized using B3LYP and MP2 in combination with various basis sets, ranging from cc-pVDZ to aug-cc-pVQZ. The geometrical parameters are summarized in Table 4-4

A PES performed along Br-Br stretching and C-Br-Br bending coordinates using B3LYP/cc-pVDZ levels of theory showed that the *iso*-CF_2Br_2 structure is a minimum. However, it is very important to distinguish the *iso*-CF_2Br_2 from the $CF_2\cdots Br_2$ complex (Figure 4.8) The main difference between these structures is the C-Br-Br angle of 157 degrees (B3LYP/aug-cc-pVTZ) for the isoform, while it is linear (180˚) for the $CF_2\cdots Br_2$ complex, at the same level of theory. The latter was characterized by performing a relaxed PES scan along C-Br stretching and C-Br-Br bending modes. The Br-Br distance was kept at ~2.3 Å, near the normal equilibrium bond length of Br_2. The shallowness in the region of the *iso*-structure on this PES suggests that multiple conformations (with relatively geometrical similarities) might be accessible.

We also calculated vibrational frequencies for all species involved in this study, to support the IR assignments. The predicted frequencies of the *iso*-CF_2Br_2 are summarized in Table 4-5

Table 4-4: Fully optimized geometrical parameters for the *iso*-CF_2Br_2 (angles are given in degrees, bondlength in angstroms)

Method	**C-F**	**C-Br**	**Br-Br**	**F-C-F**	**F-C-Br**	**C-Br-Br**
B3LYP/cc-pVDZ	1.299	2.084	2.526	108.4	119.7	160.1
B3LYP/cc-pVTZ	1.294	2.050	2.520	108.6	119.6	158.8
B3LYP/cc-pVQZ	1.294	2.022	2.529	108.8	119.7	157.6
B3LYP/aug-cc-pVDZ	1.306	1.987	2.567	108.7	120.0	156.5
B3LYP/aug-cc-pVTZ	1.296	2.026	2.528	108.6	119.6	157.4
B3LYP/aug-cc-pVQZ	1.295	2.016	2.530	108.8	119.6	157.1
MP2/cc-pVDZ	1.314	1.848	2.622	109.7	119.4	143.7
MP2/cc-pVTZ	1.307	1.824	2.565	109.6	119.8	141.9
MP2/cc-pVQZ	1.305	1.813	2.554	109.7	120.0	140.9
MP2/aug-cc-pVDZ	1.329	1.821	2.633	109.3	119.7	139.1
MP2/aug-cc-pVTZ	1.310	1.814	2.570	109.6	119.8	139.6
MP2/aug-cc-pVQZ	1.306	1.806	2.557	109.7	120.1	139.5

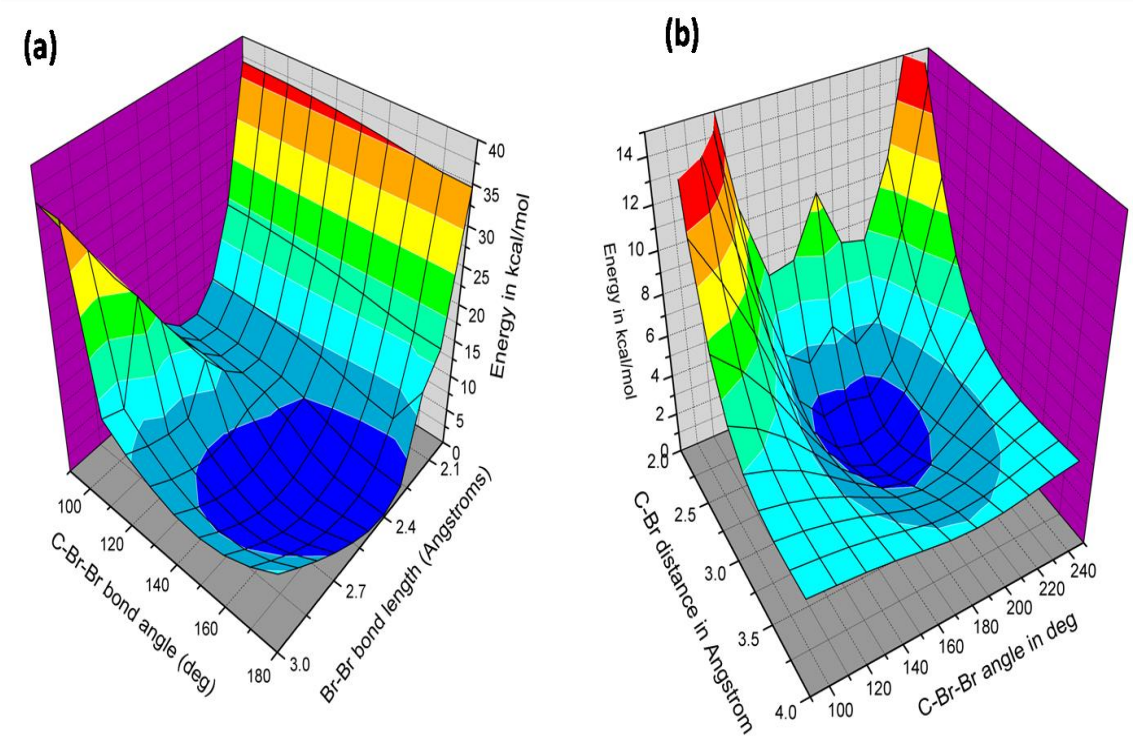


Figure 4.8: (a) Relaxed PES of *iso*-CF_2Br_2 calculated at the B3LYP/cc-pVDZ level of theory. **(b)** Relaxed PES of $CF_2\cdots Br_2$ complex calculated at the B3LYP/cc-pVDZ (the Br-Br distance was fixed at the equilibrium separation of Br_2.)

Table 4-5: Vibrational frequencies of *iso*-CF_2Br_2 (B3LYP/aug-cc-pVTZ)

Vibrational mode	**Symmetry**	**Vibrational frequency (cm^{-1})**	**Intensity (km/mol)**
ν_1	A'	1203	769
ν_2	A'	660	5
ν_3	A'	493	79
ν_4	A'	212	1.7
ν_5	A'	143	78
ν_6	A'	56	1
ν_7	A"	1234	295
ν_8	A"	268	0.3
ν_9	A"	56	1

In general the DFT methods are known to provide poor description of weakly bound systems [38], where the dispersion contributions are significant. Therefore a strong support to our computational study was found by performing single point energy calculations on all stationary points available on the CF_2Br_2 PES at the CCSD(T) level of theory. For these calculations, the structures optimized at B3LYP/aug-cc-pVTZ were taken as starting points. The results from these calculations are summarized in Figure 4.8: both *iso*-CF_2Br_2 and $CF_2\cdots Br_2$ complex have comparable energies, lying at about ~50 kcal/mol above the parent CF_2Br_2, however, lower than the energy required for the parent to dissociate into CF_2 and Br_2.

Comparing our results with the calculations done in 2000, by Cameron and Bacskay [90] at the MP2/6-31G(d) and CASSF/cc-pVDZ levels of theory, we can see one discrepancy: in their study, they were looking for the transition state for the $CF_2Br + Br \rightarrow CF_2 + Br_2$ reaction. The TS found has some properties similar to those of our *iso*-CF_2Br_2 molecule. However nothing has been reported about the minimum structure (isoform) since the optimization was performed in search of a first order saddle point. They did search for a transition state linking the parent CF_2Br_2 to the molecular products ($CF_2 + Br_2$) but did not find it. In contrast, our calculations show that *iso*-CF_2Br_2 is both a minimum on the CF_2Br_2 PES and an intermediate in the $CF_2Br + Br \rightarrow CF_2 + Br_2$ reaction. Due to this contrast, a closer look, at a higher level of theory, was needed in order to understand the chemistry of this isomer.

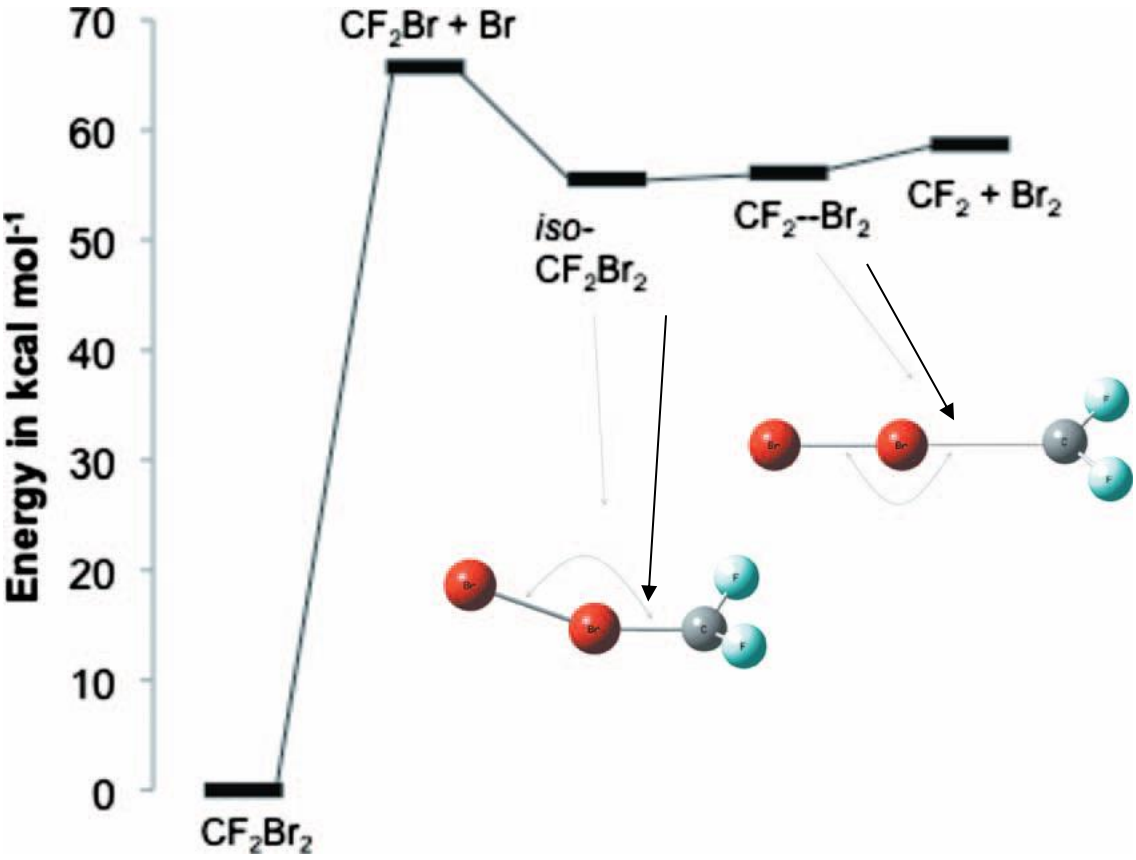


Figure 4.9: Calculated stationary points on the CF_2Br_2 potential energy surface, in gas-phase. The energies were calculated with CCSD(T)/aug-cc-pVTZ using structures optimized at the B3LYP/aug-cc-pVTZ level.

As has been observed in the *iso*-CH_2I_2 calculations,[89] where MP2 method tends to underestimate the C-I-I bond angle with respect to B3LYP and CASPT2 calculations, the MP2 calculations also underestimate the C-Br-Br bond angle in the CF_2Br_2 experiments (Table 4-4). As other *iso*-structures previously observed the *iso*-CF_2Br_2 seems to have a significant contribution from an ion pair-like structure for following reasons: the elongation of Br-Br bondlength and the large Mulliken charge on the terminal Br atom (B3LYP/aug-cc-pVTZ) (Figure 4.11)

Comparing this work with the study done previously by Jacox in 1978[96], there are some similarities and discrepancies. First, one should keep in mind that the concentrations are different for these studies: they used a more concentrated sample (CF_2Br_2:Ar = 1:270) while we used a less concentrated matrix (CF_2Br_2:Ar = 1:1500). In their work, the main photoproducts were C_2F_4, $C_2F_4Br_2$ and CF_2Br radical. In our experiments we also did see the radical (1136 and 1198 cm^{-1}) when the sample was irradiated with 266 nm laser light. However we didn't observe any dimerization products, and this can be rationalized by the low concentration of our sample. The two absorption bands that we assigned to the *iso*-CF_2Br_2 were also observed in their study, however the 1188 cm^{-1} was not assigned and the 1240 cm^{-1} was attributed to $C_2F_4Br_2$. To clear all doubts, we run a matrix deposition of pure $C_2F_4Br_2$, and the IR recorded along with computational calculations confirmed the absence of $C_2F_4Br_2$ in any of our spectra for the CF_2Br_2 experiments. The same shoulder observed in both studies at ~1235 cm^{-1} might be resulting from a site splitting in the matrix or from another conformer locally stabilized.

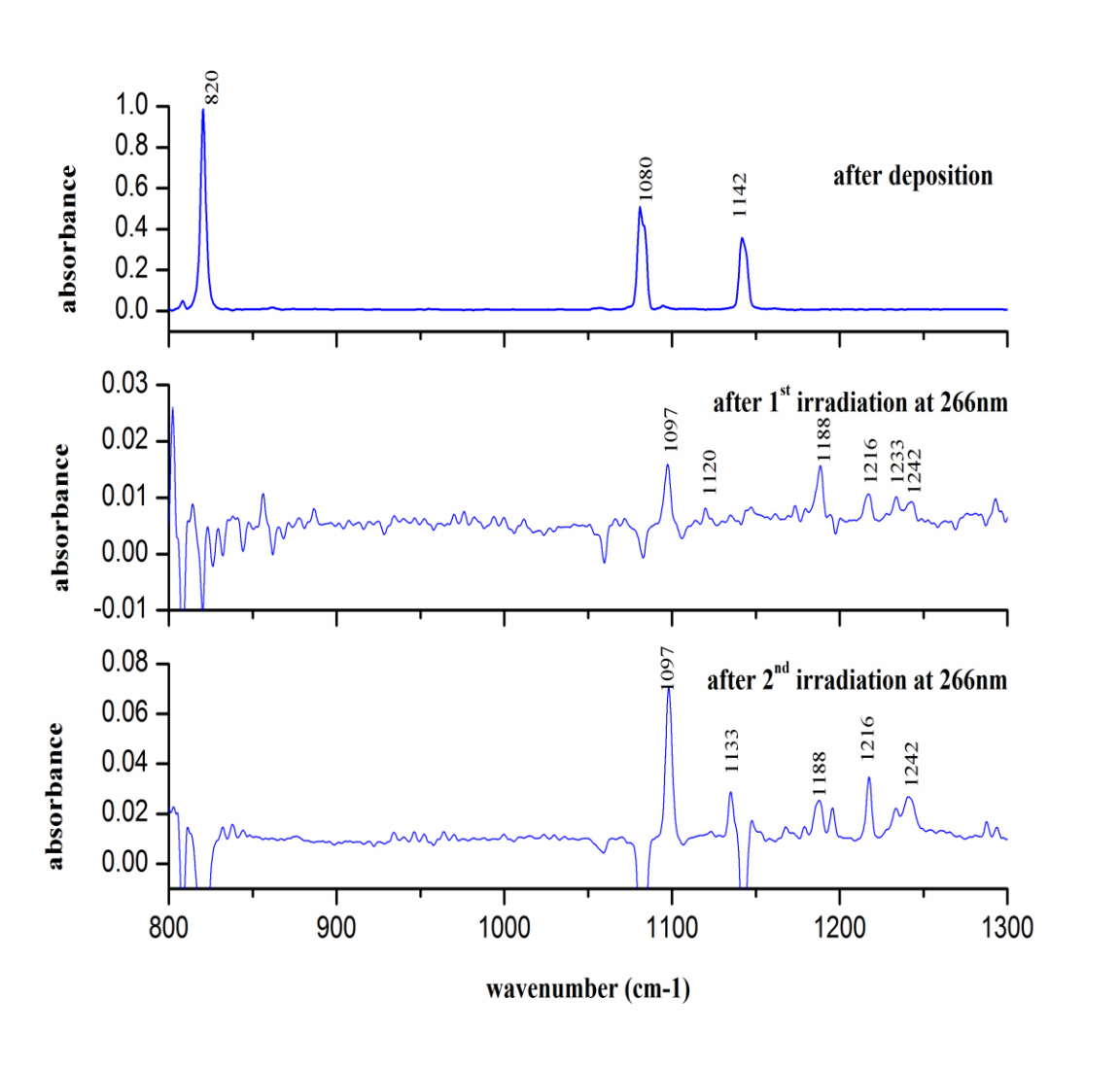


Figure 4.10 : Upper panel: Infrared spectrum of a CF_2Br_2:Ar matrix (1:5000) at 8.5 K in the C-Br and C-F stretching region. **Middle panel:** Difference spectrum obtained following irradiation of an as-deposited matrix at 266. **Lower panel:** Difference spectrum obtained following the second irradiation at 266 nm.

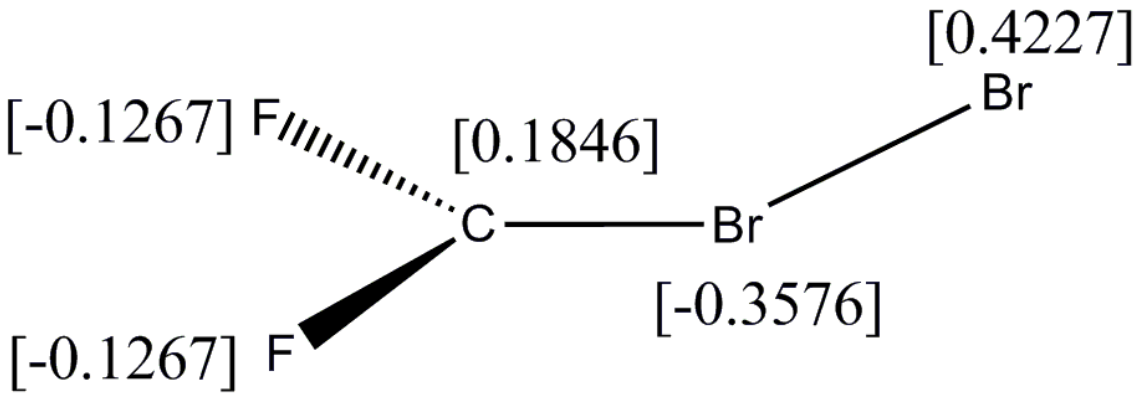


Figure 4.11: Calculated Mulliken charge on *iso*-CF_2Br_2 (MP2/aug-cc-pVTZ)

Besides the IR spectra, we also did investigation in UV/Vis region (Figure 4.12), where the parent CF_2Br_2 shows a strong band at ~ 225 nm. Upon photolysis at 240 nm laser light, the parent's band decreased in intensity and three new bands grew in: one at ~ 253 nm due to CF_2 species, and two at ~ 359 and 536 nm due to *iso*-CF_2Br_2. These results are consistent with the time-dependent density functional predictions of vertical transitions and oscillator strengths. TD-B3LYP/aug-cc-pVTZ calculations predicted a weak (f=0.005) in the visible at 528 nm assigned to the $1^1A' \rightarrow 2^1A'$ transition and another strong (f=0.27) band in the near-UV at 331 nm assigned to the $1^1A' \rightarrow 3^1A'$ transition. The predicted relative intensity was reflected in our experiments (~20 fold difference in the integrated intensities). When the *iso*-CF_2Br_2 was irradiated with 355 nm laser light, the 359 and 536 nm bands completely disappeared, and the CF_2Br_2 parent (normal isomer) was reformed (Figure 4.13).

We conducted an extensive theoretical analysis on bonding and structure of various *iso*-polyhalomethanes and the detail will be given in Chapter 4.

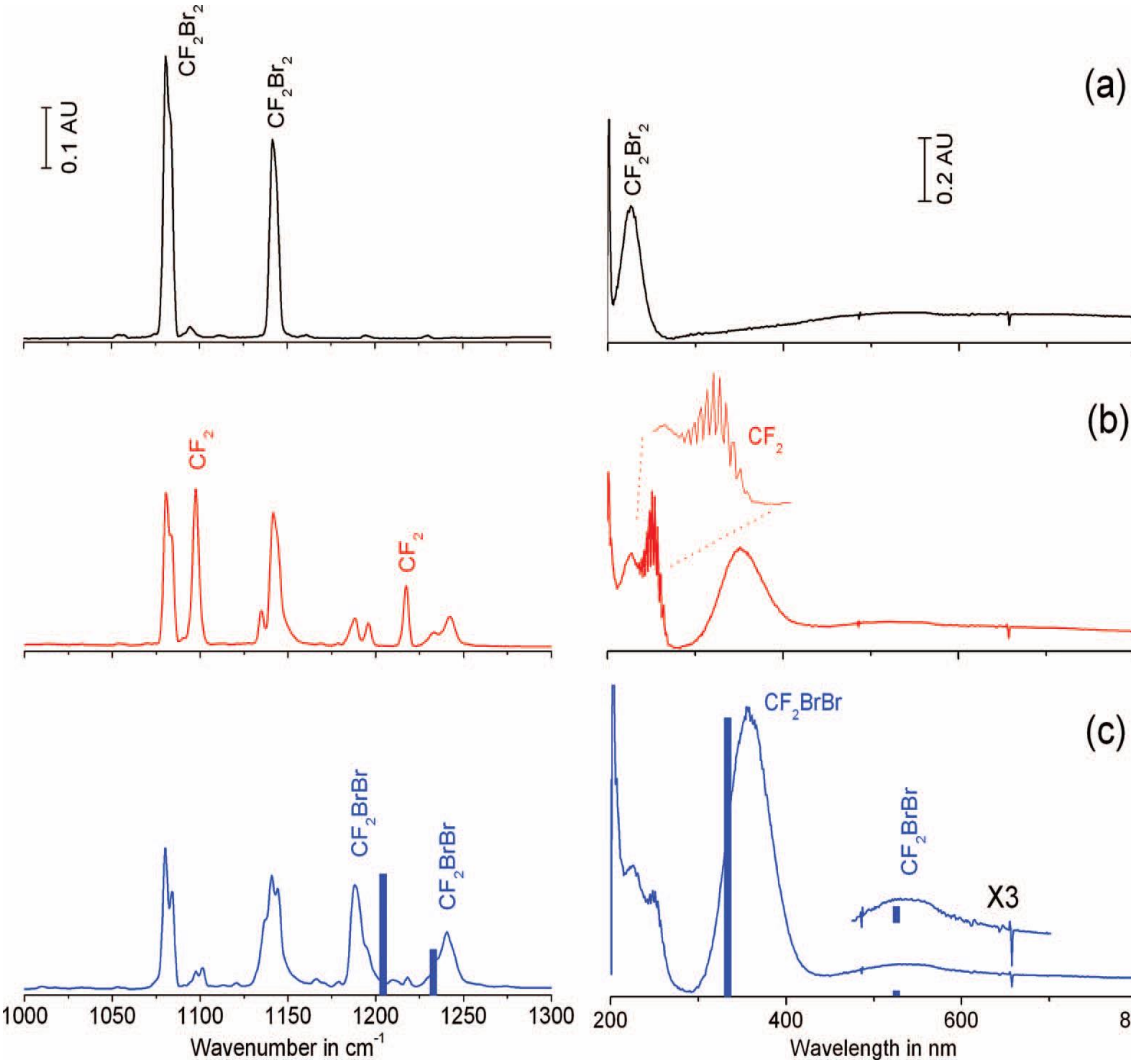


Figure 4.12(a) IR and UV/Visible spectra of a CF_2Br_2:Ar matrix at 5 K. **(b)** Spectra following irradiation at 240 nm. **(c)** Spectra following annealing to 35 K and re-cooling to 5 K. The bars in these spectra are predictions at the TD-B3LYP/aug-cc-pVTZ level

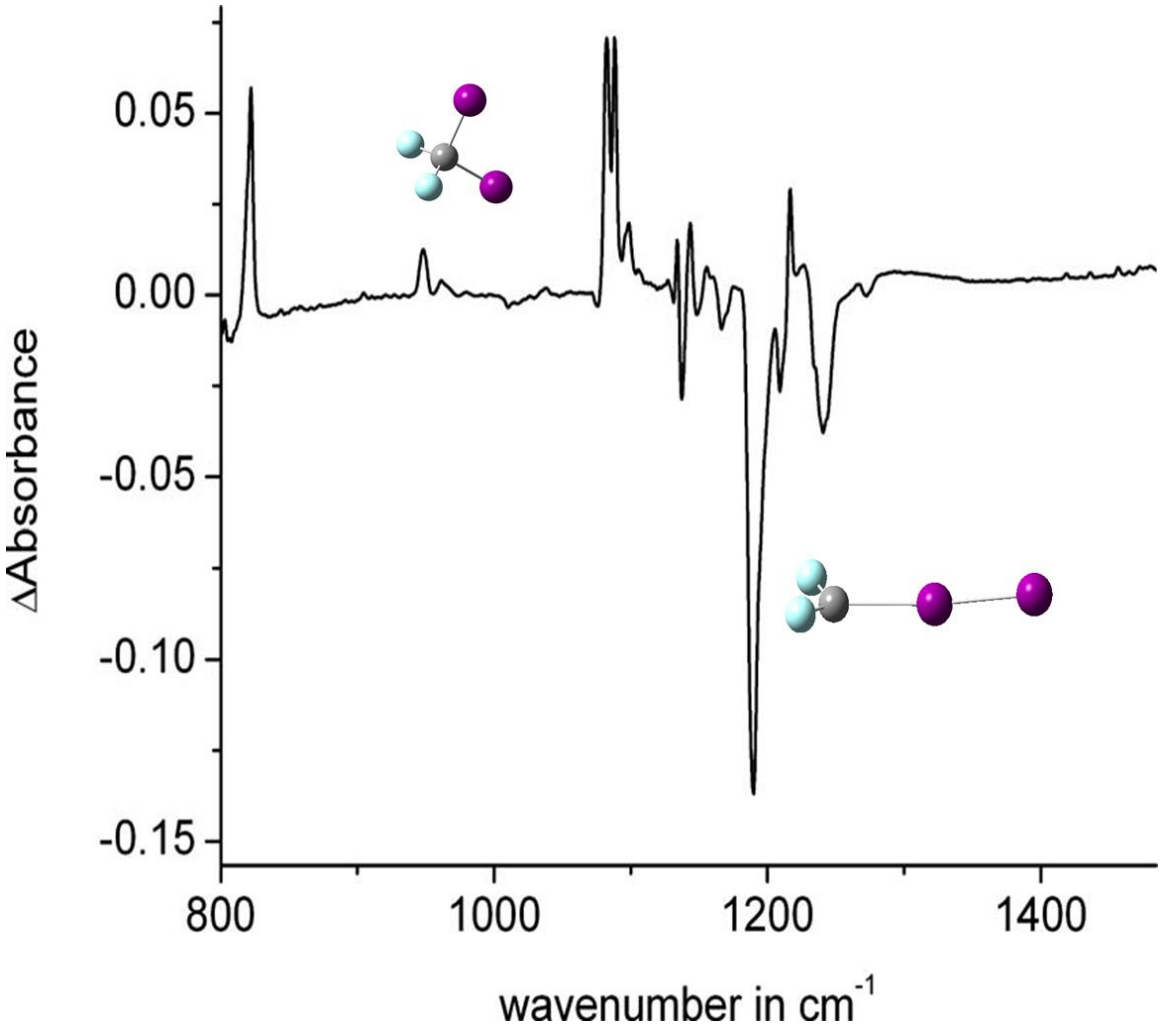


Figure 4.13 Difference IR spectrum obtained following 355 nm irradiation of matrix isolated *iso*-CF_2Br_2. The IR absorptions (1188, 1240 cm^{-1}) of the isomer decrease, while the parent CF_2Br_2 bands increase.

In previous studies done in gas phase, the C-Br bond breaking as found to be the main path following irradiation in UV range [105] and at higher energy ($\lambda < 260$ nm) the CF_2Br radical could easily undergo a secondary dissociation to produce CF_2 species[63, 69]. A more recent study has reported an elimination channel producing molecular bromine (Br_2). [75] These observations are consistent with our findings where we observed a weak band due to the CF_2Br radical upon photolysis at 240 nm.

Based on the computational predictions and our spectral observations, we propose the following sequence of reactions in the matrix:

$$CF_2Br_2 + h\nu \rightarrow CF_2Br\cdot + Br\cdot, \quad \text{(Equation 4.1)}$$

$$CF_2Br\cdot + Br\cdot \rightarrow \textit{iso}\text{-}CF_2Br_2, \quad \text{(Equation 4.2)}$$

$$\textit{iso}\text{-}CF_2Br_2 \rightarrow :CF_2 + Br_2 \quad \text{(Equation 4.3)}$$

$$CF_2Br\cdot + h\nu \rightarrow :CF_2 + Br\cdot \quad \text{(Equation 4.4)}$$

The photoproducts resulting from the first reaction may undergo a cage recombination to produce *iso*-CF_2Br_2. At the matrix low temperature this isomer can be trapped or react producing molecular products CF_2 and Br_2. The CF_2Br radical that survived the cage recombination may undergo a secondary dissociation and produce CF_2 with atomic bromine.

In our matrix isolation experiments we have found that *iso*-CF_2Br_2 is an intermediate in the reaction: $CF_2Br + Br \rightarrow CF_2 + Br_2$ and this does not exclude such a pathway.

4.3 Summary

The weakly bound *iso*-CF_2I_2, is produced and trapped upon photolysis of CF_2I_2 in cold Ar matrix. The first IR and Visible spectra of *iso*-CF_2I_2 were obtained. Unlike other dihalomethanes (CH_2IX, X=Cl, Br, I) CF_2I_2 and *iso*-CF_2I_2 have quite different UV/Vis absorption spectra due to the difference in their electronic structures. The assignment of *iso*-CF_2I_2 was based on IR signatures correlated with calculated vibrational frequencies and confirmed by annealing experiments. Together, matrix isolation and ultrafast IR absorption experiments suggested that the formation of *iso*-CF_2I_2 occurs via recombination of CF_2I radical with atomic iodine, or CF_2 with molecular iodine.

We report the first observation of the *iso*-CF_2Br_2, a weakly bound isomer of CF_2Br_2. This isomer was formed by cage recombination of CF_2Br with Br, and CF_2 with Br_2 or 2Br. The assignment is supported by high level *ab initio* calculations which show that the *iso*-CF_2Br_2 is a minimum on the CF_2Br_2 PES. Unlike in previous studies where the sample was more concentrated (CF_2Br_2:Ar = 1:270), in our experiments we do not observe any dimerization products. Our experiments indicate that *iso*-CF_2Br_2 is an intermediate in the $Br+CF_2Br \rightarrow CF_2+Br_2$ reaction, and therefore can be considered to play an important role in the formation of molecular products from CF_2Br_2 photolysis in condensed phases. This isomer may also be important in the gas-phase photochemistry of CF_2Br_2.The photochemistry of the isoform was investigated; excitation into the strong 359 nm absorption of this species results in isomerization to CF_2Br_2.

Chapter 5. FORMATION AND CHARACTERIZATION OF *iso*-TRIBROMOMETHANES (*iso*-$CXBr_3$, X=H, D, F, Cl, Br) IN SOLID MATRIX

Bromoform ($CHBr_3$) is major natural carrier of organic bromine to the atmosphere. It has a relatively short tropospheric lifetime of ~3 weeks and is believed to make a significant contribution to inorganic bromine in the upper troposphere and lower stratosphere.[19, 106-110] The major sources of $CHBr_3$ have been identified as marine in origin, namely microalgae, ocean phytoplankton and water chlorination [111-113]

The UV spectrum of bromoform shows three prominent bands at ~225, 210, 180 nm. These have been assigned based on high level *ab initio* calculations, to transitions from the ground state $\tilde{X}'A'_1$ to the $\tilde{B}'E$, $\tilde{C}'A_1$ and $\tilde{D}'E$ excited states. These transitions primarily reflect single excitations from the highest occupied orbitals, which correspond to lone pairs on Br, into C-Br σ* orbitals, and therefore excitation leads to prompt C-Br bond cleavage. As we have discussed in previous chapters, the photochemical behavior of many halons is still not well understood in detail. Many studies have been carried out to investigate the photolysis of $CHBr_3$ in the ultraviolet. The Br atom quantum yield for $CHBr_3$ photolysis was measured by Sander and co-workers, in the 266-324 nm range.[114] At longer wavelengths, the quantum yield was unity, and 0.73 at 266 nm. This suggested the existence of another probable channel, where molecular bromine (Br_2) is eliminated following internal conversion to the ground state. Consistent with several other experimental and theoretical studies [115-117], Sears and co-workers concluded that prompt C-Br bond cleavage was the dominant channel following absorption of a single UV photon, with molecular products arising from multiphoton processes.[118]

While the condensed phase photochemistry of bromoform is better understood to some extent, less is known about the substituted tribromomethanes *iso*-$CXBr_3$, and few studies have shown that they play a key role in the reactivity of halomethanes in solutions. Recently, Crim and co-workers [119] proposed a photochemical mechanism whereby ultraviolet excitation of $CHBr_3$ leads to prompt production of *iso*-$CHBr_3$, which was assigned as the carrier of an intense transient absorption band centered at 390 nm that appeared with a risetime < 0.5 ps following photolysis. This band decayed with a time constant of ~ 13 ps in neat $CHBr_3$, and the decay coincided with the rise of a new band centered at 495 nm that was assigned to the $Br\cdots CHBr_3$ complex. Thus, it was proposed that the initially formed "hot" *iso*-$CHBr_3$ could be transiently stabilized by vibrational relaxation to the solvent, or dissociate by cleavage of the Br-Br bond to form a radical pair, with subsequent association of the Br atom and a solvent molecule forming the complex. Phillips and co-workers [29] have characterized numerous fundamental vibrational frequencies for $CHBr_3$ and *iso*-$CHBr_3$ and provided additional support for the participation of *iso*-polyhalomethane species as methylene transfer agents in the cyclopropanation reactions of olefins following UV excitation of polyhalomethanes in solution. It was also suggested that *iso*-polyhalomethanes formation in water droplets and aerosol particles might release reactive halogens into the atmosphere, by both chemical and photochemical reactions.

Phillips and co-workers studied the vibrational spectra of *iso*-$CXBr_3$ (X=F, Br) in solution using picosecond TR3 spectroscopy, supported by DFT calculations [29] and characterized several fundamental vibrational frequencies for each species. Later on, they performed photolysis of CBr_4 in water and acetonitrile/water solution. They observed that

the water catalyzed O-H insertion and H-Br elimination reaction of *iso*-CBr_4 led to the final products: HBr and CO_2.[120]

In 2005, in a related study, Rentzepis and co-workers explored the photochemistry of CBr_4 in various solvents using ultrafast time-resolved spectroscopy [121] They observed a broad absorption band at 480 nm, upon excitation of the sample with 266 or 267 nm laser light. The decay time of this band depended on the solvent used, and it could persist for hundreds of ns in cyclohexane. Based upon the shift in the absorption maximum with solvent dielectric constant, this band was thought to be the signature of a cation, in particular a solvent stabilized (and solvent separated) CBr_3^+ and Br^- ion pair, and despite previous work on the *iso*-polyhalomethanes, the assignment of the 480 nm band to the *iso*-CBr_4 was not considered. Another attempt was made by Ihee and co-workers, in 2007.[122] They studied photolysis of CBr_4 using time-resolved X-ray diffraction and couldn't observe any evidence for the *iso*-CBr_4 within the signal to noise ratio in their experiments. They rather observed CBr_3 + Br, 100 ps after photolysis, and it was suggested that these radicals recombined in a non-geminate reaction to form C_2Br_6 and Br_2. However, in a theoretical paper, the same group have localized *iso*-CBr_4 on the PES of CBr_4 and calculated its vibrational frequencies using DFT methods.[123]

In this work we have carried out the matrix isolation experiments in rare gas (Ar and Ne) at ~5 K, of *iso*-bromoform and related *iso*-$CXBr_3$ (X=F, Cl, Br) species and have characterized the electronic spectroscopy of these systems for the first time. The photochemistry of the isomers was investigated by selected wavelength laser irradiation. Our experimental results are supported by extensive high level DFT and *ab initio* calculations.

5.1 Experimental methods

The detail on the matrix-isolation set-up utilized in these experiments was given in Chapter 2. The samples of $CXBr_3$ were mixed with rare gas (Ar or Ne) in typical ratios of 1:1500. The sample was deposited on a cold KBr window held at ~5 K, using the pulsed deposition technique, described in detail in Chapter 2.

The $CClBr_3$ sample was prepared according to the following procedure [124]: to a round-bottom flask equipped with a magnetic stir-bar and a rubber septum were added $CHBr_3$ (10.1g, 40 mmol) and 4-6% aqueous hypochlorite (200mL). the resulting mixture was stirred vigorously for 3 days at 22 °C and the granular solid thus formed was filtered and washed repeatedly with water (4x100mL) to afford 5.8g (705) of white solid; ^{13}C NMR (400 MHz, $CDCl_3$) δ:3.8.

After deposition, photolysis was done by irradiating the window with a laser light at 230nm ($CFBr_3$) or 220 nm (for $CHBr_3$, $CClBr_3$ and CBr_4).

5.2 Computational methods

All calculations were carried out on a personal computer using Gaussian 03 and PC Spartan 08 suites of electronic structure programs.[125] Geometry optimization was typically performed using the B3LYP and MP2 methods with a series of correlation consistent polarized basis sets, cc-pVXZ and aug-cc-pVXZ (X=D or T). To obtain a more quantitative description of the relative energies between selected stationary points, single point energy calculations were performed at the CCSD(T)/cc-pVTZ level of theory using the optimized MP2/cc-pVTZ and B3LYP/aug-cc-pVTZ structures.

5.3 Results and Discussion

5.3.1 Formation and characterization of *iso*-bromoform

In Figure 5.1 the upper panel shows the IR spectrum and the lower panel shows the UV/Vis spectrum, recorded after photolysis of a $CHBr_3$:Ar sample at 220 nm and annealing to 30 K, with their respective theoretical predictions (DFT and TD-DFT as stick spectra). At this wavelength, the *iso*-$CHBr_3$ was found to be the main photoproduct in gas rare matrix. The very small peak at 773 cm^{-1} was assigned to the $CHBr_2$ radical. As summarized in Table 5-1, the positions and relative intensities of the experimental IR spectra are in very good agreement with both the previous Raman studies[29] and *ab initio* calculations. Unfortunately, the small calculated ^{79}Br-^{81}Br isotope splitting (< 2 cm^{-1} as predicted by our calculations) could not be resolved with our FTIR instrument. We also performed the experiment in Ne matrix. Similarly the sample was irradiated with 220 nm laser light but annealed to 9 K, due to the low freezing temperature of the matrix gas. The results are shown in Table 5-1.

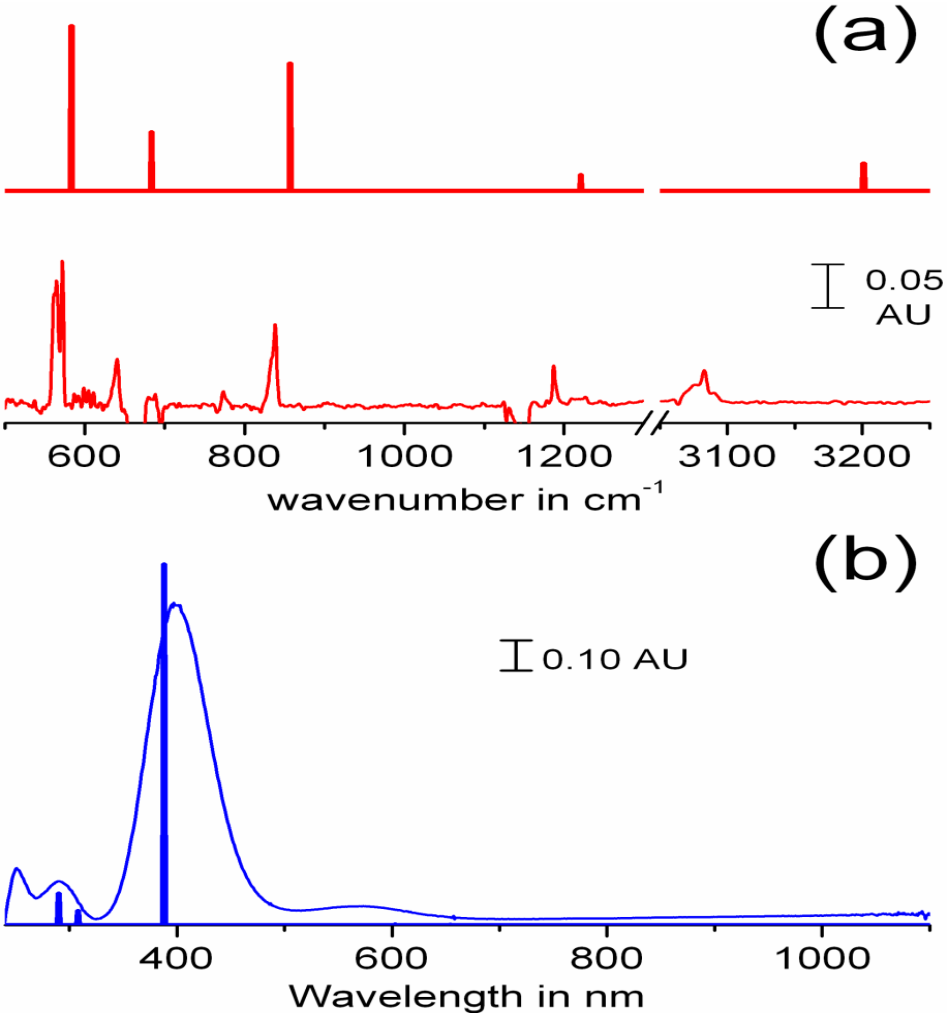


Figure 5.1: Upper panel: Infrared spectrum of a $CHBr_3$:Ar matrix (~1:500) at ~ 5 K following laser irradiation at 220 nm, and the predicted (B3LYP/aug-cc-pVTZ) infrared spectrum of *iso*-$CHBr_3$. **Lower panel:** The corresponding UV/Visible spectrum, compared with the predicted (TDB3LYP/aug-cc-pVTZ) spectrum of *iso*-$CHBr_3$.

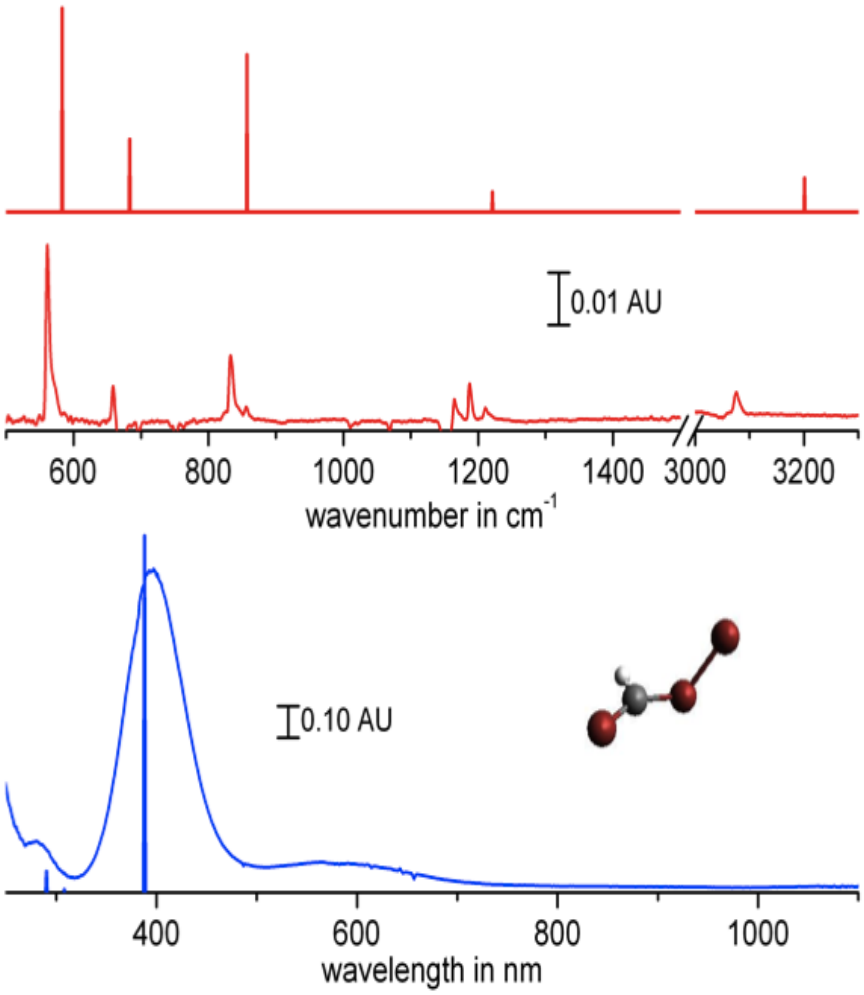


Figure 5.2: Upper panel: Infrared spectrum of a $CHBr_3$:Ne matrix (~1:500) at ~ 5 K following laser irradiation at 220 nm and annealing to 9 K. **Lower panel:** The corresponding UV/Visible spectrum

Table 5-1: Vibrational frequencies of *iso*-$CHBr_3$ determined at the B3LYP/aug-cc-pVTZ level of theory.

Mode	**Sym. (C_1)**	**Approximate Description**	**Calculated frequency in cm^{-1} (scaled by 0.97)**	**Calculated Intensity (km/mol)**	**Observed frequency in cm^{-1}**	
					this work	***ref.***
					32 Ar (Ne)	
ν_1	A	C-H stretch	3208 (3112)	22.5	3083 (3076)	…
ν_2	A	C-H scissor	1219 (1182)	31.1	1187 (1187)	…
ν_3	A	Asym. C-Br stretch	858 (832)	79	838 (833)	834
ν_4	A	Sym. C-Br stretch	696 (675)	37.2	639 (658)	658
ν_5	A	C-H wag	586 (568)	137.7	565 (561)	566
ν_6	A	i.p. Br-C-Br bend	216 (210)	14.0	…	214
ν_7	A	o.o.p Br-C-Br bend	178 (173)	4.2	…	…
ν_8	A	Br-Br stretch	169 (164)	31.2	…	169
ν_9	A	C-Br-Br bend	42 (41)	2.6	…	…

To ensure a good correlation in our assignment, oscillator strength was estimated using the method described in Chapter 2. For the main band at ~ 400 nm, this method provided a good estimate of the oscillator strength: 0.35 (ε_{max}~ 19,000 L mol^{-1} cm^{-1}) while the TD-DFT prediction was 0.34. Going back to the UV/Vis spectra, the calculated vertical excitation energies and the oscillator strengths of the lowest excited singlet states of the *iso*-$CHBr_3$ are summarized in Table 5-2. As it has been observed for the *iso*-polyhalomethanes, there are weak features ($S_0 \rightarrow S_1$, S_2) in the visible and a stronger band ($S_0 \rightarrow S_3$) in the near-UV. The latter transition seems to be charge transfer in nature and it is mostly due to a filled π-orbital corresponding to a lone pair on the carbon atom.

Calculations performed using the density functional (B3LYP) and MP2 levels of theory, in combination with a series of sufficiently large basis sets show that *iso*-$CHBr_3$ is a local minimum on the $CHBr_3$ ground state potential energy surface scan and the geometrical parameters are listed in Table 5-3

Table 5-3.**Table 5-2:** Predicted (TDB3LYP/aug-cc-pVTZ) and observed electronic absorptions for *iso*- $CXBr_3$ (X = H, F)

X	Singlet Excited State	Predicted vertical excitation λ in nm	Predicted Oscillator Strength	Observed λ_{max} in nm	Observed Oscillator Strength
H	1	654.0	1.0×10^{-4}	…	...
	2	602.7	5.0×10^{-4}	561.1	1.1×10^{-2}
	3	388.6	3.4×10^{-1}	399.3	3.5×10^{-1}
	4	308.4	1.5×10^{-2}	...	...
	5	289.6	3.4×10^{-2}	290.4	5.3×10^{-2}
F	1	686.6	1.0×10^{-4}	…	...
	2	621.7	1.2×10^{-3}	593.9	3.2×10^{-2}
	3	419.5	2.1×10^{-1}	431.9	2.3×10^{-1}
	4	313.7	9.0×10^{-3}	...	...
	5	310.3	1.8×10^{-2}	287.6	8.2×10^{-2}
	6	307.8	3.4×10^{-3}	...	...
	7	265.4	3.0×10^{-1}	243.9	2.9×10^{-1}
	8	262.8	1.4×10^{-1}	...	...

Table 5-3: Fully optimized geometrical parameters for the *iso*-$CXBr_3$ (X = H, F) species and the first-order saddle point connecting this species to the normal isomer. Angles are given in degrees and bond lengths in Ångstrøms.

Species	Method/basis set	C-X	C-Br_1	C-Br_2	Br_1-Br_3	X-C-Br_1	Br_1-C-Br_2	C-Br_1-Br_3	H-C-Br_1-Br_3
	B3LYP/								
	aug-cc-pVTZ	1.080	1.782	1.859	2.700	114.9	123.6	126.8	77.3
	6-311++G(2df,2p)	1.080	1.783	1.861	2.696	118.0	123.4	127.4	76.5
***iso*-**									
$CHBr_3$	**MP2/**								
	cc-pVTZ	1.081	1.783	1.856	2.620	117.4	121.8	119.5	78.2
	aug-cc-pVDZ	1.094	1.794	1.866	2.670	116.2	121.4	119.2	77.3
	6-311++G(2df,2p)	1.081	1.778	1.851	2.628	117.6	121.7	118.9	79.2
	B3LYP/								
	aug-cc-pVTZ	1.078	1.779	1.831	3.079	118.4	124.0	79.2	78.9
$CHBr_3$									
TS	**MP2/**								

	cc-pVTZ	1.079	1.751	1.830	2.890	118.8	123.2	76.7	83.0
	B3LYP/								
	aug-cc-pVTZ	1.308	1.865	1.878	2.650	117.6	123.0	146.6	75.2
	6-311++G(2df,2p)	1.305	1.873	1.877	2.641	117.5	123.4	148.6	74.3
iso-	**M06/**								
$CFBr_3$	cc-pVTZ	1.291	1.862	1.872	2.600	117.5	122.2	146.2	73.0
	6-311++G(2df,2p)	1.299	1.820	1.859	2.614	118.2	123.4	142.0	76.8
	MP2/								
	cc-pVTZ	1.324	1.798	1.867	2.615	117.5	121.4	128.2	77.3
	6-311++G(2df,2p)	1.323	1.790	1.858	2.625	117.6	121.8	126.7	78.0
	B3LYP/								
$CFBr_3$	aug-cc-pVTZ	1.298	1.785	1.836	3.098	118.6	124.9	104.7	91.1
TS									

MP2/								
cc-pVTZ	1.303	1.748	1.826	2.921	119.1	124.5	78.0	91.5

The MP2 and B3LYP calculations are very comparable except for ∠ C-Br-Br. The same phenomenon has been observed for *iso*-CF_2Br_2 [89] and it was thought to be related to the shallowness of the *iso*-CF_2Br_2 minimum. Although *iso*-$CHBr_3$ is quite strongly bound compared with *iso*-CF_2Br_2, they both present shallow minima and the same phenomenon was observed for both molecules: the shallowness of C-Br-Br bond angle makes this angle to be the parameter that depends most on the method used (∠C-Br-Br = ~127°/119° at the B3LYP/MP2 levels respectively). This is depicted by a relaxed potential energy surface scan along Br- Br stretching and C-Br-Br bending coordinates performed at the M06/6-311++G(2df,2p) level of theory.(Figure 5.3). All other parameters are comparable.

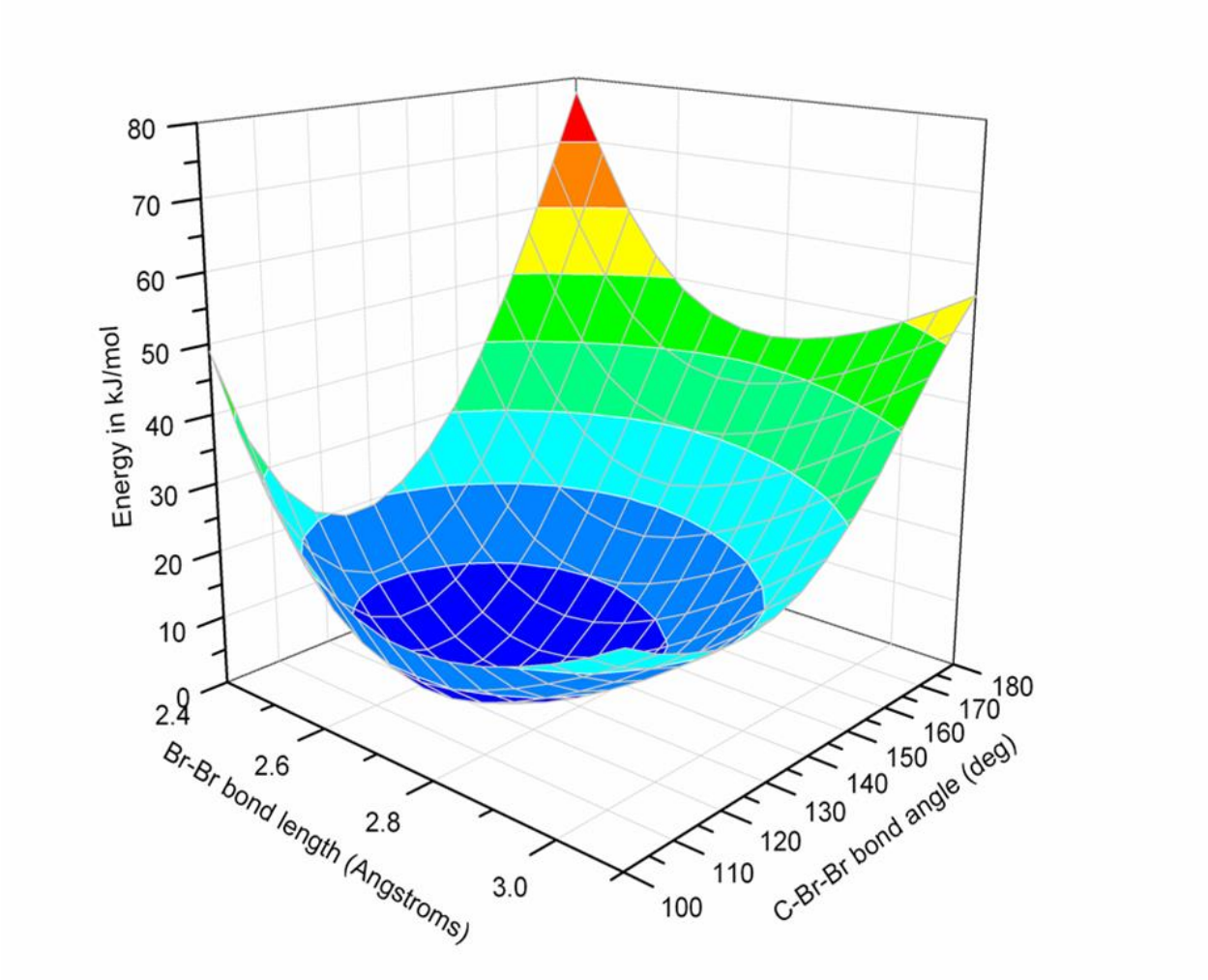


Figure 5.3 Relaxed potential energy surface scan of *iso*-$CHBr_3$ along ∠C-Br-Br and $R_{Br\text{-}Br}$, calculated at the M06/6-311++G(2df,2p) level of theory.

For more accuracy, single energy calculations were computed at higher level of theory [CCSD(T)/cc-pVTZ] using the structures optimized at the B3LYP and MP2 levels. In Figure 5.4 the energies of stationary points on the $CHBr_3$ PES calculated at the CCSD(T)//MP2 levels are compared with the MP2/cc-pVTZ and B3LYP/cc-pVTZ predictions.

As shown in Figure 5.4, *iso*-$CHBr_3$ is predicted to lie at 56 kJ/mol [CCSD(T)//MP2/aug-cc-pVTZ] to 80 kJ/mol (MP2/aug-cc-pVTZ) and 63 kJ/mol (B3LYP/aug-cc-pVTZ) below the $CHBr_2$ +Br energy level. In contrast the Br_2 elimination photoproducts are found at much higher energy level, 160 [CCSD(T)//MP2/aug-cc-pVTZ] to 205 kJ/mol (MP2) above *iso*-$CHBr_3$. Compared with CCSD(T), the B3LYP results tend to underestimate the reaction barriers, which is a well-known deficiency of DFT methods.[38]

Our experimental and computational results on *iso*-$CHBr_3$ are consistent with the recent ultrafast experiments of Crim and co-workers [119] and Tarnovsky and co-workers.[126] In particular, the assignment of *iso*-$CHBr_3$ as the carrier of an intense transient absorption band centered at 390 nm that appears with a rise-time < 0.5 ps following ultrafast photolysis of $CHBr_3$ in solution is very consistent with our UV/Visible spectrum of matrix-isolated *iso*-$CHBr_3$ (Figure 5.1)

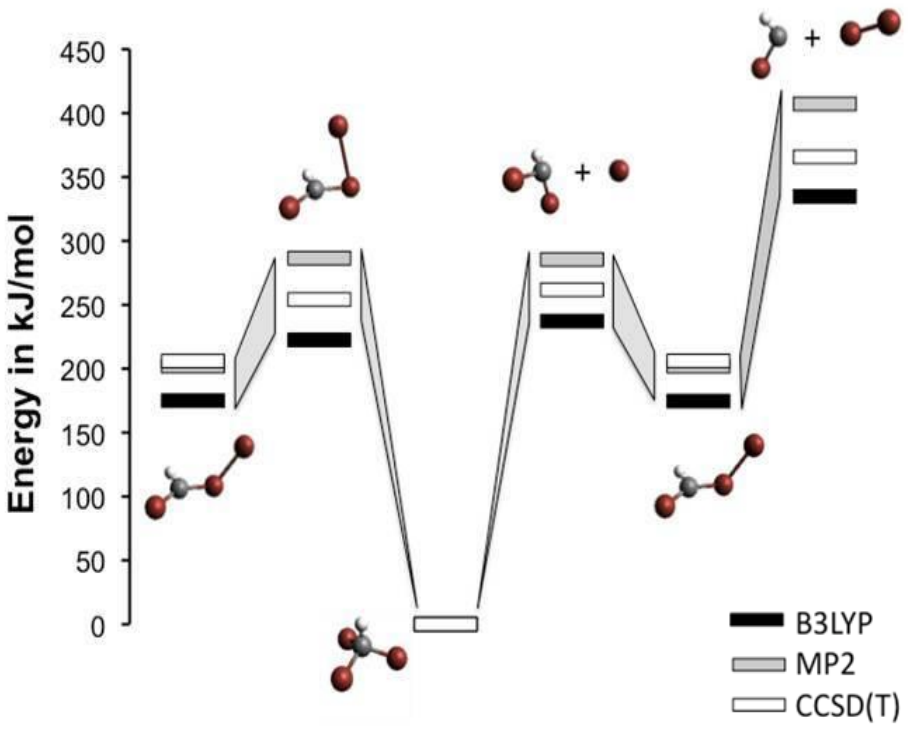


Figure 5.4 Calculated stationary points on the $CHBr_3$ potential energy surfaces at various levels of theory.

To confirm our results on *iso*-$CHBr_3$, we carried out experiments on the deuterated isotopomer. In these experiments, the $CDBr_3$:Ne 1:1500 sample was deposited at 5 K, then irradiated at 220 nm and finally annealed to 9 K. We observed the isotope chemical shifts as expected, and the most distinguishable was the C-D stretching mode, which showed a peak at 2292 cm^{-1} while this peak was observed at 3076 cm^{-1} for the hydrogen. These results are shown in Figure 5.5, and they are in good agreement with predicted frequencies (B3LYP/aug-cc-pVTZ) of 2357 and 3201 cm^{-1}, respectively for C-D and C-H.

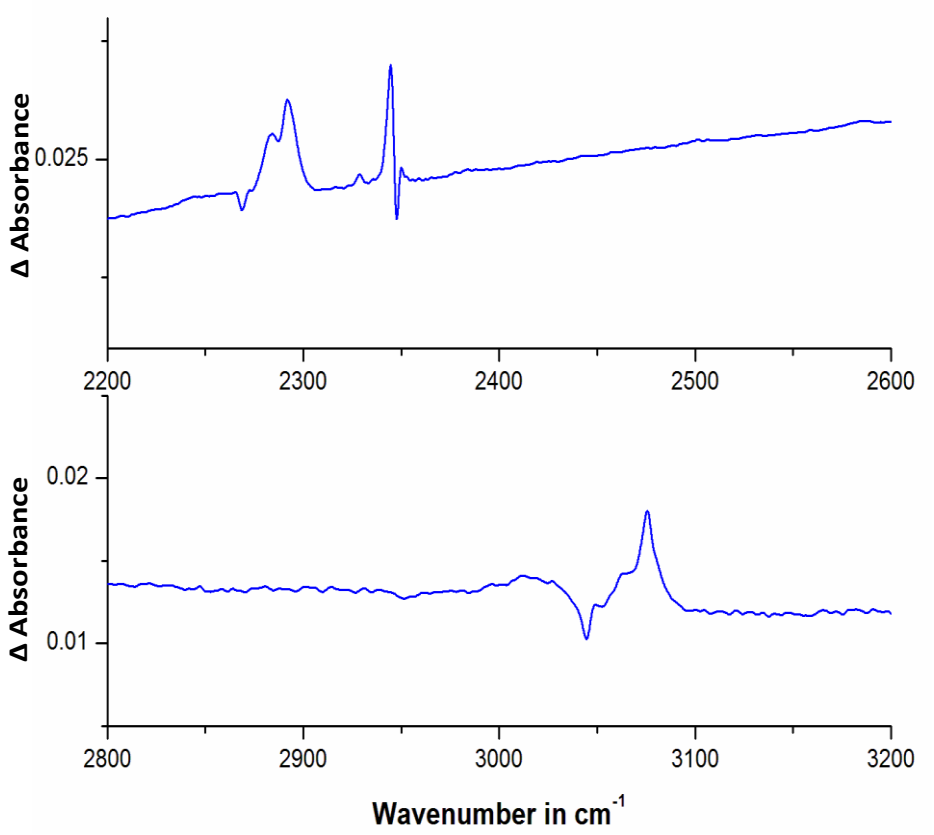


Figure 5.5 Upper panel: Infrared spectrum of a $CDBr_3$:Ne matrix (~1:1500) at ~ 5 K following laser irradiation at 220 nm and annealing to 9 K. **Lower panel:** Infrared spectrum of a $CHBr_3$:Ne matrix (~1:500) at ~ 5 K following laser irradiation at 220 nm and annealing to 9 K.

To ensure that both $CHBr_3$ and *iso*-$CHBr_3$ are connected by the same first order saddle point, a fully relaxed scan was performed along the ∠C-Br-Br angle using the B3LYP/cc-pVTZ level of theory. The results displayed in Figure 5.6, were affirmative and conclusive: both isomers are connected by the same transition with energy lying close to the $CHBr_2$ + Br asymptote. These results were supported by a second independent approach, the Intrinsic Reaction Coordinate (IRC)[127], which consists of following the reaction path from the optimized saddle point in the forward and backward directions. The IRC calculations (Figure 5.6) show that the two minima are connected by a first-order saddle point.

For bromoform, the saddle point was found to be lying at 254 kJ/mol above the $CHBr_3$, while the $CHBr_2$ + Br asymptote was at 8 kJ/mol higher. So far, the formation of *iso*-halomethanes in condensed phase has been thought to occur via photolytic mechanism involving C-Br bond breaking followed by recombination in the solvent cage. However, our results show that a direct path to produce the *iso*-$CHBr_3$ without bond-breaking, since the isomerization barrier lies below the channel involving bond breaking. In contrast, for the fluoro compound, the saddle point was close to both $CFBr_2$ + Br and CFBr + Br_2 asymptotes. At the CCSD(T)//MP2 level, this saddle point lies 6.3 kJ/mol above the $CFBr_2$ + Br asymptote, and 10.6 kJ/mol above the CFBr + Br_2 asymptote. Similar calculations were performed on other halogeno-substituted compounds, and in all cases, both isomers were found to be connected by the same first-order saddle point.

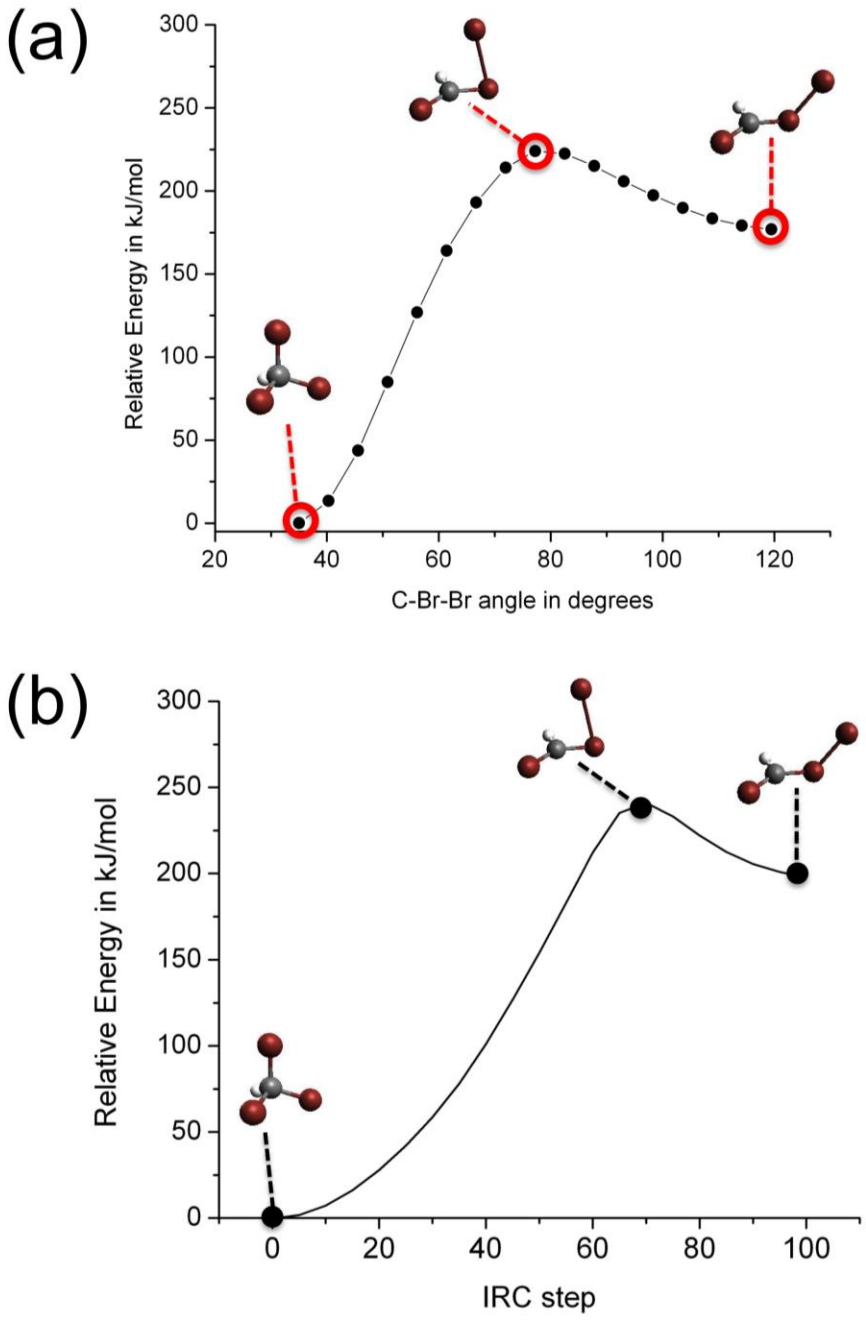


Figure 5.6: (a)Relaxed redundant scan along the C-Br-Br angle for $CHBr_3$, and (b)IRC path calculated at the B3LYP/cc-pVTZ level of theory. This illustrates that the normal and *iso*-forms of $CHBr_3$ are connected by a first order saddle point.

5.3.2 Extending the study to the characterization of iso-$CXBr_3$ (X=F, Cl and Br)

In order to understand more, regarding the structure of the *iso*-tribromomethanes, we thought to test the effects that substitution would bring on the structure, spectra and properties by conducting similar studies on the fluoro-substituted compound ($CFBr_3$). Thus a $CFBr_3$:Ar = 1:500 sample was deposited onto a cold KBr window held at ~5 K, then photolyzed at 220 nm and finally annealed by heating to 33K and re-cooling. The experimental IR and UV/Vis spectra are given in Figure 5.7 along with their *ab initio* predicted spectra.

Similarly to *iso*-bromoform, theory confirms that the *iso*-$CXBr_3$ (X=F, Cl, Br) species are minima on the respective $CXBr_3$ potential energy surfaces. The $CXBr_3$ PES's resembles other halons we have examined in our previous work including CF_2Br_2 [128], CF_2Cl_2 [129], $CHBr_3$ [130] where the isomerization transition state lies energetically near (and sometimes below) the threshold of radical products. Thus in reaction taking place on the ground PES, there will be competition between simple C-Br bond fission and isomerization process.

As it was found for the bromoform, the *iso*-$CFBr_3$ is the dominant photoproduct after irradiation at 220 nm and annealing to 33 K, however the $S_0 \rightarrow S_3$ transition is not as intense as found for the *iso*-bromoform and it is shifted to the red by some 30 nm.

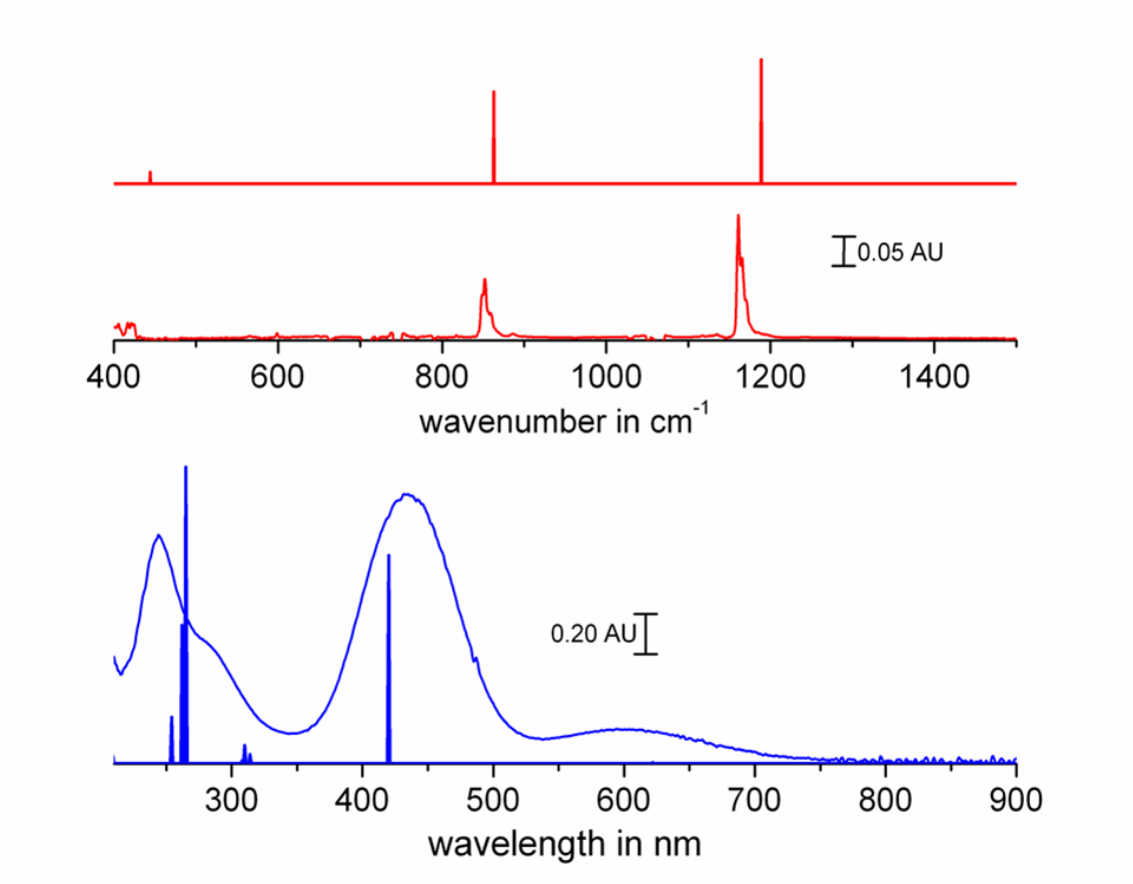


Figure 5.7 Upper panel: Infrared spectrum of a $CFBr_3$:Ar matrix (~1:500) at ~ 5 K following laser irradiation at 220 nm, and the predicted (B3LYP/aug-cc-pVTZ) infrared spectrum of *iso*-$CFBr_3$. **Lower panel:** The corresponding UV/Visible spectrum, compared with the predicted (TD-B3LYP/aug-cc-pVTZ) spectrum of *iso*-$CFBr_3$.

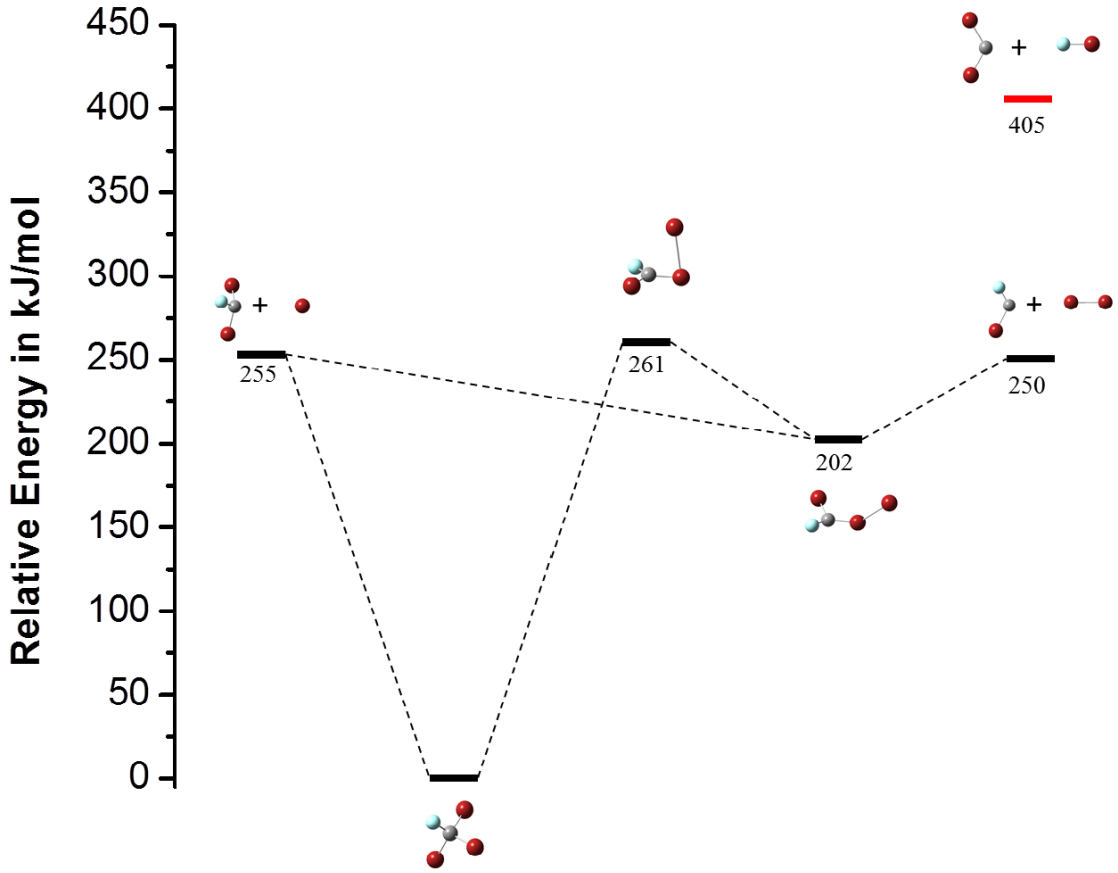


Figure 5.8 Calculated stationary points on the $CFBr_3$ potential energy surfaces at various levels of theory.

Table 5-4 Observed and calculated electronic absorptions (in nm) of *iso*-$CXBr_3$. Calculations were performed using TDDFT with the noted functionals and an aug-cc-pVTZ basis set. Oscillator strengths are given in parentheses.

Species	Assign.	Calc. (M06)		Calc. (CAM-B3LYP)		Obs.
FBrC-Br-Br	S1	657	(0.0001)	561	(0.0002)	594(0.03)
	S2	606	(0.0010)	521	(0.0006)	…
	S3	431	(0.2325)	420	(0.2736)	432(0.23)
	S4	309	(0.0060)	295	(0.0002)	…
	S5	286	(0.0023)	282	(0.1638)	288(0.082)
	S6	262	(0.0167)	252	(0.0016)	…
	S7	257	(0.2727)	248	(0.0026)	…
	S8	255	(0.1067)	243	(0.0746)	…
	S9	226	(0.0018)	229	(0.2961)	…
	S10	218	(0.0013)	201	(0.0182)	…
Br_2C-Br-Cl	S1	628	(0.0002)	532	(0.0002)	…
	S2	567	(0.0003)	488	(0.0116)	…
	S3	448	(0.1895)	440	(0.2216)	…
	S4	349	(0.0001)	328	(0.0002)	…
	S5	325	(0.0824)	303	(0.1354)	…
	S6	303	(0.0000)	279	(0.0041)	…
	S7	294	(0.0065)	263	(0.0559)	…
	S8	283	(0.0022)	257	(0.0270)	…
	S9	273	(0.2196)	252	(0.0330)	…
	S10	272	(0.0509)	236	(0.1136)	…
ClBrC-Br-Br	S1	700	(0.0001)	606	(0.0002)	…
	S2	644	(0.0004)	561	(0.0004)	…
	S3	464	(0.2420)	451	(0.2939)	…
	S4	332	(0.0480)	315	(0.0004)	…
	S5	329	(0.0549)	305	(0.1492)	…
	S6	301	(0.0005)	265	(0.0023)	…
	S7	279	(0.0508)	258	(0.0017)	…
	S8	278	(0.1214)	251	(0.0571)	…
	S9	265	(0.0556)	241	(0.1179)	…
	S10	249	(0.0473)	235	(0.0804)	…
Br_2C-Cl-Br	S1	778	(0.0000)	674	(0.0001)	…
	S2	736	(0.0002)	640	(0.0002)	…
	S3	436	(0.3520)	421	(0.4277)	…
	S4	358	(0.0691)	324	(0.0608)	…
	S5	331	(0.0000)	308	(0.0001)	…
	S6	313	(0.0001)	261	(0.0017)	…
	S7	301	(0.0729)	256	(0.0412)	…
	S8	275	(0.0492)	252	(0.0165)	…
	S9	271	(0.0177)	250	(0.0608)	…
	S10	253	(0.0084)	242	(0.0219)	…
Br_2C-Br-Br	S1	699	(0.0001)	608	(0.0002)	…
	S2	644	(0.0003)	562	(0.0004)	645(0.02)

	S3	471	(0.2316)	457	(0.2843)	458(0.43)
	S4	349	(0.1110)	329	(0.0003)	337(0.12)
	S5	348	(0.0001)	324	(0.1519)	…
	S6	314	(0.0000)	278	(0.0059)	…
	S7	292	(0.0109)	268	(0.0011)	…
	S8	291	(0.1060)	264	(0.0342)	…
	S9	281	(0.1095)	254	(0.0531)	…
	S10	273	(0.0407)	250	(0.1547)	…

Extending the study to $CClBr_3$ species, Figure 5.9 shows matrix infrared spectrum of a $CClBr_3$:Ar (1:500) sample at ~5 K following laser photolysis at 220 nm. There is possibility to form three different isomers (Figure 5.14), since the 220 nm photon energy (544kJ/mol) used in our experiments is far in excess of thermochemical thresholds for both C-Cl (293 kJ/mol) and C-Br (232 kJ/mol) bond hemolysis.[131] C-Br cleavage would lead to the ClBrC-Br-Br and Br_2C-Cl-Br isomers, while the third isomer would result from C-Cl bond dissociation followed by Br-Cl bond formation, leading to the Br_2C-Br-Cl.

Our calculations (B3LYP/aug-cc-pVTZ) level corrected of ZPE predict that ClBrC-Br-Br is the most stable of the three, lying at 16.4 kJ/mol below Br_2C-Cl-Br and 24.8 kJ/mol below Br_2C-Br-Cl. From the IR spectrum displayed in Figure 5.9, it is clear that two isomers (ClBrC-Br-Br and Br_2C-Br-Cl) were observed in our experiments, with diagnostic bands at, respectively, 879 and 779 cm^{-1}. The third isomer is formed in very small yield, if at all. Using respective IR intensity calculated, a simple Boltzmann distribution at 5 K predicts a ratio of ClBrC-Br-Br to Br_2C-Br-Cl of ~ 27:1.

Figure 5.10 shows the observed UV-Vis spectrum in comparison of TD-DFT predictions of three isomers. They are all predicted to have a strong 450 nm region, consistent with the broad band observed experimentally. In addition, the Br_2C-Br-Cl isomer is predicted to have a nearly equally strong absorption in the UV, which lies near the position of a strong band observed at 254 nm. (Figure 5.10)

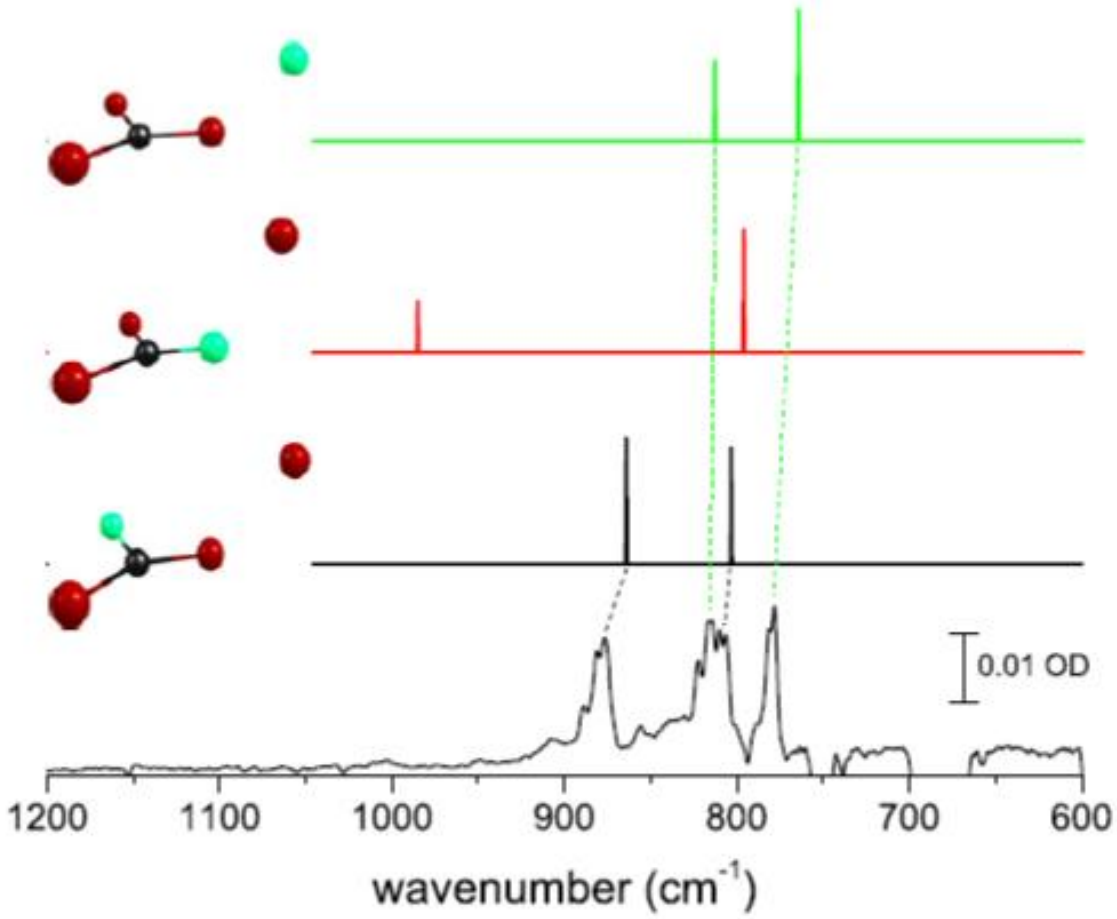


Figure 5.9 Observed difference IR spectrum following 220 nm laser photolysis of a CClBr3 sample held at 5 K and calculated (B3LYP/aug-cc-pVTZ) infrared spectra of the three possible isomers. Calculated intensities are arbitrary scaled; quantitative information is given in Table 5-5.

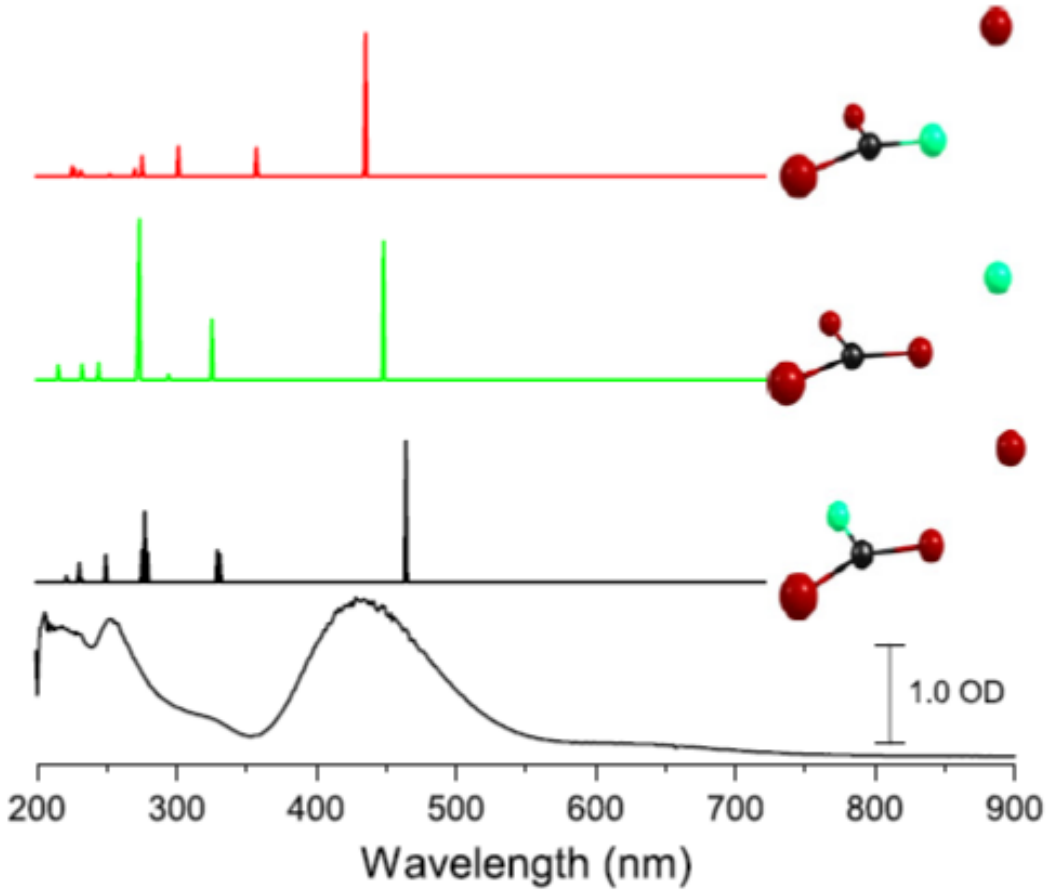


Figure 5.10 UV-Vis spectrum following 220 nm laser photolysis of a $CClBr_3$:Ar sample held at 5 K and calculated (TD-M06/aug-cc-pVTZ) electronic spectra of the three possible isomers. Calculated intensities are arbitrary scaled; quantitative information is given in Table 5-4.

Table 5-5 Observed and calculated vibrational frequencies (in cm^{-1}) of *iso*-$CClBr_3$. Calculations were performed with the methods shown and an aug-cc-pVTZ basis-set. Calculated intensities in km/mol are given in parentheses.

Species	**Mode**	**Approx. descr.**	**Calc. (B3LYP)**	**Calc. (M06)**	**Calc. (MP2)**	**Obs.**
ClBrC-Br-Br	υ_1	C-Br stretch	813 (113)	872 (99)	944 (38)	816
	υ_2	asym. C-Br stretch	763 (186)	787 (153)	815 (128)	779
	υ_3	C-Br3 rock	366 (7)	349 (7)	350 (37)	…
	υ_4	sym. C-Br stretch	282 (34)	299 (32)	324 (4)	…
	υ_5	Cl-Br stretch	223 (84)	217 (110)	281 (5)	…
	υ_6	C-Br wag	186 (0)	184 (0)	188 (0)	…
	υ_7	Br-C-Br bend	163 (0)	163 (1)	169 (0)	…
	υ_8	Torsion	64 (2)	62 (2)	60 (2)	…
	υ_9	C-Br-Cl bend	42 (0)	45 (9)	59 (2)	…
Br_2C-Cl-Br	υ_1	C-Cl stretch	864 (179)	900 (182)	944 (38)	878
	υ_2	asym. C-Br stretch	803 (165)	833 (151)	815 (128)	809
	υ_3	C-Cl wag	367 (11)	362 (19)	350 (37)	…
	υ_4	sym. C-Br stretch	347 (39)	350 (28)	324 (4)	…
	υ_5	Cl-C-Br bend	220 (3)	221 (4)	281 (5)	…
	υ_6	Br-C-Br bend	195 (15)	194 (15)	188 (0)	…
	υ_7	Br-Br stretch	155 (30)	157 (40)	169 (0)	…
	υ_8	Torsion	59 (1)	58 (1)	60 (2)	…
	υ_9	C-Br-Br bend	38 (4)	39 (5)	59 (2)	…

Br_2C-Br-Cl	υ_1	C-Cl stretch	984 (74)	1014 (65)	982 (41)	…
	υ_2	asym. C-Br stretch	796 (175)	830 (153)	829 (141)	…
	υ_3	C-Br stretch	373 (25)	379 (41)	417 (20)	…
	υ_4	C-Br3 rock	384 (53)	339 (36)	353 (7)	…
	υ_5	C-Cl wag	245 (0)	246 (0)	279 (14)	…
	υ_6	Cl-Br stretch	197 (28)	193 (34)	246 (0.1)	…
	υ_7	Br-C-Cl bend	171 (12)	168 (18)	182 (0.3)	…
	υ_8	C-Cl-Br bend	52 (4)	46 (1)	55 (1)	…
	υ_9	Torsion	49 (1)	41 (4)	49 (0)	…

To complete our study, the fully brominated compound, tetrabromomethane (CBr_4) was our final candidate. The commercially available CBr_4 sample was diluted in rare gas and deposited onto a KBr window held at 5 K. The IR spectra recorded as deposited, after irradiation and after subsequent annealing to 30 K are displayed in Figure 5.11. The parent spectrum is much simpler with only one band in the C-Br stretching region. Upon irradiation, the parent band decreased and we observed new bands. One of these bands couldn't survive the annealing process, and we believe that it was due to a transient species such as a radical. The other two peaks increased in intensity upon annealing, and as shown in Figure 5.11, they correlate with the theoretical IR spectrum of *iso*-CBr_4 calculated at the M06/aug-cc-pVTZ level of theory.

The UV-Vis spectrum displayed in Figure 5.12, resembles to what we have observed for other *iso*-$CXBr_3$ species. It shows an intense broad band at 458 nm, predicted by TD-CAMB3LYP calculations at 457 nm and other weaker bands at 645 and 337 nm.

Comparing the values given by MP2 and those from B3LYP calculations, there is a slight divergence. To test the accuracy of these two methods, a third density functional (M06) was used to optimize the structure, the results came out somewhat as intermediate to those found with MP2 and B3LYP, and they depended on the choice of the basis set. Because of the reasons stated above, the single energy calculations at higher level of theory [CCSD(T)/cc-pVTZ] were based on the structures optimized at the MP2/cc-pVTZ level. The resulting values are compared with the optimized MP2/cc-pVTZ and B3LYP/aug-cc-pVTZ energies. I*so*-$CFBr_3$ is predicted to be bound by ~53 kJ/mol with respect to the $CFBr_2$ + Br asymptote [CCSD(T)//MP2] as it was observed for $CHBr_3$. The different aspect comes with along the molecular elimination channel, where the energy of

CFBr + Br_2 products decreases significantly, lying only at ~48 kJ/mol above the *iso*-$CFBr_3$ minimum (Figure 5.8).

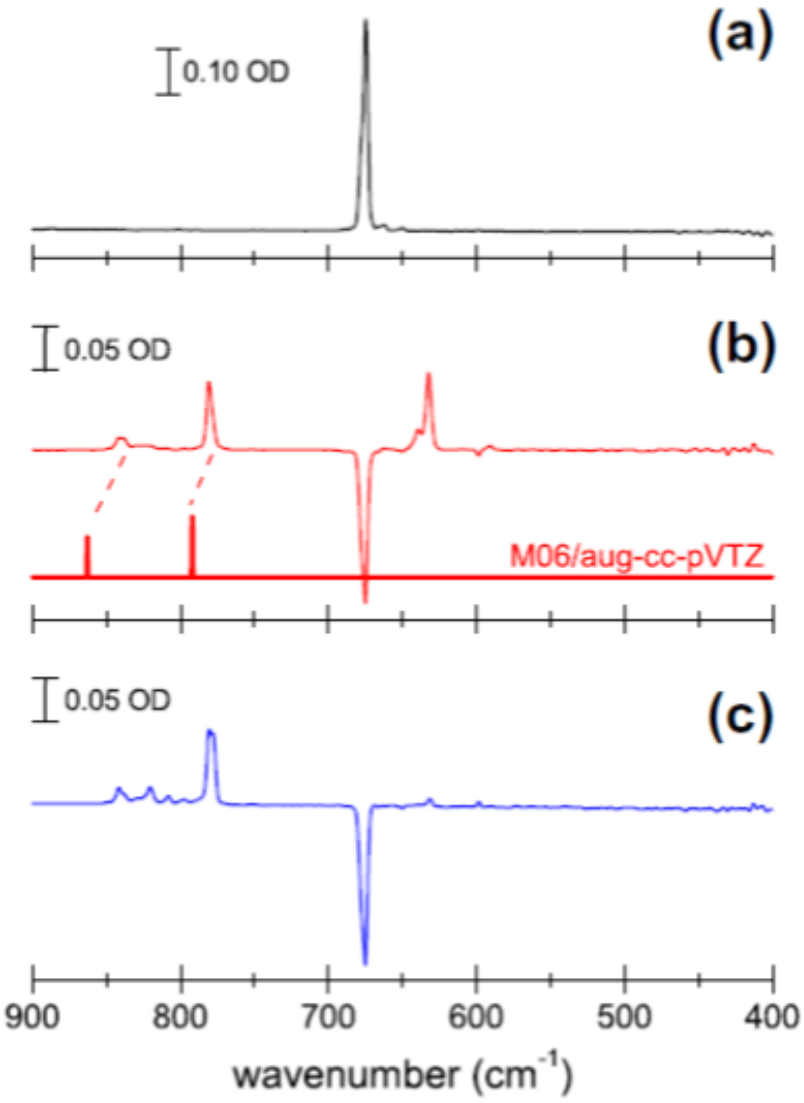


Figure 5.11 (a) Infrared spectrum of a CBr_4:Ar sample at 5 K. **(b)** Difference spectrum following photolysis of the sample at 266 nm. The calculated (M06/aug-cc-pVTZ) spectrum of *iso*-CBr_4 is shown as stick spectrum and the intensities are arbitrarily scaled; quantitative information is given in Table 5-6. **(c)** Difference spectrum following photolysis at 266 nm and subsequent annealing to 30 K, followed by re-cooling to 5 K.

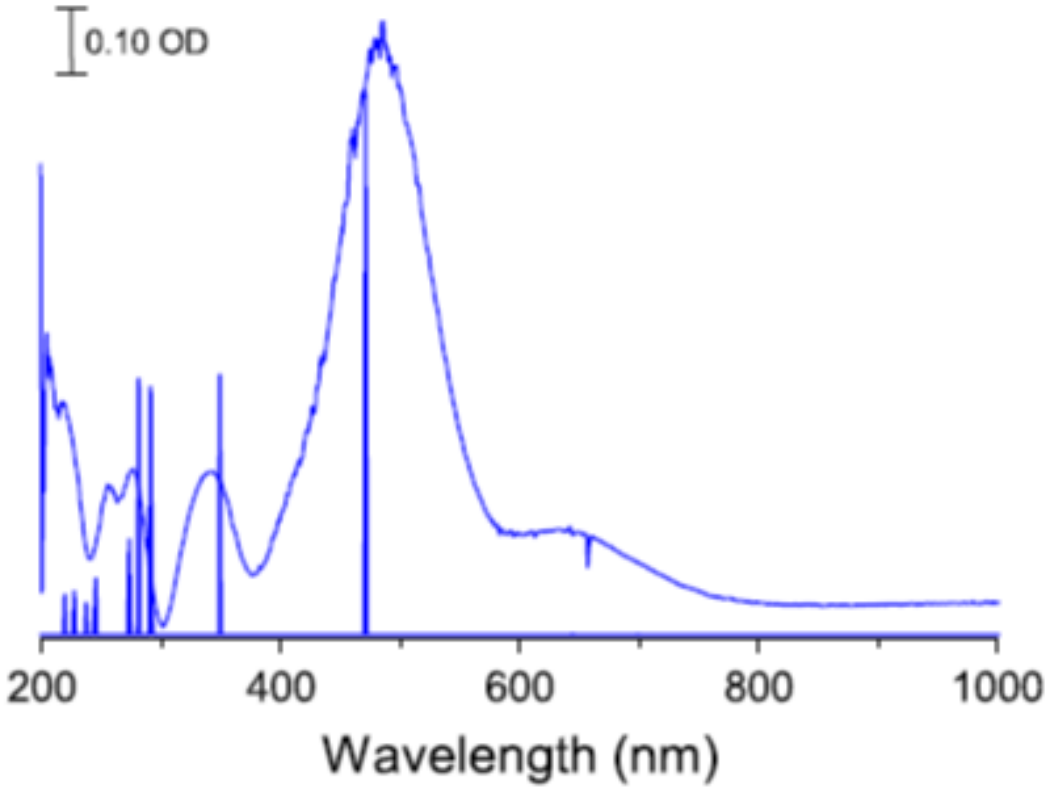


Figure 5.12 UV-Vis spectrum of a CBr_4:Ar sample following photolysis at 266 nm. The calculated (TD-M06/aug-cc-pVTZ) spectrum of *iso*-CBr_4 is shown as a stick spectrum with arbitrarily scaled intensity.

Table 5-6 Observed and calculated vibrational frequencies (in cm^{-1}) of *iso*-CBr_4. Calculations were performed with the methods shown and an aug-cc-pVTZ basis set. Calculated intensities in km/mol are given in parentheses.

Mode	**Approx. description**	**Calc. (B3LYP)**	**Calc. (M06)**	**Calc. (MP2)**	**Obs.(this work)**	**Ref. [29]**
ν_1	C-Br stretch	815 (115)	863 (97)	928 (43)	824	828
ν_2	Asym. C-Br stretch	760 (174)	793 (144)	814 (123)	781	…
ν_3	$C-Br_3$ rock	342 (20)	328 (21)	355 (28)	…	…
ν_4	Sym. C-Br stretch	282 (29)	296 (24)	294 (3)	…	…
ν_5	C-Br rock	191 (0)	180 (0)	225 (0)	…	…
ν_6	$C-Br_2$ rock	174 (26)	171 (33)	184 (0)	…	179
ν_7	Br-Br stretch	148 (18)	149 (22)	167 (2)	…	155
ν_8	Torsion	50 (1)	50 (1)	46 (0)	…	…
ν_9	C-Br-Br bend	35 (4)	37 (4)	46 (1)	…	…

5.3.3 Structure and bonding in *iso*-$CXBr_3$ and the $CXBr_3$ Potential Energy Surface

Going back to *iso*-$CHBr_3$, one may ask what could be the bonding and the correct structure for this isomer. Previous studies have shown that there may be several possible resonance structures for *iso*-polyhalomethanes.[64, 65, 132]. Figure 5.13 shows the most important resonance structures for the *iso*-$CXBr_3$ (X=H, Halogen atom): (i) a $CXBr\cdots Br_2$ complex, (ii) an ion-pair structure where the positive charge can reside on the central carbon or bromine atom, and (iii) a halonium ylide, where a negative partial charge on carbon is predicted. All C-Br bonds are not of equal length, on the free Br side, the bond is about ~0.1Å longer. The shorter C-Br bond length is similar to that calculated for $CHBr_2^+$ at the B3LYP/aug-cc-pVTZ level [Figure 5.13 (b)]; however, the calculated Mulliken charges [Figure 5.13 (c)] indicate a substantial negative partial charge on the C atom and positive partial charge on the adjacent Br atom, more consistent with the halonium ylide structure. The strongly bent C-Br-Br linkage is also consistent with an ylide structure, as an ion pair structure would access more linear geometries.

Compared with *iso*-$CHBr_3$, *iso*-$CFBr_3$ has larger C-Br-Br angle and Mulliken charge on carbon atom is more electropositive. This suggests a more important contribution from the ion-pair resonance structure. (Figure 5.13)

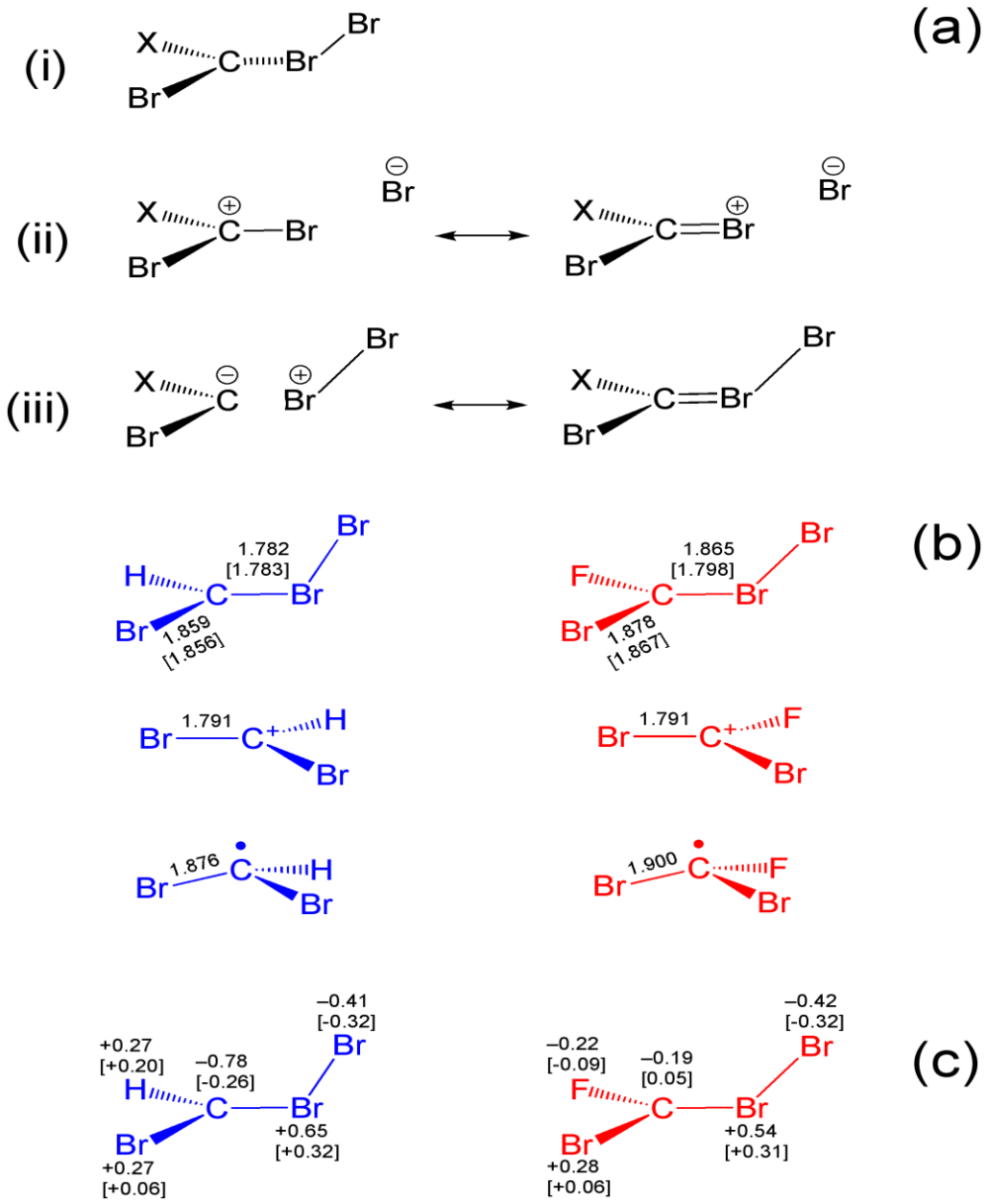


Figure 5.13 Potential resonance structures for *iso*-$CXBr_3$ species. **(b)** Comparison of calculated (B3LYP/aug-cc-pVTZ) structural parameters with those of the corresponding halomethyl cation and radical. **(c)** Calculated Mulliken charges for *iso*-$CHBr_3$ and *iso*-$CFBr_3$ at the B3LYP/aug-cc-pVTZ and (in brackets) MP2/cc-pVTZ levels of theory.

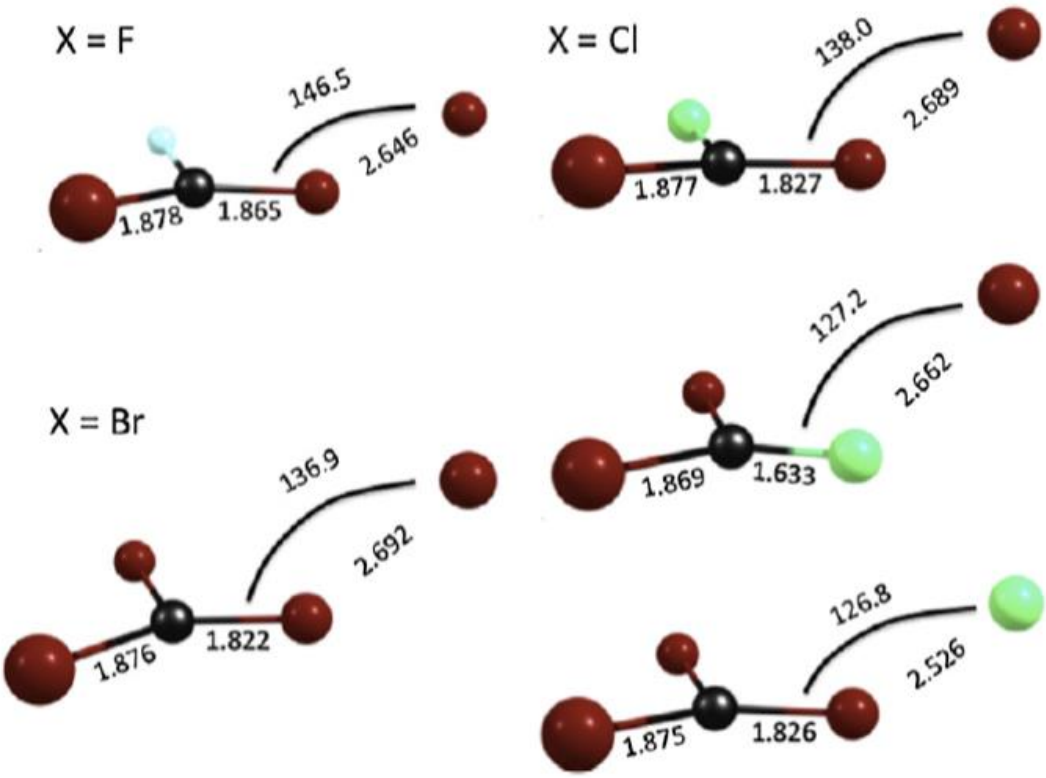


Figure 5.14 Calculated structures of *iso*-$CXBr_3$ (X=F, Cl, Br) species at the B3LYP/aug-cc-pVTZ level. Selected geometrical parameters are given. Bond angles are in degrees and bond lengths are in Angstroms.

To further examine bonding in this series, each *iso*-$CXBr_3$ was examined with MP2/aug-cc-pVTZ calculations using NBO 5.9 implemented in Gaussian 09. [133] For these calculations, first the intrinsic reaction coordinate (IRC) calculations were performed to characterize the isomerization path. Next, the bonding of each *iso*-halon species, as well as each IRC point between the halon and *iso*-species, were analyzed using Natural Resonance Theory [134-137] and the details are given in Figure 5.13 ($CHBr_3$), Figure 5.15 ($CFBr_3$), Figure 5.16 ($CClBr_3$) and Figure 5.17 (CBr_4). The most important resonance structures (weights > 5%) correspond to covalent, ion-pair and ylide structures, identified in the figures. As we have shown in our previous studies [130, 138], these species convert from a primarily covalent $CXBr_3$ structure to an *iso*-form that is dominated by an ion-pair resonance structure. This can be easily noted in the increased bond order between C and Br (4) in each of the cases, showing the contribution of a partial double bond between those two atoms, as shown in Table 5-8, Table 5-9 and Table 5-10. We can also note that the central C atom maintains a weak bond to the external Br (5) atom in each of these cases of 0.22, 0.19 and 0.27 for F, Cl, and Br respectively. The most surprising observation is the lack of change in halon substitution on the overall NBO/NRT analysis of these species. In each of the cases, the relative contributions of the ion-pair resonance structure is fairly consistent at 37, 39 and 39% for X=F, Cl, Br respectively.

One should note that, in the view of the NBO/NRT analysis, the formation and decay of the isomer will be very sensitive to the environment, as there is a differential solvation of the *iso*-form and isomerization transition state relative to the parent halon. Taking an example of CBr_4 case, Ihee and co-workers have shown that the isomerization

barrier from CBr_4 to *iso*-CBr_4 is lowered by about 32 kJ/mol in methanol as compared with the gas phase, and the *iso*-CBr_4 well is lowered by a similar amount.[123] in contrast, the radical and molecular thresholds are nearly the same in both environments. Thus, in condensed phase, the isomer is stabilized with respect to C-Br or Br-Br bond fission, so that back isomerization to the parent halon will be the lowest energy channel.

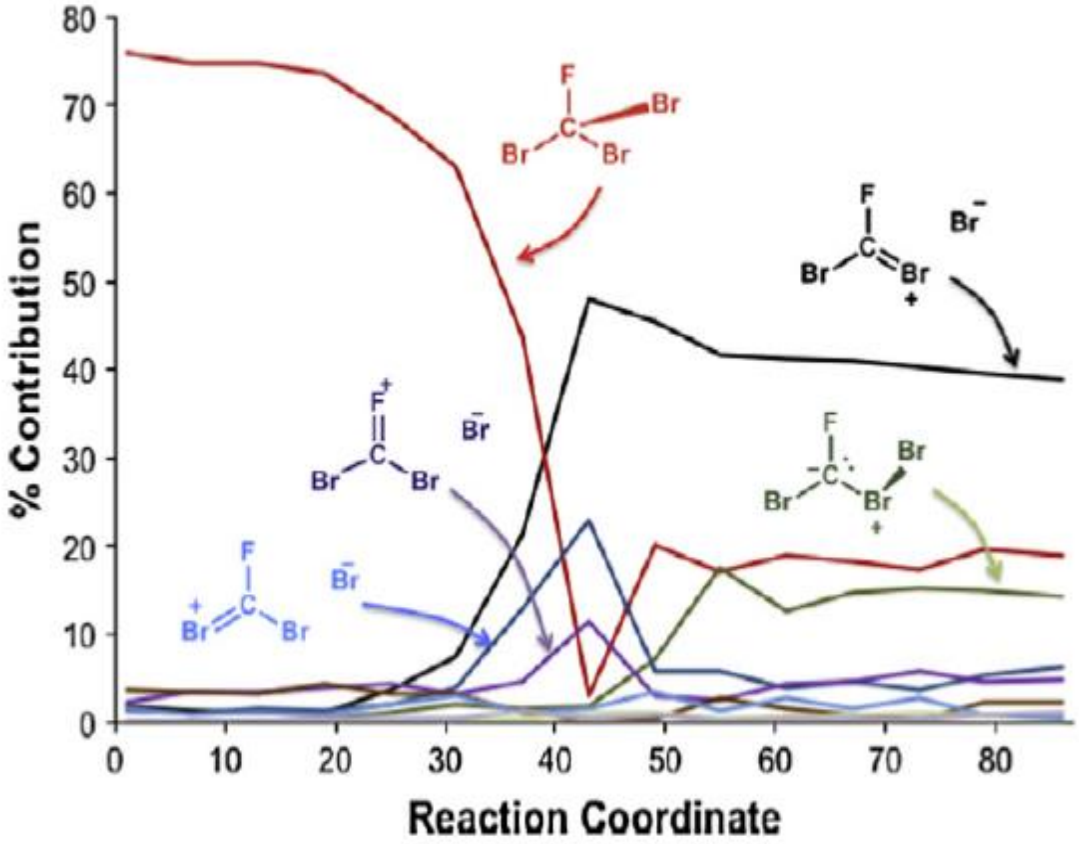


Figure 5.15 Calculated resonance structure weights along the IRC path in the isomerization of $CFBr_3$, using Natural Resonance Theory analysis at the MP2/aug-cc-pVTZ level. The transition state located near point 40, represents a cross-over from covalent to ion-pair binding. The five resonances structures with the largest weights are identified.

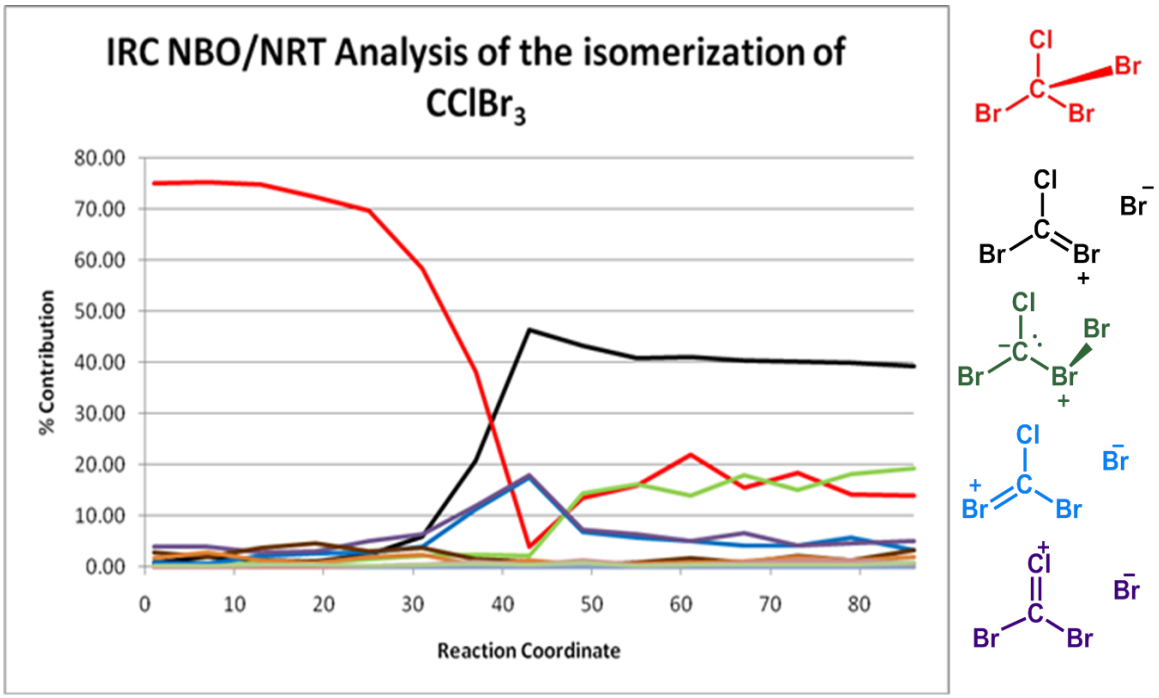


Figure 5.16 Calculated resonance structure weights along the IRC path in the isomerization of $CClBr_3$, using Natural Resonance Theory analysis at the MP2/aug-cc-pVTZ level.

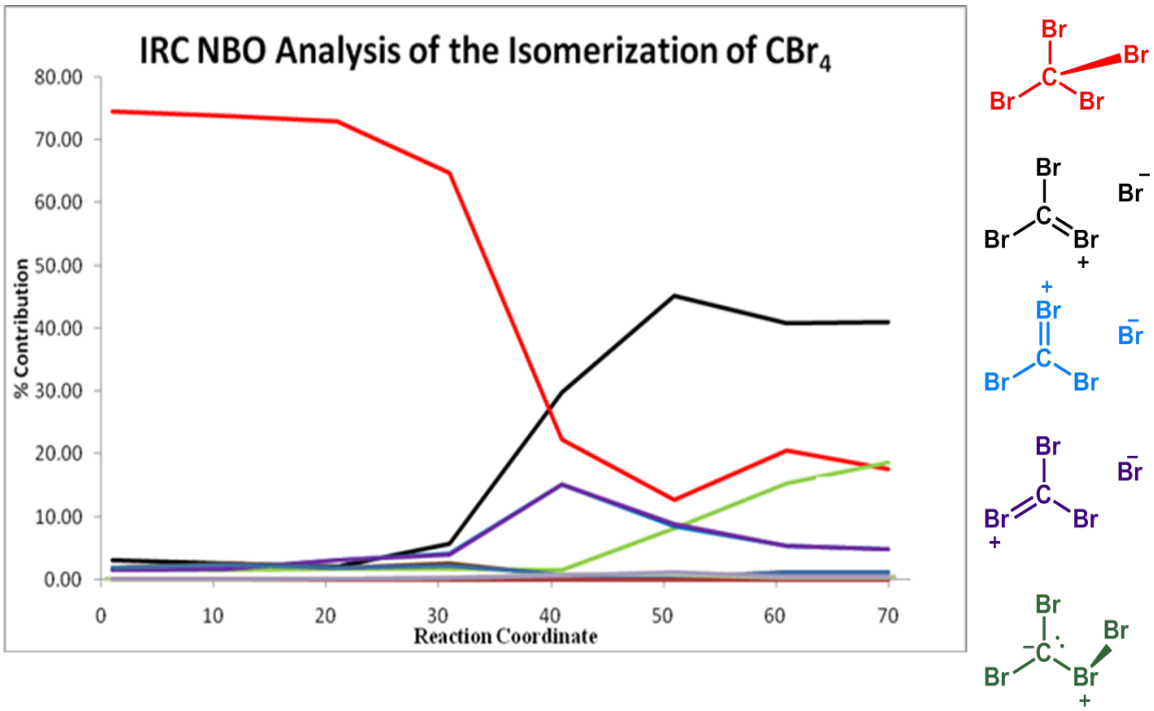
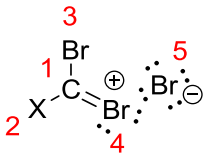
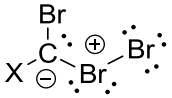
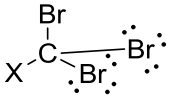


Figure 5.17 Calculated resonance structure weights along the IRC path in the isomerization of CBr_4, using Natural Resonance Theory analysis at the MP2/aug-cc-pVTZ level.

Table 5-7: Resonance contributions in the *iso*-$CXBr_3$ species derived from NRT analysis.

***iso*–$CFBr_2$–Br**	X = F	37 %	17 %	12 %
				
		ion-pair	ylide	covalent
***iso*–$CClBr_2$–Br**	X = Cl	39 %	18 %	14 %
***iso*–CBr_3–Br**	X = Br	39 %	20 %	15 %

All resonance contributions weighted above 5 %.

Table 5-8. Natural bond order analysis for *iso*–$CFBr_2$–Br (MP2/aug-cc-pVTZ in Gaussian 09, with NBO 5.9)

Bond	Natural Bond Order (covalent)	Natural Bond Order (ionic)	Natural Bond Order (total)
C 1 – F 2	0.5148	0.5687	1.0836
C 1 – Br 3	0.9166	0.1589	1.0755
C 1 – Br 4	0.9305	0.2608	1.1913
C 1 – Br 5	0.1016	0.1181	0.2196
Br 4 – Br 5	0.1387	0.1567	0.2954

All Bond orders greater than 0.05.

Atom	Natural Charge
C 1	0.12475
F 2	-0.36608
Br 3	0.18817
Br 4	0.57592
Br 5	-0.52275

Table 5-9 Natural bond order analysis for *iso*–$CClBr_2$–Br (MP2/aug-cc-pVTZ in Gaussian 09, with NBO 5.9)

Bond	**Natural Bond Order (covalent)**	**Natural Bond Order (ionic)**	**Natural Bond Order (total)**
C 1 – Cl 2	0.9504	0.1311	1.0815
C 1 – Br 3	0.8800	0.1755	1.0555
C 1 – Br 4	1.0280	0.2866	1.3147
C 1 – Br 5	0.1228	0.0710	0.1937
Br 4 – Br 5	0.1535	0.1156	0.2691

All Bond orders greater than 0.05.

Atom	**Natural Charge**
C 1	-0.45128
Cl 2	0.11656
Br 3	0.21717
Br 4	0.63772
Br 5	-0.52016

Table 5-10 Natural bond order analysis for *iso*–CBr_3–Br (MP2/aug-cc-pVTZ in Gaussian 09, with NBO 5.9)

Bond	**Natural Bond Order (covalent)**	**Natural Bond Order (ionic)**	**Natural Bond Order (total)**
C 1 – Br 2	0.8855	0.1788	1.0643
C 1 – Br 3	0.8860	0.1791	1.0651
C 1 – Br 4	1.0503	0.2741	1.3244
C 1 – Br 5	0.1338	0.1362	0.2700
Br 4 – Br 5	0.1514	0.0637	0.2151

All Bond orders greater than 0.05.

Atom	**Natural Charge**
C 1	-0.57067
Br 2	0.22021
Br 3	0.22040
Br 4	0.64397
Br 5	-0.51392

5.3.4 The photochemistry of the *iso*-$CXBr_3$.

Taking advantage of the UV-Vis absorption band at 399 nm and the laser light range available, the photochemistry of the *iso*-$CHBr_3$ was investigated by 440 nm laser photolysis the in Ar or Ne matrix. Upon photolysis the bands assigned to the *iso*-$CHBr_3$ went away and those assigned to the parent $CHBr_3$ grew back in. (Figure 5.18).

The same Figure shows that photolysis of *iso*-$CFBr_3$ led to back-photoisomerization; where all the bands due to the parent $CFBr_3$ increased at the expenses of those of the *iso*-$CFBr_3$. Similar results were observed for *iso*-$CClBr_3$ and *iso*-CBr_4 (Figure 5.19) and they are consistent with prior studies of other *iso*-halomethanes, which demonstrated facile back photoisomerization to the normal isomer. [139-141]

As mentioned earlier, our theoretical calculations, show that both isomers are connected by a first-order saddle point, however, the exact mechanism of isomerization has not been firmly established. In future experiments, we are planning to use Resonance Raman spectroscopy to probe the short time dynamics following photoexcitation.

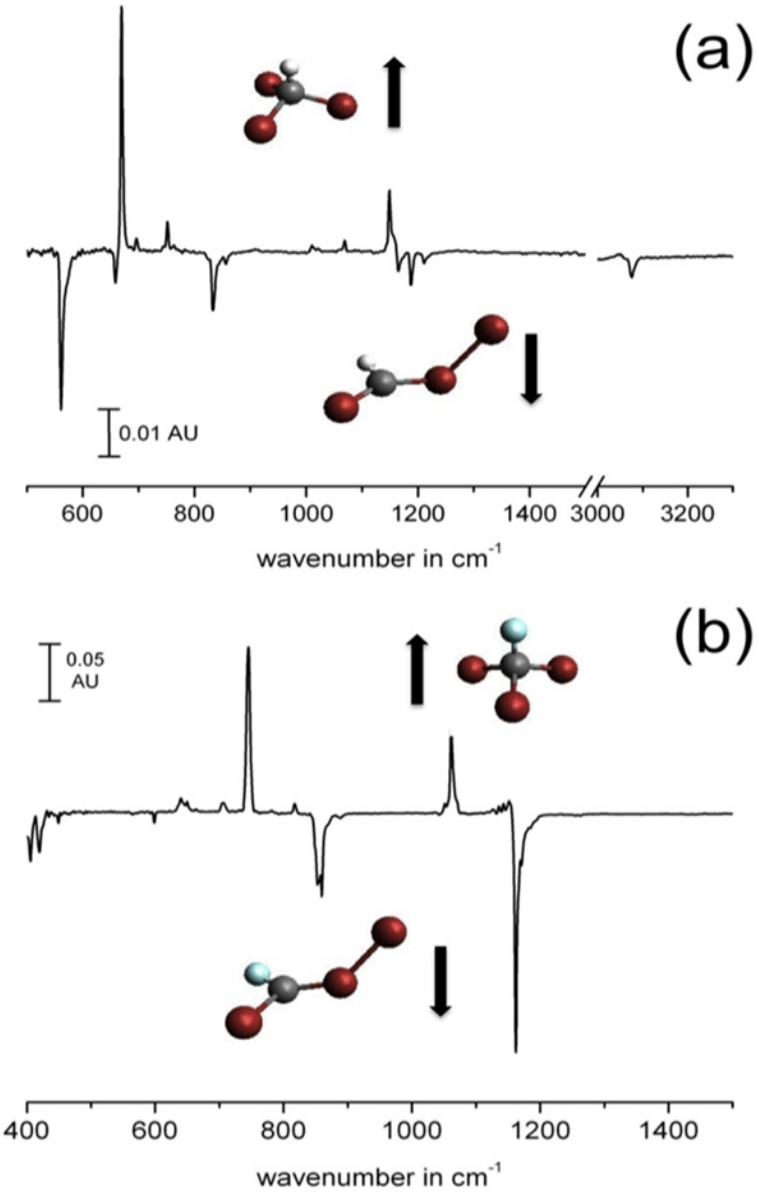


Figure 5.18 Difference IR spectra obtained following 440 nm laser irradiation of matrix isolated **(a)** *iso*-$CHBr_3$ and **(b)** *iso*-$CFBr_3$. In each case the IR absorptions of the *iso*-species decrease and the bands of the parent increase, illustrating a facile back photoisomerization.

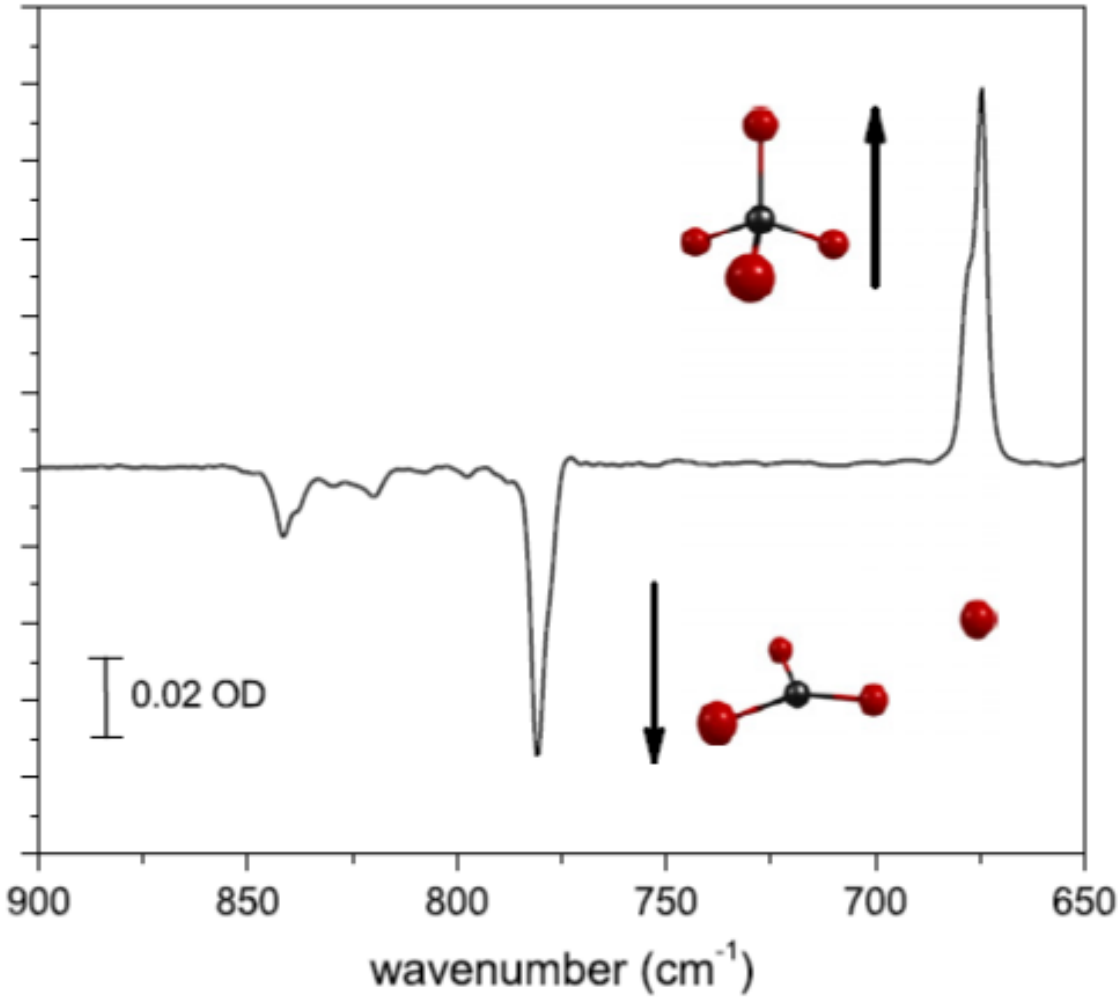


Figure 5.19 Difference spectrum following 440 nm excitation of matrix-isolated CBr_4. Laser irradiation of the isomer leads to the loss of the isomer IR bands and reformation of the parent halon.

5.3.5 Modeling the electronic absorption signature of *iso*-halons.

Similarities found in electronic absorption spectra of various *iso*-halons, led us to interrogate the nature of these transitions. With few examples shown in Figure 5.20, the electronic spectra of iso-polyhalomethanes universally exhibit a broad, very intense absorption band in the near UV to Visible region, with weaker band(s) lying at lower energy.[64, 128, 130, 132, 138] As shown in previous two chapters, the strongest band was assigned, based on our TD-DFT results, to the $S_0 \rightarrow S_3$ transition, with the overlapping $S_0 \rightarrow S_1, S_2$ transition lying to lower energy.[128, 142] One should note that while the observed intensity of $S_0 \rightarrow S_3$ transition agrees with the calculated oscillator strength, the $S_0 \rightarrow S_1, S_2$ transitions are predicted to be much weaker than they appear experimentally, suggesting that these bands borrow intensity from $S_0 \rightarrow S_3$ strong transition.[130] To our knowledge, and prior to our experiments, no studies have attempted to model the electronic absorption spectrum of the iso-halons.

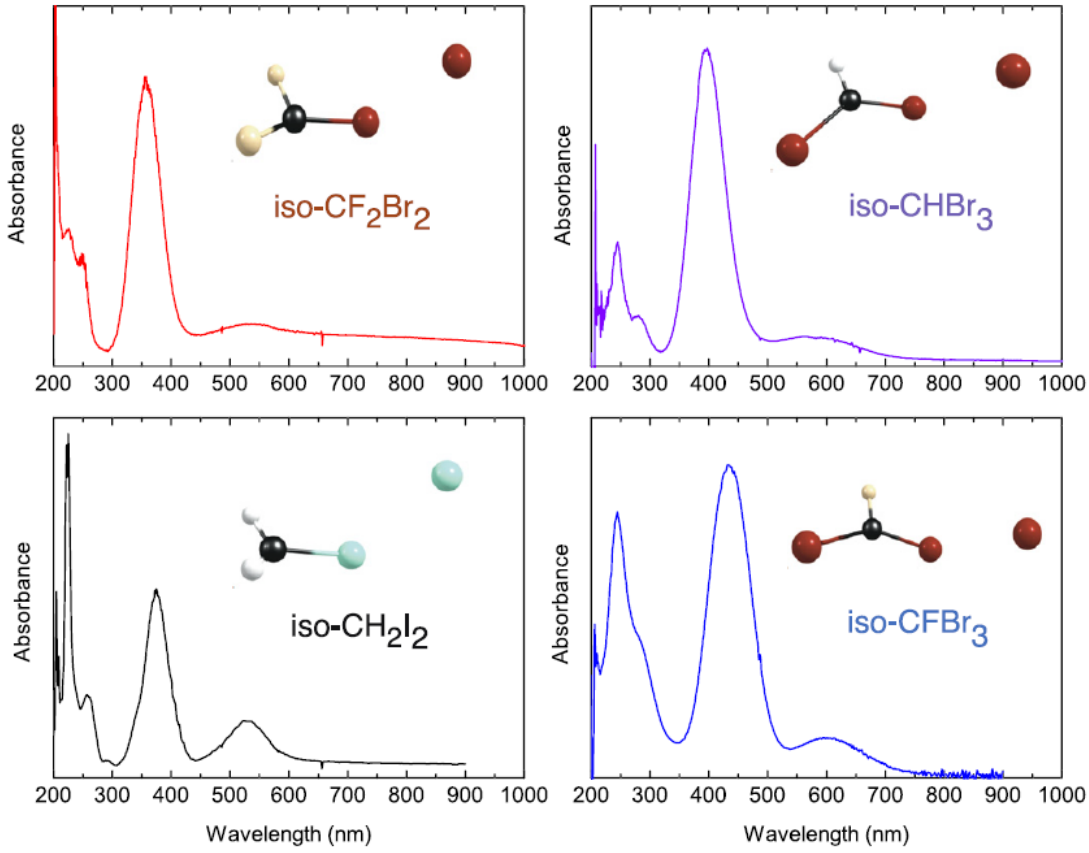


Figure 5.20 Example UV-Visible spectra of iso-polyhalomethanes trapped in rare gas cryogenic matrices at 5 K. From upper left: *iso*-CF_2Br_2 (Ar), *iso*-$CHBr_3$ (Ne), *iso*-$CFBr_3$ (Ne), *iso*-CH_2I_2 (Ar). All species show weak $S_0 \rightarrow S_1$, S_2 absorptions peaking in the visible, and a stronger ($S_0 \rightarrow S_3$) absorption in the near-UV/blue region.

Taking iso-$CHBr_3$ as representative of iso-polyhalomethanes, we did theoretical analysis, by simulating the UV-Vis spectrum, using FC approach with PGOPHER program suit.[143] As shown in Figure 5.21, our DFT and TD-DFT (CAM-B3LYP and TD-CAM-B3LYP/aug-cc-pVTZ) results show that there is a significant change in geometry due to electronic excitation from the ground S_0 state to the excited S_3 state. For instance, in the excited state, C-Br bond length increases by 0.1 Å, the Br-Br bond length increases by 0.4 Å and C-Br-Br bond angle increases by ~ 54°. These changes can be understood by visualizing the $CHBr_2^+$ subunit as having two representative resonance structures: one containing a C=Br double bond with the positive charge on the double bonded Br atom, and another structure with all single bonds and the positive charge localized on the central carbon atom. Our TD-DFT results also show that, this electronic transition is largely described by a simple HOMO-LUMO excitation, resembles a π-π^* excitation on the $CHBr_2^+$ chromophore (Figure 5.22). It's understandable that this excitation will weakens C-Br bond, in producing greater positive charge density on the central C atom, which should also weaken the Br-Br interaction.

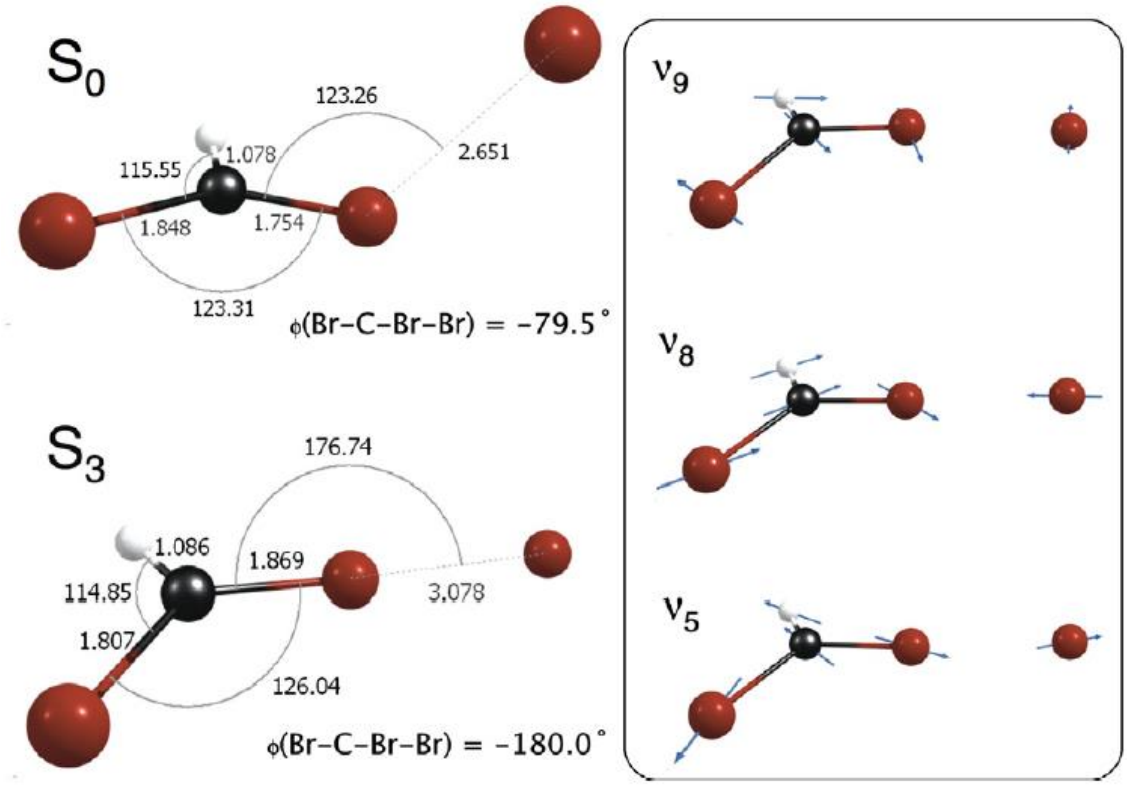


Figure 5.21 Optimized structures of the S_0 and S_3 states of iso-$CHBr_3$. The prominent Franck–Condon active modes are shown at right.

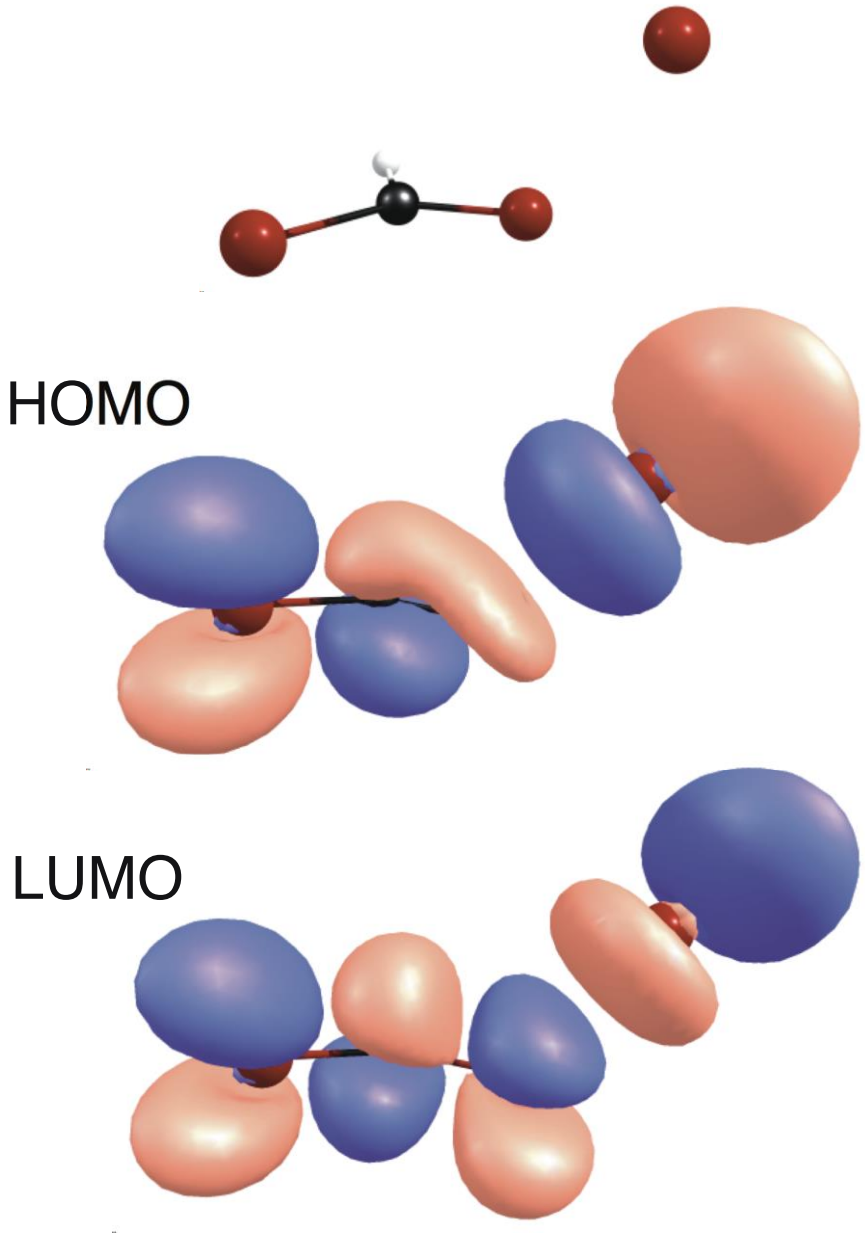


Figure 5.22 Isosurfaces (isovalue of 0.03) of the HOMO and LUMO of iso-$CHBr_3$.

There are three vibrational modes showing the largest displacements in this electronic transition (Figure 5.21) υ_5 = 618 (536) cm^{-1} (symmetric C-Br stretch), υ_8 = 175 (127) cm^{-1} (Br-Br stretch) and υ_9 = 49 (48) cm^{-1} (torsion). The calculated frequencies and mass-weighted displacements were included in the Franck-Condon (FC) simulation, taking into account the effects of Duschinsky mixing.[144] and the resulting spectrum is compared with the experimental spectrum in Figure 5.23. Only transitions from the vibrationless level of S_0 were considered, as this should be the only level populated in our experimental conditions. The simulated spectrum is shown as a stick spectrum in order to show the large density of vibrational bands in the FC envelope. The lack of structure in the experimental spectrum can be attributed to two other factors: (i) the low resolution of experimental spectrum (ca. 1 nm or ~60 cm^{-1} at λ_{max}), and (ii) broadening due to the matrix environment, which can be significant, particularly for ionic structures.[145, 146] Adding a Gaussian linewidth of ~150 cm^{-1}, will be enough to wash out this vibrational structure. This simulation shows that one can reproduce the major features of the experimental spectrum, by using input from theory with no adjustable parameters. Importantly, it shows that the width of the experimental spectrum arises primarily from the pronounced FC envelope, due to large structural changes in the electronic transition.

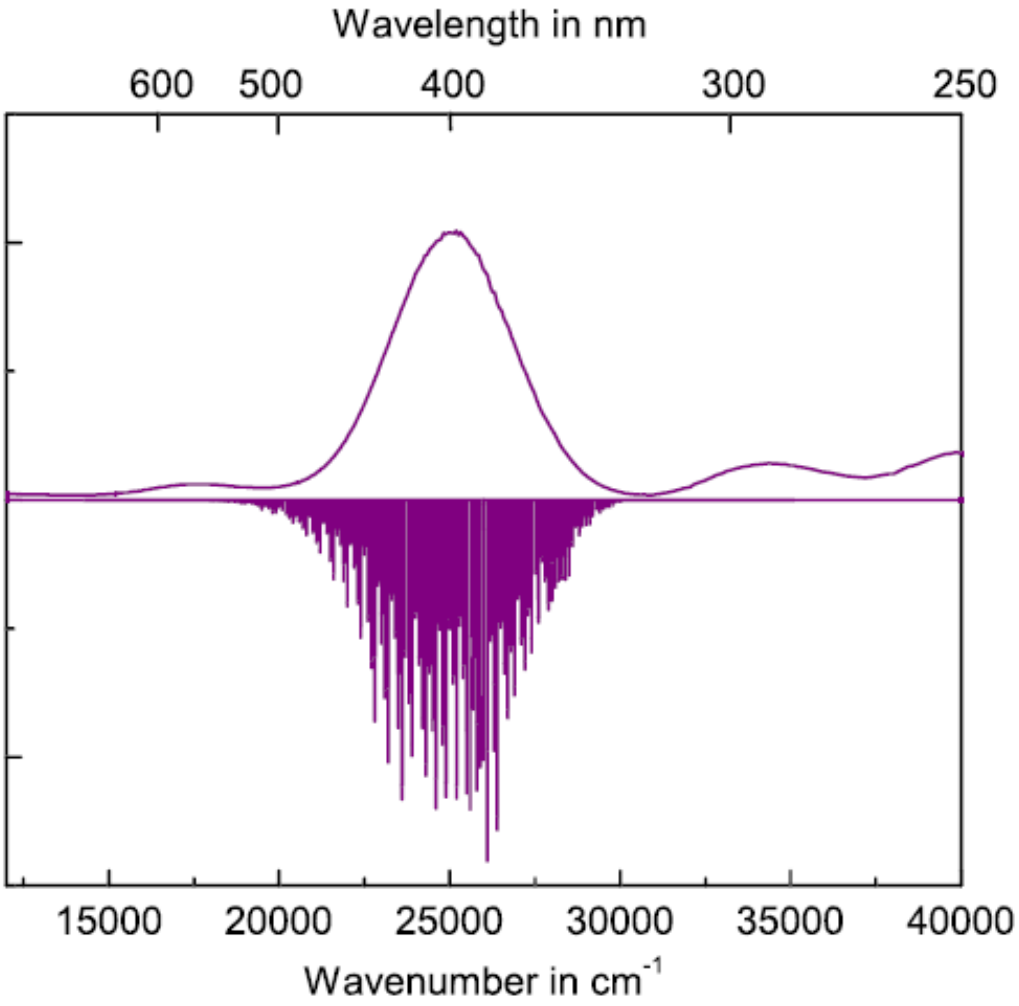


Figure 5.23 Experimental (top) and Franck–Condon simulation of the $S_0 \rightarrow S_3$ transition of iso-$CHBr_3$. The simulation included three modes, as described in the text, and is shown as a stick spectrum to illustrate the density of transitions.

5.4 Summary

A detailed experimental and computational study of the structure, spectroscopy, properties and photochemistry of the *iso*-tribromomethanes (*iso*-$CXBr_3$; X=H, D, F, Cl, Br) is reported. Isolated in high yield in Ar and Ne matrices, these species were characterized by IR and UV/Vis spectroscopy, supported by extensive *ab initio* calculations. The structure and properties of *iso*-$CXBr_3$ and energies of various stationary points on the $CXBr_3$ PESs were characterized computationally using DFT, MP2, and CCSD(T) methods in combination with double and triple-zeta quality basis sets and generally a good agreement is found between our experimental results and various level of theory. The calculations suggest that the *iso*-$CXBr_3$ are most likely to be of ion-pair type and the binding energy is about 60 kJ/mol below the $CXBr_2$ + Br asymptote. Intrinsic reaction coordinate shows that a first-order saddle point transition state connecting both isomers and the barrier to isomerization in gas-phase is energetically near the threshold for simple bond cleavage, and lower in case of *iso*-$CHBr_3$. The photolysis at 440 nm of the *iso*-$CXBr_3$ revealed a back photoisomerization to the parent molecules. NRT calculations show that in condensed-phase, the ion-pair structure will be further stabilized with respect to the bond fission thresholds, indicating that back-photoisomerization will be the most favorable decay pathway. Our future work will be focused on investigating the exact mechanism (isomerization vs. bond cleavage followed by geminate recombination).

Chapter 1. PHOTOCHEMISTRY OF 1,2-DIBROMOETHANE AND 1,2-DIBROMOTETRAFLUOROETHANE IN SOLID MATRIX.

Haloethanes constitute another important group of compounds directly involved in atmospheric chemistry. The next two chapters discuss matrix isolation and computational studies of the photochemistry of various polyhaloethanes (1, 2-dibromoethane, 1, 2-dibromotetrafluoroethane, 1, 1-dibromoethane). All the interest of these compounds turns around the delicate C-Br bond, which can be easily broken upon ultraviolet irradiation in upper atmosphere. This photodissociation would result in releasing a bromine atom, which has high ozone depletion potential (some 30-50 times that of atomic chlorine).[26]

1,2-dibromoethane (ethylene dibromide: EDB) is a chemical with the formula $BrCH_2$-CH_2Br, found in trace amounts in marine environment, but is mostly derived from anthropogenic sources. ($CH_2=CH_2 + Br_2 \rightarrow BrCH_2CH_2Br$) The EDB has been used as additive in gasoline, and as fumigating agent. In a recent study of Sturges and co-workers[147], the EDB was found to be the most abundant halon in tropical troposphere and lower stratosphere. Despite its short lifetime (hundreds of days), the photochemistry and the abundance of EDB make it of high interest.

In past years the tropospheric concentration in EDB has been measured experimentally: Hanwant and co-workers performed measurements in different sites in US (San Jose, CA; Downey, CA; Houston, TX and Denver, CO). They determined mean tropospheric concentrations of 21, 102, 293 and 122 ppt, respectively.[148] Another study conducted in New Jersey reported a value of 30 ppt.[149]

In 1989, Bose and co-workers performed an experimental and computational study in which they characterized the 1,2-dibromoethane and its 1,2-dideteurio isotopomer.[150] In 2008, Francisco and Christiansen [151], carried out an extensive computational study on the atmospheric oxidation of 1,2-dibromoethane, where they discuss about 32 species and 22 transition states. This shows the complexity of EDB degradation and highlights the problems associated with EDB in atmosphere.

Several studies have been conducted on the UV photodissociation of EDB. As for bromoform, initial excitation in the UV accesses an $n \rightarrow \sigma^*$ transition and induces C-Br bond cleavage. Until recently it was thought that this process was occurring by a three-body decay to C_2H_4 + Br + Br, as the initially formed haloethyl radical undergoes a spontaneous secondary decomposition due to the very weak C-Br bond in the radical (dissociation energy = ~33 kJ/mol). Recently, the detection of molecular bromine, following 248 nm photolysis, was reported and suggested to occur via a four center elimination process.

1,2-dibromotetrafluoroethane: (Halon-2402 or tetrafluoroethylenedibromide: TFEDB) is another halon studied in this work. It is a fluoro substituted analogue to EDB with much longer lifetime (~20 years), long enough to reach the stratosphere. TFEDB has been used as flame retardant and fumigating agent. Although many studies have been carried out on the gas-phase photodissociation of TFEDB at different wavelength[115] much less is known about the C_2F_4Br radical. The main concern is about the true structure of C_2X_4Br radical (X=H,F): bridged [152] versus classical (non-bridged) radical.[153]

The photochemistry of these halons has been investigated in condensed phase, where they are supposed to play a key role in stereospecific control of halogenation reactions in solution.[154] Therefore, in this work our principal goal was to trap and spectroscopically investigate the C_2X_4Br radical (X=H, F) along with an extensive computational examination.

5.5 Experimental methods

The detail on the matrix-isolation set-up utilized in these experiments was given in Chapter 2. The EDB sample (Sigma-Aldrich, 98% stated purity) or TFEDB sample (SynQuest Labs, >99% stated purity) was mixed with Ar, to produce a mixture of typically 1:560 $C_2H_4Br_2$: Ar (bath temperature = 267 K) and 1:2000 $C_2F_4Br_2$:Ar (bath temperature = 195 K). Similar to previous studies, we used a pulsed deposition technique to deposit the sample on a KBr window. After deposition, photolysis was done at 220 nm and the irradiated sample were annealed by heating the window up to 33 K and re-cooling back down. At each step IR and UV/Vis spectra were recorded.

5.6 Computational methods

In order to investigate the radical structure, we carried out an extensive computational study using *Gaussian 03*[125], *Gaussian 09*[155] or *GAMESS*[156] suites of electronic structure programs. Geometry optimization and vibrational frequency calculation were performed using various DFT functionals (B3LYP, CAM-B3LYP, M06 and M06-2X) and post Hartree-Fock (MP2, CCSD) combined with a wide range of large basis sets [6-311++G(2df, 2p), (aug-)cc-pVXZ (X=D, T, Q)]. The time-dependent

density functional theory served to compute the vertical excitation energies and oscillator strength. For the parent compounds, barriers to internal rotation were investigated by performing relaxed redundant coordinate scans on the ground state potential energy surface at the B3LYP/aug-cc-pVXZ (X= D, T) levels.

5.7 Results and discussion

5.7.1 Conformational distribution in the matrix

EDB and TFEDB molecules exist under two conformers: anti- and gauche- and their respective IR spectra have been calculated at the B3LYP/6-311++G(2df, 2p) level. These spectra are shown in Figure 1.1 and they are in excellent agreement with experimentally recorded IR spectra. The first intriguing observation in this study was made at this stage: using the calculated IR intensities, the conformational ratio (anti:gauche) was determined to be (30:1) for EDB and (3:1) for TFEDB. However, in previous Ar matrix study done by Maier [157] utilizing continuous deposition, this ratio was found to be (8:1) for EDB molecule. In comparison with conventional continuous deposition methods, these results lead us to understand that pulsed deposition produces a transient heat load at the cold surface that leads to a transient temperature rise in the matrix surface layers and self-annealing. For systems with low barriers to rotation, annealing can result in substantial conformational cooling, and we believe that this is the origin of the enhanced anti:gauche ratio relative to continuous deposition; i.e., ~30:1 vs. ~8:1. This phenomenon was not observed for the TFEDB, since the higher barrier to rotation did not allow the facile conversion to the anti-conformer.

This issue was investigated by performing a relaxed potential energy surface scans at B3LYP/aug-cc-pVDZ level along the Br-C-C-Br dihedral angle for both EDB and TFEDB, and the results are shown in Figure 1.2. The calculated barriers to gauche → anti conversion calculated at this level of theory were 9.8 kJ/mol for EDB and 19.6kJ/mol for TFEDB. At a higher level (B3LYP/aug-cc-pVTZ) these values increased to 11.5 and 22.6 kJ/mol, respectively.

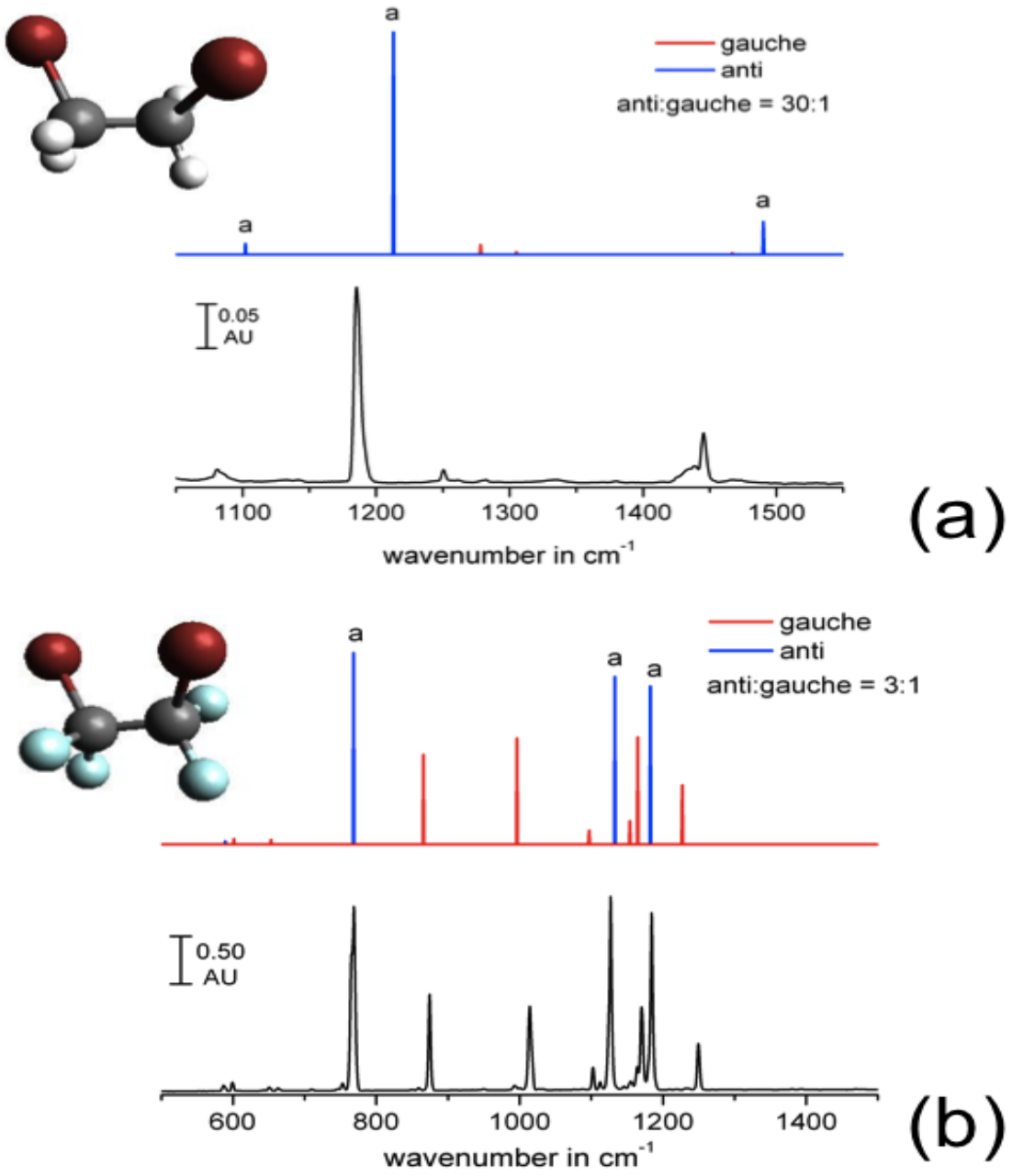


Figure 1.1:(a) Infrared spectrum of EDB in an Ar matrix at 5 K, with the calculated spectra for the anti- and gauche-conformers. The calculated spectrum indicates a 30:1 anti:gauche ratio. **(b)** Experimental and calculated spectra of matrix isolated TFEDB, indicating a 3:1 anti:gauche ratio.

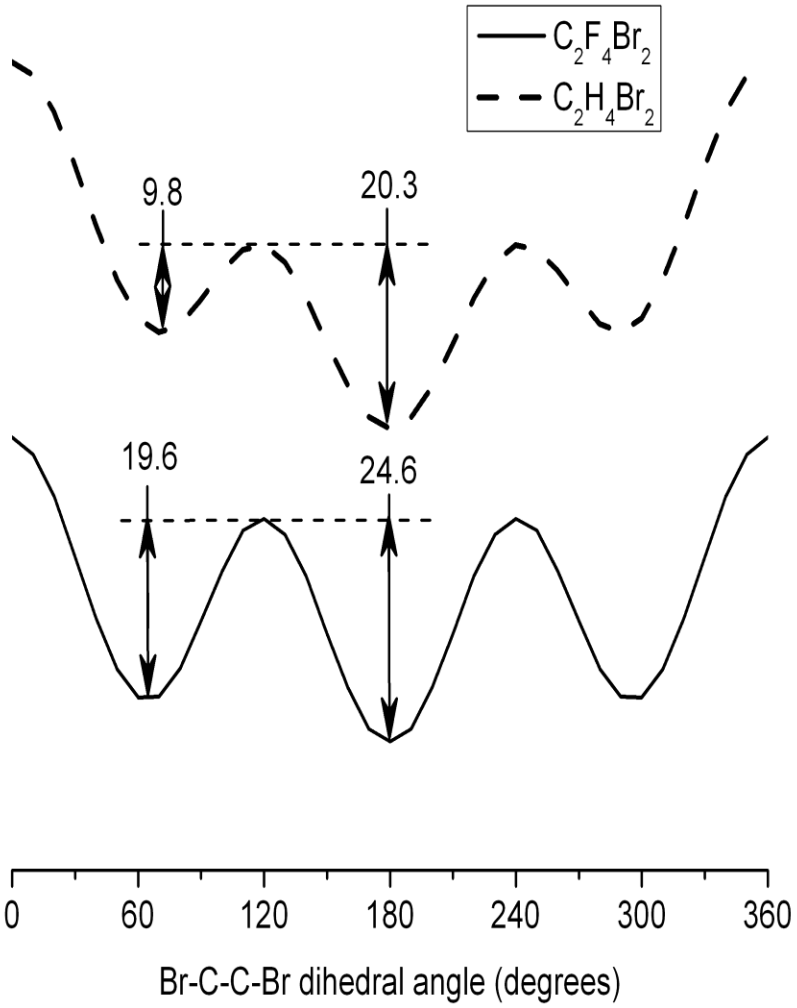


Figure 1.2: Calculated (B3LYP/aug-cc-pVDZ) relaxed energy profiles for C-C bond rotation in EDB and TFEDB.

5.7.2 Photolysis of matrix isolated 1,2-$C_2H_4Br_2$

Figure 1.3 shows the IR spectrum recorded after photolysis of the sample (EDB:Ar = 1:500) at 220 nm. New bands due to different photoproducts, initially absent in the parent spectrum, grew in and all the bands assigned to the target species (EDB) decreased in intensity. Two dominant photoproducts were observed, the $C_2H_4\cdots Br_2$ charge transfer complex and the EDB gauche conformer along with two minor photoproducts, the C_2H_4Br radical and $C_2H_3Br\cdots HBr$ charge transfer complex. All the peaks were assigned based on computational predictions (gauche EDB at B3LYP/6-311++G(2df, 2p) and $C_2H_4\cdots Br_2$ complex at MP2/aug-cc-pVTZ level). Different methods, in combination with large basis sets, were used to interrogate in detail the $C_2H_4\cdots Br_2$ complex. The observed results (960, 1338, 1441, 1612 cm^{-1}) are listed in Table 1-1 and they are in good agreement with previous studies.[157, 158] Consistent with our assignment, the charge transfer complex absorption was enhanced by annealing, and the bands due to the radical disappeared.

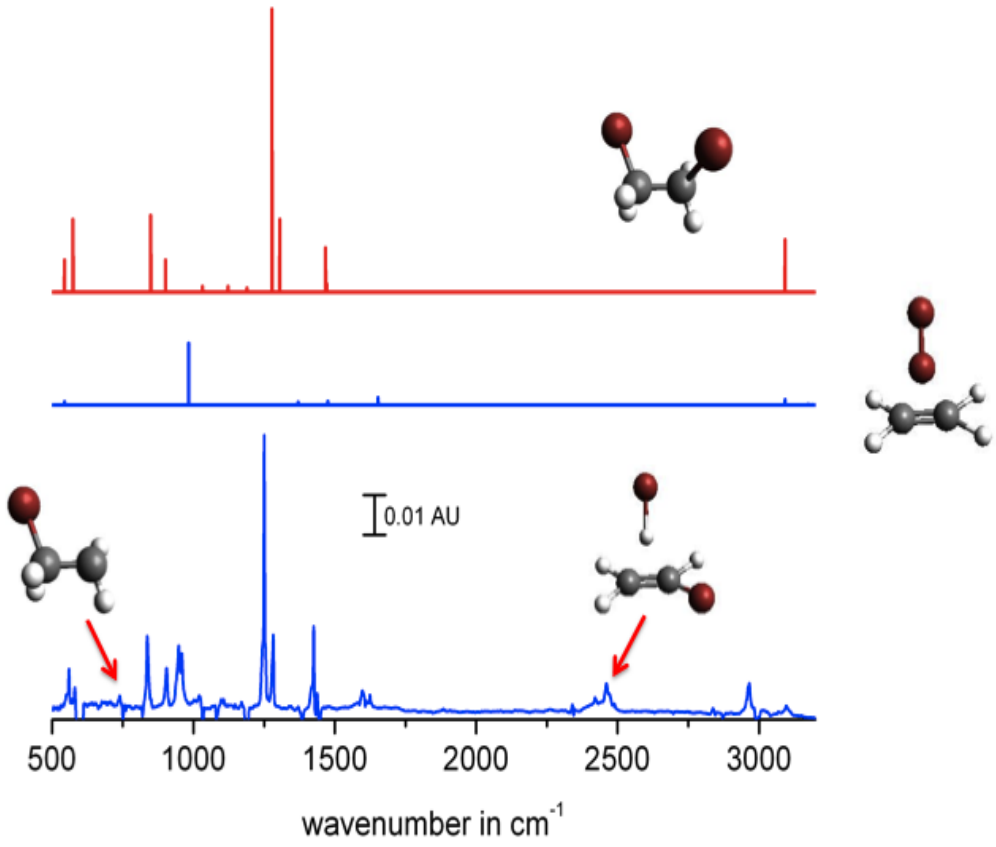


Figure 1.3: IR difference spectrum following 220 nm laser photolysis of an EDB:Ar (1:560) sample at 5 K. The calculated spectrum of the gauche-conformer of EDB [B3LYP/6-311++G(2df,2p)] and $C_2H_4\cdots Br_2$ complex [MP2/cc-pVTZ] are shown.

Table 1-1: Calculated harmonic vibrational frequencies in cm^{-1} (intensities in km/mol) of the $C_2H_4\cdots Br_2$ complex.

Mode	B3LYP/ aug-cc-pVDZ aug-cc-pVTZ	CAM-B3LYP/ aug-cc-pVDZ aug-cc-pVTZ	M06/ aug-cc-pVDZ aug-cc-pVTZ	M06-2X/ aug-cc-pVDZ aug-cc-pVTZ	MP2/ aug-cc-pVDZ aug-cc-pVTZ	CCSD/ aug-cc-pVDZ
ν_1	63 (0.4)	53 (0.1)	67 (0.4)	50 (0.2)	70 (0.3)	50 (0.1)
	58 (0.2)	49 (0.1)	61 (0.3)	59 (0)	70 (0.2)	
ν_2	65 (0.4)	55 (0.2)	70 (0.3)	56 (0.1)	71 (0.4)	51 (0.1)
	59 (0.3)	51 (0.1)	83 (0.5)	50 (0.2)	71 (0.3)	
ν_3	100 (20)	85 (11)	124 (13)	112 (10)	110 (25)	87 (7)
	86 (15)	76 (7)	135 (9)	111 (7)	107 (19)	
ν_4	132 (0.5)	113 (0.3)	140 (0.5)	127 (0.3)	142 (0.3)	105 (0.2)
	119 (0.4)	102 (0.3)	149 (0.4)	129 (0.2)	140 (0.3)	
ν_5	241 (0.3)	187 (0.3)	239 (0.4)	219 (0.3)	242 (0.4)	164 (0.3)
	209 (0.4)	161 (0.3)	245 (0.2)	190 (0.3)	222 (0.5)	
ν_6	266 (35)	302 (18)	288 (28)	314 (18)	276 (28)	291 (8)
	281 (28)	313 (13)	303 (20)	323 (13)	304 (24)	
ν_7	830 (0.2)	834 (0.1)	801 (0)	823 (0)	823 (0)	826 (0)
	837 (0.1)	842 (0.1)	803 (0)	835 (0)	823 (0)	
ν_8	988 (0)	1011 (170)	983 (0)	1019 (166)	951 (0)	958 (0)
	998 (158)	1005 (163)	972 (146)	1013 (158)	936 (0)	
ν_9	1004 (159)	1019 (0)	988 (148)	1023 (0)	991 (159)	988 (147)
	1000 (0.1)	1021 (0)	976 (0)	1021 (0)	983 (152)	
ν_{10}	1024 (0)	1048 (0)	1023 (0)	1048 (0)	1035 (0)	1032 (0)
	1046 (0)	1066 (0)	1022 (0)	1069 (0)	1049 (0)	
ν_{11}	1230 (0)	1237 (0)	1191 (0)	1223 (0)	1226 (0)	1234 (0)
	1247 (0)	1254 (0)	1205 (0)	1244 (0)	1242 (0)	
ν_{12}	1364 (13)	1377 (5)	1341 (5)	1371 (5)	1363 (9)	1370 (2)
	1375 (11)	1388 (4)	1349 (4)	1384 (4)	1370 (7)	
ν_{13}	1463 (11)	1467 (12)	1413 (14)	1452 (12)	1466 (8)	1473 (7)
	1482 (10)	1487 (12)	1429 (13)	1477 (11)	1475 (9)	
ν_{14}	1654 (49)	1696 (25)	1663 (31)	1687 (24)	1642 (25)	1674 (9)
	1667 (39)	1705 (17)	1673 (26)	1695 (16)	1653 (18)	
ν_{15}	3146 (4)	3163 (4)	3130 (5)	3159 (3)	3177 (2)	3152 (7)
	3136 (5)	3152 (5)	3148 (4)	3150 (3)	3174 (2)	
ν_{16}	3156 (5)	3178 (2)	3144 (4)	3174 (1)	3192 (1)	3170 (0)
	3146 (4)	3166 (1)	3159 (2)	3164 (1)	3189 (0.5)	
ν_{17}	3231 (0)	3251 (0)	3217 (0)	3246 (0)	3277 (0)	3241 (0)
	3209 (0)	3227 (0)	3223 (0)	3229 (0)	3266 (0)	
ν_{18}	3258 (4)	3275 (5)	3245 (6)	3273 (4)	3304 (3)	3268 (10)
	3236 (6)	3253 (6)	3248 (5)	3255 (4)	3292 (2)	

The UV/Vis spectrum of the parent EDB shows a band at ~200 nm. As shown in Figure 1.4, this band significantly decreased upon photolysis at 220 nm, and three new bands came in: one strong band assigned to the $C_2H_4\cdots Br_2$ complex at ~237 nm, and two weaker bands due to molecular Br_2 at ~260 and 363 nm. When the sample was annealed by heating the window up to 33 K and re-cooling, the weaker bands disappeared and the charge complex signal grew much stronger. This represents, to our knowledge, the first report of the UV-Visible spectrum of this complex. Our reported position of the charge-transfer band is in excellent agreement with TDDFT predictions (Table 1-2) using the B3LYP, CAM-B3LYP and M06 family of gradient-corrected functionals with augmented double- and triple-zeta quality basis sets.

In 1997, Maier and co-workers have studied the photochemistry of $C_2H_4\cdots Br_2$ complex, by excitation at $\lambda > 300$ nm. They found that gauche and anti-conformers photoproducts were produced in a nearly 1:1 ratio, as a consequence of an addition reaction inside the same cage ($C_2H_4Br + Br \rightarrow C_2H_4Br_2$). Since the bromine atom could attack via cis- or trans-, there was no predominance. However analysis shows that excitation of the matrix-isolated complex at $\lambda > 300$ nm does not access the charge-transfer band, but rather transitions localized on the Br_2 chromophore. In the next chapter we discuss how we selectively formed this complex in the matrix by co-deposition of ethylene and Br_2 using a late-mixing nozzle, and investigated the photochemistry associated with charge-transfer excitation.

Table 1-2: Calculated wavelengths (oscillator strengths) of the vertical electronic transitions of the $C_2H_4\cdots Br_2$ complex.

State	B3LYP/ aug-cc-pVDZ aug-cc-pVTZ aug-cc-pVQZ	CAM-B3LYP/ aug-cc-pVDZ aug-cc-pVTZ aug-cc-pVQZ	M06/ aug-cc-pVDZ aug-cc-pVTZ aug-cc-pVQZ	M06-2X/ aug-cc-pVDZ aug-cc-pVTZ aug-cc-pVQZ
S_1	456.0 (0.0006)	426.8 (0.0005)	414.6 (0.0006)	436.9 (0.0004)
	434.3 (0.0006)	406.2 (0.0006)	395.0 (0.0006)	406.1 (0.0005)
	431.5 (0.0007)	403.6 (0.0006)	393.0 (0.0006)	404.1 (0.0005)
S_2	452.0 (0.0003)	424.8 (0.0003)	412.2 (0.0002)	434.8 (0.0002)
	431.7 (0.0004)	404.8 (0.0004)	393.3 (0.0003)	404.4 (0.0003)
	429.0 (0.0004)	402.3 (0.0004)	391.4 (0.0003)	402.5 (0.0003)
S_3	274.4 (0.0002)	248.5 (0.0002)	255.6 (0.0002)	245.3 (0.0002)
	270.0 (0.5220)	235.7 (0.0002)	247.1 (0.5031)	230.6 (0.0002)
	269.7 (0.5138)	234.3 (0.0002)	246.7 (0.4966)	229.6 (0.0002)
S_4	273.3 (0.0010)	248.1 (0.0005)	255.0 (0.0006)	244.9 (0.0004)
	259.2 (0.0001)	235.4 (0.0006)	241.6 (0.0001)	230.3 (0.0008)
	257.5 (0.0001)	234.1 (0.0006)	240.4 (0.0001)	229.3 (0.0008)
S_5	269.7 (0.5819)	238.1 (0.5988)	252.7 (0.5903)	235.8 (0.5725)
	258.7 (0.0004)	231.3 (0.5293)	241.3 (0.0005)	224.5 (0.5533)
	257.0 (0.0004)	230.2 (0.5222)	240.1 (0.0005)	223.4 (0.5471)

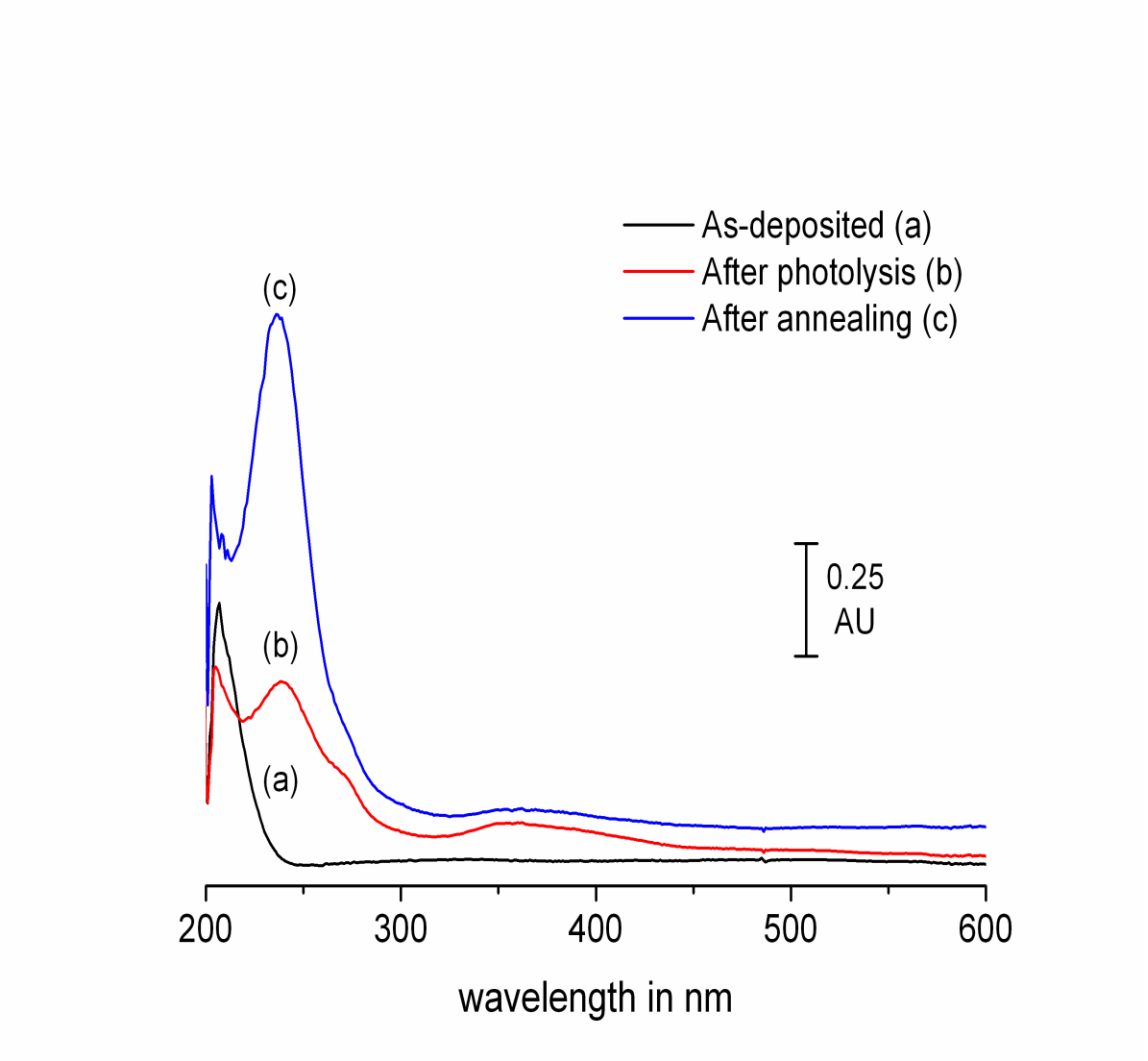


Figure 1.4: UV/Visible spectrum of: **(a)** an EDB:Ar (1:560) sample at 5 K, **(b)** the same sample following laser photolysis at 220 nm, and **(c)** the irradiated sample following annealing

5.7.3 Photolysis of matrix isolated TFEDB

Following deposition on a cold KBr window, TFEDB sample (TFEDB:Ar 1:2000) was photolyzed using a 220 nm laser light. Contrary to the EDB, the major photoproduct of TFEDB photolysis were the gauche- and anti- conformers of the C_2F_4Br radical which grew in at the expense of the parent signal (Figure 1.5)

Upon photolysis at 220 nm, a new band appeared in the UV/Vis spectrum (λ_{max} = 306 nm in Figure 1.6), and disappeared with annealing at 33 K. Following the trends observed in the IR spectrum, this band was assigned to a transient radical species (C_2F_4Br). This observation is supported by *ab initio* calculations, where the TD-DFT results have predicted a strong absorption with oscillator strength of 0.05 in that region. Using the approach described earlier, the experimental oscillator strength was determined to be 0.052.

Conveniently, the C_2F_4Br radical UV band does not overlap with the spectrum of the parent TFEDB, and advantage was taken to explore the photochemistry of the radical using a 266 nm laser light. As shown in Figure 1.7, this photolysis led to the cleavage of the second C-Br bond. All the IR bands associated with the radical decreased and new features assigned to the C_2F_4 species appeared.

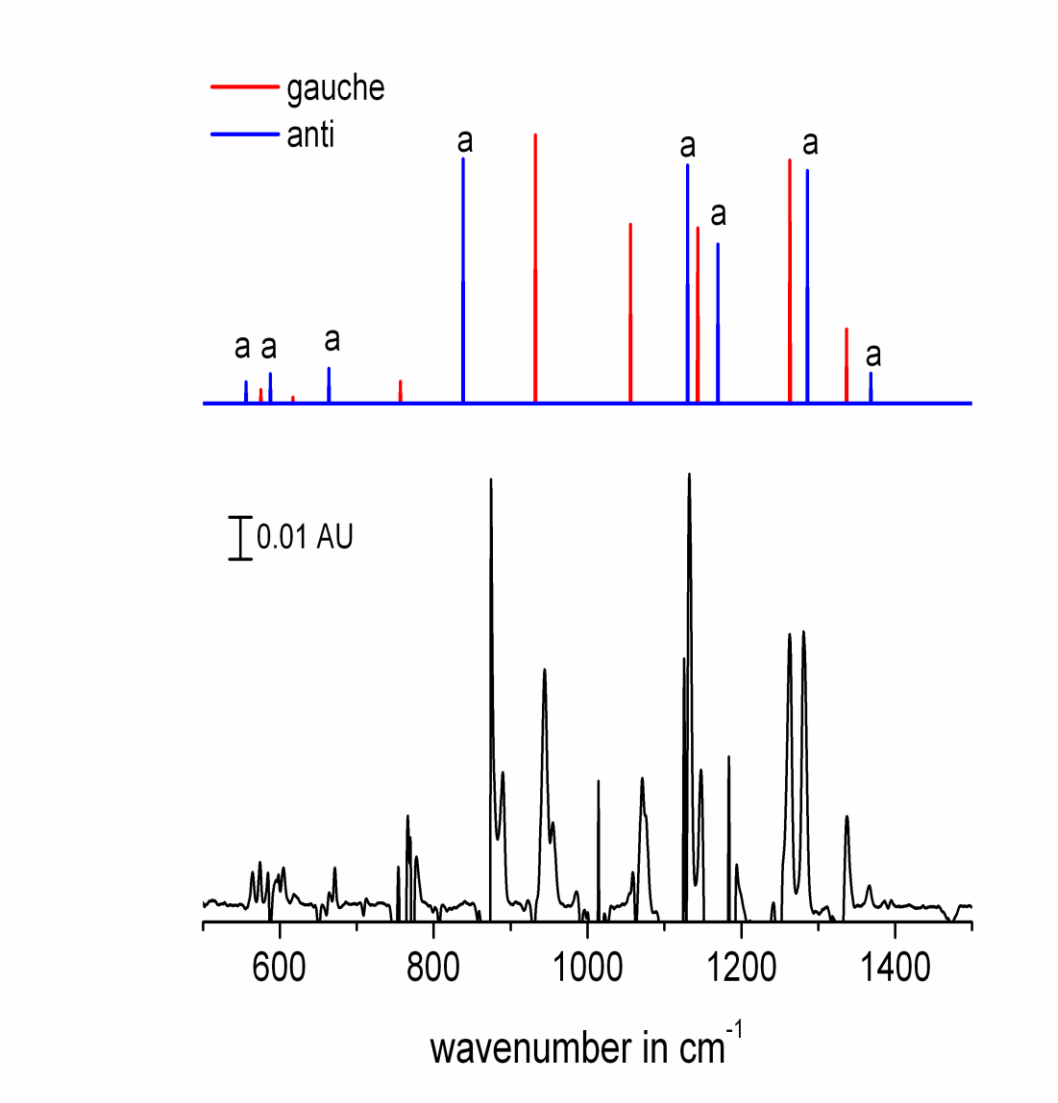


Figure 1.5: IR spectrum recorded after photolysis of TFEDB with 220 nm laser light, in comparison with predicted spectra of photoproducts: anti and gauche C_2F_4Br radicals. (B3LYP/aug-cc-pVTZ).

Table 1-3: Calculated harmonic vibrational frequencies in cm^{-1} (intensities in km/mol) of the anti- and gauche conformers of the C_2F_4Br radical.

Mode	**anti**		**gauche**	
	B3LYP/ aug-cc-pVTZ	**Observed**	**B3LYP/ aug-cc-pVTZ**	**Observed**
ν_1	72 (0)	…	59 (0.1)	…
ν_2	132 (0.3)	…	150 (0.5)	…
ν_3	211 (2)	…	218 (2)	…
ν_4	293 (0)	…	297 (1)	…
ν_5	295 (7)	…	302 (3)	…
ν_6	365 (0.3)	…	321 (0.1)	…
ν_7	513 (0)	…	438 (2)	…
ν_8	556 (22)	564	573 (14)	574
ν_9	588 (31)	605	615 (6)	…
ν_{10}	664 (36)	672	757 (23)	766
ν_{11}	838 (252)	874	923 (275)	944
ν_{12}	1130 (246)	1132	1051 (177)	1071
ν_{13}	1170 (164)	…	1139 (175)	1147
ν_{14}	1286 (240)	1281	1256 (240)	1263
ν_{15}	1368 (31)	1366	1332 (76)	1337

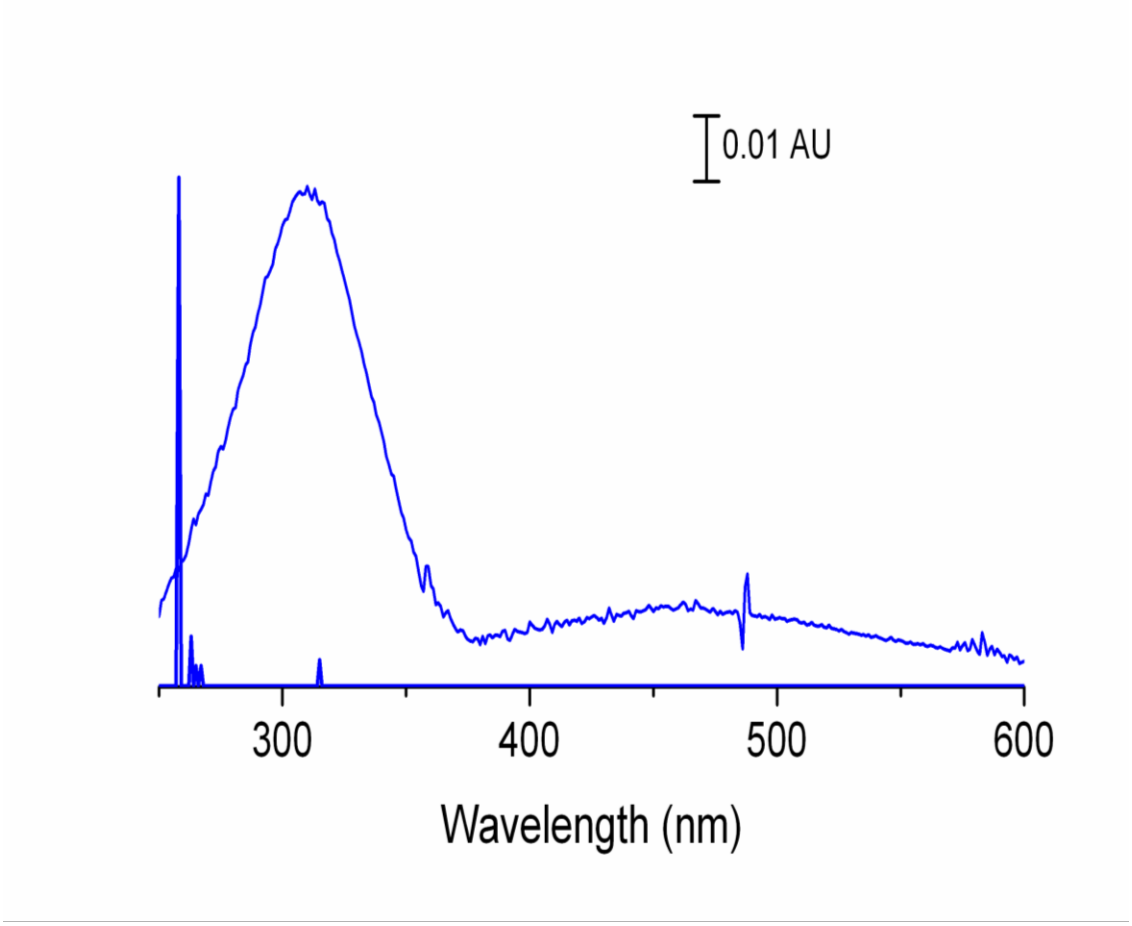


Figure 1.6: UV/Visible spectrum following laser photolysis (220 nm) of a TFEDB:Ar (1:2000) sample at 5 K. Shown as a stick spectrum are the predicted transitions at the TD-B3LYP/aug-cc-pVTZ level.

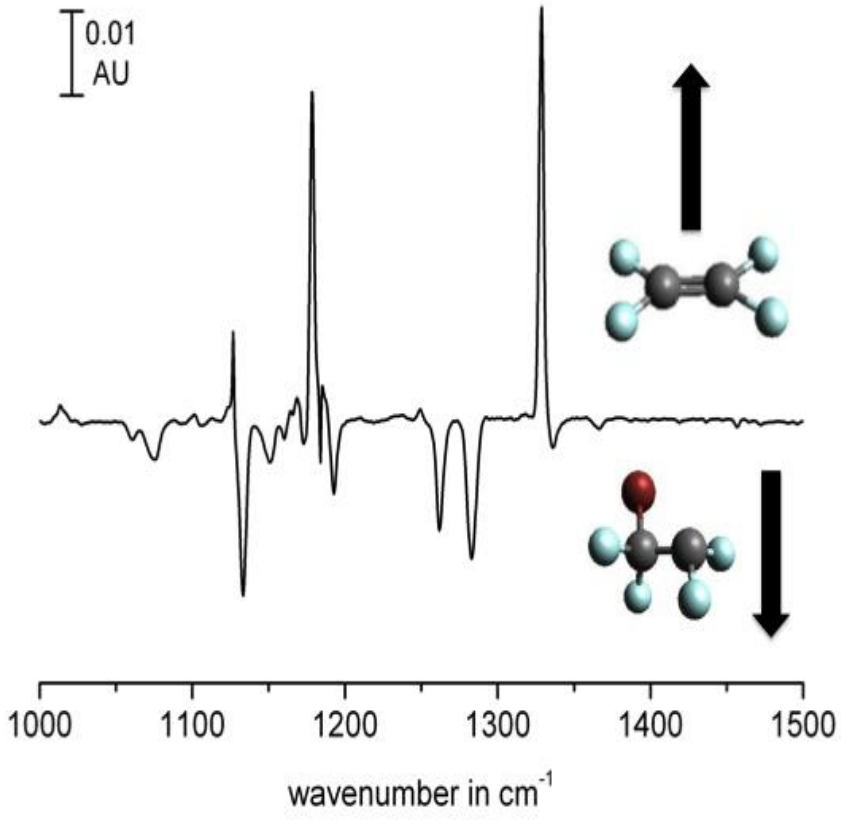


Figure 1.7: IR difference spectrum following sequential 220 and 266 nm photolysis of a TFEDB:Ar (1:2000) sample at 5 K. The disappearance of bands assigned to the gauche- and anti-conformers of the C_2F_4Br radical and growth of bands assigned to C_2F_4 is observed.

5.7.4 Photolysis mechanism(s): comparison with the gas-phase

The photodissociation of EDB has been studied before, by Lee and co-workers, at 248 nm, and the process was dominated by a three-body decay to C_2H_4 + 2Br and an elimination channel leading to C_2H_4 + Br_2. The photolyis in matrix was known to produce free C_2H_4 and trace amount of C_2H_4Br radical. In our study we have found that after dissociation, the photoproducts inside the cage undergo a recombination to form four sets of products: 1) gauche 1,2-$C_2H_4Br_2$, resulting from trans addition of Br to C_2H_4Br; 2) anti 1,2-$C_2H_4Br_2$, resulting from cis addition; 3) the $C_2H_4\cdots Br_2$ complex, resulting from Br abstraction or recombination following secondary decomposition; and 4) the vinyl bromide---HBr complex, resulting from H abstraction.

It is obvious that the most important species in all these processes is the C_2H_4Br radical, via which all final photoproducts are obtained (Figure 1.8). However the structure of this radical has been controversial for many years since several structures are possible: i) a classical (non-bridged) structure, ii) a symmetrical bridged structure, and iii) an asymmetrical bridged structure. The theoretical studies done by Goddard and co-workers in 1999, using different methods (HF, MP2, various DFT functionals) in combination with 6-31G** basis set for C, H and an effective core potential for the halogen atom found the bridged radical to be the lowest energy structure in gas-phase. In a more recent study, done by Phillips and co-workers using the DFT methods, only the non-bridged radical structure was taken into account.[159] In order to solve the problematic structure of C_2H_4Br radical, we performed *ab initio* calculations at higher

level (gradient-correlated DFT, MP2, CCSD) in combination with more robust correlation-consistent basis sets.

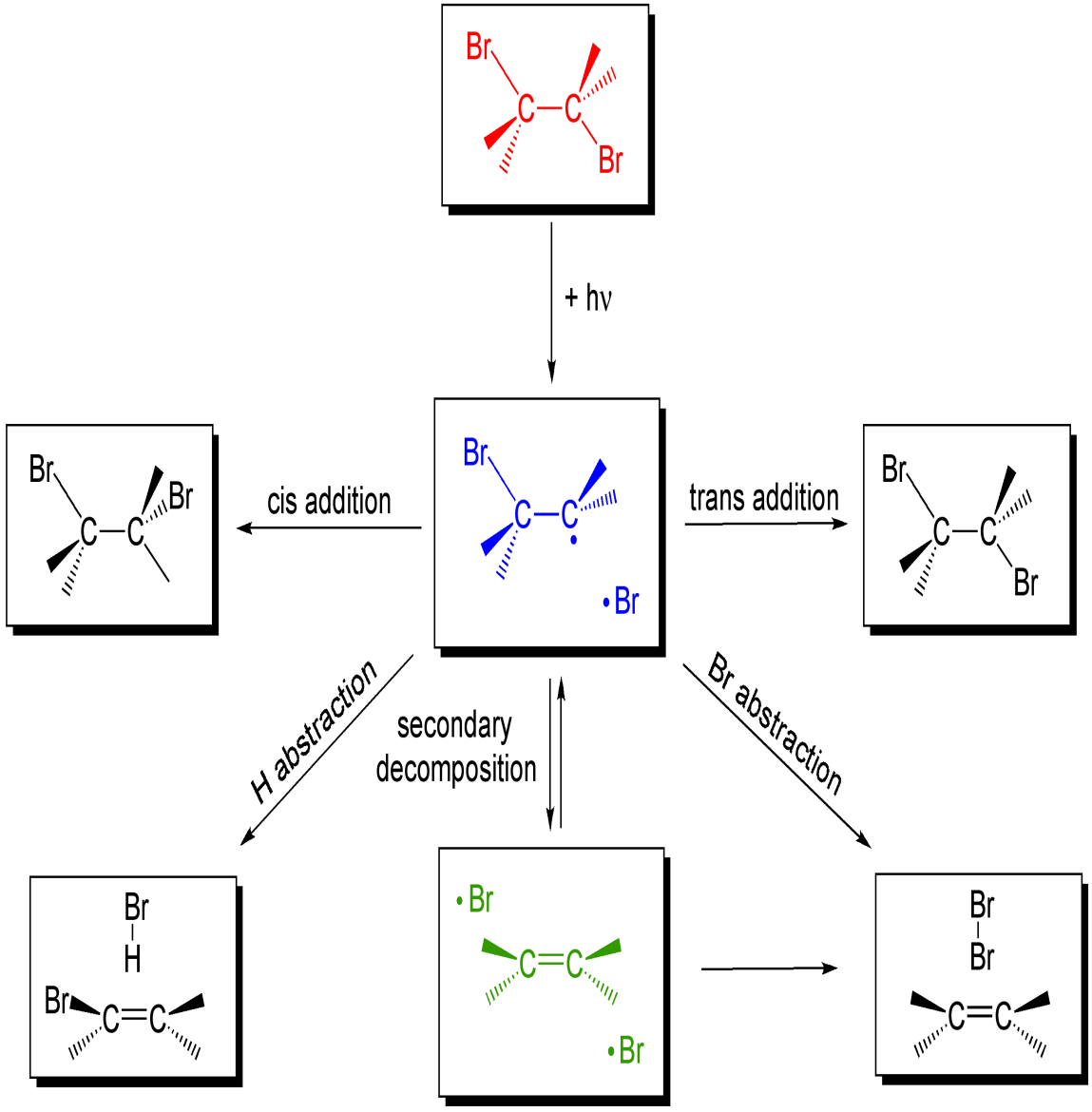


Figure 1.8: Schematic mechanism for the photolysis of matrix isolated EDB.

Analyzing a relaxed scan performed along the C-Br-Br-H dihedral angle and the C-C-Br angle in the classical (non-bridged) C_2H_4Br radical at (a) UB3LYP/aug-cc-pVDZ and (b) UMP2/aug-cc-pVDZ levels of theory, we have found that the classical (non-bridged) radical is the global minimum in both cases.

In Figure 1.9 we can see that the bridged radical was optimized as a local minimum at the MP2/aug-cc-pVDZ, while it was a first order saddle point at the UB3LYP/aug-cc-pVDZ. To get a closer insight on this structure by doing more accurate calculations, we performed relaxed redundant coordinate scans along C-Br-Br bond angle in the classical radical structure using various DFT functionals and post Hartree-Fock methods.

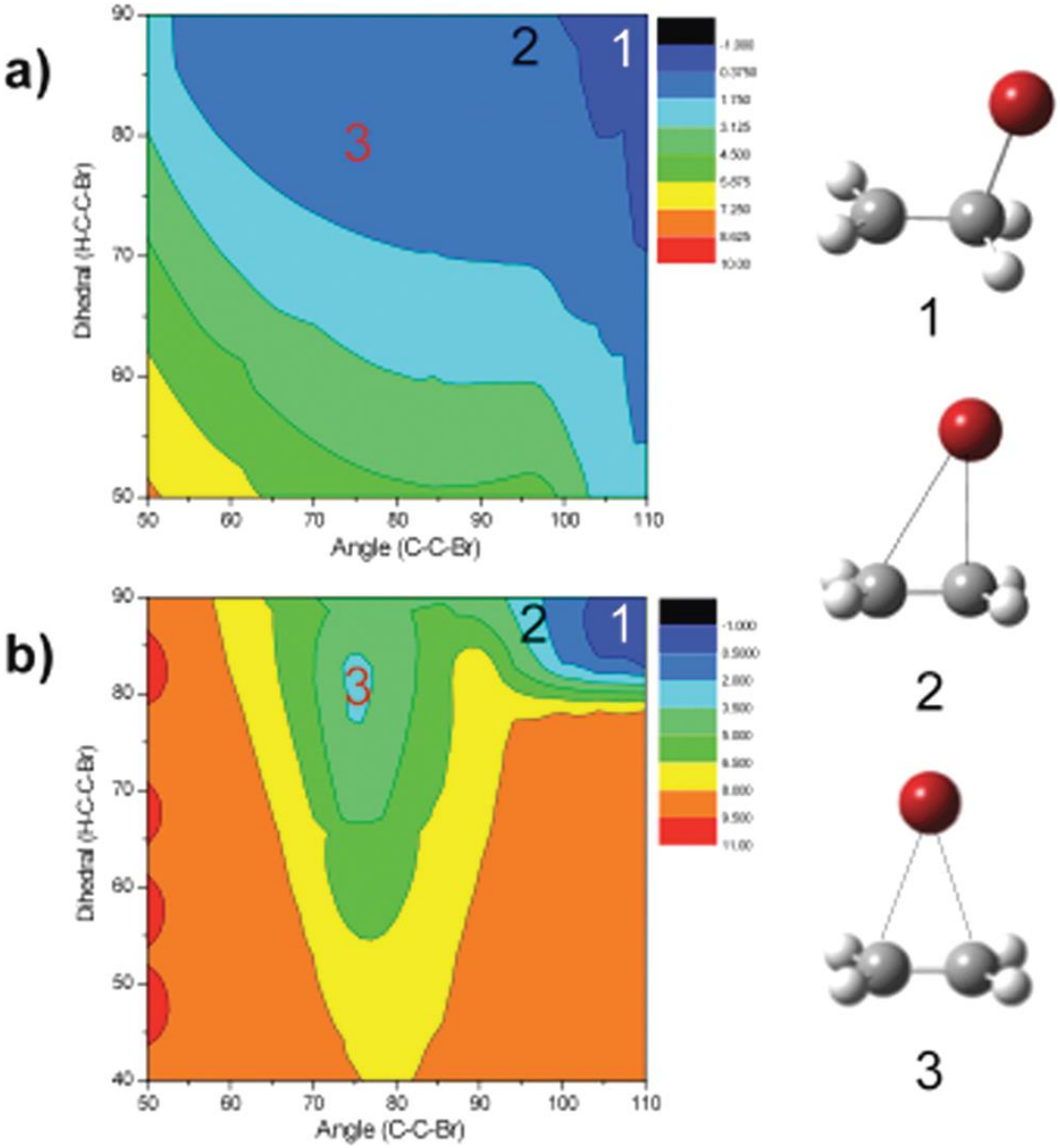


Figure 1.9: A color map surface representing the **(a)** UB3LYP/aug-cc-pVDZ and **(b)** UMP2/aug-cc-pVDZ relaxed redundant coordinate scans along the C-C-Br angle and H-C-C-Br dihedral in the classical (non-bridged) C_2H_4Br radical. Energies are given in kcal/mol.

As shown in Figure 1.10, the methods used for this scan did not all agree about the relative energies of the structures considered. The symmetrically bridged radical was found to be a local minimum at UM06-2X, UMP2 and UCCSD levels of theory. However the same structure was optimized as a transition state at the UB3LYP and UCAM-B3LYP levels of theory. In contrast, the asymmetrically bridged radical, was a local minimum on UB3LYP and UCAM-B3LYP PES, while it was a local minimum at the UM06-2X, UMP2 and UCCSD levels of theory. The only structure with consistent results was the classical radical, which was found to be the global minimum on all PES performed. Taking the coupled cluster CCSD method as our reference, the UMP2 method overestimated the relative energies for the transition state structures. The UB3LYP and UCAM-B3LYP seemed to be in error (TS and local minima were switched). The UM06-2X density functional proved a good accuracy on the open shell system treatment. Although the MP2 method is well known to capture general topological feature, is did not offer good treatment in this case. We note that the general topological features are independent of the choice of basis set, as similar results were obtained using an aug-cc-pVTZ basis set.

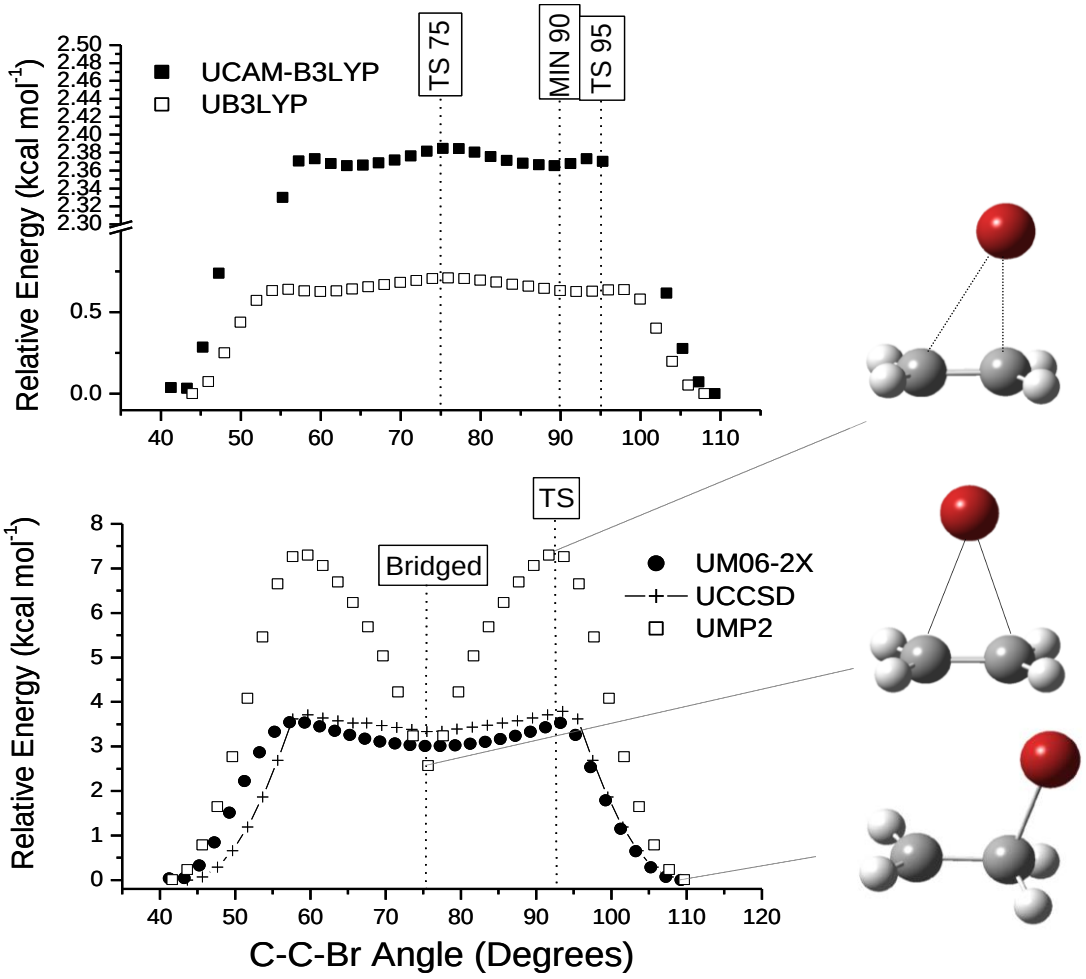


Figure 1.10: Relaxed redundant coordinate scans along the C-C-Br angle of the C_2H_4Br radical using different DFT and *ab initio* methods and the aug-cc-pVDZ basis set. The critical points extracted from this Figure were used as guess structures for full geometry optimization

For further investigation, we performed a full unconstrained geometry optimization starting from the critical points obtained from the scan mentioned above scan: in all cases the classical radical showed the lowest energy, < 10 kJ/mol below the bridged radical structure (Table 4.5). These findings were reproducible and very coherent with the experimental results for two major reasons: (i) no evidence about the IR absorption of the bridged radical absorption, (ii) in presence of the bridged radical, the cage recombination would lead exclusively to the formation of the anti-conformer of the parent.

Recently in 2009, Lin and co-workers have shown that molecular bromine could be formed directly at 248 nm, presumably via a four center elimination [160], however in our experiments we could not distinguish by which mechanism this reaction might happen.

Regarding TFEDB photolysis at 220 nm, the first step looks like what has been observed in the case of EDB; one C-Br bond is broken and two radicals are formed: C_2F_4Br + Br. However the second C-Br bond does not break easily due to the increased strength of this bond in the fluoro- compound. The substitution of H with F changes the electronic density in the molecule by enhancing electron deficiency on carbon atoms. Under the same cage the two radicals can undergo a recombination via a cis addition of Br producing the anti-conformer or via a trans- addition producing the gauche-conformer.

Table 1-4: Energies (in kcal mol^{-1}) of the fully optimized transition state (TS) and bridged structures of C_2H_4Br relative to the energies of the classical radical.

Species	**M06-2X/ aug-cc-pVDZ aug-cc-pVTZ**	**MP2/ aug-cc-pVDZ aug-cc-pVTZ**
TS	14.9	30.7
	13.7	37.1
bridged	12.6	10.8
	10.9	19.4

Under atmospheric conditions, photolysis of TFEDB will produce two radicals, C_2F_4Br + Br, and the secondary C-Br bond breaking will depend upon the photolysis wavelength. In previous study, North and co-workers suggested that in the upper stratosphere (where the solar flux is concentrated at wavelengths >290 nm), the TFEDB will dissociate to produce Br atom and C_2F_4Br radical. It was thought that the latter will be stable with respect to a secondary dissociation and will rather react rapidly with O_2 to form a peroxy radical. However according to our calculations and UV/Vis data, the C_2F_4Br radical absorbs in the region suggested (band at λ_{max} = 306).

To investigate the photochemistry of the radical, we exposed the radical to a secondary irradiation with a 266 nm laser light. As shown in Figure 1.7, the IR bands due to the CF_2Br radical disappeared and the bands assigned to C_2F_4 appeared. This suggests that at the wavelength considered, the radical decomposes by C-Br bond cleavage and losing the second bromine atom.

5.8 Summary

In matrix isolation experiments pulsed deposition can lead to self-annealing and therefore to conformational relaxation for systems with low barriers to internal rotation. This is reflected by the difference in conformational distribution: EDB (30:1) versus TFEDB (3:1). The photolysis of these two atmospherically important 1,2-dibromoethanes (EDB and TFEDB) reveals a different photochemical behavior. Photolysis of EDB at 220 nm yields four sets of photoproducts: $C_2H_3Br\cdots HBr$ complex and C_2H_4Br radical (as minor products), gauche-conformer of $C_2H_4Br_2$ and $C_2H_4\cdots Br_2$ charge transfer complex (as major products). The later has a strong absorption band in UV/Vis spectrum at ~237 nm that significantly grows upon annealing. In contrast, the photolysis of matrix-isolated TFEDB at 220 nm yields as the dominant photoproducts the anti- and gauche-conformers of the C_2F_4Br radical, and the vibrational and electronic spectra and photochemistry of this radical were characterized here for the first time, supported by *an initio* calculations. The increase in yield of radical for TFEDB vs. EDB is consistent with the stronger C-Br bond in the fluoro-substituted radical species. The longtime controversial C_2H_4Br radical structure is elucidated by an extensive *ab initio* study and in accord with our experimental data: in both, gas-phase and matrix environment, the classical structure is the global minimum energy structure.

Chapter 6. PHOTOLYSIS OF 1,1-DIBROMOETHANE: A NEW VIEW OF PROTON-COUPLED ELECTRON TRANSFER.

Small polyhaloalkanes molecules have received much attention in the past years, due to their role in various area of chemistry going from atmospheric to biochemistry. For instance it has been shown that the photolytic release of halogen atom from chlorofluorocarbons represent an important contribution to catalytic cycles of ozone depletion. [161-165]

In our recent studies we have investigated the photochemistry of simple polyhalomethanes and found a general tendency to photoisomerize, in condensed phase, where the bonding in the *iso*-halon is best described as an ion-pair between a halide ion and halocarbocation.[128-130, 138, 166, 167] Extending this investigation to polyhaloethane, we studied the photodissociation of 1,2-dibromoethane and in the previous chapter have demonstrated that irradiation with 220 nm laser light leads to multiple photoproducts via the classical C_2H_4Br radical.[168] Although 1,2-EDB has been extensively investigated by several groups [160, 169, 170], less is known about its structural isomer 1,1-dibromoethane (denoted as 1,1-EDB in this work). Using translational spectroscopy technique, Lin and co-workers demonstrated that upon irradiation bromoethane and 1,1-dibromoethane undergo a simple C-Br bond cleavage contrary to the 1,2 dibromoethane which photodissociates in an asynchronous concerted reaction.[170] Nguyen and co-workers have studied the heterogeneous photocatalysis of EDB's and showed that they can be converted completely to CO_2 and HBr products.[171] Vinyl bromide was detected as intermediate in case of 1,2 EDB, however no intermediate

was observed in case of 1,1 EDB.[171] Earlier studies have investigated the complex of hydrogen halide with different electron donors [172, 173] or π-systems forming halogen-bonding complexes, in which the acidic proton interacts with the π electron density of ethylene. [174-178]

In this work, we are experimentally and computationally exploring the photochemistry of 1,1EDB, isolated in Ar matrix, which turns out to be more complex than that of 1,2-EDB due to the accessibility to multiple channels including a proton-coupled electron transfer (PCET) and other sequential channels, all leading to the formation of charge-transfer complexes. Proton-coupled electron transfer (PCET), where an electron and proton are transferred in the same kinetic step [179-181], thus bypassing high energy reactive intermediates, are key reactions in a diverse array of biochemical [182-185], catalytic [186-188], and solar energy conversion processes.[189, 190] While recent progress has been made [191], it has generally proven difficult to experimentally distinguish *concerted* PCET, a single step process where no intermediates are expected, from *sequential* electron transfer/proton transfer (ET/PT), or PT/ET. Here we describe an apparently simple and fundamental organic reaction, hydrogen halide elimination, where both mechanisms are operative and can be distinguished. We find that concerted PCET is energetically favored over sequential ET/PT, which involves a well-defined reactive intermediate, the corresponding *iso*-halon. Unfortunately we couldn't experimentally observe this intermediate, although in the past we have succeeded in trapping weakly bound molecules. [128, 130, 166] In this work we are exploring the role of the missing *iso*-halon intermediate in the molecular elimination mechanisms.

We have also found another sequential channel corresponding to the elimination of Br_2 from the *iso*-halon and leading to the formation of observed Br_2-ethylene charge transfer complex. Similar complexes, in which the σ-hole (positively charged) on the halogen atom interacts with a variety of electron-donors, have been studied either computationally [192-195] or experimentally [196-201]. More recently, we have identified Br_2-ethylene complex as minor photoproduct of 1,2EDB [168] and this complex was produced in a following study by co-deposition of Br_2 and Ethylene in Ar matrix.

Our experimental results are supported by high-level *ab-initio* and DFT calculations, predicting the accessibility to several photodissociation channels and provide more information on the structure, energy and relation of different stationary points involved in this process.

6.1 Experimental set-up

The experimental set up used in this chapter has been described in detail in Chapter 2. A mixture of 1,1 EDB:rare gas (~ 1:500) was deposited onto the cold KBr window held at ~ 5 K using the pulsed deposition method. Following deposition, the cold window was irradiated with laser light at 220 nm or 240 nm.

6.2 Computational methods

Calculations were carried out on a local (Pere) 128 node cluster using the Gaussian 09 suite of electronic structure programs.[133] Geometry optimizations were performed using M06-2X and MP2 in combination with aug-cc-pVTZ basis set.

Electronic absorptions and oscillator strengths were calculated using time-dependent DFT methods, with the M06-2X, B3LYP and CAM-B3LYP density functionals. Single point energy calculations were performed at the CCSD(T) level of theory using structures optimized with MP2 and M06-2X, and were corrected from ZPE and BSSE for the complex structures.

6.3 Results and Discussion

Figure 6.1 displays the difference infrared spectrum obtained after photolysis of the freshly deposited matrix (1/500 1,1-EDB/Ar) with 220 nm laser light (b), in comparison with theoretical spectra of precursor (a) and photoproducts (c-e), calculated at the M06-2X/aug-cc-pVTZ level of theory. Upon photolysis, all the peaks due to the 1,1-EDB decreased in intensity, and new peaks were observed. The fact that these peaks increased significantly with annealing process, suggested that they belong to stabilized species. The major photoproduct was found to be HBr-vinyl bromide complex and its peaks were assigned within a good correlation to our calculation results. We have also observed other peaks at 738.7 and 757.7 cm^{-1} and these were assigned to the complexes of Br_2 with ethylene or acetylene, as shown in Figure 1. The presence of these Br_2 complexes, also explain the enhancement of the HBr•••CH_2-CHBr complex peak at 943.2 cm^{-1} where the predicted intensity is nearly doubled because of the CH_2 wagging mode present in, both, CH_2-CH_2 and CH_2-CHBr.

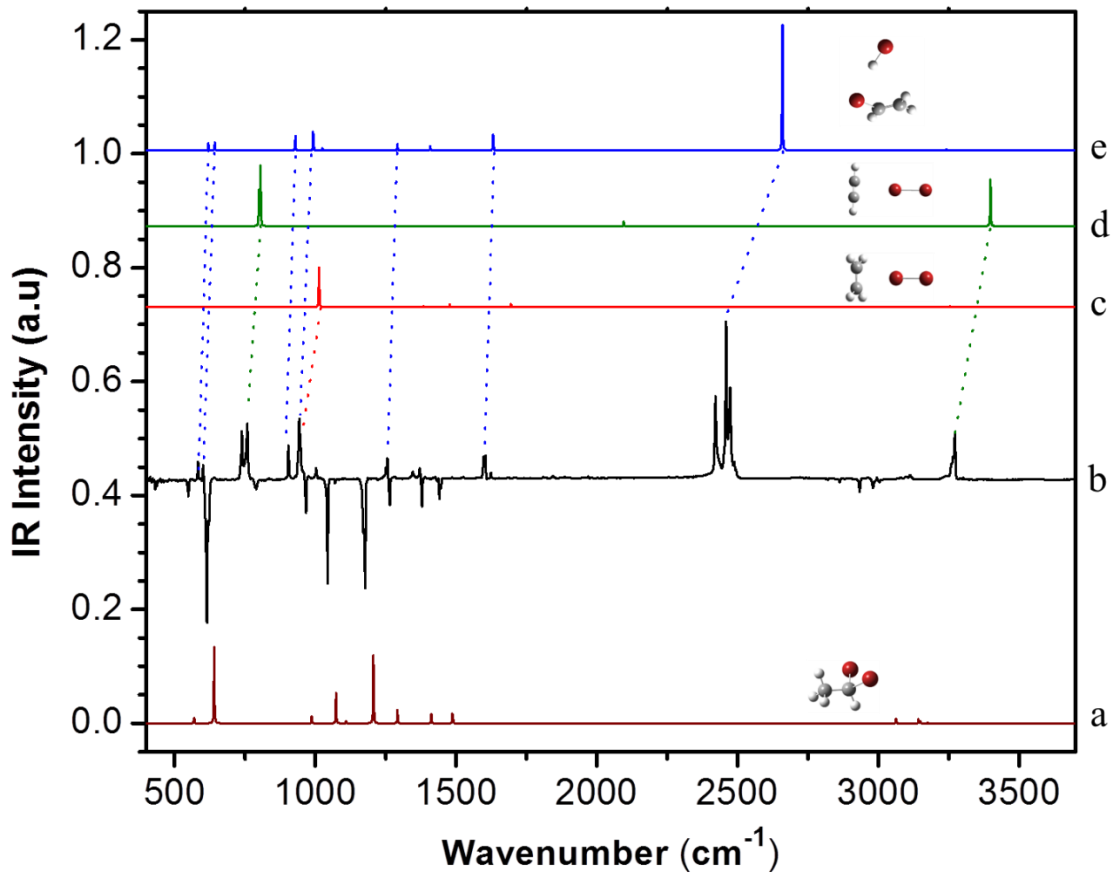


Figure 6.1: (a) Calculated infrared spectrum of 1,1-EDB, **(b)** experimental difference spectrum following photolysis of matrix isolated 1,1-dibromoethane at 5 K in comparison with calculated unscaled spectra of various photoproducts: **(c)** C_2H_4-Br_2**, (d)** C_2H_2-Br_2 and **(e)**HBr-CH_2CHBr Complex calculated at M06-2X/aug-cc-pVTZ level.

Table 6-1 Observed and calculated vibrational frequencies (cm^{-1}) and their intensities (km/mol)

Species	B3LYP/ aug-cc-pVTZ	CAMB3LYP aug-cc-pVTZ	M02x/ aug-cc-pVTZ	MP2/ aug-cc-pVTZ	Observed
HBr-CH_2CHBr (Complex 1)	18 (0.3)	16 (0.4)	31 (0.2)	30 (0.2)	…
	56 (0.3)	59 (0.4)	67 (0.5)	76 (0.6)	…
	66 (1)	60 (0.7)	77 (1)	88 (0.3)	…
	255 (5)	239 (5)	355(5)	260 (3)	…
	281 (5)	274 (5)	361 (0.4)	307 (3)	…
	348 (0.1)	354 (0.1)	450 (4)	351 (0.1)	…
	606 (27)	624 (21)	622 (18)	619 (17)	582.8
	615 (21)	629 (23)	636 (23)	642 (18)	601.2
	950 (40)	978 (52)	971 (42)	928 (34)	904.1
	984 (41)	1003 (30)	1000 (37)	992 (43)	943.4
	1023 (10)	1035 (9)	1030 (8)	1025 (7)	1002.2
	1285 (25)	1298 (23)	1290 (21)	1291 (17)	1255.8
	1409 (12)	1420 (10)	1415 (9)	1408 (10)	1370.8
	1649 (67)	1688 (59)	1685 (47)	1631 (42)	1598.4
	2564 (213)	2628 (199)	2687 (212)	2659 (318)	2421.3, 2459.1, 2473.3
	3142 (0.1)	3165 (0.3)	3157 (1)	3182 (0.7)	…
	3208 (3)	3230 (3)	3223 (0.6)	3242 (4)	…
	3233 (0.5)	3257 (0.3)	3252 (0.6)	3289 (0.3)	…
Br_2-C_2H_4	58 (0.2)	49 (0.1)	59 (0)	70 (0.2)	…
	59 (0.3)	51(0.1)	60 (0.2)	71 (0.4)	…
	86 (15)	76 (7)	111 (10)	107 (19)	…
	119 (0.4)	102 (0.3)	129 (0.2)	140 (0.3)	…
	209 (0.4)	161 (0.3)	190 (0.3)	222 (0.5)	…
	281 (28)	313 (13)	323 (13)	304 (24)	…
	837 (0.1)	842 (0.1)	835 (0)	823 (0)	…
	998 (158)	1005 (163)	1013 (158)	936 (0)	939.6
	1000 (0.1)	1019 (5)	1021 (0)	983 (152)	…
	1046 (0)	1021 (0)	1069 (0)	1049 (0)	…
	1247 (0)	1048 (0)	1244 (0)	1242 (0)	…
	1375 (11)	1254 (0)	1384 (4)	1370 (7)	…
	1482 (10)	1487 (12)	1477 (11)	1475 (9)	…
	1667 (39)	1705 (17)	1695 (16)	1653 (18)	1603.6
	3136 (5)	3152 (5)	3150 (3)	3174 (2)	…
	3246 (4)	3166 (1)	3164 (1)	33189 (0.5)	…
	3209 (00	3227 (0)	3229 (0)	3266 (0)	…
	3236 (60	3253 96)	3255 (40	3292 (2)	…
Br_2-C_2H_2	49 (0.2)	45 (0.1)	52 (0.1)	56 (0.1)	…
	49 (0.1)	45 (0.1)	55 (0.1)	58 (0.2)	…
	74 (8)	70 (4)	111 (4)	100 (7)	…
	104 (0.4)	100 (0.3)	131 (0.5)	108 (0.6)	…
	296 (13)	322 (6)	328 (7)	324 (9)	…

	658 (0.1)	706 (0.1)	716 (0)	597 (0)	…
	674 (0.1)	717 (0.1)	723 (0.1)	597 (0)	…
	767 (87)	782 (89)	800(84)	752 (78)	738.7
	779 (146)	791 (146)	805 (141)	759 (132)	757.7
	2059 (24)	2097 (11)	2095 (10)	1955 (7)	…
	3412 (107)	3417 (109)	3398 (111)	3422 (111)	3272.5
	3515 (0.1)	3526 (0.1)	3512 (0.2)	3521 (0.1)	….

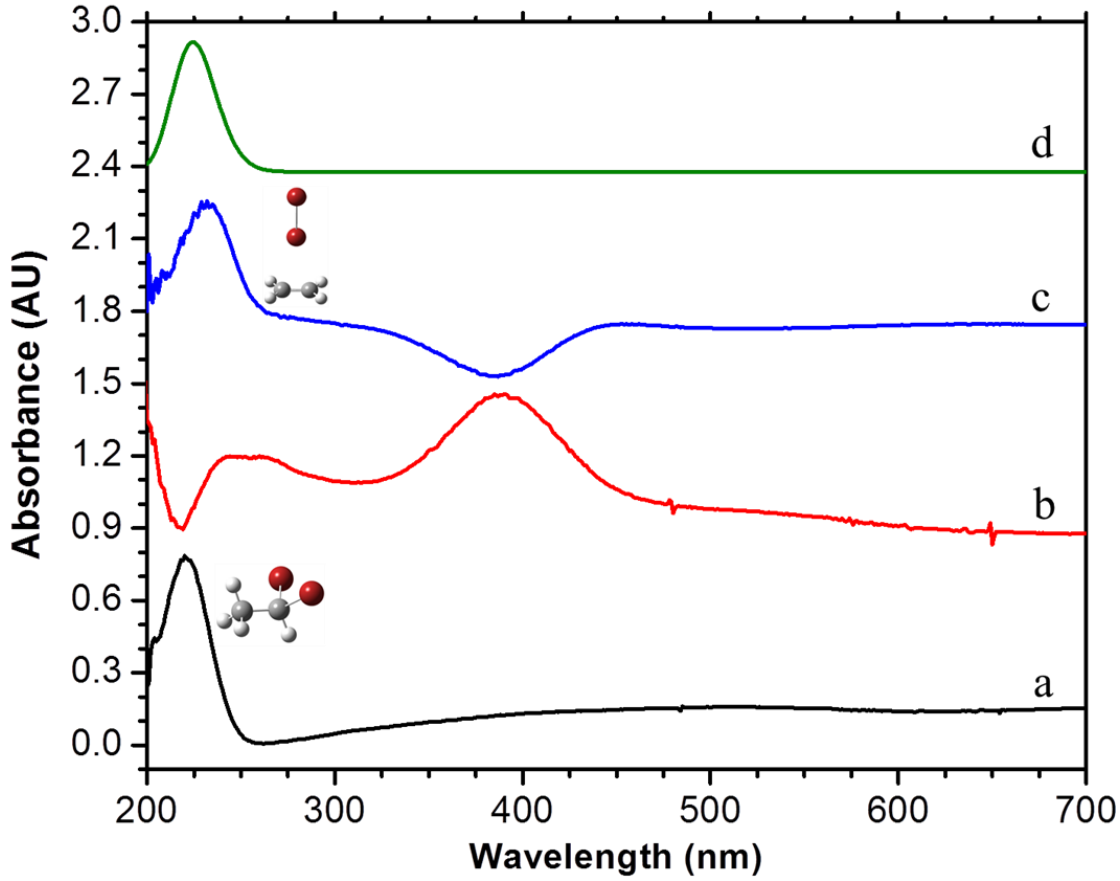


Figure 6.2: UV-Visible spectrum **(a)** matrix isolated 1,1-dibromoethane as deposited at 5 K, **(b)** difference spectrum recorded after photolysis at 220 nm, **(c)** spectrum recorded after annealing to 32K following irradiation and **(d)** theoretical spectrum of C_2H_4-Br_2 calculated at the TD-M06-2X/aug-cc-pVTZ level of theory.

Table 6-2 Calculated and Observed Electronic absorptions with their oscillator strength

Species	TD-M06-2X	TD-B3LYP	TD-CAM-B3LYP	Observed
Complex 1	207.25 (0.0005)	208.88 (0.1627)	206.44 (0.0014)	…
	195.19 (0.1527)	198.50 (0.0253)	194.85 (0.1933)	…
Complex 2	209.91 (0.0007)	217.59 (0.0398)	208.94 (0.0012)	…
	195.18 (0.1084)	202.21 (0.0682)	193.46 (0.1768)	…
Complex 3	210.02 (0.0004)		208.60 (0.0005)	…
	189.25 (0.1184)		189.95 (0.1485)	…
Complex 4	211.01 (0.0007)	220.34 (0.0008)	209.82 (0.0008)	…
	188.91 (0.2359)	200.59 (0.0002)	189.06 (0.2451)	…
Complex 5	211.29 (0.0006)	220.69 (0.0008)	210.00 (0.0006)	…
	198.81 (0.1466)	199.92 (0.1476)	189.31 (0.1770)	…
C_2H_4-Br_2	406.41 (0.0005)	433.97 (0.0006)	406.17 (0.0006)	…
	404.41 (0.0003)	431.30 (0.0004)	404.82 (0.0004)	…
	230.32 (0.0005)	269.86 (0.5222)	235.68 (0.0004)	…
	224.46 (0.5335)	259.05 (0.0001)	231.27 (0.5291)	232.92
C_2H_2-Br_2	412.54 (0.0005)	443.60 (0.0006)	413.03 (0.0006)	…
	407.20 (0.0004)	437.08 (0.0006)	408.70 (0.0005)	…
	232.69 (0.0003)	285.91 (0.0010)	237.61 (0.0005)	…
	230.30 (0.0003)	259.17 (0.3919)	235.48 (0.0002)	…
	210.59 (0.0018)	257.27 (0.0018)	217.77 (0.0016)	…
	205.95 (0.5175)	256.51 (0.0060)	213.33 (0.4420)	…

In the UV-Visible spectrum (Figure 6.2), the precursor 1,1-EDB has a strong band at ~ 221 nm, which overlapped with our dye laser (220 nm) for better photolysis conditions. Upon 0.5 hour photolysis, the 221 nm band decreased in intensity and a new broad band appeared at ~ 392 nm corresponding to molecular Br_2 [202]. Following irradiation, the matrix was annealed to 32 K and a strong absorption was observed in the at ~ 233 nm (layer c), corresponding to the Br_2-C_2H_4 complex as we have reported in our previous work [168]. This band was predicted by time-dependent density functional calculations with oscillator strength of about 0.52. (Table 6-2) The increase of Br_2-C_2H_4 band, upon annealing, is well correlated with the decrease of free molecular Br_2 band. No band due to HBr-Vinyl bromide complex was observed in the UV-Visible range, since the strongest absorptions were predicted to appear deep in the UV region and our experimental set-up did not allow measurement below 200 nm, due to the KBr window cutoff.

6.3.1 HBr elimination pathways

Our calculations results show that there are two main pathways for the formation of HBr complex: the first channel corresponds to a concerted proton-coupled electron transfer process, in which, the bromine atom on one carbon can abstract hydrogen from the other carbon, via a four center transition state denoted as TS1, lying at about ~52 kcal/mol above the 1,1-EDB (Figure 6.3). The existence of this path was confirmed by an IRC calculation linking transition state TS1 to 1,1-EDB and HBr-vinyl bromide complex (Figure 6.7). The second channel involves first formation of the *iso*-1,1-EDB (~54.5 kcal/mol) via a transition state TS2 (~62.5 kcal/mol) obviously higher in energy than

TS1, but still easily accessible given the amount of energy used for photolyis and according to our previous studies. The vibrational motions of the flexible *iso*-structure would facilitate the abstraction of H by the terminal bromine via a transition state denoted as TS3, lying at only ~5 kcal/mol above the *iso*-intermediate.

Exploring how general was this halogen halide elimination, we performed the same theoretical analysis to a related compound, 1,1-dichloroethane. As shown in Figure 6.4, our computational results (CCSDT//M06-2X/aug-cc-pVTZ) show that, very similarly to HBr elimination, HCl molecule can be produced either by a concerted PCET or by sequential ET/PT mechanisms, with two slight differences: the concerted pathway is more favored in HCl case, where the barrier to concerted reaction lies 44 kJ/mol below the isomerization transition state. The second difference is that in the sequential mechanism, the two steps are isoenergetic, while the transition state to PT was lower than the ET transition state in case of HBr.

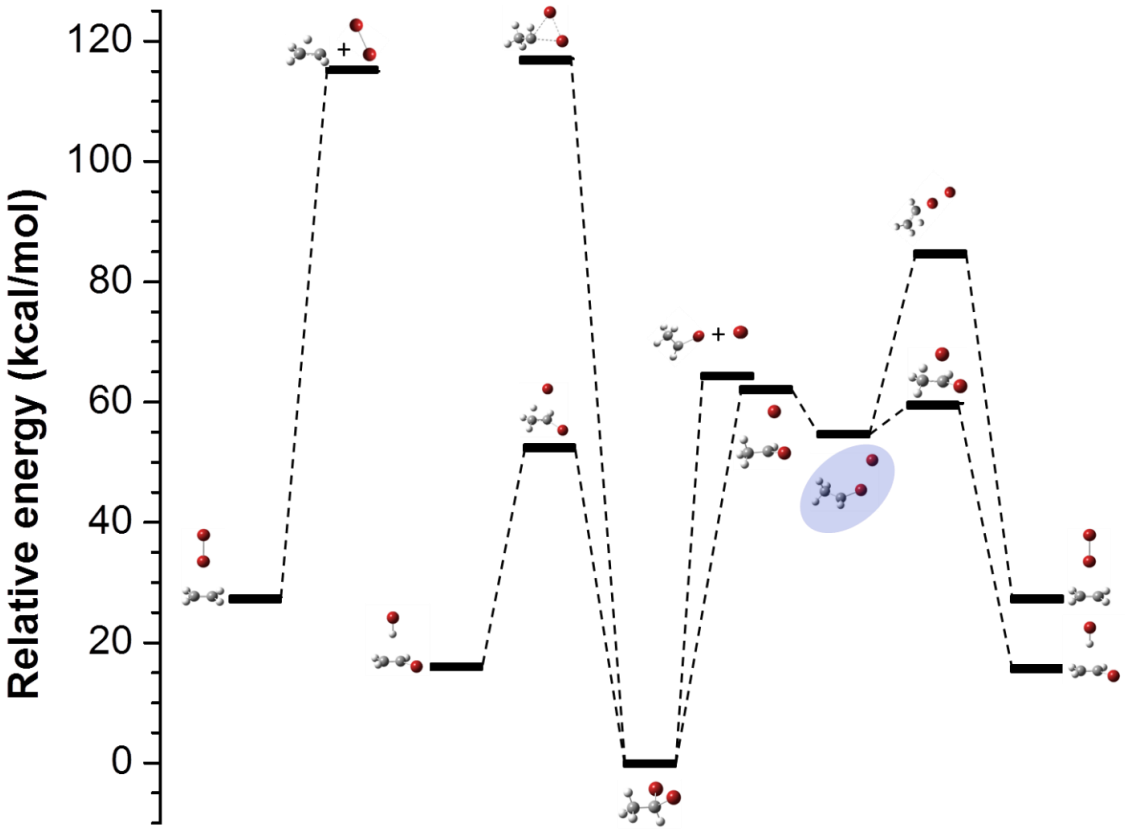


Figure 6.3 Calculated Stationary points on the 1,1-dibromoethane Potential Energy Surface (PES) at the CCSD(T)//M06-2X/aug-cc-pVTZ level of theory.

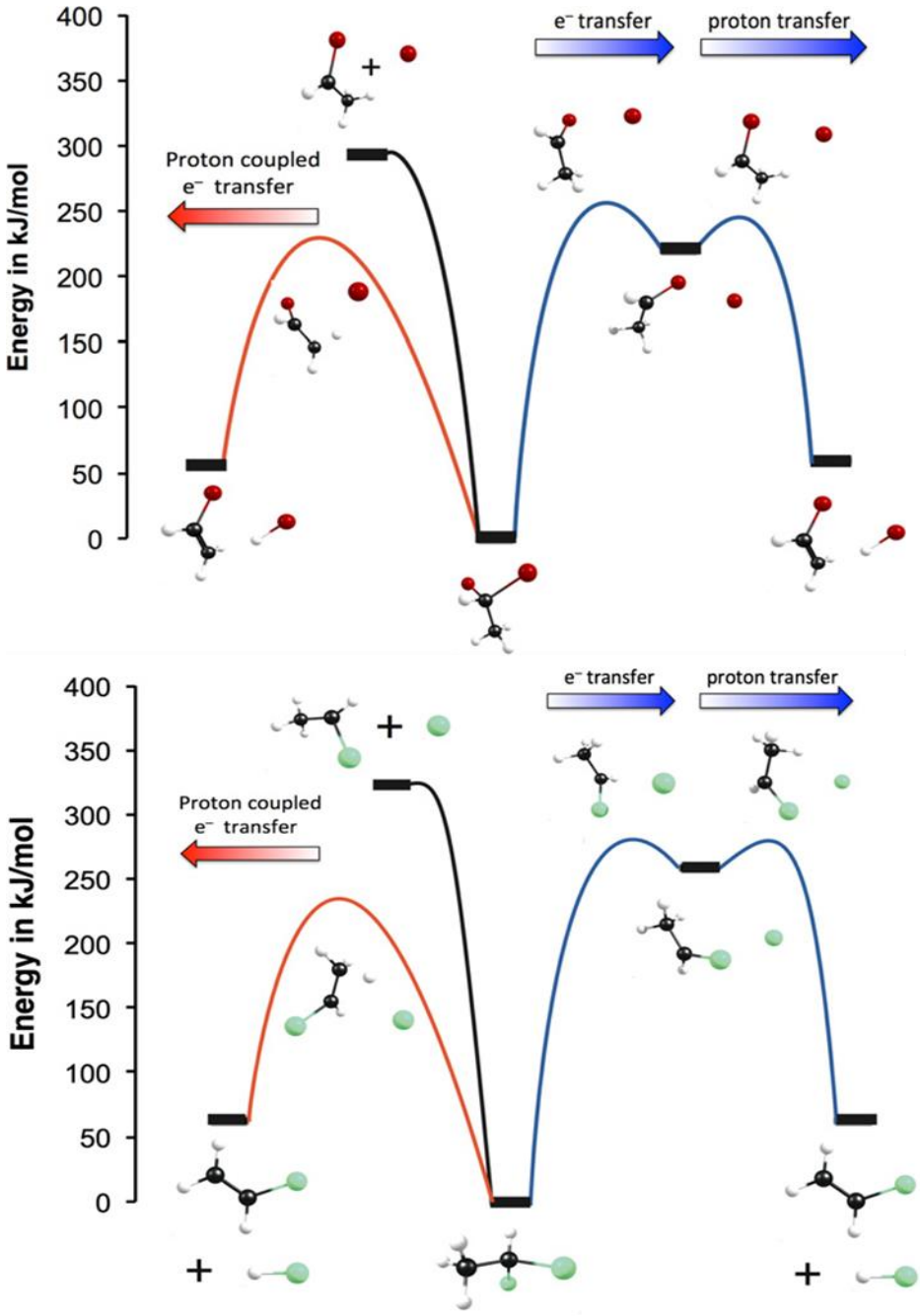


Figure 6.4: Calculated partial potential energy surface (PES) for HX (X=Br, Cl) elimination from 1,1-dihaloethane, at the CCSD(T)//M06-2X/aug-cc-pVTZ

6.3.2 Elimination of Br_2 from 1,1EDB

As mentioned before, we have observed in the matrix, complexes of Br_2 with ethylene and acetylene. Using theoretical calculations, we have explored different possible reaction mechanisms governing Br_2 elimination case. Contrary to the HBr loss, our calculations results show that the concerted mechanism where two C-Br bonds break and Br-Br bond forms simultaneously is the least plausible because of the relatively high energy three-center transition state TS5 lying at ~ 117 kcal/mol (CCSD(T)//M06-2X/aug-cc-pVTZ). Another pathway similar to what we observed in HBr case, is a sequential mechanism, where the first and limiting step is an Electron-Transfer by isomerization of 1,1-EDB via transition state TS1 located at ~61 kcal/mol above the normal isomer. The second step consists of two simultaneous processes, namely, cleavage of C-Br bond and 1,2-Hydrogen shift, to avoid the unstable CH_3CH carbene. A first-order transition state TS4 (~30 kcal/mol) was found to connect *iso*-1,1-EDB to the molecular products (Br_2 and C_2H_4), and this was confirmed by IRC calculation as shown in Figure 6.7. In cryogenic environment, these molecular products interact to form a weakly bound complex, as shown in Figure 1 and in our previous study.[203] A related complex formed between molecular Br_2 and acetylene, previously characterized [204] was also observed in our IR spectrum. The observation of these unsaturated hydrocarbons in our experiments is consistent with previous studies, where Y-T Lee and co-workers demonstrated that CH_3CH intermediate can easily isomerize to $H_2C\text{-}CH_2$ with a barrier of about ~2 kcal/mol or decompose into $C_2H_2 + H_2$ with a relative barrier of ~34 kcal/mol.[205]

Elimination of molecular Br_2 might also occur by a radical mechanism; however it is very clear that while getting closer, Br atom and C_2H_4Br radical will naturally fall into the well of the *iso*-1,1-EDB, which is a minimum on the PES, and the rest will happen as previously described in the sequential isomerization channel.

6.3.3 Role of the missing *iso*-1,1-dibromoethane.

From a general perspective, our calculations show that half of possible pathways readily involve the *iso*-1,1-EDB as key intermediate. Our lack of success in trapping this isomer might be explained by the fact that the laser light used in our experiments has enough energy (~130 kcal/mol) to overcome any barrier height on the PES and the final photoproducts have much low energies, relatively to the *iso*-halon intermediate. The *iso*-halon is formed vibrationally hot and tends to decompose into stable products. It's understandable that the combination of these factors in a steady state experiment will drive the reaction to completion. Prospective ultrafast spectroscopy studies will be more revealing on formation and decay time of the *iso*-halon intermediate.

In a different, but related, experiment, we studied photolysis of 1,1-dibromo-2,2,2-trifluoroethane in Ne matrix at 5 K, and the only photoproduct observed was the *iso*-1,1-dibromo 2,2,2,-trifluoro ethane (Figure 6.5). For example, in this case, since there was not fluorine atom shift, the final products after Br_2 elimination would have been CF_3CH and Br_2 lying at about ~50 kcal/mol above the *iso*-halon. This experiment provided additional information to understand the 1,1-EDB photodecomposition: first, the loss of Br_2 from the *iso*-1,1-EDB was facilitated by H-shift process, which is

quenched in the case of trifluoro- compound. Second, the hydrogen in the HBr fragment comes from the other carbon than the one bearing bromine atoms.

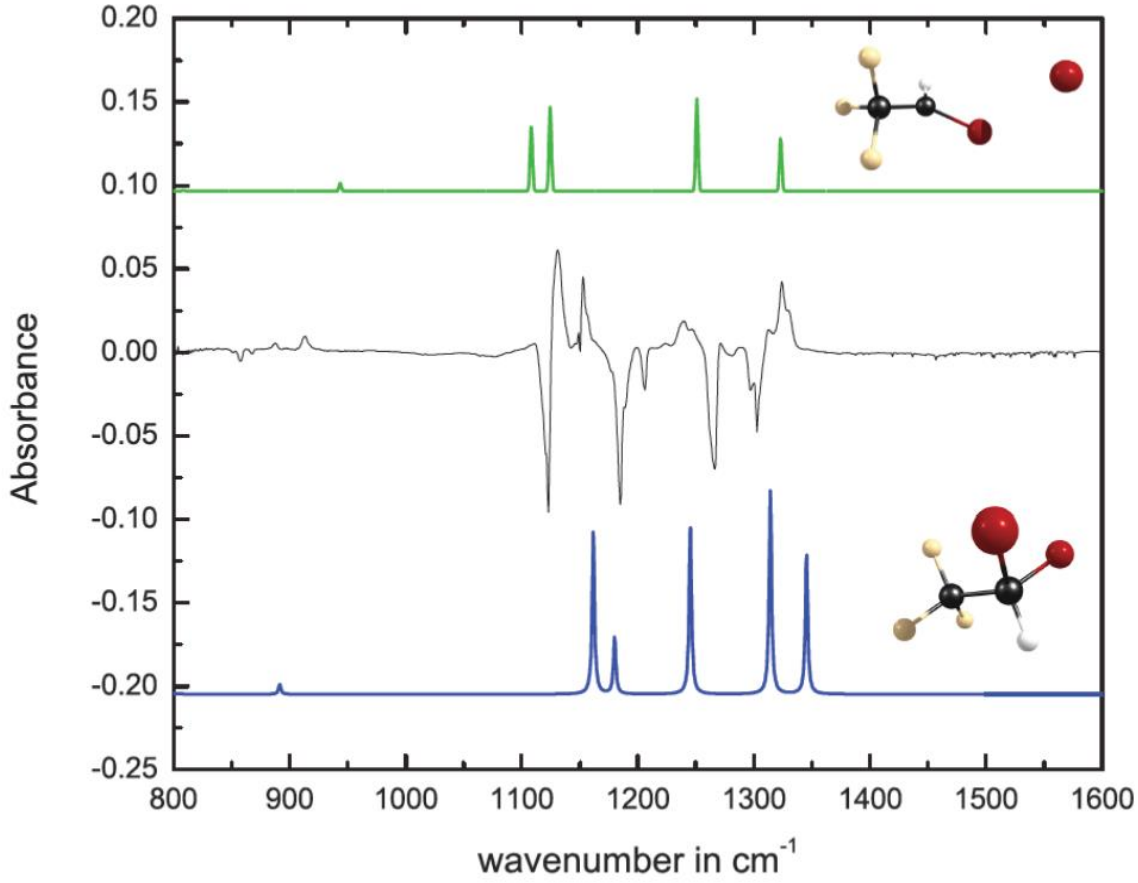


Figure 6.5: Difference spectrum following 240 nm irradiation of 1,1dibromo2,2,2-trifluoroethane in a Ne matrix at 5 K, in comparison with calculated spectra of parent and photoproduct, calculated at the M06-2X/aug-cc-pVTZ level.

The key role if the *iso*-1,1-EDB intermediate would be more relevant in liquid phase whereby barrier heights of transition state structures involved in this process are lowered by solvation. In Figure 6.6 using the polarized continuum medium (PCM) approach [133] with dichloromethane as solvent, our calculation results show that the *iso*-halon intermediate is stabilized by about -5 kcal/mol, as well transition state to isomerization and transition states to HBr and Br_2 elimination are lowered by about -11, -9 and -17 kcal/mol respectively. Due to the ion-pair character of these TS structures, the sequential mechanism will be much favored over the radical mechanisms in liquid phase.

Mimicking the isomerization coordinate, we have performed a relaxed scan along C-Br-Br bond angle, in both singlet and first triplet states and we found that their PES cross twice at about ~75 and 84° (Figure 6.8). With respect to C-Br-Br coordinate, the isomerization TS on the singlet state corresponds to a minimum on the triplet state potential and this suggests that spin-orbit coupling might influence the dynamics of the reaction. In the future, we are planning to run photolysis experiments on 1,1-dichloroethane where most of properties are similar to 1,1-dibromoethane except that PES do not cross since the singlet-triplet gap becomes more important as the halogen gets lighter.

A column density in our matrix sample was derived by dividing the integrated IR peaks by the calculated IR intensity. It was found that HBr and Br_2 were produced in about 1:1 ratio, consistent with the amount of energy used for photolysis relatively to the barrier heights involved. This observation is also reflected by estimation of the microscopic rate for both HBr and Br_2 elimination from the *iso*-halon intermediate as shown in Figure 6.9.

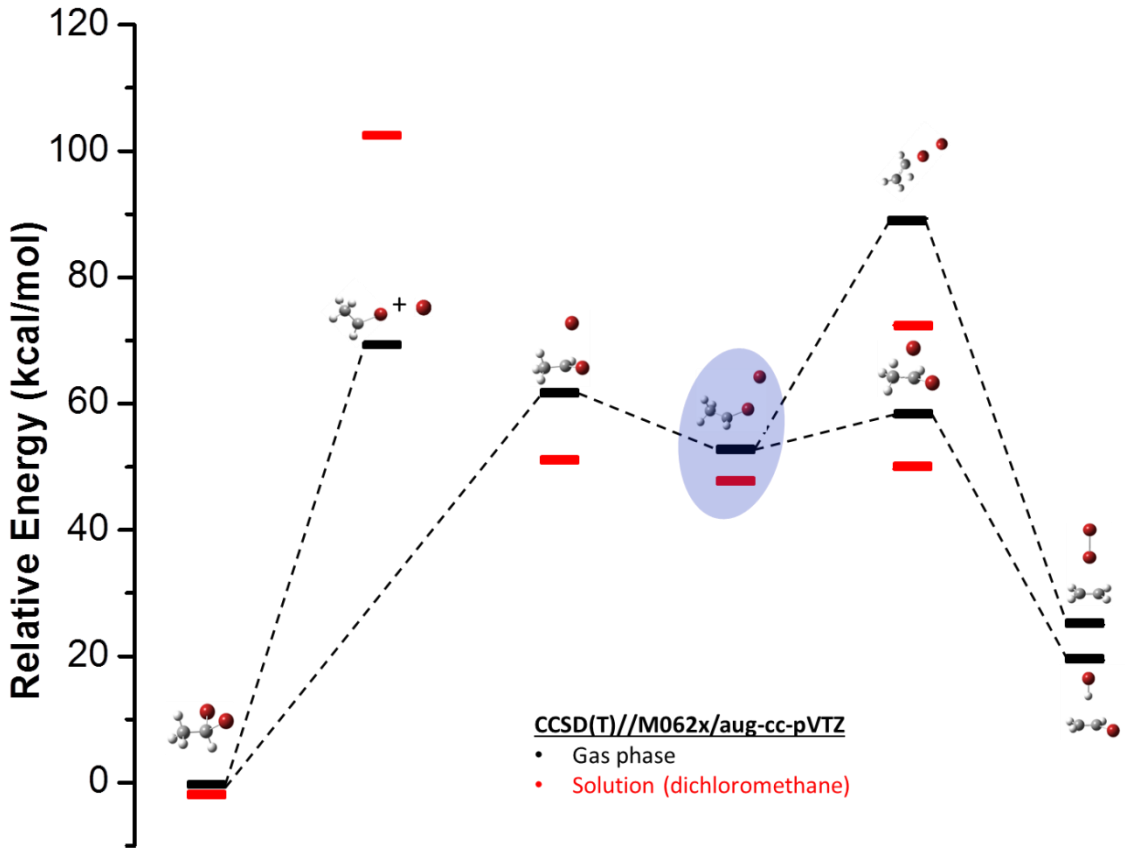


Figure 6.6: Partial Potential Energy Surface (PES) of 1,1-EDB showing the sequential pathway of the molecular elimination involving the *iso*-halon intermediate (CCSD(T)//M06-2X/aug-cc-pVTZ level).

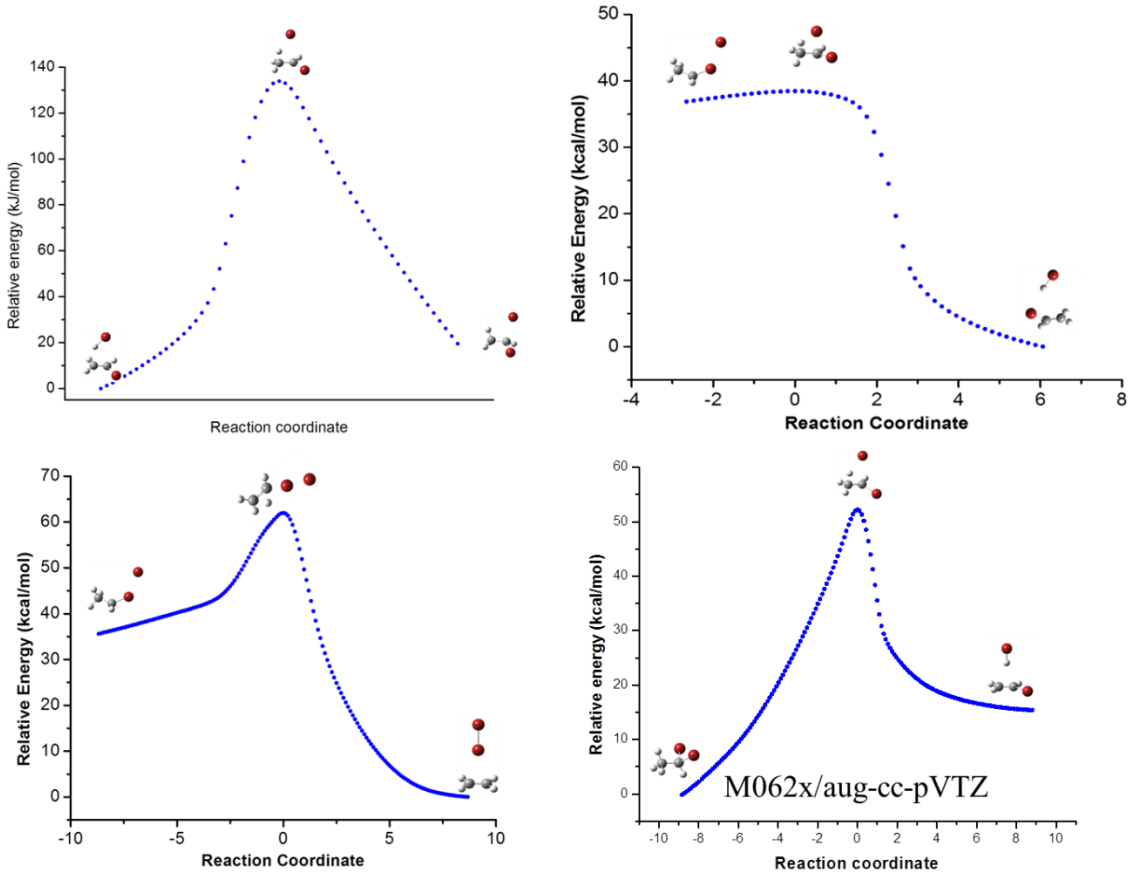


Figure 6.7 Intrinsic Reaction Coordinate calculations of the reaction paths linking 1,1-dibromoethane and *iso*-1,1-dibromoethane to the elimination of molecular products HBr and Br_2, performed at M06-2X/aug-cc-pVTZ

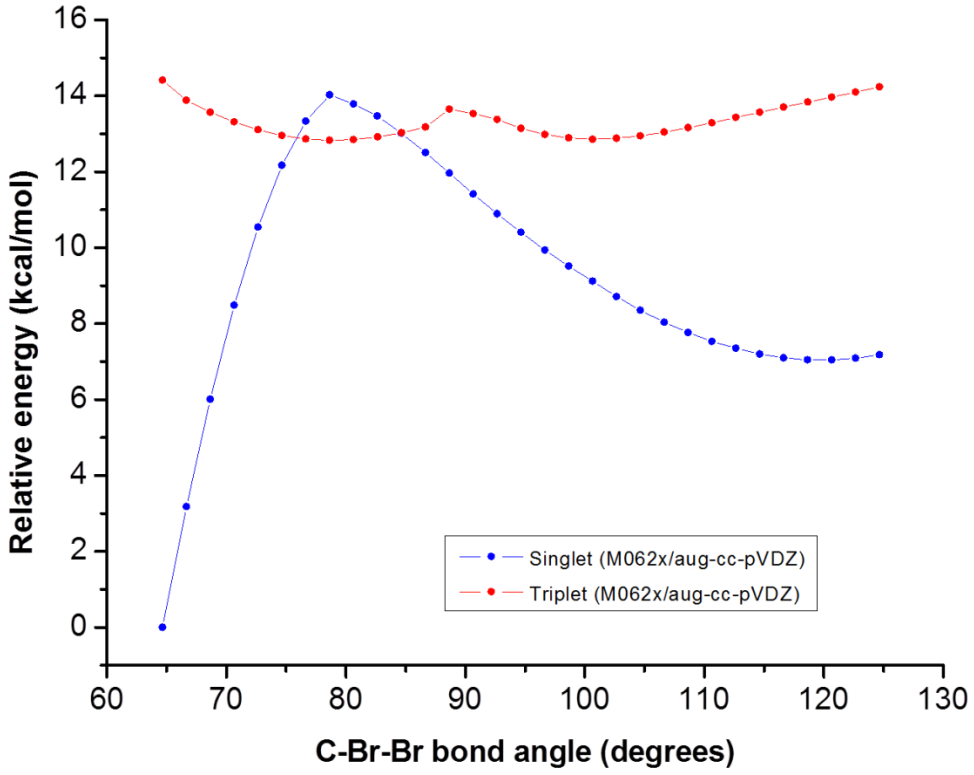


Figure 6.8: Relaxed scans along C-Br-Br bond angle, in both singlet and triplet PES (M06-2X/aug-cc-pVDZ).

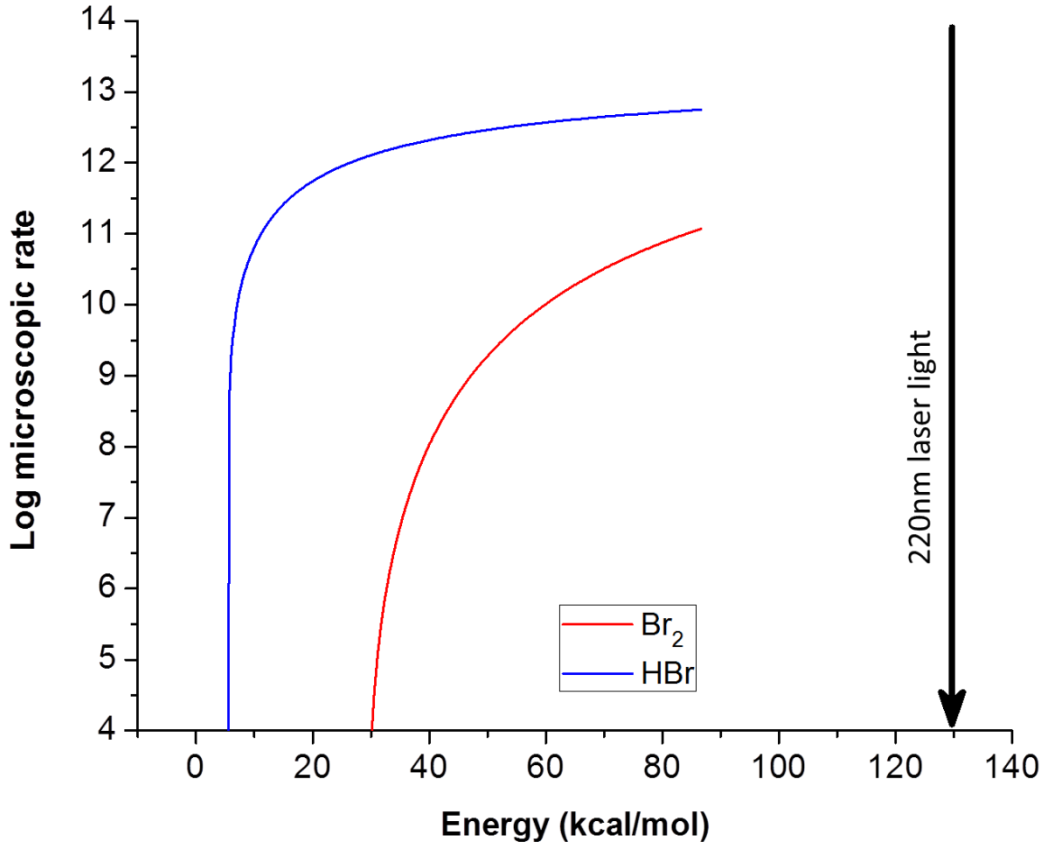


Figure 6.9: Prediction of microscopic rates as function of energy (kcal/mol), using input values from MP2/aug-cc-pVTZ results.

6.3.4 HBr⋯Vinyl bromide complexes.

In cryogenic environment or in solution, photofragments can recombine to form new molecular species or complexes. In our experiments we have observed HBr⋯CH_2-CHBr, Br_2⋯CH_2-CH_2 and Br_2⋯CH-CH complexes. Concerning the HBr-vinyl bromide complex, five different structures (Figure 6.10), with nearly equal binding energies (Table 6-3) were optimized at the MP2 and M06-2X/aug-cc-pVTZ level. They have similar Infrared and UV-Visible spectra and their intermolecular interactions can be rationalized by electrostatic potential on complex subunits, as depicted in Figure 6.11. In complex 1, HBr fragment is perpendicularly aligned with vinyl bromide, in such way that the π-electron cloud of C=C bond is forming a H-bonding with HBr, with an intermolecular distance of ~ 2.001 Å (MP2/aug-cc-pVTZ). Complex 2 is the least bound and has similar T-shape structure, except that the HBr fragment is inversed so that the π-cloud is interacting with the small σ-hole (positively charged) on the Br atom and the intermolecular distance (~ 3.135 Å) is much longer than in complex 1. Complex 3 results from H-bonding, where instead of being perpendicular to C=C bond, HBr is pointing toward the large negative belt on bromine atom of vinyl bromide, which is the most negatively charged portion of the subunit. The intermolecular distance is ~2.464 Å with C-Br-H of about 84°. The most strongly bound complexes 4 and 5 are planar structures resulting from double H-bonding interactions as shown in Figure 6.11.

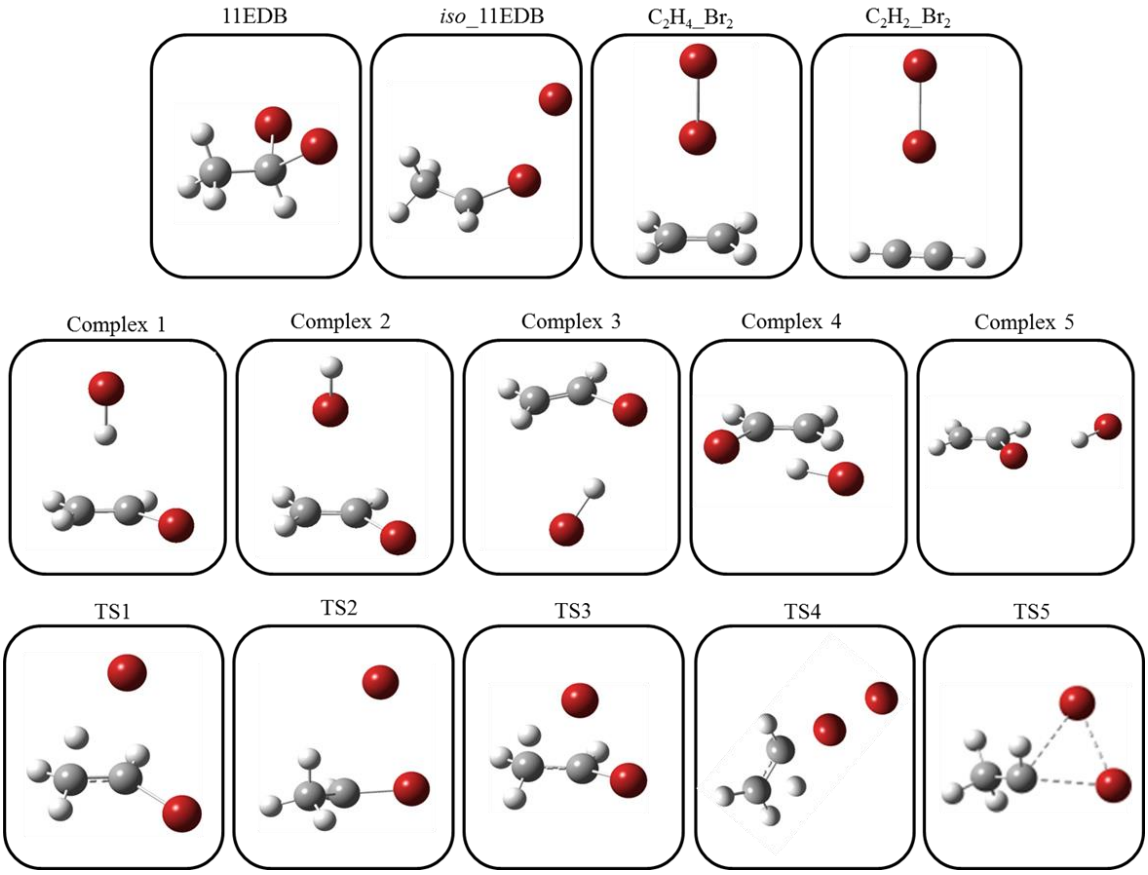


Figure 6.10 Optimized structures for various stationary points calculated on the PES of 1,1-Dibromoethane.

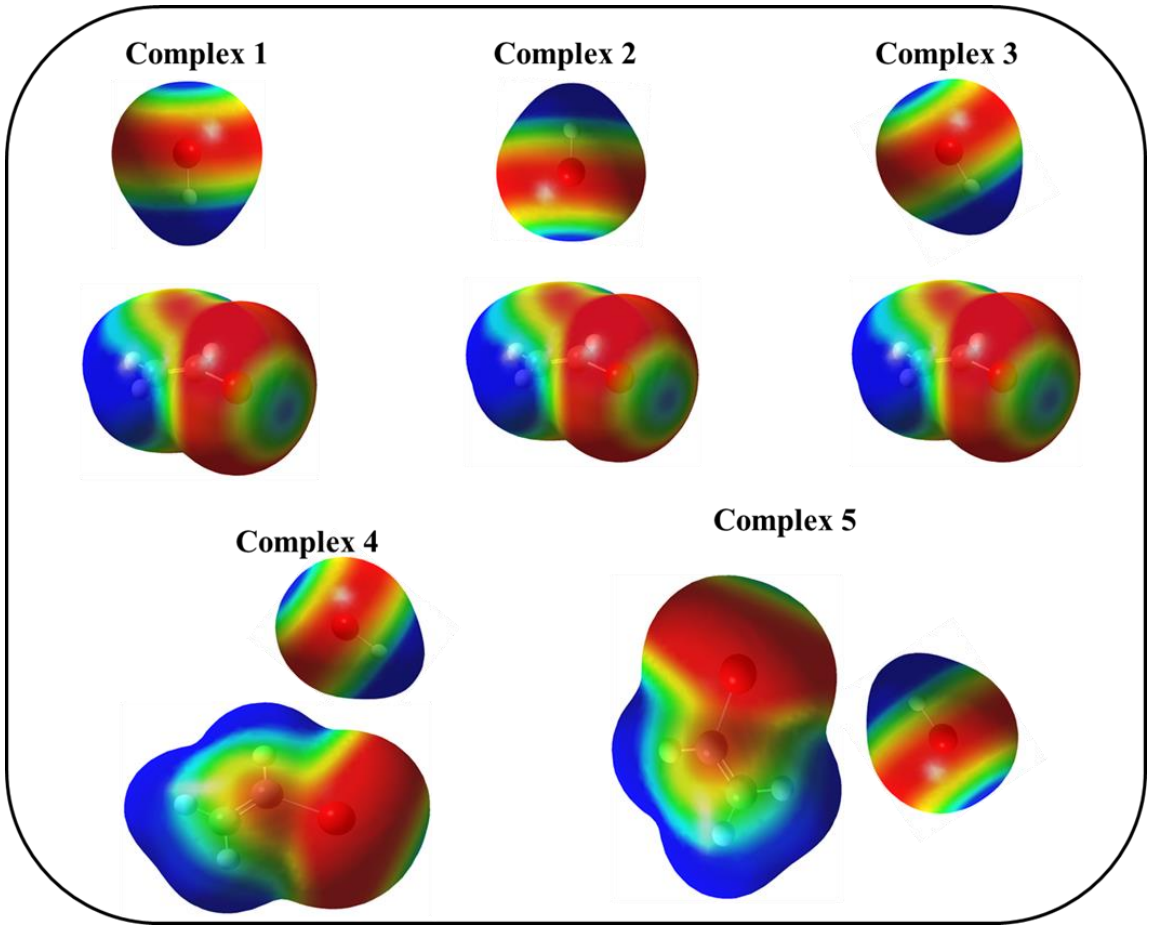


Figure 6.11: Electrostatic potential surface maps showing intermolecular interactions for various HBr···Vinyil bromide complexes, calculated at the MP2/aug-cc-pVTZ (isovalue=0.0004).

Table 6-3 Predicted Binding Energies (in kJ/mol)

Species	**M06-2X/ aug-cc-pVTZ**	**CCSDT//M06-2X aug-cc-pVTZ**	**MP2/ aug-cc-pVTZ**	**CCSDT//MP2 aug-cc-pVTZ**
Complex 1	-4.4	-9.4	-15.7	-14.8
Complex 2	0.5	-3.1	-10.6	-10.1
Complex 3	-5.6	-11.0	-25.5	-24.2
Complex 4	-6.7	-12.4	-46.9	-50.4
Complex 5	-4.8	-10.9	-24.4	-17.4

Binding energy in kJ/mol corrected from ZPE and BSSE

6.4 Summary

We have explored the photodissociation of matrix isolated 1,1-dibromoethane with 220 nm laser light and have observed elimination of hydrogen halide (HBr) via a concerted proton-coupled electron transfer mechanism (PCET), energetically favored over a sequential electron-transfer followed by proton-transfer (ET/PT) mechanism. Following observation of Br_2 complexes and by our calculations, we have demonstrated that in the very plausible, but intriguing, sequential pathway the *iso*-1,1-dibromoethane is still a key intermediate in both elimination of HBr and Br_2, although we couldn't trap it experimentally.

Weakly bound complexes resulting from the interactions between photo-fragments were stabilized and characterized in Argon matrix, using Fourier Transform infrared and UV-Visible spectroscopy. Calculations show that there a five different structures for HBr-vinyl bromide complex with nearly equal binding energy. Unfortunately, we couldn't distinguish them due to their similar IR and UV-Visible signatures. The lack of HBr photoproduct from photolysis of CF_3CHBr_2, led us to the conclusion that H and Br atoms in HBr fragment come from different carbons and H-shift in TS3 facilitates Br_2 elimination from *iso*-1,1-dibromoethane intermediate. To complete our steady state experiments, we are planning to probe the dynamics of the short-lived *iso*-1,1-EDB intermediate by doing ultrafast experiments on this molecule.

Chapter 7. PRODUCTION AND PHOTOCHEMISTRY OF $C_2H_4\cdots Br_2$ CHARGE TRANSFER COMPLEX IN SOLID MATRIX.

Also called "electron-donor-acceptor complex", a charge transfer (CT) complex is a chemical structure associating two molecules (or two parts of larger molecule) and characterized by electronic transition(s) to an excited state in which there is a partial transfer of electronic charge from the donor to the acceptor moiety. In general, a CT complex is weakly bound and relatively unstable. The excitation energy of the intense charge transfer resonance occurs very frequently in the visible region of the electro-magnetic spectrum. This produces the usually intense colors characteristic for these complexes and therefore, they are mostly detected by optical spectroscopy. In CT excitation a single electron is transferred from the highest occupied molecular orbital (HOMO) of the donor to the lowest unoccupied molecular orbital (LUMO) of the acceptor. This process yields the ion-radical pair which can react irreversibly to products or regenerate the complex by giving back the electron to the donor:

$$\mathrm{D} \cdots \mathrm{A} \xrightarrow{h\nu_{CT}} \mathrm{D}^{+} \cdots \mathrm{A}^{-} \rightarrow \mathrm{Products}$$

Example: CH_3-CO-CH_3 + Br_2 → $(CH_3)_2$-CO$\cdots Br_2$ [206] (Figure 7.1)

Generally, the charge transfer complex can be easily characterized in IR spectrum, by the appearance of new bands or by frequency shift for modes affected by complexation. For instance, for homopolar diatomic acceptor such as I_2, Br_2, Cl_2, the infrared forbidden stretching vibration of the free molecule becomes IR active and decreases in frequency on interaction with an electron donor. [206]

In this study, we are going to discuss about one of the simplest CT complexes, often used as prototype of donor-acceptor complex: the one involving ethylene as donor and Br_2 (or other dihalogen) as acceptor.

This study was triggered by the observations done in our 1, 2dibromoethane experiments, whereby upon photolysis of 1,2-$C_2H_4Br_2$ at 220 nm in Ar matrix, we have detected the $C_2H_4 \cdots Br_2$ complex as one of the major photoproducts.

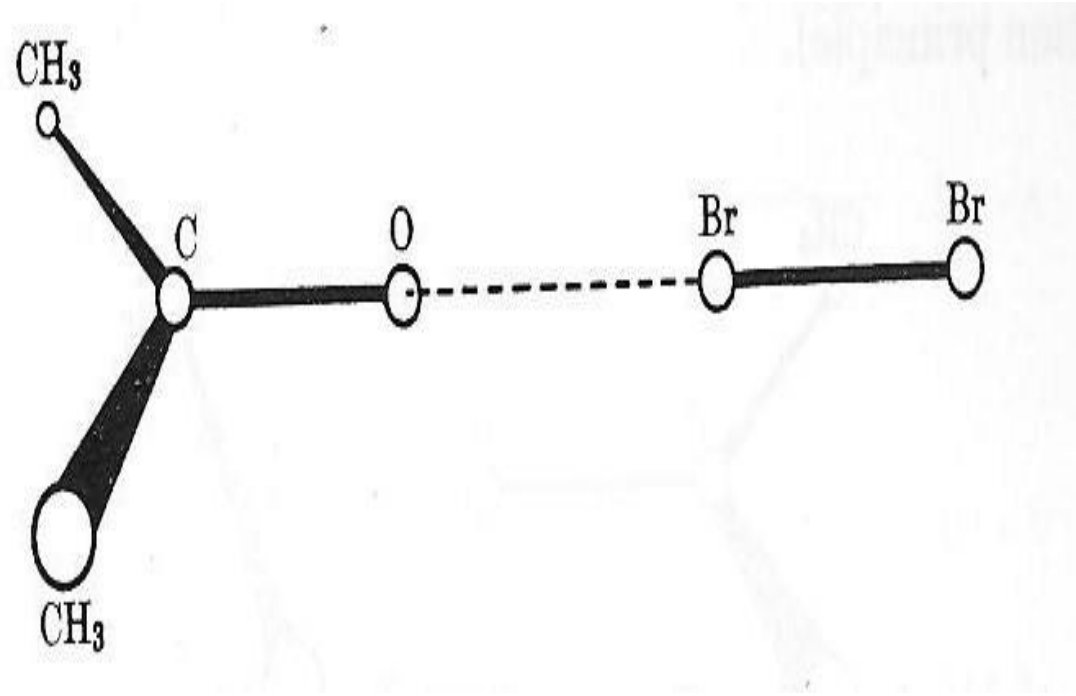


Figure 7.1: Orientation of bromine in its complex with acetone as determined from X-Ray crystallographic studies.[206]

7.1 Experimental methods

In our previous experiments, the C_2H_4---Br_2 charge transfer was produced by photolysis of 1,2-$C_2H_4Br_2$ at 220 nm. In this study our goal was to isolate and investigate the photochemistry of $C_2H_4\cdots Br_2$ complex produced by a different method than the photolysis. Our first choice was to co-deposit ethylene and bromine mixture and trap the complex in a rare matrix.

For that, a new "dual nozzle late mixing" apparatus was specifically designed and it was described in detail in Chapter 2 (Figure 2.3). The rest of the matrix isolation setup was the same as described in previous Chapter 2.

In this case, two mixtures were prepared separately: ethylene:argon (C_2H_4:Ar =1:450) and bromine:argon, and each mixture was sprayed onto the cold window through a different nozzle. One great advantage of this new design is to avoid the addition reaction between ethylene and the molecular bromine inside the line. The second advantage is that the timing at which the two nozzles are fired can be adjusted and controlled. Following deposition, the sample was irradiated with a 220 nm The irradiated sample was annealed by heating the window up to 33K and re-cooling back down to 5 K. At each step IR and UV/Vis spectra were recorded.

7.2 Computational methods

The calculations used in this study are those performed for the 1,2-dibromoethane experiments and described in detail earlier in section 6.2.

7.3 Results and discussion

This complex had been previously detected in a couple of different studies: in gas-phase by microwave spectroscopy by Legon and co-workers[158] and more recently in Ar matrix using a co-condensation approach.[157] The photochemistry has been studied in UV range ($\lambda > 300$ nm), and the excitation at this wavelength has proven to produce in nearly equal abundance, the anti- and gauche-conformer of $C_2H_4Br_2$ via a radical addition reaction of which the mechanism is shown in Figure 1.8

However these results are not consistent with the Mulliken theory of the charge transfer complex. The charge transfer excitation will initiate electron transfer from the donor to the acceptor leading to an ion-pair bromonium intermediate; and the final addition reaction would exclusively produce the anti-conformer as shown on Figure 7.5

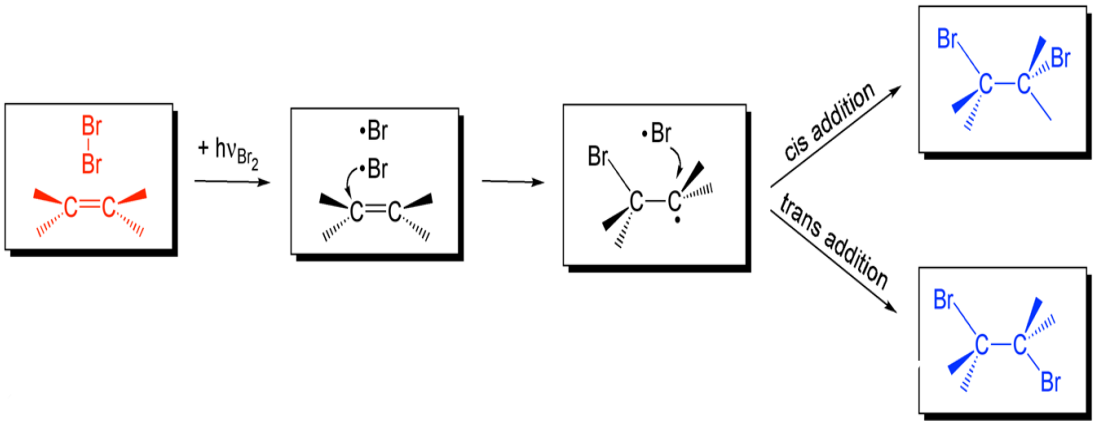


Figure 7.2: Radical mechanisms for reaction of the C_2H_4…Br_2 complex.

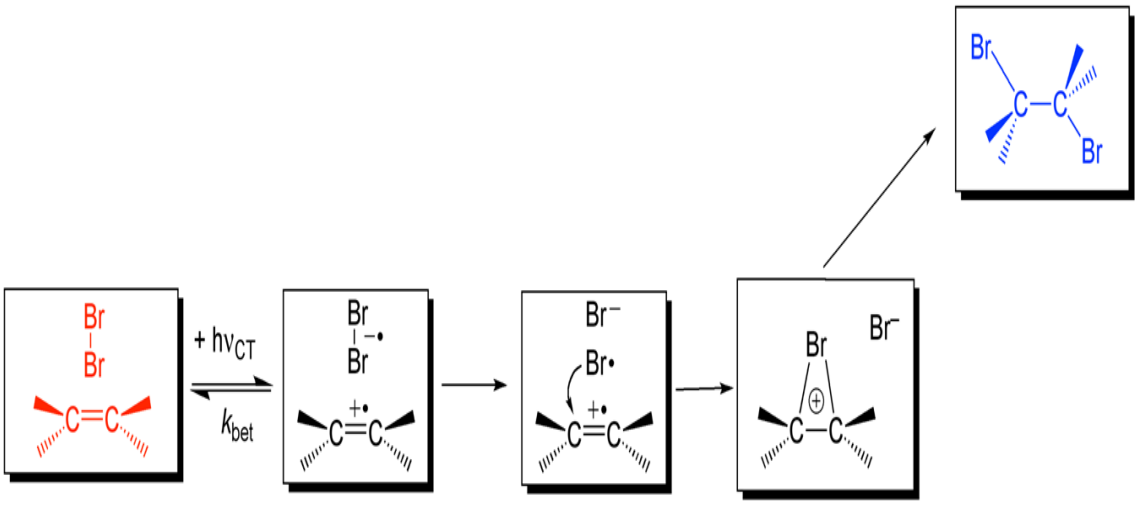


Figure 7.3 charge transfer mechanisms for reaction of the C_2H_4…Br_2 complex.

In our 1,2-dibromoethane experiments, the C_2H_4---Br_2 complex was observed as major photoproduct following photolysis at 220 nm laser light. This first UV/Vis characterization was in good agreement with *ab initio* predictions (CT band at λ_{max} = 237 nm), and from Figure 4.4 it is obvious that the excitation at $\lambda > 300$ nm does not access the charge transfer band, but rather transitions localized on Br_2 chromophore.

Based on these controversies, we thought to investigate in detail the photochemistry of the C_2H_4-Br_2 complex and for that, we needed a new method which could produce the complex in higher yield. This is what initiated the idea of the dual pulsed nozzle late mixing design (Figure 2.3). The Figure 7.4 shows the results from three different attempts to produce the $C_2H_4 \cdots Br_2$ complex, together with the IR calculated spectra.

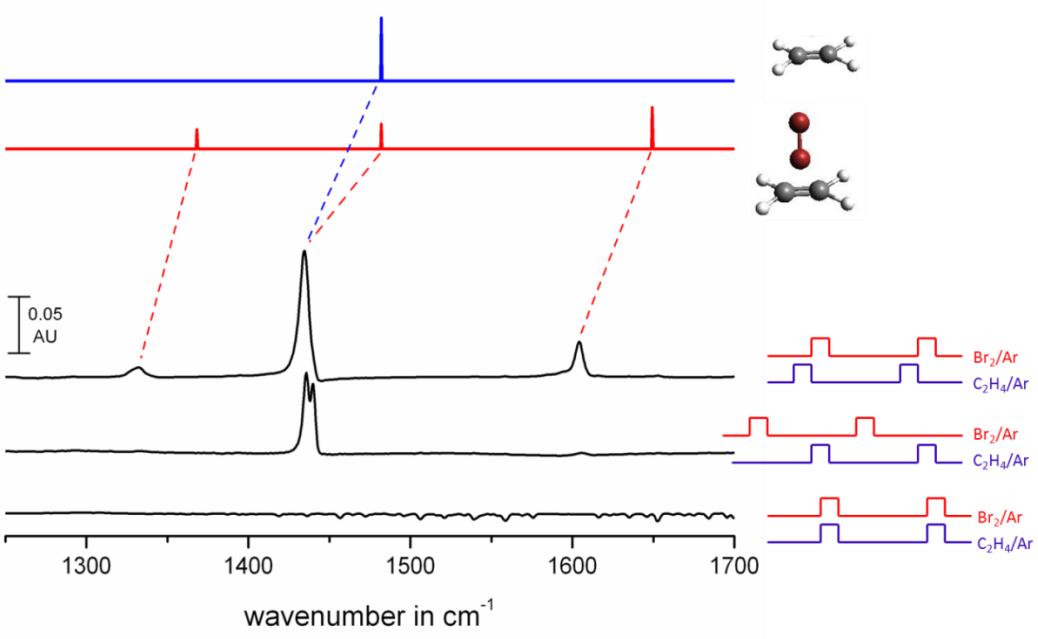


Figure 7.4 Spectra for three different experiments. (detail in the text) The calculated (MP2/aug-cc-pVTZ) spectra of C_2H_4 and the $C_2H_4\cdots Br_2$ complex are shown.

In the first trial, the pulses from two nozzles were totally overlapping and the two gases were meeting in the mixing channel. The resulting complete thermal reaction between Br_2 and C_2H_4 is shown by the lack of C_2H_4 IR signatures. In the second trial, the relative nozzle timing was delayed by ½ the inverse repetition rate (160 ms). The nozzles were fired alternatively and produced a sandwiched matrix on the cold window. By annealing the matrix to 33K, a very small amount of $C_2H_4\cdots Br_2$ complex was formed. The inefficiency of this annealing experiment can be explained by the fact that C_2H_4 monomer could not afford transport to Br_2 matrix site. The ratio of monomer to complex was estimated to be >50:1, based on our IR calculated intensities (MP2/aug-cc-pVTZ). In the final trial, the nozzles timing were slightly delayed to avoid the mixing in the channel, but the gases were deposited on the cold window in a very rapid succession. As shown on Figure.2 this approach was successful and the complex was produced in larger yield. The ν_7 band (CH_2 wag) largely affected by complexation was used in order to compare the C_2H_4 monomer with the complex, we used and the ratio of monomer to complex was estimated to be 2:1. In the free monomer, the vibrational mode predicted to be observed at ~ 926 cm^{-1} at CCSD/aug-cc-pVTZ level of theory , showed a weak peak at ~ 925 cm^{-1}. Upon complexation with bromine the peak was observed at 960 cm^{-1}.

The photochemistry of complex was studied at a more reasonable wavelength. The excitation with a 266 nm laser light led to the decomposition of the complex and this according to Mulliken theory: only the anti-1,2- dibromoethane was produced (Figure 7.5).

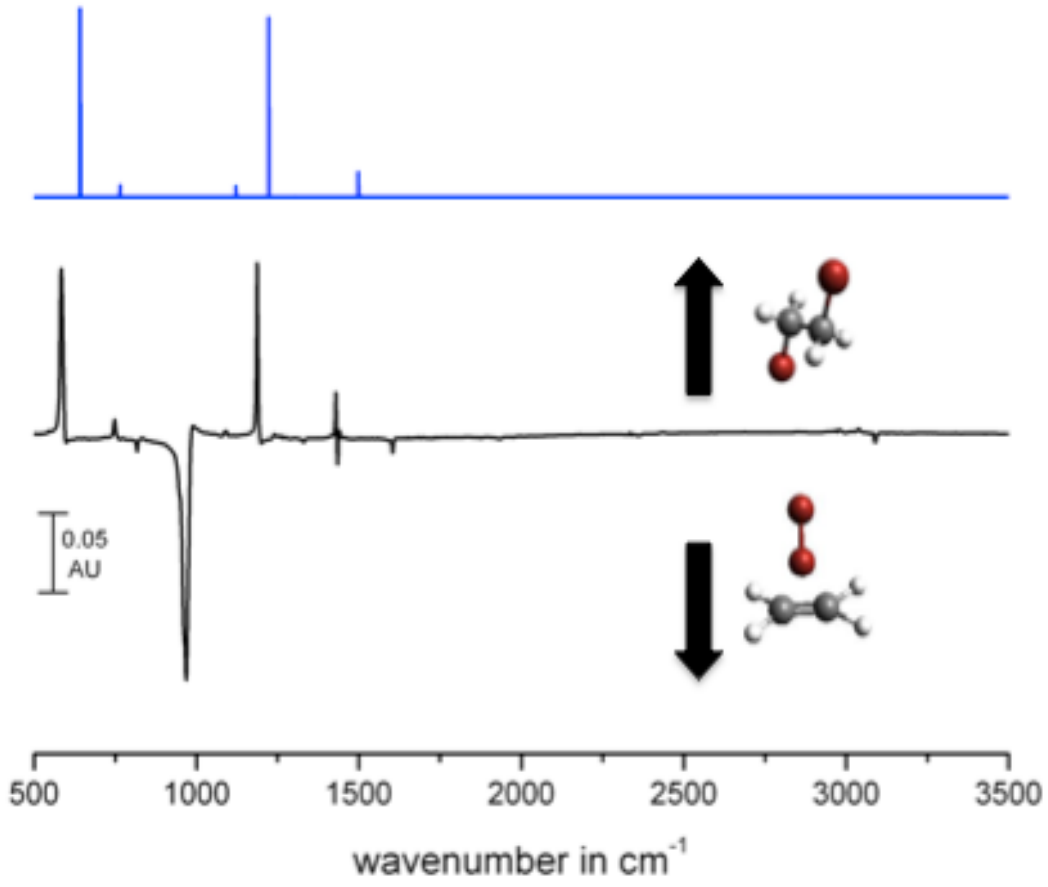


Figure 7.5: Difference IR spectrum obtained following photolysis of the C_2H_4—Br_2 complex at 266 nm. A single photoproduct is observed, *anti*-1,2-dibromoethane. The calculated (unscaled MP2/aug-cc-pVTZ) spectrum of the product is shown.

In this process the electron transfer following charge transfer excitation leads to formation of the ion radical pair (C_2H_4+•···Br_2–•). The breakup of the Br_2–• anion radical, and subsequent fast reaction of Br• with C_2H_4+•, leads to a bromonium ion intermediate, which rapidly reacts with Br^- in the matrix cage to produce the final product. The bridged structure of the bromonium ion [207-213] which blocks cis-addition, is responsible for the conformational preference in the photoproduct. The 266 nm excitation wavelength was chosen in order to avoid a secondary photolysis, which would convert 1,2-dibromoethane photoproduct into gauche-conformer as seen in our previous studies. Note that this conformer was not at all observed under our experimental conditions.

7.4 Summary

A new method for the trapping and study of pre-reactive donor-acceptor complexes was developed. This method was used to investigate photoinduced electron transfer in a prototypical Mulliken donor-acceptor π-complex, C_2H_4---Br_2. We found that excitation into the intense charge transfer band of the complex leads exclusively to the anti-conformer in agreement with Mulliken theory.

Chapter 8. PRODUCTION AND PHOTOCHEMISTRY OF $C_2H_2\cdots I_2$ CHARGE TRANSFER COMPLEX: PROBING RADICAL PATHWAYS IN ELECTROPHILIC ADDITION OF HALOGENS.

This work follows the study of $C_2H_4\cdots Br_2$ charge transfer complex, described in the previous chapter. Several organic text-books use the addition of halogens to simple olefins as typical example of electrophilic addition. However the exact mechanism governing this reaction has seen much controversy over the elusive haloalkyl radical intermediate. [61, 214-222] In 1964, Skell and co-workers observed stereospecificity in trans photoinitiated addition reaction of iodine to olefins, and they explained it by the role of bridged radical intermediate. [221] However, there was no experimental evidence of such intermediate at that time, and its search proved to be difficult. It was not until 2005 when Ihee and co-workers experimentally identified the bridged $C_2H_4\cdots I$ radical in solution using time-resolved X-ray diffraction techniques.[61] To date, however, the intermediate(s) along the electrophilic addition path have not been identified, and to our knowledge of spectroscopy, structure and reactivity of these intermediates is lacking. Haloalkyl radical intermediates can have different but related structures as shown in Figure 8-1, but the open shell character and the small energy difference separating these structures make even theoretical characterization a challenge.[168, 214-216, 223] For example, in our previous chapter, density functional theory calculations (UB3LYP and UCAM-B3LYP) show that asymmetrically bridged structure is a local minimum, while the same structure is a transition state on the UM062-2x , UMP2 and UCCSD potential

energy surfaces. However, at all levels of theory used, the symmetrically bridged radical lays at more than 10 kJ/mol, above the classical, non-bridged structure.

An attractive approach used by our group and others groups, is to study radical addition mechanism, starting from the pre-reactive dihalogen-olefin complex, formed by co-condensation of molecular halogen (Br_2 or I_2) and olefin (C_2H_4) diluted in rare gas, and photolytically initiate the reaction by shinning the matrix sample with a laser light. In 1997, Maier and co-workers excited the $C_2H_4 \cdots Br_2$, isolated in Ne matrix, with wavelength $\lambda > 300$ nm, this led to the Br-Br bond cleavage and formation, in nearly equal (1:1.2) yield, of the two (*anti*- and *gauche*-) stereoisomers of the single reaction product, 1,2-dibromoethane. This result is explained, as shown in Figure 8-2, by the participation of a bromoalkyl radical, although it couldn't be trapped experimentally. In our study (chapter 7), we excited the CT band of the same complex and observed the single (*anti*-) stereoisomer of the reaction product.[203] One can understand these findings by the mechanism involving a bridged bromonium ion intermediate as shown in Figure 8-2. In this work, we are discussing studies of radical addition pathways in $C_2H_4 + I_2$ reaction, where the participation of a bridged radical intermediate is confirmed by direct observation of the intermediate trapped in solid matrix following photolysis of $C_2H_4 \cdots I_2$.

8.1 Experimental set-up

The details of the experimental approach have been previously described in detail.[128, 130] Briefly, ethylene:I_2:Ne mixtures (_2:1:1000) were generated by passing an ethylene:Ne mixture prepared on a manifold using standard manometric techniques

over a temperature controlled vessel containing solid I_2. The resulting mixture was deposited on the cold window (~5 K) using pulsed deposition technique. The pulsed deposition method is particularly advantageous for forming complexes, due to self-annealing. Following deposition, the cold window was irradiated with 450.

8.2 Computational methods

Calculations were carried out using the GAUSSIAN 09 [42] and NBO 5.9 [134] programs on the MU Pere cluster. Geometry optimization was performed using DFT and post-Hartree Fock methods with an aug-cc-pVTZ basis set. [50, 224-226] For Iodine, we used Peterson's effective core potential basis (aug-cc-pVTZ-pp).[54] Time-dependent DFT (TDDFT) methods are now widely used for modeling electronically excited states, and it is known that local exchange functionals perform poorly for states involving significant charge transfer.[227] Thus, in this work we employed the CAM-B3LYP and M06 functionals, which have shown good performance for related systems. [130, 142]

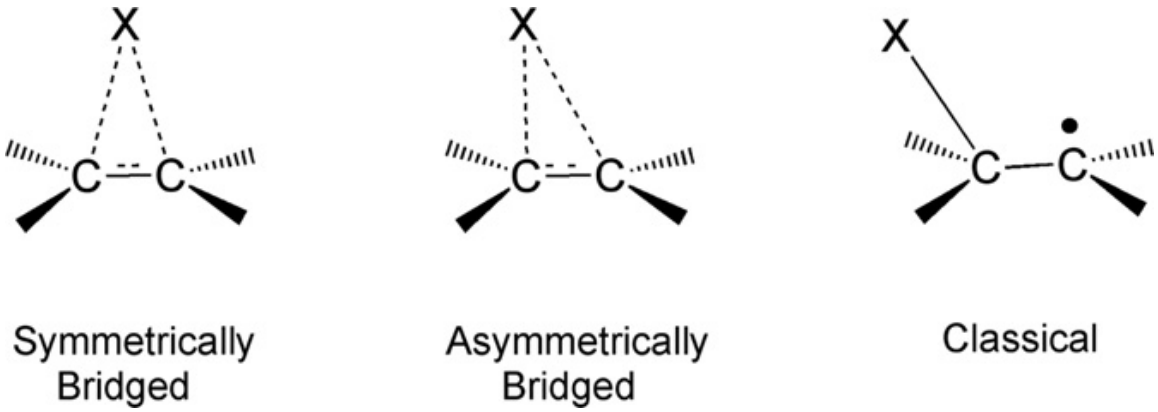


Figure 8.1 Structural motifs for haloalkyl radicals (X=Cl, Br, I)

8.3 Results and Discussion

8.3.1 Formation and characterization of $C_2H_4\cdots I_2$ complex

Figure 8.2 displays UV/Visible spectrum of C_2H_4:I_2:Ne (~1:2:500) sample at ~5 K, and a stick spectrum representing the TDDFT prediction of the spectrum of ethylene-iodine complex at the (TD)M06/Sadlej-pVTZ level. When ethylene and iodine were co-deposited in neon matrix, an intense band appeared at 247 nm, which is in excellent agreement with theoretical predictions (Table 8-1), being essentially bracketed by the TD-CAM-B3LYP and TD-M06 predictions. The position of the charge-transfer band in the Ne matrix is similar to previous results in Ar and nitrogen matrices (248.5 nm in Argon and 246.5 nm in N_2).[228] Note that the B–X band of molecular iodine, observed at 500 nm in the Ne matrix, is blue shifted to 451 nm in the complex; again, similar shifts were previously reported in Ar (510 nm to 453 nm) and N_2 (505 nm to 450 nm) matrices.[228]

Under the assumption that the IR and UV/Visible spectra sample the same region of the matrix, the integrated IR and UV/Vis intensities can be combined with calculated IR intensities to estimate the oscillator strength of the UV/Vis transitions.[57] Using this approach, the derived oscillator strength of the charge transfer band is ~ 0.46 (εmax = 12,900 M^{-1} cm^{-1}), similar to the TD-M06 prediction (Table 8-1).

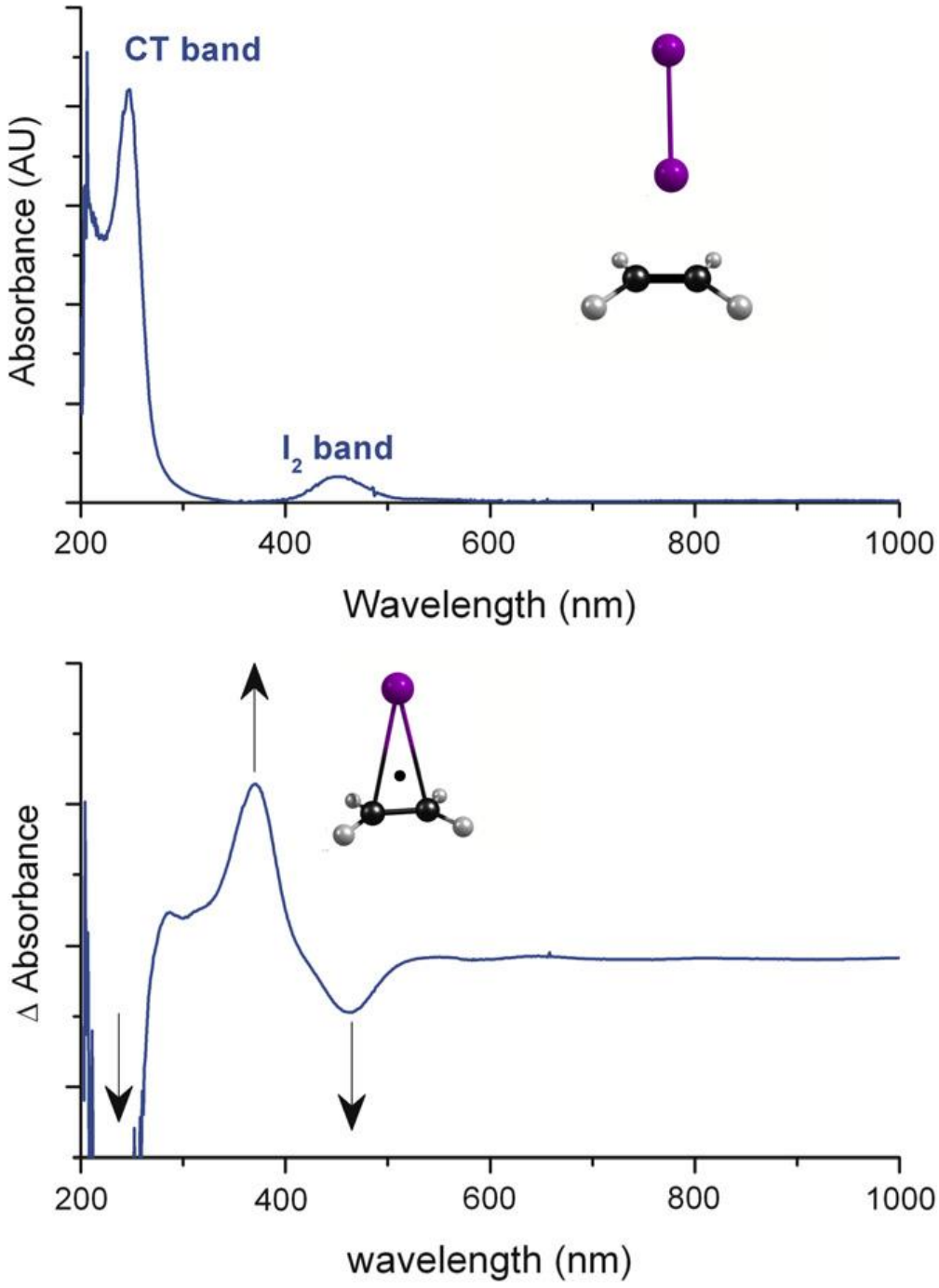


Figure 8.2: UV/visible spectrum of (a) Ethylene−I2 complex, as deposited in Ar matrix. (b) Difference spectrum after photolysis at 355 nm laser light.

Table 8-1 Observed and predicted electronic absorptions with their oscillator strengths.

Complex	**Singlet Excited State**	**Predicted vertical excitation λ in nm (oscillator strength, *f*)**		**Observed λ_{max} (*f*) in Ne**
		CAM-B3LYP[a]	**M06[a]**	
$C_2H_4\cdots I_2$	1	497.3(0.0009)	505.0(0.0008)	…
	2	494.7(0.0005)	502.6(0.0001)	…
	3	296.9(0.0001)	310.6(0.0000)	…
	4	296.3(0.0003)	310.1(0.0002)	…
	5	**237.4(0.7591)**	**257.6(0.4240)**	**247 (0.46)**
$C_2H_4I\bullet$ (bridged)	1	2434.2(0.0000)	2525.6(0.0000)	…
	2	2337.5(0.0001)	2460.1(0.0001)	…
	3	**356.4(0.2036)**	**383.5(0.1724)**	**366 (0.20)**
	4	306.9(0.0008)	304.1(0.0012)	…
	5	229.2(0.0000)	264.4(0.0000)	…
$C_2H_4I\bullet$ (classical)	1	384.9(0.0004)	430.7(0.0004)	…
	2	380.8(0.0031)	428.3(0.0045)	…
	3	300.0(0.0341)	329.2(0.0155)	…
	4	252.8(0.0000)	292.3(0.0381)	…
	5	248.8(0.0002)	275.8(0.0000)	…
1,2-$C_2H_4I_2$ (anti)	1	258.9(0.0000)	280.9(0.0000)	…
	2	255.7(0.0147)	276.4(0.0209)	…
	3	255.3(0.0000)	275.0(0.0001)	…
	4	253.3(0.0000)	273.8(0.0000)	…
	5	201.5(0.0000)	241.6(0.0262)	…
1,2-$C_2H_4I_2$ (gauche)	1	265.8(0.0040)	292.5(0.0082)	…
	2	255.0(0.0001)	276.7(0.0006)	…
	3	251.5(0.0005)	271.9(0.0013)	…
	4	251.3(0.0006)	270.1(0.0005)	…
	5	201.0(0.0033)	243.9(0.0203)	…

The formation of the complex is also evident in the IR spectra, most strikingly by the appearance of bands that are IR inactive in ethylene due to symmetry lowering. This is illustrated in Figure 8.3, which displays a difference spectrum following 240 nm photolysis of the complex. The IR inactive ethylene bands ν_2 (C-C stretch) and ν_3 (CH_2 deformation) appear at 1342 and 1613 cm^{-1}, respectively, upon formation of the complex. In contrast, the infrared active ethylene bands display only small shifts upon complex formation. The observed IR frequencies are compared with the calculated values at the M06/Sadlej-pVTZ level in Table 8-2. All of the bands observed in the IR spectrum can be assigned to the complex (or free ethylene) with the exception of a weak band at 1145 cm^{-1} that is assigned to the strongest IR transition of the anti-conformer of 1,2-diiodoethane (calculated at 1119 cm^{-1}, M06/Sadlej-pVTZ), which is presumably formed in the (slow) thermal reaction of the precursors in the source prior to deposition.

8.3.2 Excitation of the CT versus I_2 chromophore band

The charge transfer (CT) photochemistry of the complex was probed by 240 nm laser irradiation. Figure 8.2 demonstrates that irradiation leads to the loss of the $C_2H_4\cdots I_2$ band at 247 nm and the appearance of an intense band at 373 nm, which is readily assigned to the bridged $C_2H_4\cdots I\bullet$ complex based upon the following considerations. First, the observed shift is similar to that observed for the corresponding complexes with benzene ($Bz\cdots I_2$, λmax = 295 nm; $Bz\cdots I\bullet$, λmax = 430 nm). Second, the position of this band is in excellent agreement with TDDFT predictions, particularly when the M06 functional is used (Table 8-1). Third, the experimental oscillator strength determined as described above is also in good agreement with theory (Table 8-1). As discussed above,

previous studies of arene···I_2 complexes in the gas-phase and solution have shown that CT excitation followed by rapid back electron transfer (BET) leads to formation of a neutral I_2 molecule on an excited repulsive potential energy surface, resulting in rapid fission of the I−I bond. [196, 200, 229-232] Zewail and co-workers identified a second "harpoon" like mechanism that led to a smaller translational energy release, [196] and in the gas-phase accounts for some 30-40% of products.[233, 234] In the matrix, cleavage of the I-I bond leads to formation of the separated radical pair C_2H_4···I• and I•

Further information comes from experiments where we excited the I_2 chromophore in the complex rather than CT band. This was achieved via irradiation at 450 nm, using the fundamental of the dye laser. As noted above, the B–X band of molecular iodine, observed at 500 nm in the Ne matrix, is blue shifted to 451 nm in the complex. Therefore, an excitation wavelength of 450 nm cleanly excites the complexed I_2, leading to cleavage of the I-I bond. As shown in Figure 8.4, the difference spectrum obtained following irradiation shows the loss of complex and the rise of a band at 366 nm. That the same bridged C_2H_4···I• complex is observed following excitation into both the UV and Visible bands of the C_2H_4···I_2 complex (Figure 1) speaks to the fast BET that must follow CT excitation in this system. It is also important to note that, following either 240 or 450 nm excitation, there is no evidence in our spectra for the formation of any photoproduct other than the C_2H_4···I• complex.

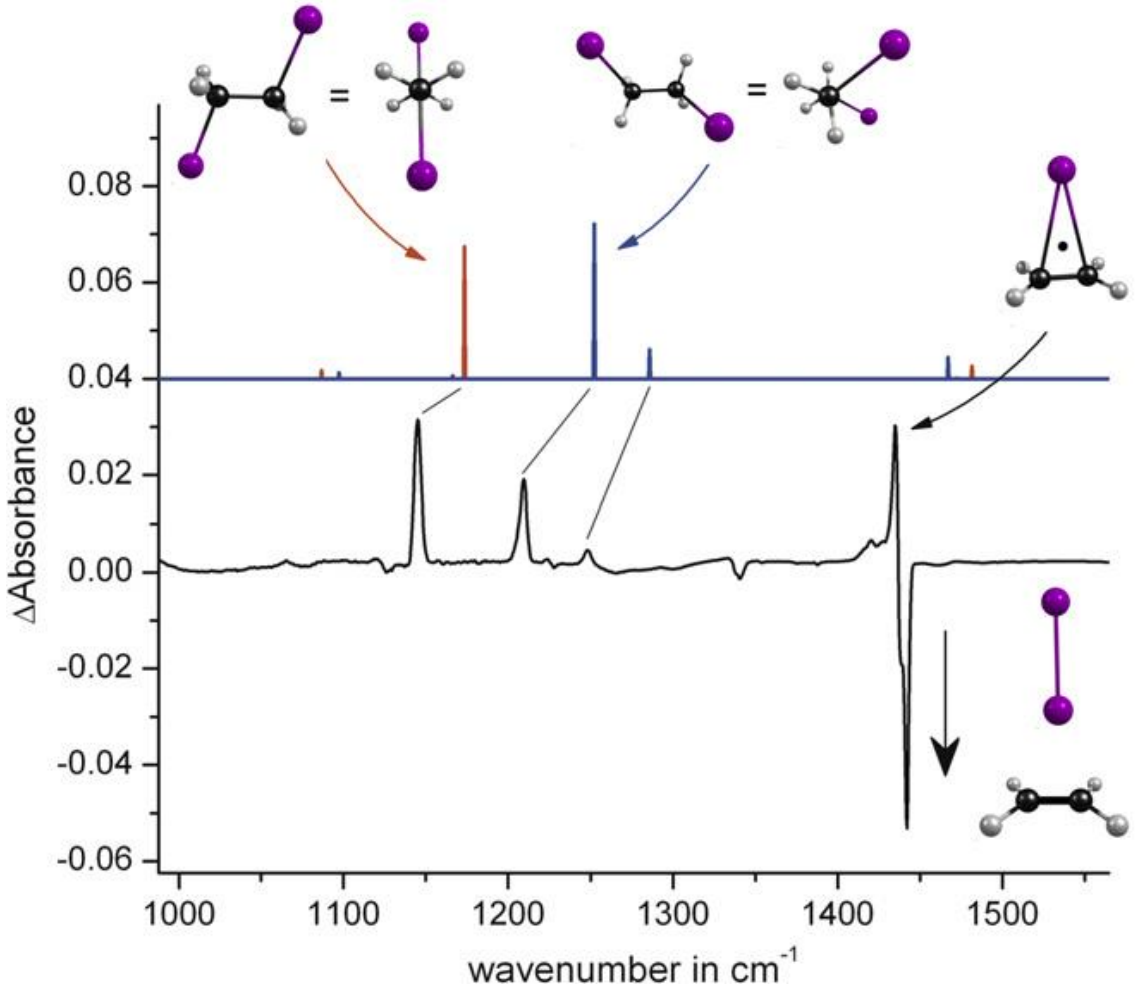


Figure 8.3: Difference infrared spectrum after photolysis of Ethylene-I_2 complex with 240 nm laser light. In comparison spectra of photoproducts calculated at the M06-2X-aug-cc-pVTZ-PP level.

8.3.3 Photochemistry of $C_2H_4\cdots I\bullet$ complex

To probe the spectroscopy of the $C_2H_4\cdots I\bullet$ complex, a second irradiation was performed at 355 nm, following a first irradiation at 240 nm. Upon 355 nm irradiation, the 366 nm band of the $C_2H_4\cdots I\bullet$ complex diminished, with a concomitant increase in bands of the $C_2H_4\cdots I_2$ complex (Figure 8.4). In this way the IR bands of the radical complex were determined, and these are compared in Table 8-2 with theoretical predictions. Previously, IR bands at 3099.1, 1440.0, and 948.6 cm^{-1} were assigned to the $C_2H_4\cdots I\bullet$ complex in studies of the photolysis products of ethyl iodide in a *p*-H_2 matrix.[235] Barbara and co-workers have examined the dynamics following CT excitation in arene-halogen atom complexes in various solvents using ultrafast transient absorbance spectroscopy over a range of probe wavelengths. Typically, the observed BET kinetics exhibited multiexponential behavior, with a fast component (ca. 1 ps), a slow component (ca. 0.2–1 ns), and intermediate components. The multiexponential behavior was attributed to a distribution of $arene^+/Br^-$ geometries in the initial ion pair state, which was presumed to involve specific, geometry dependent electronic interactions between donor and acceptor. This was further supported by the observation that the early time dynamics was not sensitive to solvent polarity.

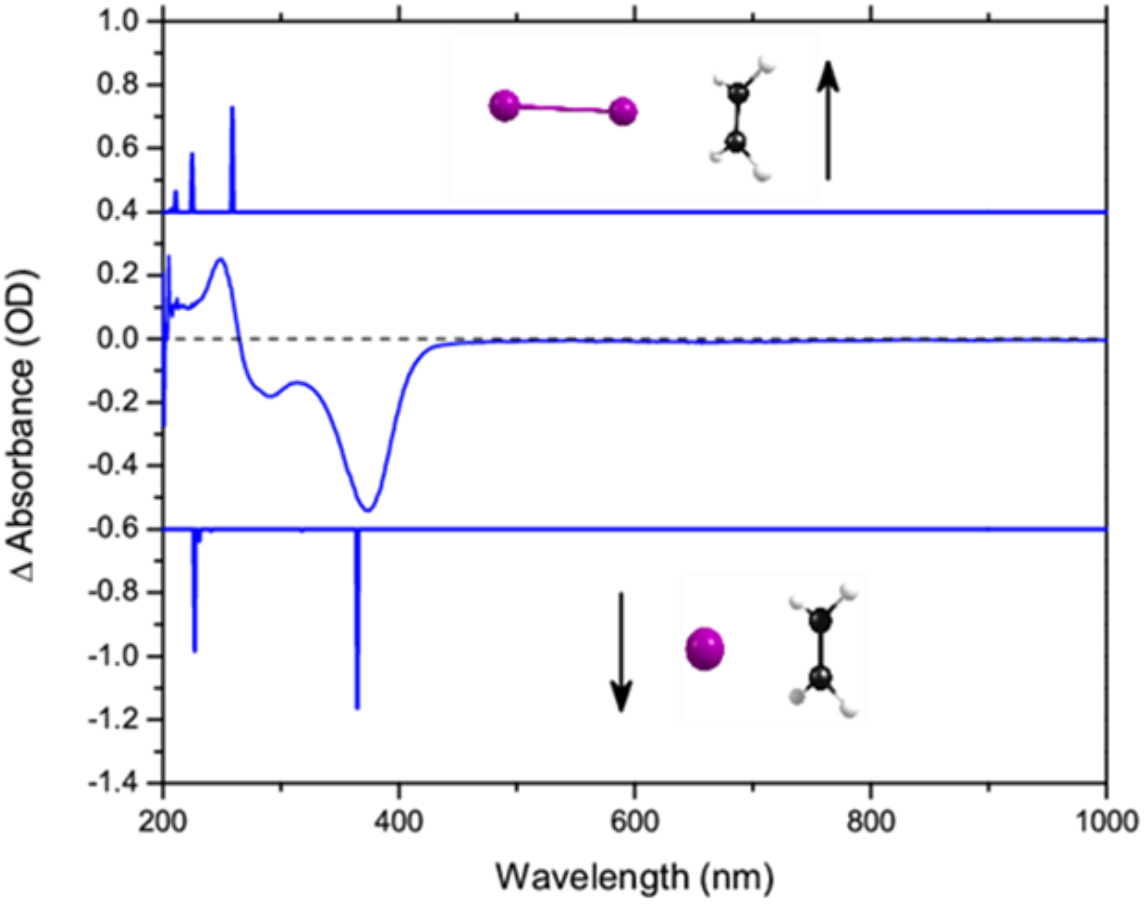


Figure 8.4 UV-Vis spectrum obtained after irradiation of $C_2H_4\cdots I$ complex with 355 nm laser light. In comparison with calculated spectra of $C_2H_4\cdots I_2$ and $C_2H_4\cdots I$.

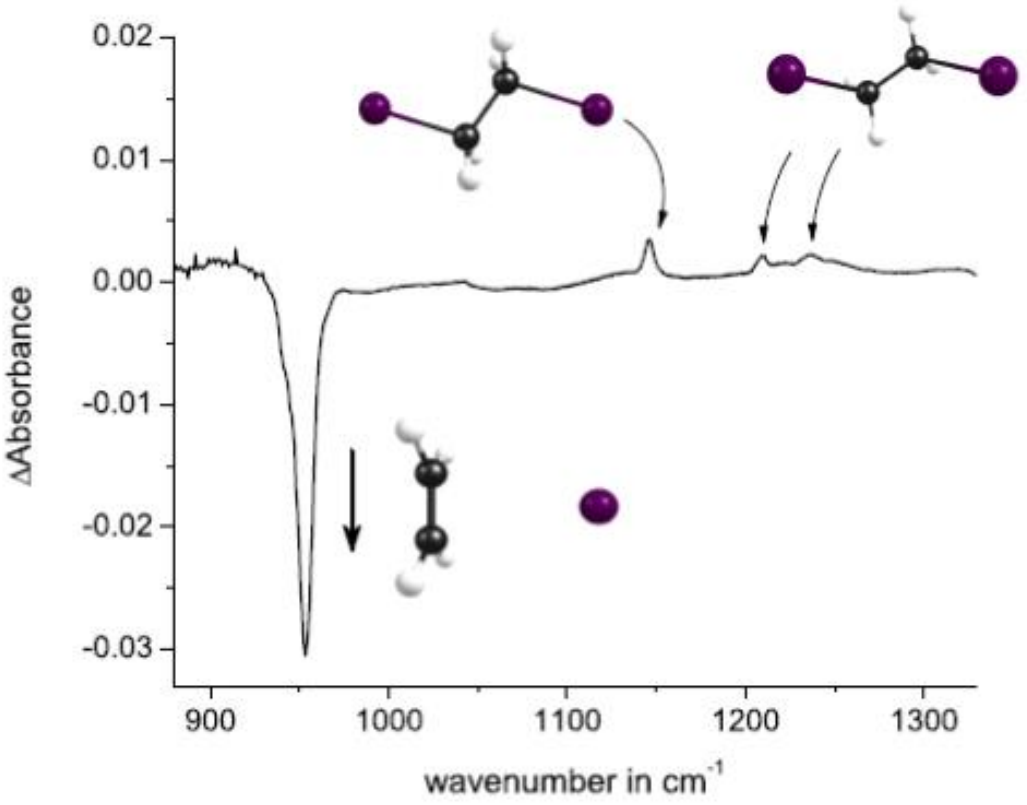


Figure 8.5 Difference IR spectrum obtained following 355 nm irradiation of an ethylene:I_2:Ne (~1:2:500) matrix that was pre-irradiated at 240 nm

As shown in Figure 8.4, a band at 1145 cm^{-1} also appeared after the 355 nm photolysis, assigned as before to *anti*–1,2-diiodoethane.[229] In addition, new IR bands were also observed at 1210 and 1237 cm^{-1}, in good agreement with the calculated positions of the strongest IR bands of *gauche*–1,2-diiodoethane (1204, 1246 cm^{1}). Following electron transfer, the $C_2H_4^{+\bullet}\cdots I^-$ intermediate can decay via back electron transfer (BET) to ethylene and a secondary iodine atom, which can recombine with the primary atom to form I_2. Alternatively, a sequential radical addition to ethylene can yield *anti*– and *gauche*–1,2-diiodoethane. The observation of both conformers of the final photoproduct confirms that the reaction proceeds by radical addition, rather than through an iodonium ion intermediate.

Note that attempts were also made to probe the spectroscopy of the $C_2H_4\cdots I\bullet$ complex in the vicinity of the I atom spin-orbit transition, which lies in the near-IR region.[236] Although overtone and combination bands associated with the ethylene moiety were observed, we did not observe any signals in the region of the iodine atom spin-orbit transition that were above the noise level of our instrument. This failure is likely due to the relatively small yield of the radical products in these steady state experiments.

The minimum energy structures and binding energies of the $C_2H_4\cdots I_2$ and $C_2H_4\cdots I\bullet$ complexes were calculated using the M06 method with a Sadlej-pVTZ basis set, and corrected for zero point energy. The predicted binding energy is 16.5 kJ/mol for the $C_2H_4\cdots I_2$ complex, and 29.3 kJ/mol for the bridged $C_2H_4\cdots I\bullet$ complex. The optimized geometries of the complexes are shown, and selected structural parameters given, in Figure 8.8.

Finally, it is instructive to compare the CT photochemistry of $C_2H_4\cdots I_2$ with our previous study of the $C_2H_4\cdots Br_2$ complex. For the latter, CT excitation leads to only one product, *anti*– 1,2-dibromoethane, which is explained by a single electron transfer mechanism proceeding via a bridged bromonium ion intermediate. For this ion to form, the breakup of the $Br_2^{-\bullet}$ anion radical generated following CT must be sufficiently fast to compete with BET. Such is not the case for the I_2 complex, where the lower reactivity of $I_2^{-\bullet}$ favors BET.[237] This work illustrates that, following CT excitation, the competition between BET and fragmentation of the radical anion is important in controlling the subsequent chemistry.

Table 8-2: Observed and calculated vibrational frequencies of species relevant to this work.

Species	Calc. Freq. (cm^{-1}) and Intensity (km/mol)	Obs. Freq. (cm^{-1}) in Ne	Obs. intensity	Obs. Freq. (cm^{-1}) in Ar matrix [(a)]	Obs. Freq. (cm^{-1}) in N_2 matrix[(a)]
C_2H_4	797 (0)	⋯	⋯	⋯	⋯
	964 (85)	953	1.00	⋯	⋯
	984 (0)	⋯	⋯	⋯	⋯
	1025 (0)	⋯	⋯	⋯	⋯
	1184 (0)	⋯	⋯	⋯	⋯
	1327 90)	⋯	⋯	⋯	⋯
	1366 (12)	1442	0.09	⋯	⋯
	1687 (0)	⋯	⋯	⋯	⋯
	3081 (23)	2985	0.15	⋯	⋯
	3107 (0)	⋯	⋯	⋯	⋯
	3177 (0)	⋯	⋯	⋯	⋯
	3207 (23)	3101	0.24	⋯	⋯
$C_2H_4\cdots I_2$ complex	53 (0.2)	⋯	⋯	⋯	⋯
	55 (0.2)	⋯	⋯	⋯	⋯
	86 (9)	⋯	⋯	⋯	⋯
	99(0.2)	⋯	⋯	⋯	⋯
	208 (9)	⋯	⋯	⋯	⋯
	225 (0.4)	⋯	⋯	⋯	⋯
	798 (0)	⋯	⋯	⋯	⋯
	977 (148)	953	1.00	949	948
	982 (0)	⋯	⋯	⋯	⋯
	1028 (0)	⋯	⋯	⋯	⋯
	1181 (0)	⋯	⋯	⋯	⋯
	1323 (4)	1342	0.03	1337	⋯
	1367 (12)	1442	0.14	1438	1439
	1665 (25)	1613	0.04	1621	1616
	3088 (9)	2985	0.21	2981	2989
	3110 (2)	⋯	⋯	⋯	⋯
	3186 (0)	⋯	⋯	⋯	⋯
	3216 (8)	3102	0.29	3097	3108
$C_2H_4\cdots I$ complex	83 (0)	⋯	⋯	⋯	⋯
	121 (2.9)	⋯	⋯	⋯	⋯
	225 (0.3)	⋯	⋯	⋯	⋯
	798 (0)	⋯	⋯	⋯	⋯
	976 (101)	953	1.00	⋯	⋯
	981 (0)	⋯	⋯	⋯	⋯
	982 (0.1)	⋯	⋯	⋯	⋯
	1318 (7.6)	1335	0.03	⋯	⋯
	1363 (14)	1438	0.21	⋯	⋯
	1639 (52)	1604	0.15	⋯	⋯
	3093 (5)	2983	0.06	⋯	⋯
	3112 (8)	⋯	⋯	⋯	⋯
	3191 (0)	⋯	⋯	⋯	⋯
	3222 (4)	3100	0.13	⋯	⋯

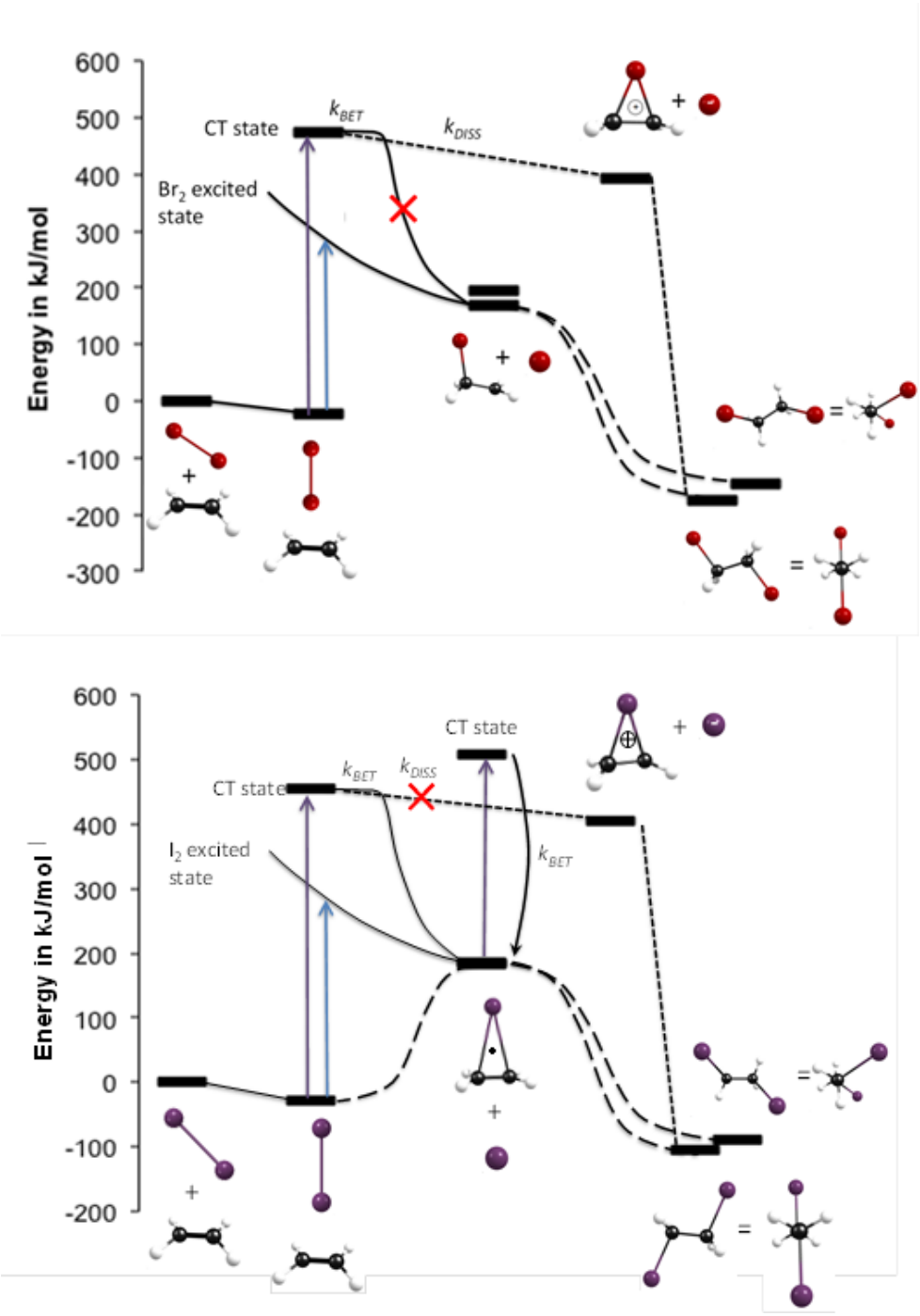


Figure 8.6 Photoinitiated the reaction mechanisms of (a) Br_2 and (b) I_2 with ethylene.

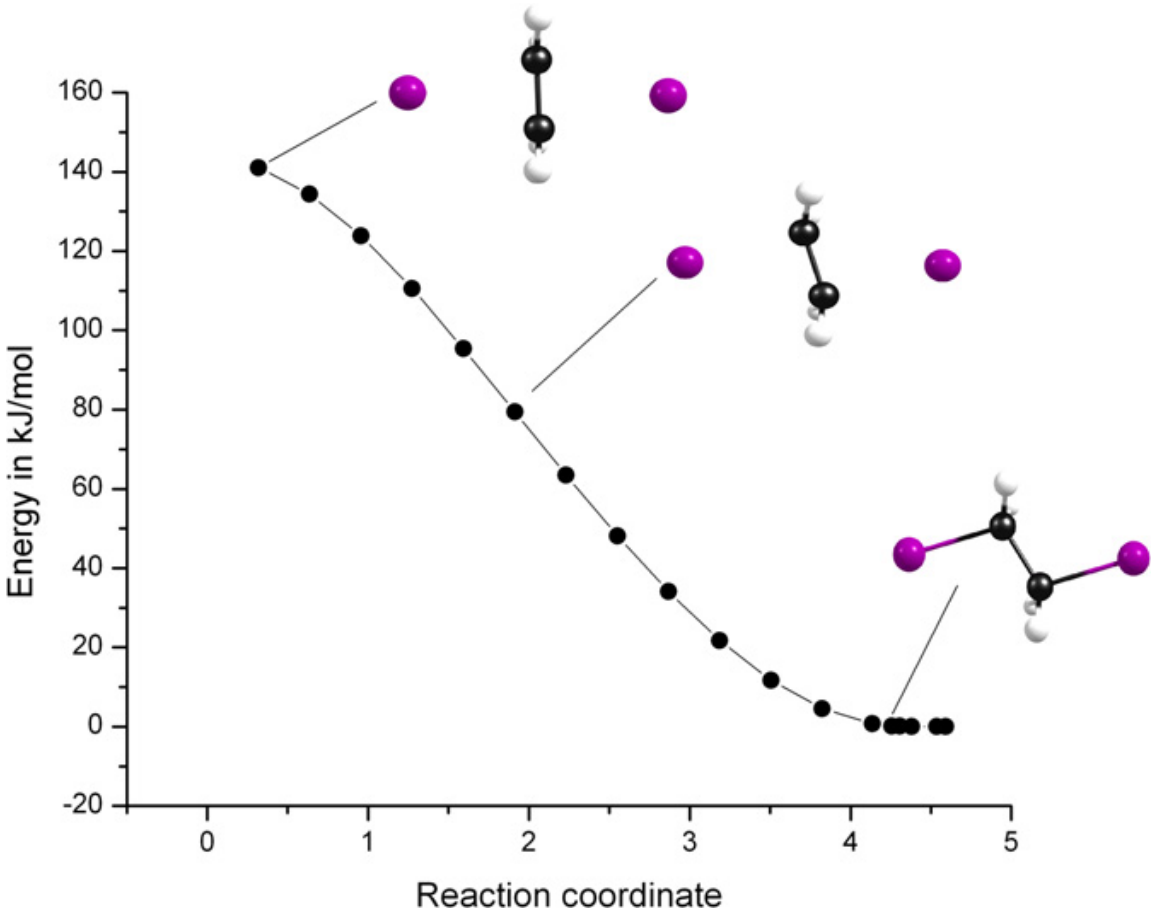


Figure 8.7 Intrinsic reaction coordinate scan from symmetric bridged transition state, illustrating concerted stereospecific addition.

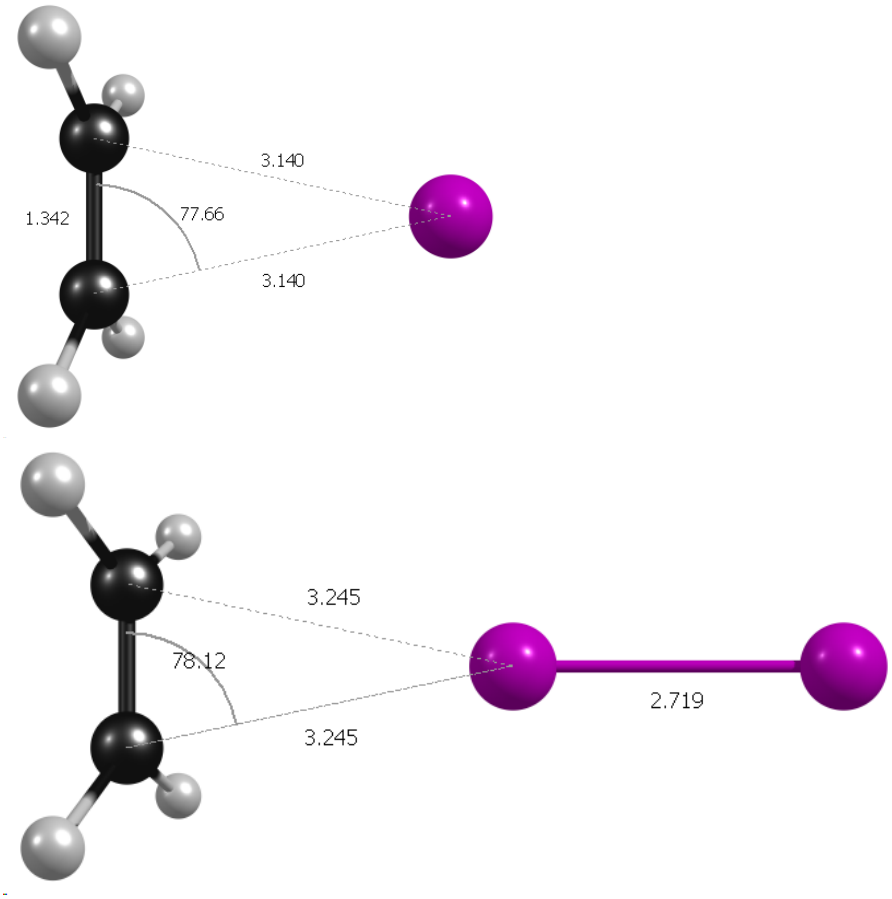


Figure 8.8 Selected geometrical parameters of the optimized structures of the ethylene complexes with atomic and molecular iodine, calculated at the M06/aug-cc-pVTZ-pp level.

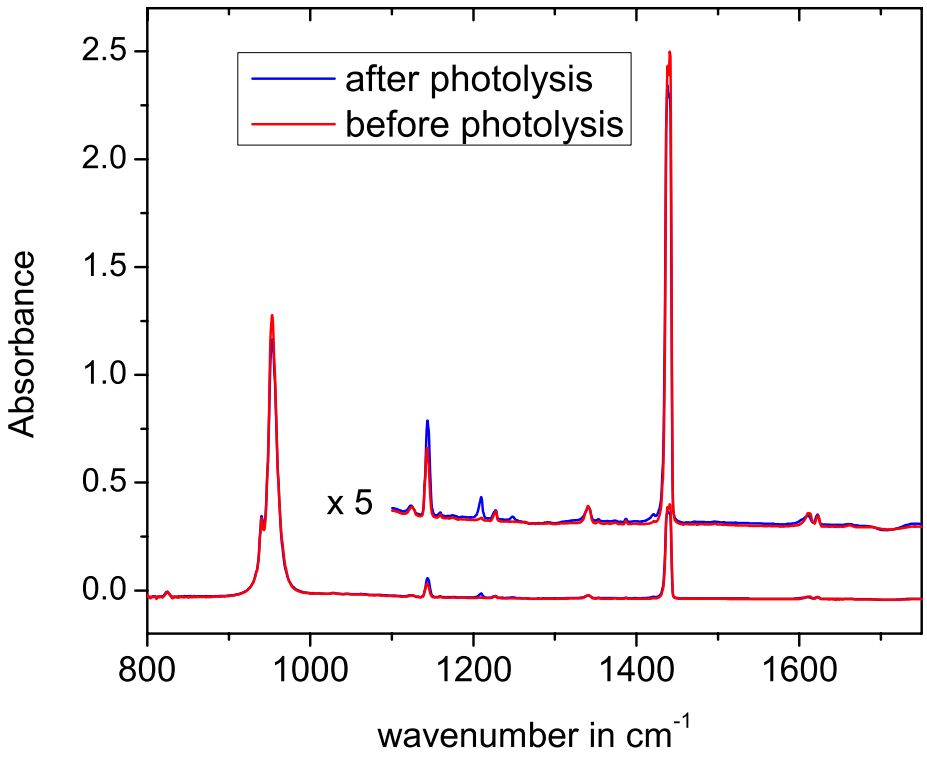


Figure 8.9 IR spectra obtained before and after photolysis of the $C_2H_4\cdots I_2$ complex

Chapter 9. FORMATION AND CHARACTERIZATION OF BROMINE ATOM COMPLEXES: Br···$BrXCH_2$ (X= H, Cl, Br)

In addition to the role of halogen atoms in the troposphere, it has been suggested that halogen atom reactions in both gas- and condensed-phase environments will typically involve weakly bound pre-reactive donor-acceptor complexes with the halogen atom as donor it has been shown that the presence of these complexes can affect both rate and selectivity of reaction. This type of interaction has been studied theoretically and experimentally by different groups.[238-240]

In 1996, McKee and co-workers performed a theoretical study on a series of adducts between chlorine atom and NH_3, NMe_3, NCl_3, $HN=CH_2$ and pyridine.[241] The calculations predicted a two-center three-electron bond for all chlorine adducts, favored by the high electron affinity of the radical. The formation of a 2c-3e was also favored by the low ionization energy of nitrogen bases. In case of methyl radical, no such interaction was predicted due to the very low electron affinity of CH_3.

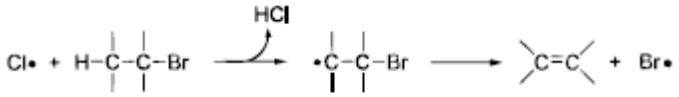
Experimentally, the halogen tom complexes have been studied in both gas phase, based on infrared spectroscopy and in condensed phases, where the intense charge transfer band was studied using UV-Visible spectroscopy.

Early studies were focused on small complexes such as Cl···HCl studied by Wittig and co-workers in 1999.[242] In their experiments they used infrared-ultraviolet double resonance to remove H atom from a tagged HCl···HCl dimer.

Later on, Bondybey and co-workers recorded the infrared spectrum of a similar complex H···HBr, produced by photolyzing $(HBr)_n$ (n=2, 3) in solid Ne [243] and more

recently, in 2006, the X···HF (X=Cl, Br and I) complex was observed by Miller and co-workers in helium nanodroplets.[244]

In 1998, Dneprovskii and co-workers[245] studied the chlorination of alkanes in various solvents, and they found that chlorine atom was complexing with halogenated solvents resulting in an enhanced selectivity explained by a β-Hydrogen abstraction from solvent as shown in the following equation:



They showed that the olefin-halogen complex is much more selective than the free halogen radical.

9.1 Experimental methods

The method employed in these experiments combines pulsed-jet high voltage discharge source with matrix isolation technique it can be used to study a variety of transient species (radicals, carbocations and carbanions). The experimental setup was described, in detail, in chapter 2.

9.2 Results and Discussion

9.2.1 Spectroscopy and Structure of Br atom complexes

Figure 9.1 shows infrared spectra of matrix isolated CH_3Br/Ar 1:220 mixture without discharge (black, lower trace) and with discharge (red, upper trace). Without discharge, the parent molecules shows bands at 1300.1 and 1434.7 cm^{-1} corresponding to

the well-known bands at 1305.9 and 1442.7 in gas phase.[246] In the spectrum recorded after deposition with discharge, one can see new peaks appearing next to the parent's bands at lower wavenumber (1295 and 1426 cm^{-1}). These bands are assigned to the $Br\cdots BrCH_3$ complex. This complex forms in good yield when deposition occurs at an elevated surface temperature (23 K for Ar and 9 K for Ne)

Figure 9.2 shows the full IR range difference spectrum of the discharged versus the undischarged sample, in comparison with the predicted spectrum calculated at the B3LYP/aug-cc-pVTZ level of theory, where a good agreement can be observed not only in frequency shift but also in relative intensities. The full set of vibrational frequencies (in cm^{-1}) calculated at the B3LYP, M06 and MP2 levels are given in Table 9-1, along with the experimentally determined frequencies in Ar and Ne matrices. In our calculations, the ^{79}Br - ^{81}Br isotope splittings were found to be uniformly small and could not be resolved in our experiments.

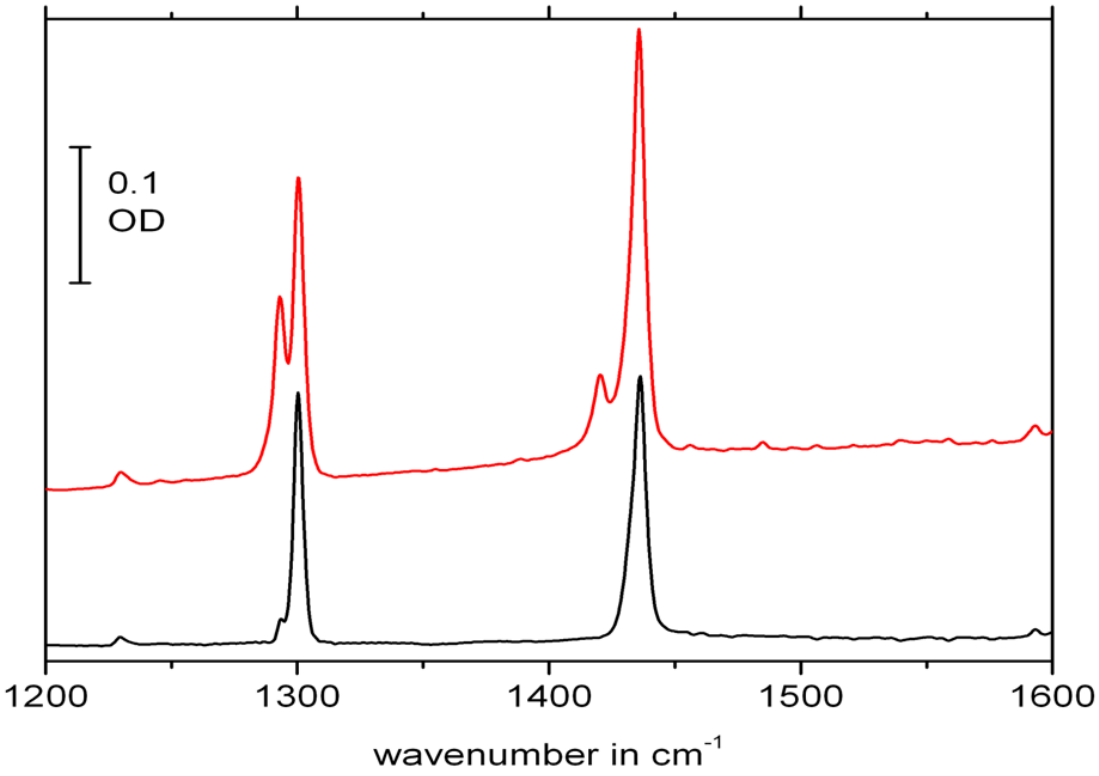


Figure 9.1: Infrared spectrum of a CH_3Br/Ar (1:220) matrix following pulsed deposition on a KBr window at 23 K and subsequent cooling to 5 K, with (red, upper) and without (black, lower) discharge.

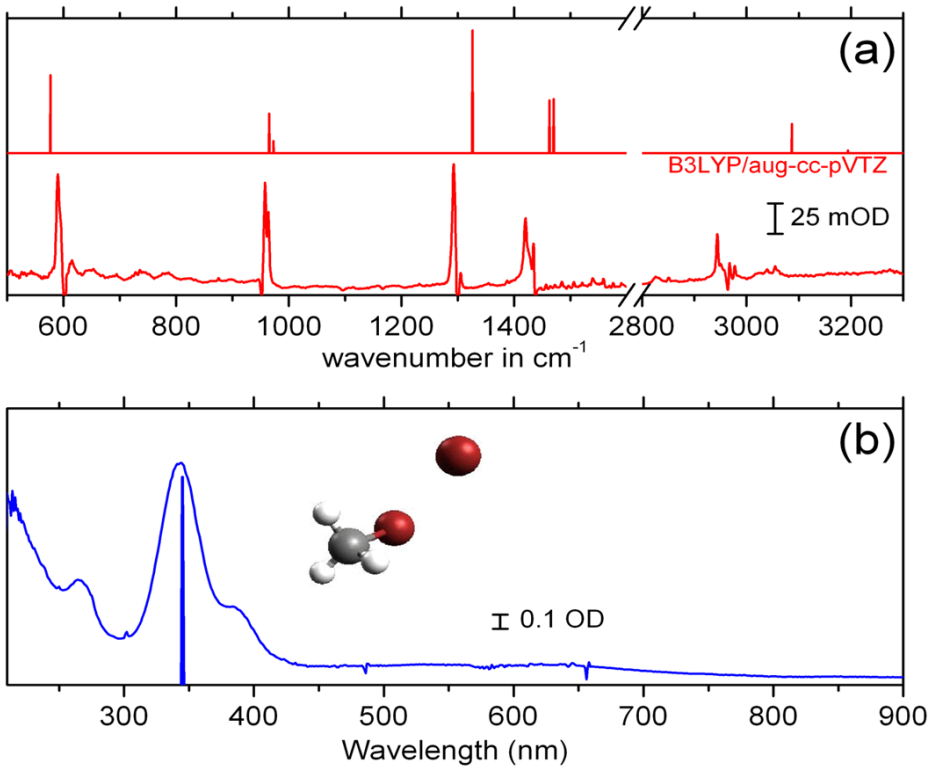


Figure 9.2: (a) The difference spectrum of the scans shown in Figure 6.1, compared with the predicted IR spectrum of the Br•••$BrCH_3$ complex. **(b)** the corresponding UV-Visible spectrum of the complex, with the predicted spectrum at the TD-CAM-B3LYP/aug-cc-pVTZ level.

Br···$BrCH_2X$ complexes were optimized at different levels, and the pertinent geometrical parameters are shown in Table 9-2, the Br-Br bond of about ~ 3 Å long and a strongly bent C-Br-Br angle (~90°) were the typical characteristics of these complexes. This structure can be understood from a consideration of the charge density surrounding the Br atom in CH_2BrX. In their study, Politzer and co-workers [247] have shown that in CH_3Br molecule, the Br atom has a belt of negative electrostatic potential surrounding a small positively charged region centered on the C-Br axis referred to as the σ hole. This reflects the extent of sp hybridization of unshared valence electrons on the Br atom in CH_3Br. In formation of the complex, the electrophilic Br atom (acceptor) is attracted to this negatively charged belt, and thus, the geometry features a C-Br-Br angle of ~ 90°.

In the UV region, "bromine atom···halon" complexes have a characteristic feature corresponding to the strong CT band at 342 nm, as shown in Figure 9.2. This band is in good agreement with TD-DFT predictions at B3LYP, CAM-B3LYP, M06 and M06-2X levels with aug-cc-pVTZ basis (Table 9-3). Assuming that the IR and UV-Visible spectra sample the same region in the matrix, the integrated IR and UV absorbance can be combined with calculated IR intensities to estimate the oscillator strength of the charge transfer band. The oscillator strength derived from our experiment was about ~0.2 and it was consistent with the TD-DFT predictions as shown in Table 9-3.

Following these experiments, the study was extended to other halons such as CH_2Br_2 and CH_2BrCl. The positions of observed IR absorptions of the Br···$BrCH_2Cl$ and Br···$BrCH_2Br$ complexes in Ar and Ne are shown in Table 9-1, and a good agreement was observed in comparison with theoretical predictions. Formation of Br···$BrCH_2Br$ complex was straightforward and much similar to the formation of

Br···$BrCH_3$, however the discharge of $BrCH_2Cl$ was a bit more complicated, due to the presence of two different halogen atoms: Br and Cl. Theoretically, the energy provided by the high-voltage discharge is enough to break either C-Br or C-Cl bond. Four different isomers have been optimized, Br···$BrCH_2Cl$, Br···$ClCH_2Br$, Cl···$BrCH_2Cl$ and Cl···$ClCH_2Br$ and they could all contribute to the IR spectrum since the observed transitions are associated with the CH_2BrCl chromophore. On one side, calculations of binding energies show that the stabilization energy of the Br···$BrCH_2Cl$ complex is about twice that Br···$ClCH_2Br$ and therefore Br···$BrCH_2Cl$ is the global minimum-energy structure. On the other side, formation of the other two complexes relies on C-Cl bond breaking in the discharge. In the IR spectrum, transitions due to the CH_2Br and CH_2Cl can be identified in as-deposited matrix, and using the experimentally measured IR intensities and calculated (B3LYP/aug-cc-pVTZ) intensities, the ratio of column densities for these two radicals is $N(CH_2Br) / N(CH_2Cl) \approx 1:3$. Thus a minor contribution from Cl···$BrCH_2Cl$ complex and, to a lesser degree Cl···$ClCH_2Br$ complex is expected. As mentioned before, these complexes have similar IR and UV/visible spectra, and they couldn't be distinguished in our experiments, where for instance, the Br···$BrCH_2Cl$ and Cl···$BrCH_2Cl$ IR spectra are predicted to be similar to within $2cm^{-1}$.

Table 9-1 Calculated and Observed Vibrational Frequencies, Intensities of the Br···$BrCH_2X$ (X=H,Cl,Br)

Species	**Mode**	**Approximate Description**	**Calculated (aug-cc-pVTZ basis) B3LYP**	**MP2**	**M06**	**Observed Ne (*Ar*)**
Br···$BrCH_3$	ω_1	CH_3 torsion	54 (0.0)	85 (0.0)	105 (1.8)	…
	ω_2	C-Br-Br bend	77 (2.4)	98 (0.1)	110 (6.6)	…
	ω_3	Br-Br stretch	115 (4.0)	107 (19)	144 (0.1)	…
	ω_4	C-Br stretch	575 (14)	641 (11)	618 (10)	588 (*590*)
	ω_5	CH_3 rock	965 (7.0)	992 (4.6)	952 (4.8)	952 (*954*)
	ω_6	CH_3 rock	973 (2.2)	996 (2.3)	958 (2.3)	952 (*958*)
	ω_7	CH_3 sym. def.	1326 (22)	1354 (19)	1312 (17)	1284 (*1295*)
	ω_8	CH_3 a. def.	1463 (9.3)	1489 (9.4)	1433 (10)	…
	ω_9	CH_3 a. def.	1470 (9.6)	1493 (7.6)	1440 (8.9)	1427 (*1426*)
	ω_{10}	CH_3 a. stretch	3087 (5.2)	3118 (7.5)	3070 (8.2)	2969 (*2962*)
	ω_{11}	CH_3 sym. str.	3194 (0.5)	3240 (0.5)	3188 (0.2)	…
	ω_{12}	CH_3 sym. str.	3204 (0.0)	3244 (0.1)	3191 (0.2)	…
Br···$BrCH_2Cl$	ω_1	CH_2 torsion	31 (6.3)	44 (5.8)	64 (1.2)	…
	ω_2	C-Br-Br bend	45 (1.2)	61 (1.1)	79 (4.9)	…
	ω_3	Br-Br stretch	107 (2.9)	92 (12)	103 (4.1)	…
	ω_4	C-Br-Cl scis.	218 (0.3)	233 (1.0)	224 (0.2)	…
	ω_5	C-Br str.	571 (56)	635 (25)	606 (35)	600 (*599*)
	ω_6	C-Cl str.	726 (110)	784 (106)	753 (119)	752 (*744*)
	ω_7	CH_2 rock	861 (1.9)	881 (2.1)	856 (1.8)	…
	ω_8	CH_2 twist	1133 (0.3)	1163 (0.3)	1134 (0.4)	…
	ω_9	CH_2 wag	1243 (70)	1263 (63)	1222 (70)	1227 (*1230*)
	ω_{10}	CH_3 scis.	1444 (1.2)	1467 (1.3)	1412 (0.4)	…
	ω_{11}	CH_2 sym. str.	3139 (0.6)	3160 (0.5)	3111 (1.2)	…
	ω_{12}	CH_2 asym. str.	3227 (4.3)	3249 (4.9)	3192 (1.6)	3054 (*3046*)
Br···$BrCH_2Br$	ω_1	CH_2 torsion	21 (5.1)	40.9 (4.7)	46 (4.3)	…
	ω_2	C-Br-Br bend	38 (1.0)	53 (0.9)	70 (3.9)	…
	ω_3	Br-Br stretch	102 (2.6)	91 (12)	100 (3.7)	…
	ω_4	C-Br-Br scis.	168 (0.3)	180 (1.9)	171 (0.5)	…
	ω_5	C-Br asym. str.	564 (17)	611 (3.2)	592 (5.4)	583 (*582*)
	ω_6	C-Br sym. str.	616 (100)	697 (86)	666 (82)	650 (*644*)
	ω_7	CH_2 rock	821 (3.2)	843 (3.6)	801 (3.3)	…
	ω_8	CH_2 twist	1103 (0.3)	1135 (0.3)	1083 (0.3)	…

	ω_9	CH_2 wag	1211 (84)	1232 (77)	1182 (75)	1194 (*1194*)
	ω_{10}	CH_3 scis.	1431 (1.9)	1453 (1.8)	1398 (2.1)	…
	ω_{11}	CH_2 sym. str.	3143 (0.3)	3165 (0.3)	3109 (0.3)	…
	ω_{12}	CH_2 asym. str.	3234 (6.4)	3255 (7.0)	3191 (3.4)	3052

Table 9-2 Optimized geometrical parameters of the Br···$BrCH_2X$ (X=H,Cl,Br) complexes. Bond lengths are in Å and angles in degrees.

Species	Method (aug-cc-pVTZ)	C-H	C-X	C-Br_1	Br_1-Br_2	H-C-Br_1	X-C-Br_1	C-Br_1-Br_2	X-C-Br_1-Br_2	H-C-Br_1-Br_2
Br···$BrCH_3$	**MP2**	1.083	1.083	1.928	2.896	107.4	107.4	86.8	180.0	59.7
	B3LYP	1.082	1.084	1.962	2.974	106.9	106.7	92.5	180.0	59.9
	M06	1.084	1.084	1.936	3.009	107.4	107.6	87.5	180.0	59.8
Br···$BrCH_2Cl$	**MP2**	1.082	1.758	1.930	2.926	106.6	111.9	82.9	180.0	60.0
	B3LYP	1.080	1.769	1.969	2.985	106.0	112.1	87.8	180.0	60.2
	M06	1.083	1.758	1.943	3.022	106.6	111.8	84.1	180.0	59.7
Br···$BrCH_2Br$	**MP2**	1.082	1.909	1.925	2.921	107.0	112.4	83.1	180.0	60.2
	B3LYP	1.080	1.935	1.960	2.986	106.6	112.5	88.8	180.0	60.5
	M06	1.083	1.916	1.935	3.022	107.1	112.1	84.8	180.0	60.0

Table 9-3 Observed (Ne matrix) and predicted electronic absorptions (in nm) and oscillator strengths (*f*) of the Br···$BrCH_2X$ (X=H,Cl,Br) complexes.

Species	**States**	**TD-B3LYP/ aug-cc-pVTZ**	**TD-CAM-B3LYP/ aug-cc-pVTZ**	**TD-M06 aug-cc-pVTZ**	**TD-M06-2X/ aug-cc-pVTZ**	**Observed λ_{max} (osc. Strength)**
Br···$BrCH_3$	D_1	1575.0 (0.0001)	1625.8 (0.0001)	1530.6 (0.0001)	1828.2 (0.0001)	
	D_2	1433.1 (0.0001)	1507.8 (0.0001)	1403.0 (0.0001)	1671.3 (0.0001)	
	D_3	489.3 (0.0001)	406.2 (0.0001)	456.0 (0.0001)	368.6 (0.0001)	
	D_4	**344.8 (0.2546)**	**335.5 (0.2660)**	**350.2 (0.2345)**	**348.0 (0.2396)**	342 (0.2)
	D_5	252.2 (0.0007)	234.3 (0.0009)	252.0 (0.0005)	232.3 (0.0007)	
Br···$BrCH_2Cl$	D_1	1784.6 (0.0001)	1916.7 (0.0001)	1731.6 (0.0001)	2063.3 (0.0001)	
	D_2	1602.9 (0.0001)	1723.2 (0.0001)	1589.1 (0.0001)	1871.4 (0.0001)	
	D_3	519.0 (0.0001)	416.9 (0.0001)	478.4 (0.0001)	369.6 (0.0001)	
	D_4	392.7 (0.0866)	**346.2 (0.2479)**	**374.7 (0.1597)**	**343.2 (0.2181)**	333 (0.2)
	D_5	**346.7 (0.1599)**	277.8 (0.0055)	338.1 (0.0000)	256.5 (0.0022)	
	D_6	250.1 (0.0048)	262.8 (0.0000)	338.0 (0.0646)	240.5 (0.0000)	

Br···BrCH$_2$Br	D_1	1771.5 (0.0001)	1902.4 (0.0001)	1719.3 (0.0001)	2056.8 (0.0001)	
	D_2	1597.0 (0.0001)	1717.5 (0.0001)	1590.0 (0.0001)	1857.1 (0.0001)	
	D_3	519.1 (0.0001)	412.0 (0.0001)	474.3 (0.0001)	366.3 (0.0001)	
	D_4	460.1 (0.0481)	**356.6 (0.2370)**	414.3 (0.0792)	**353.1 (0.2172)**	351 (0.2)
	D_5	445.3 (0.0000)	300.6 (0.0246)	391.1 (0.0001)	280.7 (0.0103)	
	D_6	**355.6 (0.2025)**	299.6 (0.0000)	**353.4 (0.1509)**	276.7 (0.0000)	

The geometrical parameters of the optimized structures of these complexes are given in Table 9-2 and the NRT analysis yielded very similar results to those found for Br···CH_3Br complex. Table 9-3 shows comparison of experimentally derived and theoretical oscillator strengths of the charge transfer (CT) band of the complexes, and once again we can see a good agreement. However it's important to note that the CT band for the Br···$BrCH_2Br$ complex observed here in Ne matrix (λ_{max}=351nm) is significantly shifted from the position reported by Shoute and Neta in solution (390nm). [248-250] This finding is consistent with previous studies whereby Br atom complexes have shown much larger solvochromatic shifts in comparison with those found for molecular halogen complexes. This is well illustrated by the case of Br···C_6H_6 which shows a maximum absorption at ~ 469 nm in Ar matrix, significantly shifted from the position observed in solution (λ_{max}=535-560 nm, solvent dependent). [251-254] This difference in solvochromatic shift can be understood from the point of view of the formalism developed by Mulliken.[255-257] In this model, the wavefunction of a donor-acceptor complex D···A is described as a linear combination of zeroth-order wavefunctions corresponding to a "no-bond" configuration (ψ_0), representing the separated constituents, and a "dative" (ψ_1) configuration corresponding to the $D^{+\bullet}\cdots A^{-\bullet}$ ion pair that follows electron transfer from the donor to the acceptor. The solution to the secular determinant gives the transition energy as follows [254, 258]:

$$E_{CT} = \frac{1}{1-S^2}\left[(I_D - C)^2 + 4\beta_0\beta_1\right]^{1/2} \qquad \text{Equation 9.1}$$

Where S represents the overlap integral of the no-bond and dative wavefunction and I_D is the ionization energy of the donor. The terms β_0 and β_1 represent resonance integrals which are related according to the expression:

$$\beta_1 = \beta_0 - S(I_D - C) \quad \text{Equation 9.2}$$

In equations 1 and 2, the term C is related to the electron affinity of the acceptor and also contains electrostatic terms related to the solvation energy of the ions and the ion pair electrostatic interaction. This can be expressed as[258]

$$C = E_A + \frac{e^2}{2}\left(1 - \frac{1}{\varepsilon}\right)\left(\frac{1}{r_{D^+}} + \frac{1}{r_A}\right) + \frac{e^2}{r_{AD}\varepsilon} \quad \text{Equation 9.3}$$

Where E_A is the electron affinity of the acceptor, ε is the dielectric constant of the medium, and the radii represent, respectively, the solvent cavities around the donor and the acceptor, and the donor-acceptor distance in the complex.

In modeling the solvent dependence of the CT excitation energy, we used values of S (=0.1) and β_0 (= -0.95 eV) that were previously determined for Br···arene complexes.[254] The molar volume of the donor was used to calculate the radius of a donor molecule, which was assumed to be the same for the cation radical. This radius added to that of bromine (1.14 Å)[259] provided an estimate for the radius of the complex (r_{DA}), while the radius of the anion acceptor was taken as the ionic radius of the bromide anion (1.96 Å).[259] Using these parameters together with the dielectric constant of solid Ne (ε=1.24)[260] and Ar (ε=1.67)[260] gives the E_{CT} of 4.07 (Ne) and 3.39 eV (Ar) for the Br···$BrCH_2Br$ complex, corresponding to excitation maxima of 302 (Ne) and 366 nm (Ar), in reasonable agreement with our experimental results of 351 (Ne) and 356 nm (Ar). When the dielectric constant is changed to that of cyclohexane

(ε=2.0), the CT band is predicted to appear at 400 nm, which is in good agreement with the position reported by Shoute and Neta in cyclohexane solution.[248, 250]

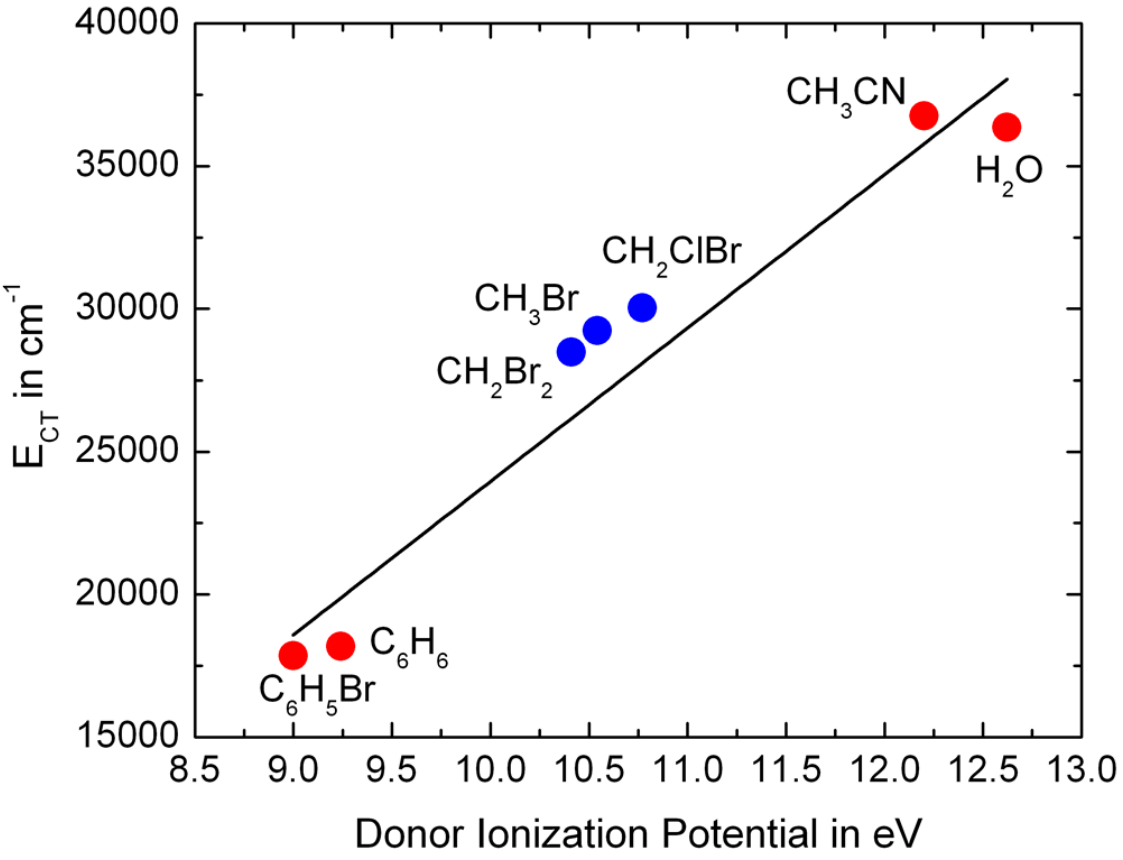


Figure 9.3: Mulliken plot of the CT band energy (in cm^{-1}) versus the donor ionization energy for a range of Br atom complexes with various donors, as described in the text.

Equations 9.1-9.3 show that for a given acceptor, the energy of the CT band should scale approximately linearly with the ionization energy of the donor, which is the Mulliken correlation. Figure 9.3 shows a plot of E_{CT} (in eV) versus the donor ionization energy (in eV) for a range of Br atom complexes with various donors, including those studied here and H_2O,[258] CH_3CN,[261] C_6H_6,[262] and C_6H_5Br.[263]

9.2.2 Binding Energy of Br atom complexes

As a routine step in our calculations, the binding energy was initially calculated at various levels of theory used for optimization (B3LYP, M06 and MP2) in combination with aug-cc-pVTZ basis set and corrected for zero-point energy. The predicted values, shown in Table 9-4, vary from 5.9 (UMP2) to 7.7 kcal/mol (M06) for Br···$BrCH_3$ complex, and similar results are obtained for other Br···$BrCH_2X$ complexes. As mentioned earlier, the predicted binding energy for Br···$ClCH_2Br$ complex is around ½ of this value, that is between 3 and 3.5 kcal/mol. The use of DFT methods to calculate the binding energy of halogen atom-molecule complex has been discussed at some length in the literature [264, 265], where Croft and Howard-Jones performed a systematic evaluation of DFT and ab-initio methods for predicting the binding energy of the prototypical chlorine atom-benzene complex. While many standard DFT methods lack long-range electron correlation and are therefore suspect for the calculation of binding energies of weakly bound complexes, [266] there are a number of recently developed functionals recommended for noncovalent interactions, including Truhlar's M06 family of functionals.[267] For the complexes examined here, M06 and B3LYP gave similar results, slightly higher than the UMP2 values.

Starting from the optimized structure at the M06/aug-cc-pVTZ level of theory, we carried out single point energy calculations using CCSD(T)/aug-cc-pVTZ method and the zero-point energy was taken from M06 results. The CCSD(T) results are in very close agreement with UMP2 values and consistently smaller than the DFT results. Table 9-4 compiles binding energy values, and globally it was predicted to be ~ 5 kcal/mol for all the complexes examined. The effect of basis set superposition error was evaluated using the counterpoise method [56], and it was found to be uniformly small, less than 0.5 kcal/mol.

Table 9-4 Predicted binding energies (in kcal/mol, including zero-point energy) of the Br···$BrCH_2X$ (X=H,Cl,Br) complexes.

Species	**B3LYP/ aug-cc-pVTZ**	**MP2/ aug-cc-pVTZ**	**M06/ aug-cc-pVTZ**	**CCSD(T)-aug-cc-pVTZ// M06/aug-cc-pVTZ**
Br···$BrCH_3$	6.9	5.9	7.7	5.3
Br···$BrCH_2Cl$	5.9	5.5	7.1	5.3
Br···$BrCH_2Br$	6.0	5.7	7.2	5.3

Table 9-5 Natural Bond Orders, Charges and Natural Spin Densities in Doublet $Br\cdots BrCH_3$.

Natural bond orders		**Natural charge and spin densities**		
Bond	**Natural bond order (total)**	**Atom**	**Natural charge**	**Natural spin density**
C1-Br2	1.0120	C	-0.53537	-0.01134
C1-H3	0.9946	Br	0.05182	0.12695
C1-H4	0.9946	H	0.20018	0.00107
C1-H5	0.9934	H	0.20018	0.00107
Br2-Br6	0.4970	H	0.19474	-0.00096
		Br	-0.11156	0.88320

9.2.3 Charge Transfer photochemistry of Br atom complexes

After deposition in solid matrix and characterization of Br atom complexes, the CT photochemistry was investigated by selective laser wavelength photolysis at 355 nm using the frequency tripled output of a Minilite-II Nd:YAG laser. Upon irradiation, and this for all complexes, the CT band decreased in intensity and the peaks assigned to the uncomplexed parent halon were observed appearing in IR and UV/visible spectra as shown in Figure 9.5 and Figure 9.4. These findings can be explained by the following scheme:

First, excitation into the CT band leads to rapid CT and formation of a Br^- $\cdots BrCH_2X^{+\bullet}$ ion pair.

$$\bullet Br \cdots BrCH_2X + h\vartheta_{CT} \rightarrow Br^- \cdots BrCH_2X^{+\bullet} \qquad \text{(Equation 9.4)}$$

In the matrix cage, the back electron transfer is expected to be rapid, leading to re-formation of a hot complex that will rapidly dissociate, with subsequent diffusion yielding a separated pair

$$Br^- \cdots BrCH_2X^{+\bullet} \xrightarrow{k_{BET}} [\bullet Br \cdots BrCH_2X]^* \rightarrow \bullet Br + BrCH_2X \qquad \text{(Equation 9.5)}$$

This scheme agrees with our observations, and it is consistent with ultrafast studies of the CT photochemistry of complexes between Br atom and various arenes.[268, 269] For instance, considering the $Br\cdots C_6H_6$ complex, it was found that $k_{BET} \gg k_{diffusion}$, and the recovery occurred much faster in neat benzene than in dilute solution, which was attributed to quenching by a 2:1 complex, which was presumed to undergo very rapid charge recombination. The measured k_{BET} for 1:1 $Br\cdots C_6H_6$ complex in dilute solution was 0.21 x 10^{10} s^{-1}, corresponding to a lifetime of ~ 500 ps.

Unfortunately our experiments probes steady-state concentration of photoproducts; however, ultrafast experiments on these complexes that probe directly the time scales for electron transfer would be highly desirable.

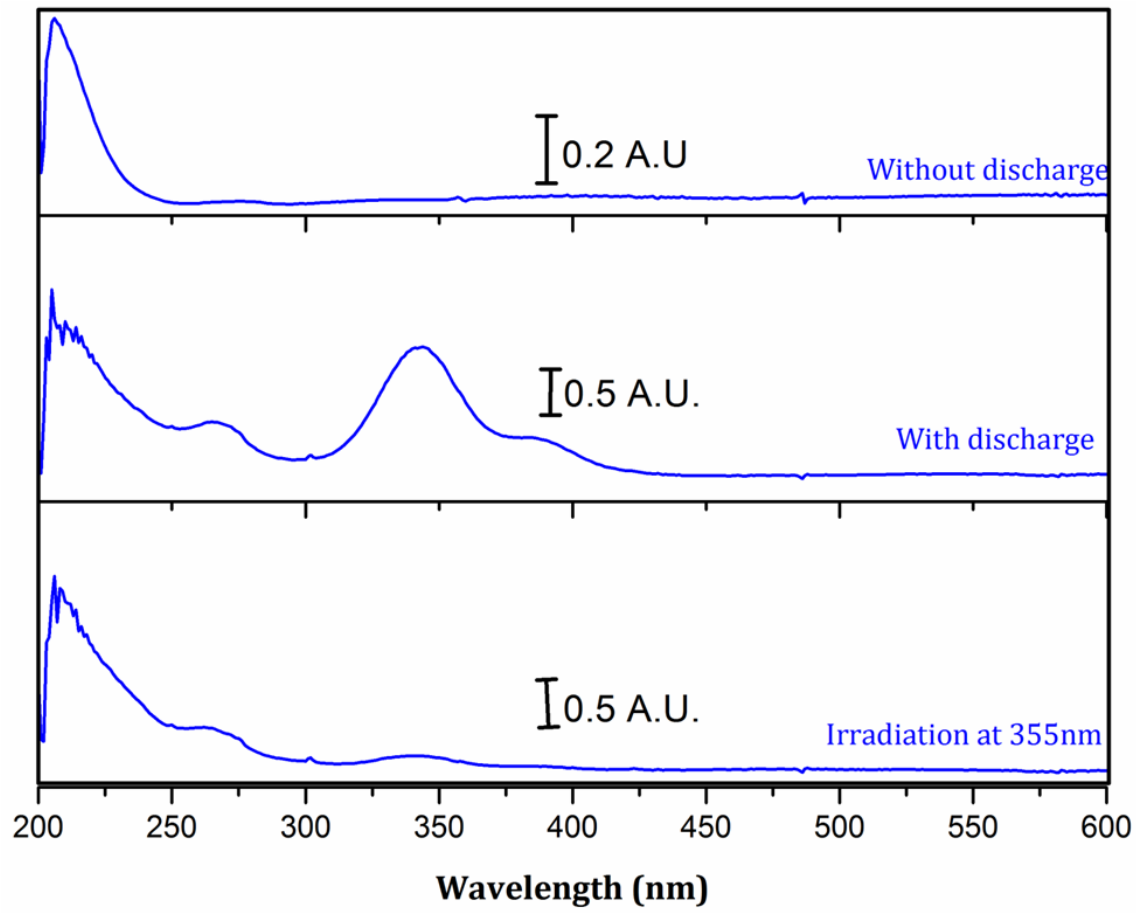


Figure 9.4: photochemistry of the CT of Br···$BrCH_2Br$ complex. **Upper panel:** UV-Vis spectrum of $BrCH_2Br$ in Ar without discharge. **Middle panel:** UV-Vis spectrum of $BrCH_2Br$ in Ar with discharge. **Lower panel:** UV-Vis spectrum after photolysis with 355 nm laser light.

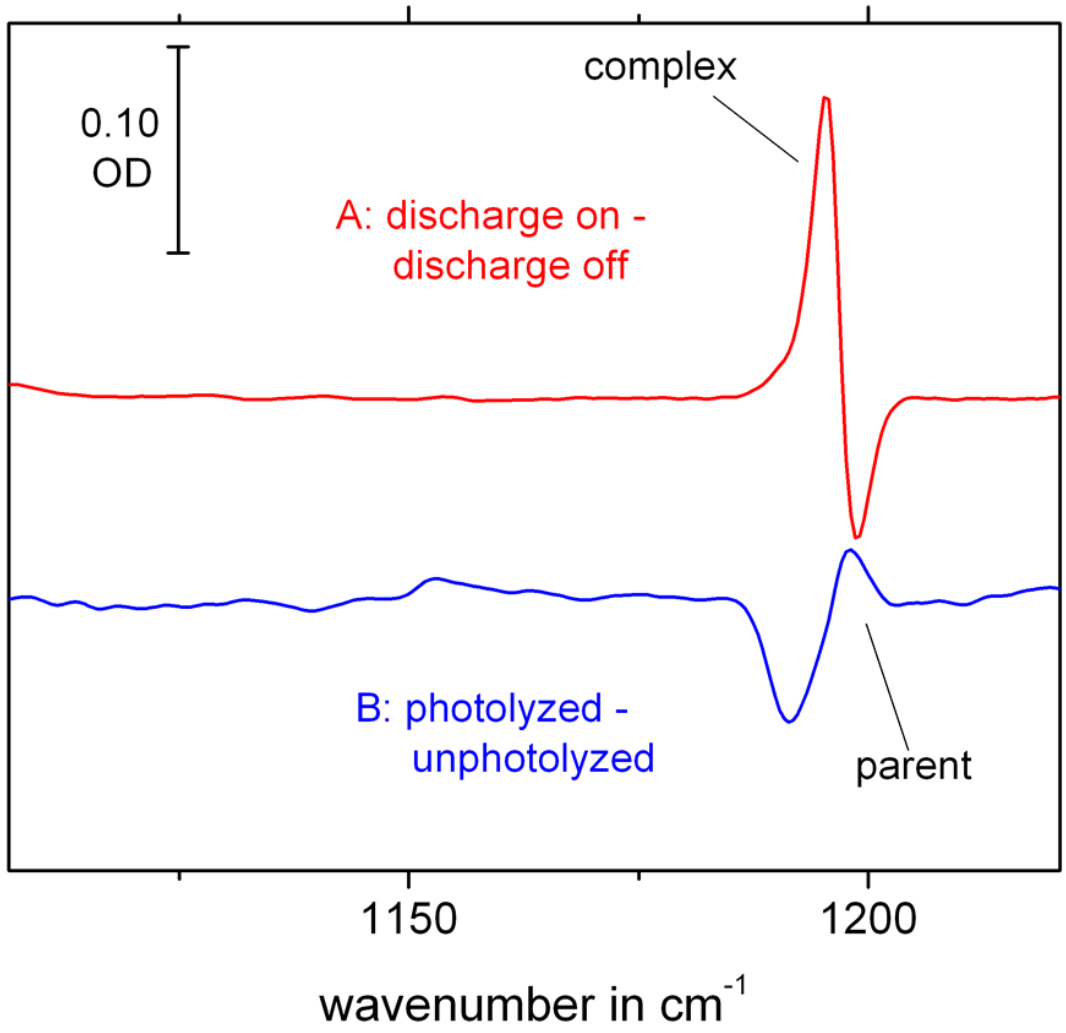


Figure 9.5: difference spectrum illustrating the formation and destruction of the Br•••$BrCH_3$ complex. **Upper trace:** the difference spectrum of discharge on and off is shown. The loss of the parent absorption near 1200cm^{-1} and growth of the complex band at slightly lower cm^{-1} is apparent. Upon photolysis of the complex at 355 nm (**blue, lower trace**), the complex bands decrease, and the parent band increases.

9.3 Summary

In this study, pulsed jet discharge matrix isolation spectroscopy and computational methods were utilized to characterize pre-reactive Br atom complexes with simple halons, CH_2BrX (X=H, Cl, Br). We have demonstrated a new method of producing these complexes, which combines matrix isolation techniques with a pulsed DC discharge nozzle, where a dilute CH_2BrX/Ar (Ne) sample mixture was gently discharged and deposited onto a cold KBr window. The resulting $Br\cdots CH_2BrX$ (X=H, Cl, Br) complexes were characterized by infrared and electronic spectroscopy, supported by ab-initio and DFT calculations. Our spectra are in good agreement with those calculations, predicting the binding energy to be ~ 5 kcal/mol, in gas-phase. The photochemistry of the complexes was investigated and following excitation into the CT band, the disappearance of the CT band was correlated with the growth of the bands assigned to the uncomplexed halon. This is explained by a rapid back electron transfer leading to the formation of a hot complex that subsequently dissociates. Finally, the CT band energies of these complexes were compared with those of Br atom complexes with other donors and with the predictions of Mulliken theory, a reasonable linear relationship (Mulliken correlation) was found on a broad range of donor ionization energies.

Chapter 10. PULSED-JET DISCHARGE MATRIX-ISOLATION AND COMPUTATIONAL STUDY OF CX_2Br^+ (X=H, F).

As we have shown in earlier chapters, due to their long-standing use as flame retardants and potential for ozone depletion, bromine-containing halocarbons (halons) have received extensive scrutiny [75, 160, 270-281] and more recently the interest was focused on the ionization and thermochemistry of these compounds.[282-287] Once again, in order to understand the chemistry of these halons; we use the approach of studying reactive intermediates generated from these halons. In this specific case, we are focusing our attention on carbocations formed from two bromine-containing halomethanes (CH_2Br_2 and CF_2Br_2).

There is significant recent interest in the study of halocarbocations, focusing on the effect of halogen substitution on their structure, stability and reactivity, and understanding these trends in terms of substituent σ and π-donor ability. In 1996, G. Olah and co-workers conducted study on various halomethyl cations (CX_3^+ , X=Cl, Br, I) using ^{13}C NMR and came up to conclusion that the degree of π-back-donation decreased in the order Cl > Br > I.[288] This conclusion contradicted earlier studies, done by Lampe and co-workers in gas-phase [289] and a computational study conducted by Venturini and co-workers [290], and subsequent studies have shown the increase in π-donor ability in the order F < Cl < Br < I.[291, 292] Grutzmacher and co-workers suggested that the importance of the doubly bonded resonance structure for the CX_2Y+ (i.e., X_2C^+-Y ↔ $X_2CY=Y^+$) will increase in the series Y = F < Cl < Br < I.

More recently, our laboratory had the privilege to observe the first gas-phase spectrum of halocarbocation, measuring fluorescence excitation and emission spectra of the triplet π-π* system of CH_2I^+ and its deuterated isotopomers using pulsed discharge source.[293, 294] The ground-state C-I stretching mode was observed at 755 cm^{-1}. The short bond length reflects the doubly bonded resonance structure of $H_2C{=}I^+$, as it has been shown by *ab* initio calculations. However no experimental evidence was observed for CH_2Br^+, predicted to be weak and lying in the visible range. The only spectroscopic information available, to the date we conducted this study, was coming from photoelectron experiments of the CH_2Br radical, which gave a C-Br stretching frequency of ~860 ± 30 cm^{-1}. Measurement of the vibrational spectrum, particularly the C-Br stretching frequency is highly desirable, as it can help to distinguish between two possible resonance structures (Figure 10.1).

In this study, we discuss and report the first measurement of the vibrational spectrum of CH_2Br^+, using pulsed-jet discharge matrix isolation spectroscopy. We also report the initial measurement of the corresponding frequency in the CF_2Br^+ cation, which provides an insight into the effect of halogen substitution on the structure and stability of this class of ions.

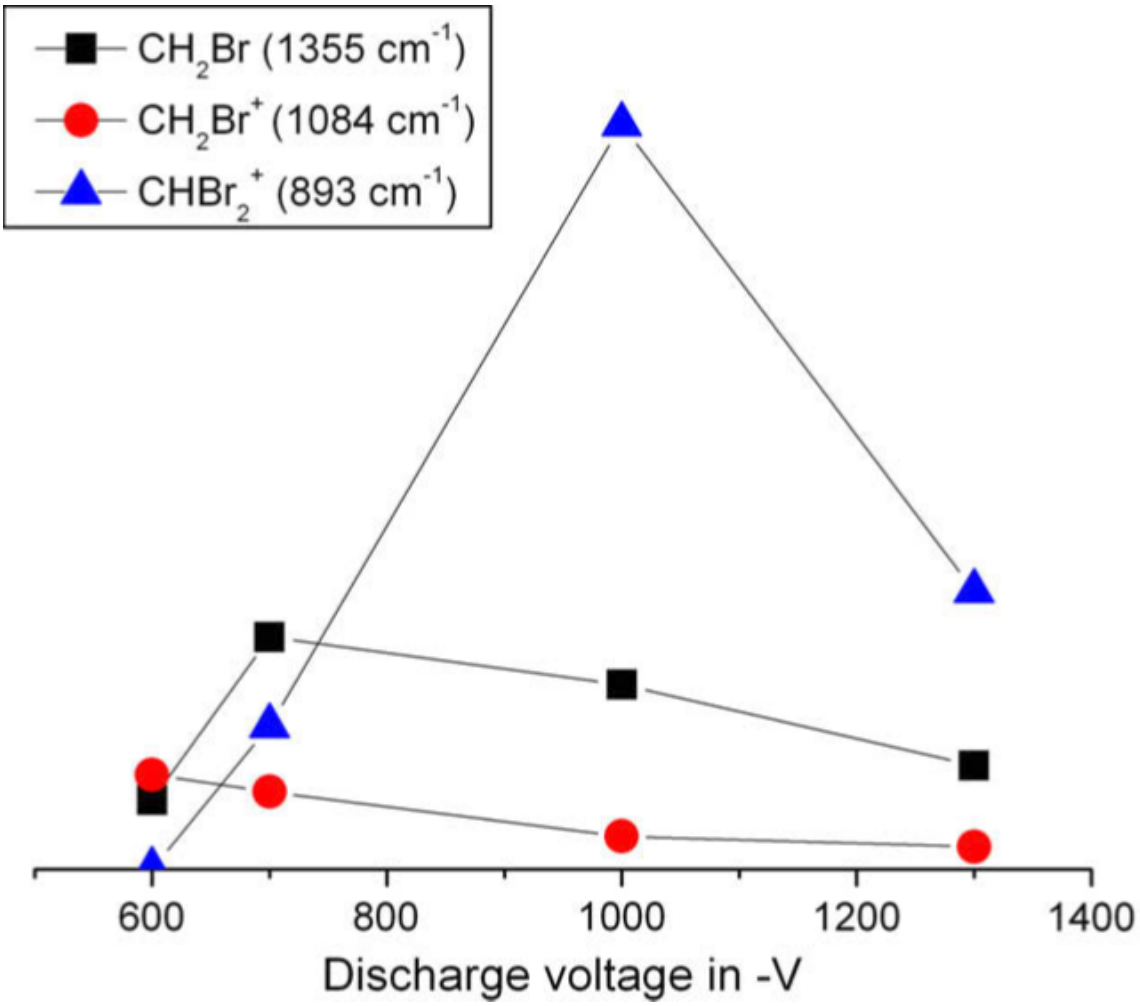


Figure 10.1: Dependence on discharge voltage of the integrated infrared absorbance of three species (CH_2Br, CH_2Br^+ and $CHBr_2^+$) formed in CH_2Br_2:Ar discharge and subsequently trapped using the pulsed-jet discharge matrix isolation technique.

10.1 Experimental set up

The method used in this study combines a pulsed discharge source with matrix isolation technique and it has been described in detail in Chapter 2.

Sample preparations used two different approaches, based upon the vapor pressure of the precursor. The CF_2Br_2 (Synquest labs, 99% stated purity, used without further purification) was in a 0.5 L tank with high purity Argon gas, in a ratio of ~1:5000. The CH_2BrX (X=Cl,Br,I):Ar mixture was obtained by passing Ar gas over a liquid held in a stainless steel bubbler that was in turn held in a temperature controlled bath, in order to reach a maxing ration of ~1:1000.

10.2 Computational Methods

Calculations were carried out on a personal computer using the GAUSSIAN 98 suite of electronic structure programs. All stationary points were characterized by calculating the associated vibrational frequencies. Geometry optimization was performed using density functional theory (B3LYP) in combination with an augmented correlation consistent triple zeta quality basis set (aug-cc-pVTZ basis set).

10.3 Results and Discussion

Figure 10.2 (a) displays the infrared Spectrum of an as-deposited CF_2Br_2:Ar (~1-5000) matrix sample, deposited on a KBr window held at ~7 K. It shows two main bands 1080 and 1142 cm^{-1} due, respectively, to the symmetric and asymmetric CF_2 stretching mode of the precursor CF_2Br_2.[128, 295] The middle layer (b), shows the spectrum

obtained after irradiation of the freshly deposited sample with 240 nm laser light. In this spectrum one can notice the appearance of new bands due to the isomer CF_2Br-Br (1188 and 1240 cm^{-1}) and bands due to the difluorocarbene CF_2 (1098 and 1217 cm^{-1}). The lower layer spectrum was obtained after discharge at -600 V and subsequent deposition of the similar sample CF_2Br_2:Ar (~1-5000). The pulsed-jet discharge process allows more fragmentation as it can be seen by the presence of new weak peaks, absent in photolysis experiment. Those peaks were assigned to various fragments CF, CF_2, CF_2Br and CF_2Br^+ (736 and 1365 cm^{-1}). This figure clearly shows the advantage of discharge over photolysis in trapping highly reactive fragments: in the latter, due to the cage effect, the dissociated fragments can easily undergo a geminate recombination to form the *iso*-CF_2Br-Br, which can be trapped or undergo, at its turn, a molecular dissociation to produce Br_2 and CF_2. Using the calculated infrared intensities, $[CF_2Br]$ / $[CF_2Br^+]$ ratio was determined to be ~ 8:1. The derived positions of the C-F stretching bands of CF_2Br^+ (1483 and 1365 cm^{-1}) are in good agreement with previous studies.[296-298]

The observation of CF_2Br^+ led us to the search of CH_2Br^+ species, which we conducted by discharging CH_2Br_2:Ar (~1:1000) sample. In this experiment we found that, at the threshold voltages, the primary absorptions rise from CH_2Br and CH_2Br^+ and they were in a good agreement with calculations as shown in Table 10-1

Table **10-1** and Figure 10.3. The only previous experiment of which we are aware is that of Dyke and co-workers, who measured photoelectron spectra of CH_2X (X=F, Cl, Br, I) and reported a C-Br stretching frequency of CH_2Br^+ ion of 860 ± 30 cm^{-1}, while our value was 876 cm^{-1} in Ar matrix. In addition to this band, we have also found the CH_2 rocking mode frequency at 1084 cm^{-1}: note that the band of nearly equal strength at 1100cm^{-1} was not observed in CH_2BrI discharge. we couldn't observe the C-H band at 3118 cm^{-1} predicted by our calculations, due to the presence of the absorption of the parent in that region. Note that our derived vibrational frequencies are in good agreement with higher level CCSD(T) calculations of Li and Francisco.[299]

Our assignment was supported by:

- The use of a different precursor (CH_2BrI), which gave the same absorption at 876 and 1084 cm^{-1}).
- The dependence on discharge voltage (current), which we ensured was similar for bands assigned to the same species.
- Observation of the spectrum of the fully deuterated isotopomer, obtained by discharging CD_2Br_2:Ar (~1:1000) sample. The vibrational frequencies for CD_2Br^+ are reported in table 7-1 in comparison with previous studies and theoretical predictions.

CH_2Br^+ ion has two possible resonance structures:

$$H_2C^+ - Br \leftrightarrow H_2C = Br^+$$

and the C=Br double bond in the latter is consistent with the vibrational frequency of 876 cm^{-1}. In contrast, the corresponding frequency for the CH_2Br radical is 693 cm^{-1}. This is reflected in the calculated (B3LYP/aug-cc-pVTZ) C-Br bond lengths: 1.752 Å (ion) and 1.857 Å (radical). Note that the frequency shift in the fluorinated ion

CF_2Br^+ drops to 736 cm^{-1}, closer to that found in the CF_2Br radical (648 cm^{-1}), suggesting a more important contribution from F_2C^+-Br structure. This trend can be understood by considering the singlet-triplet gap of the corresponding carbenes: CH_2 vs CF_2.[300] the pronounced stabilization of the singlet in the latter is attributed to back-donation of electron density to from halogens into the unfilled carbon-centered p_x orbital. In a similar way, the back-donation into the out-of-plane carbon-centered *p* orbital in the planar CX_2Y^+ ions stabilizes the X_2C^+-Y structure, as it has been discussed in previous studies.[286, 291, 292]

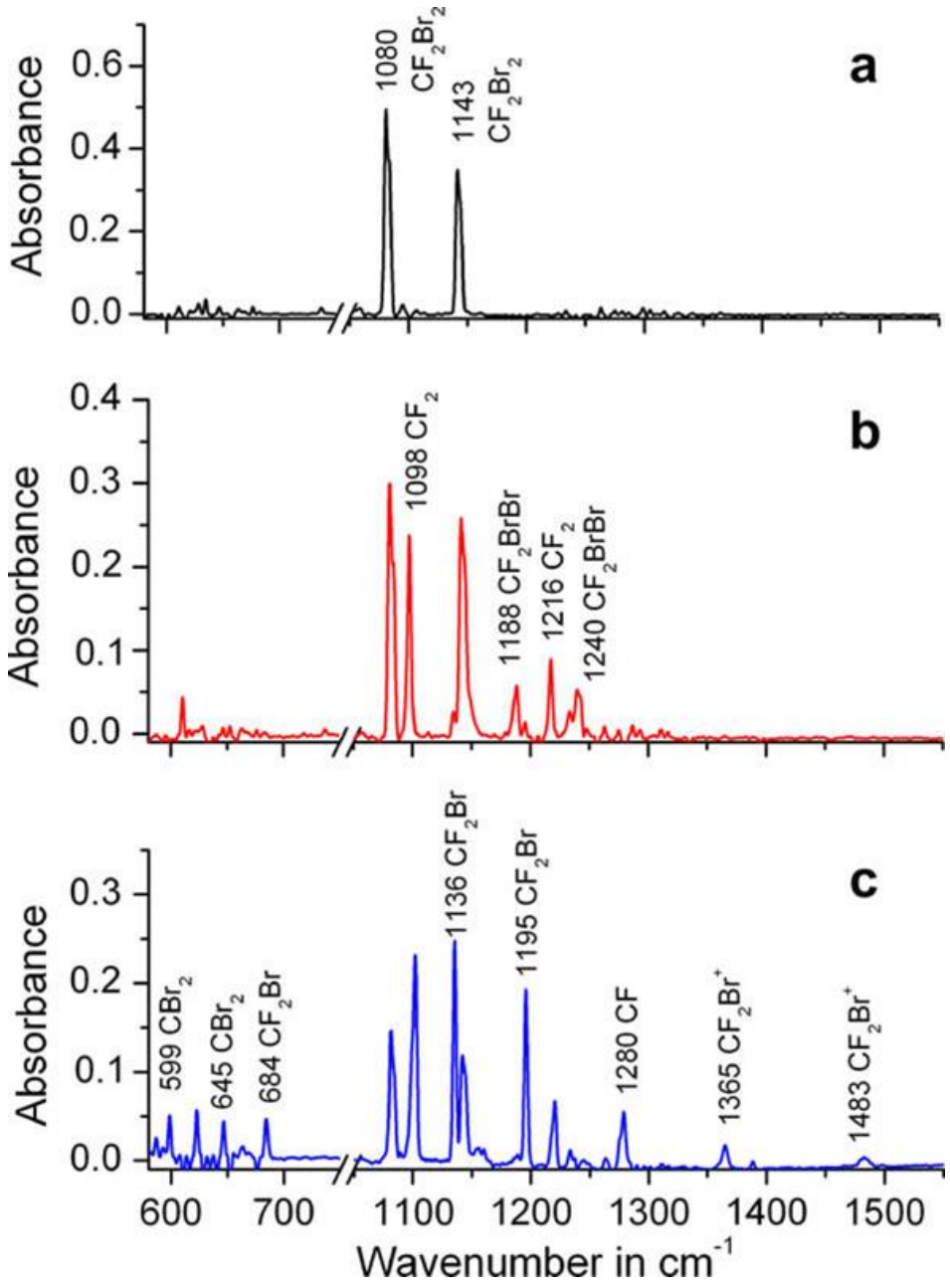


Figure 10.2: (a) Infrared spectrum of a CF_2Br_2:Ar matrix (~1:5000) at 8.5 . **(b)** Spectrum obtained following irradiation of an as-deposited matrix at 240 nm. **(c)** Spectrum obtained following trapping of the discharge products of a CF_2Br_2:Ar sample (~1-5000) using pulsed-jet matrix isolation technique: the strongest absorptions are assigned.

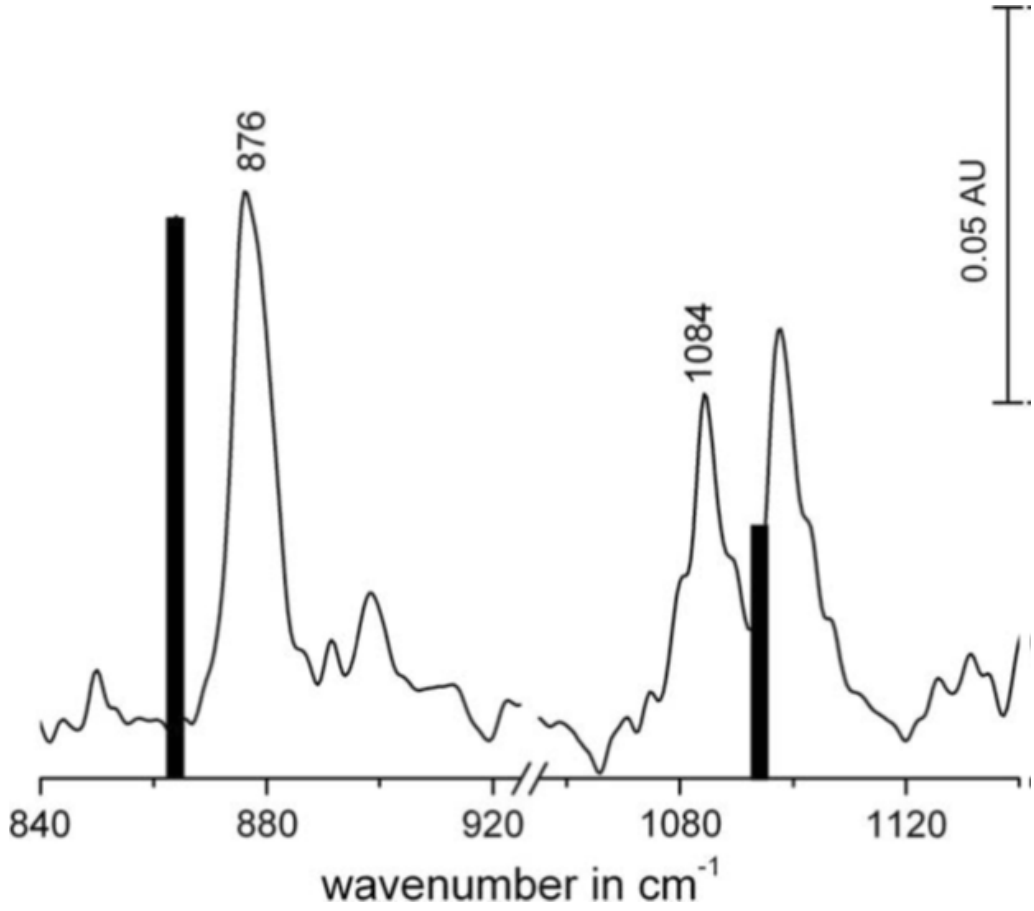


Figure 10.3: Experimental (line) and calculated (Bars) infrared spectra of the CH_2Br^+ ion. The calculated frequencies and intensities of the ion are given in Table 10-1

Table 10-1 Comparison of experiment and theory for vibrational spectra of CX_2Br^+ (X=H,F)

Species	**Method**	**Vibrational frequencies**					
		ν_1	**ν_2**	**ν_3**	**ν_4**	**ν_5**	**ν_6**
$CF_2{}^{79}Br^+$	B3LYP [(i)]	1369.0 (532)	745.5 (32)	418.1 (0)	629.8 (12)	1491.9 (274)	355 (2)
$CF_2{}^{81}Br^+$	B3LYP	1368.9	745.0	416.4	629.7	1491.9	355.0
	Exp. [(ii)]	1362	…	…	…	1480	…
	This work	**1365**	**736**	**…**	**…**	**1483**	**…**
$CH_2{}^{79}Br^+$	B3LYP	3098.2 (24)	1445.8 (0)	863.9 (72)	1094.2 932)	3236.6 (52)	973.3 (0.8)
	CCSD(T)[(iii)]	3138	1460	885	1070	3264	981
$CH_2{}^{81}Br^+$	B3LYP	3102.0	1445.4	862.6	1092.9	3238.3	970.4
	Exp. [(iv)]	…	…	860 ±30	…	…	…
	This work	**…**	**…**	**876**	**1084**	**…**	**…**
$CD_2{}^{79}Br^+$	B3LYP	2242.9 (5)	1102.6 (12)	791.0 (52)	855.6 (21)	2420.6	728.7 (0.2)
$CD_2{}^{81}Br^+$	B3LYP	2242.9	1102.5	789.4	855.6	2420.6	728
	Exp. [(v)]	…	1130 ±30	780 ±30	…	…	…
	This work	**…**	**…**	**787**	**…**	**…**	**…**

(i) For all B3LYP calculations, the aug-cc-pVTZ basis set was used
(ii) References [296-298]
(iii) Reference [300]
(iv) References [283, 301]
(v) Reference [283]

The dependence of the CH_2Br^+ yield on precursor was used to examine the mechanism of formation in the discharge, and our results suggest that the primary mechanism is ionization/fragmentation of the precursor induced by collision with metastable rare gas atoms. Baer and co-workers have examined the thresholds for a series of dihalomethanes compounds using threshold photoelectron-photoion coincidence methods.[285] The reported appearance thresholds for CH_2Br^+ formation from CH_2ClBr, CH_2Br2 and CH_2BrI are, respectively, 11.982, 11.339 and 10.813 eV. Given that the lowest lying excited states of Ar lie in the range of 11.54-11.83 eV, precursor ionization/fragmentation by Ar metastable should lead to CH_2Br^+ formation when CH_2Br_2 and CH_2BrI are used, but not CH_2ClBr. This is exactly what we observed experimentally. These findings led us to use Neon as rare gas, for the systems with high thresholds, since the lowest excited states lie in the range of 16.6-16.85 eV for Neon.[302, 303] In a recent review, Jacox has pointed out some of difficulties in direct discharge sampling matrix isolation experiments, which include possibilities of extensive atomization and reformation leading to small, stable species such as C_3.[302] This was observed in our experiments while discharging CH_2Br_2:Ar sample at high currents, we could observe the characteristic 2039 cm^{-1} line due to C_3, however we found that extensive fragmentation can be minimized by operating the discharge at near the threshold; for example, under the conditions used to obtain the spectra (Figure 10.2 and Figure 10.3) , C3 was not present. Jacox and co-workers also found that fragmentation can be minimized by discharging a pure rare gas and adding the precursor downstream of the discharge. This approach was successfully used in ones of our subsequent experiments.[304]

10.4 Summary

We have reported the first spectroscopic observation of CH_2Br^+ and the first report of the C-Br stretching frequency of CF_2Br^+, using pulsed-jet discharge matrix isolation spectroscopy. Our experiments combined matrix isolation techniques with a pulsed DC discharge nozzle, where a dilute CH_2Br_2:Ar sample was discharged and products deposited onto a KBr window held at ~7 K. The C-Br stretching frequency of 876 cm^{-1} in CH_2Br^+ reflects the nature of the double bond and is consistent with one of the two resonance structures for the ion: $H_2C^+ - Br \leftrightarrow H_2C = Br^+$. In contrast, fluorine substitution results in significance decrease in this frequency, which is more consistent with $F_2C^+ - Br$ structure. These trends are supported by ab initio calculation of properties of these ions.

This study has further demonstrated the utility of pulsed-jet discharge matrix isolation spectroscopy for the trapping and spectroscopic interrogation of molecular ions.

Chapter 11. CONCLUSION

This work provides a comprehensive study on various reactive species pertinent to atmospheric chemistry. The investigated transient species were trapped in solid matrix by means of "matrix isolation technique" and were subject to further spectroscopic measurements. The characterization of considered species was performed based on vibrational transitions using the infrared spectroscopy (FTIR) and the UV/vis spectroscopy served to study the electronic transitions.

This study was focused on photochemistry and degradation of polyhalogenated molecules, which have been detected in atmosphere and are thought to have an important contribution to stratospheric ozone depletion. This work complements a series of research effort developed since the discovery of ozone depletion in 1980's and the rozone low relation between ozone low concentration zones and high concentration in halogenated species (derived from chlorine, iodine and especially bromine).

The first molecule studied in this work was the CF_2I_2 and upon photolysis at 355 or 266 nm, we observed several degradation products isomer trapped in Ar matrix among which the most interesting was its. *Ab initio* calculations, performed at different and relatively high levels of theory, show that the *iso*-CF_2I_2 is a minimum on the ground state potential energy surface scan and is formed by recombination of photoproducts radicals (CF_2I and I) The results observed in this study were confirmed by a parallel study on CF_2I_2 performed by another group using "ultrafast IR absorption" method.

The experiments conducted in Ar and Ne matrix on CF_2Br_2, another important molecule in atmospheric chemistry, has revealed similarities with the previous study on

CF_2I_2. Photolysis at 240 nm, shows formation of various photoproducts, among which the *iso*-CF_2Br_2 that was observed for the first time and found to be a minimum on the PES. Based on computational and experimental information (appearance, disappearance and change in intensities of various photoproducts,) we found that the *iso*-CF_2Br_2 is an intermediate in the $Br+CF_2Br \rightarrow CF_2+Br_2$ reaction, and therefore can be considered to play an important role in the formation of molecular products from CF_2Br_2 photolysis in condensed phases.

As continuation of two previous studies, we extended our research to other polybrominated molecules ($CXBr_3$, X=H, D, F, Cl, Br) in Ar and Ne matrices. Here once, again, we observed an isomer species that is a minimum on PES. The computational results show that this isomer is formed by isomerization, and a first-order saddle point transition state connecting $CXBr_3$ to *iso*-$CXBr_3$ was optimized. Calculations show that the *iso*-$CXBr_3$ structure is best described as halonium ylides, bound by about 60 kJ/mol, with respect to the $CXBr_2$ + Br asymptote. The photolysis of *iso*-$CXBr_3$ resulted in back photoisomerization to the parent $CXBr_3$.

The study conducted on 1,2-dibromoethane (EDB) and 1,2-dibromotetrafluoroethane (TFEDB) in Ar matrix, revealed that pulsed deposition can lead to self-annealing and therefore to conformational relaxation for system with low barrier. Although similar in some points, EDB and TFEDB showed different photochemical behavior. Upon irradiation at 220 nm, EDB produced a charge transfer complex (C_2H_4 ··Br) as major photoproduct, while the TFEDB decomposed to C_2F_4Br radical, characterized in UV/Vis range for the first time in this study. These experiments were

supported by an extensive *ab initio* study, which revealed that in both gas-phase and matrix environment, the classical structure is the global minimum energy structure.

The $C_2H_4\cdots Br_2$ charge-transfer complex was investigated in a different and independent study, whereby the complex was generated by co-deposition of molecular bromine and ethylene. The excitation into the CT band, at appropriate wavelength led exclusively to the anti-conformer in agreement with Mulliken theory, while the excitation of Br_2 chromophore produced both, anti- and gauche-isomers. The related $C_2H_4\cdots I_2$ complex was also produced by similar method, and contrarily to the bromine case, the excitation of the CT or I_2 chromophore both lead to the anti- and gauche-isomer. These observations can be rationalized by the back-electron transfer and subsequent dissociation of the complex, producing $C_2H_4\cdots I$ and I radicals.

Combining the matrix-isolation technique with the high-voltage pulsed-jet discharge, $CXBr_3\cdots Br$ complexes were produced and characterized in Ar or Ne matrix. The photochemistry of the complexes was investigated and following excitation into the CT band, the disappearance of the CT band was correlated with the growth of the bands assigned to the uncomplexed halon. This is explained by a rapid back electron transfer leading to the formation of a hot complex that subsequently dissociates. Finally, the CT band energies of these complexes were compared with those of Br atom complexes with other donors and with the predictions of Mulliken theory, a reasonable linear relationship (Mulliken correlation) was found on a broad range of donor ionization energies. Using the same high voltage pulsed jet discharge technique, we have also produced and characterized CX_2Br^+ (X=H, F) ions. The vibrational spectroscopy analysis revealed the nature of a C=C bond consistent with one of the two resonances structures for the ion: :

$H_2C^+ - Br \leftrightarrow H_2C = Br^+$, while the fluorinated species is more likely to be of $F_2C^+ - Br$ structure.

All the studies presented in this works were supported by extensive high level calculations using various methods (ab initio and Density Functional Theory) depending on the nature of molecules studied and the parameters of interest. This work provides a comprehensive discussion about accuracy and efficiency of various methods and basis sets.

Finally, we have developed and designed different experimental set-ups, adapted to the need experiment into consideration, such as phase of the sample used, target species or products to avoid.

Chapter 12. BIBLIOGRAPHY

1. Bottenheim, J.W., et al., *Depletion of Lower Tropospheric Ozone during Arctic Spring - the Polar Sunrise Experiment 1988.* Journal of Geophysical Research-Atmospheres, 1990. **95**(D11): p. 18555-18568.

2. Brasseur, G.P.O., J.J.; Tyndall, G.S., *Atmospheric Chemistry and Global Change*. 1999, New york: Oxford University Press, Inc.

3. Hausmann, M. and U. Platt, *Spectroscopic Measurement of Bromine Oxide and Ozone in the High Arctic during Polar Sunrise Experiment 1992.* Journal of Geophysical Research-Atmospheres, 1994. **99**(D12): p. 25399-25413.

4. Parker, L.M., W.A., *Stratospheric Ozone Depletion*. 2003, New York: Nova Science Publishers Inc.

5. Dantus, M., P. Gross, and U. Marvet, *Femtosecond control of bimolecular reactions: Experiments and theory.* Abstracts of Papers of the American Chemical Society, 1997. **213**: p. 371-PHYS.

6. Dunkin, I.R., *Matrix Isolation Techniques, A practical approach*. 1998, Glasgow: Oxford University Press.

7. Andrews, L.M., M., *Chemsitry and Physics of Matrix-Isolated Species*. 1989, Amsterdam: Elsevier Science Publishers B.V.

8. Nieminen, J., M. Pettersson, and M. Rasanen, *Matrix-Isolation Infrared and Ab-Initio Studies on Conformers of Fluoroacetic and Chloroacetic Acid.* Journal of Physical Chemistry, 1993. **97**(42): p. 10925-10936.

9. Gribble, G.W., *Naturally occurring organohalogen compounds: Recent developments.* Abstracts of Papers of the American Chemical Society, 2001. **222**: p. U435-U436.

10. Gribble, G.W., *Naturally occurring organohalogen compounds.* Accounts of Chemical Research, 1998. **31**(3): p. 141-152.

11. program), W.W.M.O.U.U.N.E., *Scientific Assessment of Ozone Depletion*, 1994: Montréal.

12. Davies, H., et al., *Mutations of the BRAF gene in human cancer.* Nature, 2002. **417**(6892): p. 949-954.

13. Halliday, G.M., S.N. Byrne, and D.L. Damian, *Ultraviolet A Radiation: Its Role in Immunosuppression and Carcinogenesis.* Seminars in Cutaneous Medicine and Surgery, 2011. **30**(4): p. 214-221.

14. Hogan, C.M. and P. Saundry, *Sunlight*, in *The Encyclopedia of Earth*2010, Eds. Cutler J. Cleveland: Washignton D.C.

15. Parker, L., Morrisey, W.A., *Stratospheric Ozone Depletion*. 2003, New York: Nova Science Publishers, Inc.

16. Brasseur, G.P., J.J. Orlando, and G.S. Tyndall, *Atmospheric Chemistry and Global Change* 1999, New York Oxford University Press, Inc. .

17. Solomon, S., R.R. Garcia, and A.R. Ravishankara, *On the Role of Iodine in Ozone Depletion.* Journal of Geophysical Research-Atmospheres, 1994. **99**(D10): p. 20491-20499.

18. Bottenheim, J.W., A.G. Gallant, and K.A. Brice, *Measurements of Noy Species and O-3 at 82-Degrees-N Latitude.* Geophysical Research Letters, 1986. **13**(2): p. 113-116.

19. Barrie, L.A., et al., *Ozone Destruction and Photochemical-Reactions at Polar Sunrise in the Lower Arctic Atmosphere.* Nature, 1988. **334**(6178): p. 138-141.

20. Barrie, L.A., et al., *Lower Tropospheric Measurements of Halogens, Nitrates, and Sulfur-Oxides during Polar Sunrise Experiment 1992.* Journal of Geophysical Research-Atmospheres, 1994. **99**(D12): p. 25453-25467.

21. Tuckermann, M., et al., *DOAS-observation of halogen radical-catalysed arctic boundary layer ozone destruction during the ARCTOC-campaigns 1995 and 1996 in Ny-Alesund, Spitsbergen.* Tellus Series B-Chemical and Physical Meteorology, 1997. **49**(5): p. 533-555.

22. Kreher, K., *Spectroscopic Measurements of Atmospheric OClO, BrO and NO_2 and their Relation to Antarctic Ozone Depletion* 1996, UNiversity of Heidelberg

23. Kreher, K., et al., *Ground-based measurements of OClO and HCl in austral spring 1993 at Arrival Heights, Antarctica.* Geophysical Research Letters, 1996. **23**(12): p. 1545-1548.

24. Richter, A., et al., *GOME observations of stratospheric trace gas distributions during the splitting vortex event in the antarctic winter of 2002. Part I: Measurements.* Journal of the Atmospheric Sciences, 2005. **62**(3): p. 778-785.

25. Wagner, T. and U. Platt, *Satellite mapping of enhanced BrO concentrations in the troposphere.* Nature, 1998. **395**(6701): p. 486-490.

26. *Scientific Assessment of Ozone depletion:1994*, 1994, WMO (World Meteorological Organization)/ UNEP (UNited Nations Environment Programme): Montreal.

27. Simons, J.P. and P.E.R. Tatham, The Journal of Chemical Society, A., 1966: p. 854-859.

28. Brown, G.P. and J.P. Simons, Transactions of the Faraday Society, 1969. **65**: p. 3245.

29. Zheng, X.M., W.H. Fang, and D.L. Phillips, *Transient resonance Raman spectroscopy and density functional theory investigation of iso-polyhalomethanes containing bromine and/or iodine atoms.* Journal of Chemical Physics, 2000. **113**(24): p. 10934-10946.

30. Lewis, G.N. and M. Kasha, *Phosphorescence and Triplet State.* Journal of American Chemical Society, 1944. **66**(12): p. 2100-2116.

31. Whittle, E., D.A. Dows, and G.C. Pimentel, Journal of Chemical Physics, 1954. **22**: p. 1943.

32. Thoma, A., et al., *A Pulsed Discharge Source of Transients for Matrix-Isolation Spectroscopy 2.* Journal of Physical Chemistry, 1992. **96**(18): p. 7231-7235.

33. Smith, A.M., et al., *Rare gas matrix studies of absorption and fluorescence of reactive intermediates formed in discharges through acetylene.* Chem. Phys., 1994. **189**(2): p. 315-34.

34. Yariv, A., *Quantum Electronics*. 3rd ed. 1989: Wiley.

35. Schafer, F.P., *Dye Lasers*. 1990, Berlin: Springer-Verlag.

36. *Origin 8.0*, OriginLab: Northampton, MA.

37. Leach, A.L., *Molecular Modelling, Principles and Applications, advanced ab initio methods*. Vol. Volume second. 2001, Essex, England: Pearson Education Limited.

38. Cramer, J.C., *Essentials of Computational Chemistry: theories and models*. Second Edition ed. 2004, West Sussex: John Wiley & Sons Ltd.

39. Kato, T., *Perturbation Theory for Linear Operators*. Corrected printing of the Second Edition ed. 1980, New York: Springer-Verlag Berlin Heidelberg.

40. Leach, A.L., *Molecular Modelling, Principles and Applications, advanced ab initio methods*. Vol. second 2001, Essex, England: Pearson Education Limited.

41. Ramachandran, K.I., G. Deepa, and K. Namboori, *Computational Chemistry and Molecular Modeling, Principles and Applications*. 2008, Berlin: Springer.

42. Frisch, M.J.T., G. W.; Sclegel, H. B. et al., *Gaussian 09*, 2009, Gaussian Inc.: Wallingford, CT.

43. Fermi, E., *Un Metodo Statistico per la Determinazione di alcune Proprietà dell'Atomo.* Rend. Accad. Naz. Lincei, 1927. **6**: p. 602-607.

44. Thomas, L.H., *The calculation of atomic fields.* Mathematical Proceeddings of the Cambridge Philosophical Society

1927. **23**(05): p. 542-548.

45. Becke, A.D., *A New Mixing of Hartree-Fock and Local Density-Functional Theories.* Journal of Chemical Physics, 1993. **98**(2): p. 1372-1377.

46. Zhao, Y. and D.G. Truhlar, *Density functional for spectroscopy: No long-range self-interaction error, good performance for Rydberg and charge-transfer states, and better performance on average than B3LYP for ground states.* Journal of Physical Chemistry A, 2006. **110**(49): p. 13126-13130.

47. Dunning, T.H., *Gaussian-Basis Sets for Use in Correlated Molecular Calculations .1. The Atoms Boron through Neon and Hydrogen.* Journal of Chemical Physics, 1989. **90**(2): p. 1007-1023.

48. Kendall, R.A., T.H. Dunning, and R.J. Harrison, *Electron-Affinities of the 1st-Row Atoms Revisited - Systematic Basis-Sets and Wave-Functions.* Journal of Chemical Physics, 1992. **96**(9): p. 6796-6806.

49. Woon, D.E. and T.H. Dunning, *Gaussian-Basis Sets for Use in Correlated Molecular Calculations .4. Calculation of Static Electrical Response Properties.* Journal of Chemical Physics, 1994. **100**(4): p. 2975-2988.

50. Woon, D.E. and T.H. Dunning, *Gaussian-Basis Sets for Use in Correlated Molecular Calculations .5. Core-Valence Basis-Sets for Boron through Neon.* Journal of Chemical Physics, 1995. **103**(11): p. 4572-4585.

51. Hay, P.J. and W.R. Wadt, *Abinitio Effective Core Potentials for Molecular Calculations - Potentials for the Transition-Metal Atoms Sc to Hg.* Journal of Chemical Physics, 1985. **82**(1): p. 270-283.

52. Wadt, W.R. and P.J. Hay, *Abinitio Effective Core Potentials for Molecular Calculations - Potentials for Main Group Elements Na to Bi.* Journal of Chemical Physics, 1985. **82**(1): p. 284-298.

53. Hay, P.J. and W.R. Wadt, *Abinitio Effective Core Potentials for Molecular Calculations - Potentials for K to Au Including the Outermost Core Orbitals.* Journal of Chemical Physics, 1985. **82**(1): p. 299-310.

54. Peterson, K.A., et al., *Systematically convergent basis sets with relativistic pseudopotentials. II. Small-core pseudopotentials and correlation consistent basis sets for the post-d group 16-18 elements.* Journal of Chemical Physics, 2003. **119**(21): p. 11113-11123.

55. Sadlej, A.J., *Medium-Size Polarized Basis-Sets for High-Level-Correlated Calculations of Molecular Electric Properties .5. 4th-Row Atoms - Sn through I.* Theoretica Chimica Acta, 1992. **81**(4-5): p. 339-354.

56. Boys, S.F. and F. Bernardi, *Calculation of Small Molecular Interactions by Differences of Separate Total Energies - Some Procedures with Reduced Errors.* Journal of Molecular Physics, 1970. **19**: p. 553.

57. Kjaergaard, H.G., T.W. Robinson, and K.A. Brooking, *Calculated CH-stretching overtone spectra of naphthalene, anthracene and their cations.* Journal of Physical Chemistry A, 2000. **104**(48): p. 11297-11303.

58. Phillips, D.L., W.H. Fang, and X.M. Zheng, *Isodiiodomethane is the methylene transfer agent in cyclopropanation reactions with olefins using ultraviolet photolysis of diiodomethane in solutions: A density functional theory investigation of the reactions of isodiiodomethane, iodomethyl radical, and iodomethyl cation with ethylene.* Journal of the American Chemical Society, 2001. **123**(18): p. 4197-4203.

59. Phillips, D.L., et al., *Isopolyhalomethanes: Their formation, structures, properties and cyclopropanation reactions with olefins.* Current Organic Chemistry, 2004. **8**(9): p. 739-755.

60. Li, Y.L., et al., *Water-catalyzed dehalogenation reactions of isobromoform and its reaction products.* Abstracts of Papers, 227th ACS National Meeting, Anaheim, CA, United States, March 28-April 1, 2004, 2004: p. PHYS-381.

61. Ihee, H., et al., *Ultrafast x-ray diffraction of transient molecular structures in solution.* Science, 2005. **309**(5738): p. 1223-1227.

62. Kwok, W.M., et al., *Picosecond time-resolved resonance Raman observation of the iso-CH_2I-I photoproduct from the "photoisomerization" reaction of diiodomethane in the solution phase.* Journal of Chemical Physics, 2000. **113**(17): p. 7471-7478.

63. Kwok, W.M., et al., *Picosecond time-resolved resonance Raman observation of the iso-CH_2Cl-I and iso-CH_2I-Cl photoproducts from the "photoisomerization" reactions of CH2ICl in the solution phase.* Journal of Chemical Physics, 2001. **114**(17): p. 7536-7543.

64. Maier, G. and H.P. Reisenauer, *Photoisomerization of Dihalomethanes.* Angewandte Chemie-International Edition in English, 1986. **25**(9): p. 819-822.

65. Maier, G., et al., *Photochemical Isomerization of Dihalomethanes in Argon Matrices.* Journal of the American Chemical Society, 1990. **112**(13): p. 5117-5122.

66. Tarnovsky, A.N., et al., *Photodissociation dynamics of diiodomethane in solution.* Chemical Physics Letters, 1999. **312**(2-4): p. 121-130.

67. Tarnovsky, A.N., et al., *Photodissociation dynamics of chloroiodomethane in acetonitrile studied by ultrafast pump-probe spectroscopy.* Journal of the Chinese Chemical Society, 2000. **47**(4A): p. 769-772.

68. Zheng, X.M. and D.L. Phillips, *Density functional theory and resonance Raman investigation of the ultraviolet electronic excited states of CF_2I_2.* Chemical Physics Letters, 2000. **316**(5-6): p. 524-530.

69. Zheng, X.M. and D.L. Phillips, *Photoisomerization reaction of CH_2BrI following A-band and B-band photoexcitation in the solution phase: Transient resonance Raman observation of the iso-CH_2I-Br photoproduct.* Journal of Chemical Physics, 2000. **113**(8): p. 3194-3203.

70. Zheng, X.M. and D.L. Phillips, *Solvation effects on the iodoform ultraviolet direct photodissociation reaction. opening the photoisomerization channel.* Chemical Physics Letters, 2000. **324**(1-3): p. 175-182.

71. Tarnovsky, A.N., et al., *Photochemistry of diiodomethane in solution studied by femtosecond and nanosecond laser photolysis. Formation and dark reactions of the CH_2I-I isomer photoproduct and its role in cyclopropanation of olefins.* Journal of Physical Chemistry A, 2004. **108**(2): p. 237-249.

72. Jones, C.E. and L.J. Carpenter, *Solar photolysis of CH_2I_2, CH_2ICI, and CH_2IBr in water, saltwater, and seawater.* Environmental Science & Technology, 2005. **39**(16): p. 6130-6137.

73. Guan, X.G., et al., *Comparison of the dehalogenation of polyhalomethanes and production of strong acids in aqueous and salt (NaCl) water environments: Ultraviolet photolysis of CH_2I_2.* Journal of Chemical Physics, 2004. **121**(17): p. 8399-8409.

74. Kwok, W.M., et al., *Water-catalyzed dehalogenation reactions of isobromoform and its reaction products.* Journal of the American Chemical Society, 2004. **126**(10): p. 3119-3131.

75. Cameron, M.R. and G.B. Bacskay, *Stabilities, excitation energies, and dissociation reactions of CF_2Cl_2 and CF_2Br_2: Quantum chemical computations of*

heats of formation of fluorinated methanes, methyls, and carbenes. Journal of Physical Chemistry A, 2000. **104**(47): p. 11212-11219.

76. Xu, D.D., et al., *Ultraviolet photodissociation of bromoform at 234 and 267 nm by means of ion velocity imaging.* Journal of Chemical Physics, 2002. **117**(6): p. 2578-2585.

77. Huang, H.Y., et al., *Molecular elimination of Br_2 in 248 nm photolysis of bromoform probed by using cavity ring-down absorption spectroscopy.* Journal of Chemical Physics, 2004. **121**(11): p. 5253-5260.

78. Bergmann, K., et al., *Resonance enhanced multiphoton ionization time-of-flight study of CF_2I_2 photodissociation.* Journal of Chemical Physics, 1998. **109**(2): p. 474-483.

79. Farmanara, P., et al., *Analysis of the ultrafast photodissociation of electronically excited CF_2I_2 molecules by femtosecond time-resolved photoelectron spectroscopy.* Journal of Chemical Physics, 2000. **113**(5): p. 1705-1713.

80. Roeterdink, W.G. and M.H.M. Janssen, *Femtosecond velocity map imaging of concerted photodynamics in CF_2I_2.* Journal of Chemical Physics, 2002. **117**(14): p. 6500-6510.

81. Scheld, H.A., A. Furlan, and J.R. Huber, *Formation of molecular iodine by photodissociation of CF_2I_2 at 193 nm.* Chemical Physics Letters, 2000. **326**(5-6): p. 366-374.

82. Radloff, W., et al., *Ultrafast photodissociation dynamics of electronically excited CF_2I_2 molecules.* Chemical Physics Letters, 1998. **291**(1-2): p. 173-178.

83. El-Khoury, P.Z. and A.N. Tarnovsky, *Ultrafast formation of I-2 following 350-nm photodissociation of CF_2I_2 in n-hexane.* Chemical Physics Letters, 2008. **453**(4-6): p. 160-166.

84. El-Khoury, P.Z., et al., *Structure of the Photochemical Reaction Path Populated via Promotion of CF_2I_2 into Its First Excited State.* Journal of Physical Chemistry A, 2009. **113**(40): p. 10767-10771.

85. El-Khoury, P.Z., M. Olivucci, and A.N. Tarnovsky, *Switching on molecular iodine elimination through isomerization: The F_2C-I-I isomer of difluorodiiodomethane.* Chemical Physics Letters, 2008. **462**(4-6): p. 192-195.

86. Fraser, P.J., et al., *Southern Hemispheric halon trends (1978-1998) and global halon emissions.* Journal of Geophysical Research-Atmospheres, 1999. **104**(D13): p. 15985-15999.

87. Mann, D.E. and B.A. Thrush, *On the Absorption Spectrum of CF_2 and Its Vibrational Analysis.* Journal of Chemical Physics, 1960(33): p. 1732.

88. Walton, J.C., *Photolysis of dibromodifluoromethane at 265 nm.* Journal of Chemistry Society, Faraday transactions 1, 1972(68): p. 1559.

89. El Khoury, P.Z., et al., *Characterization of iso-CF_2I_2 in frequency and ultrafast time domains.* Journal of Chemical Physics, 2010. **132**(12).

90. Cameron, M.R., et al., *Photodissociation dynamics of the reaction $CF_2Br_2+h\upsilon \rightarrow CF_2+2Br$. Energetics, threshold and nascent CF_2 energy distributions for lambda=223-260 nm 2.* Physical Chemistry Chemical Physics, 2000. **2**(11): p. 2539-2547.

91. Molina, L.T. and M.J. Molina, *Quantum Yields for the Photo-Dissociation of CBr_2F_2 in the 200-300-Nm Region 3.* Journal of Physical Chemistry, 1983. **87**(8): p. 1306-1308.

92. Talukdar, R.K., G.L. Vaghjiani, and A.R. Ravishankara, *Photodissociation of bromocarbons at 193, 222, and 248 nm: Quantum yields of Br atom at 298 K.* Journal of Chemical Physics, 1992. **96** (11): p. 8194.

93. Felder, P., et al., *Photofragment Translational Spectroscopy of Fluorinated Halomethanes 7.* Israel Journal of Chemistry, 1994. **34**(1): p. 33-42.

94. Park, M.S., et al., *Avoided curve crossing between the A_1 and B_1 states in CF_2Br_2 photolysis at 234 and 265 nm 4.* Journal of Physical Chemistry A, 2001. **105**(23): p. 5606-5612.

95. Hsu, C.Y., H.Y. Huang, and K.C. Lin, *Br_2 elimination in 248-nm photolysis of CF_2Br_2 probed by using cavity ring-down absorption spectroscopy 5.* Journal of Chemical Physics, 2005. **123**(13).

96. Jacox, M.E., *Matrix isolation study of the photolysis of dibromodifluoromethane. Infrared spectrum of the monobromodifluoromethyl free radical.* Chemical Physics Letters, 1978. **53**: p. 192.

97. Allamandola, L.J., D. Lucas, and G.C. Pimentel, *Synchronized flash photolysis and pulse deposition in matrix isolation experiments* Review of Scientific Intruments, 1978(49): p. 913.

98. Perutz, R.N. and J.J. Turner, *Pulsed Matrix isolation. A Comparative Study.* Journal of Chemistry Society, Faraday transactions 2, 1973. **69** p. 452.

99. Rochkind, M.M., *Infrared Analysis of Multicomponent Gas Mixture.* Analytical Chemistry, 1967(39): p. 567 -574.

100. Frisch, M.J.T., G. W.; Sclegel, H. B. et al., *Gaussian 03*, 2003, Gaussian Inc.: Wallingford, CT.

101. Zhao, Y. and D.G. Truhlar, Accounts of Chemical Research, 2008.

102. Zhao, Y. and D.G. Truhlar, *The M06 suite of density functionals for main group thermochemistry, thermochemical kinetics, noncovalent interactions, excited states, and transition elements: two new functionals and systematic testing of four M06-class functionals and 12 other functionals.* Theoretical Chemistry Accounts, 2008. **120**(1-3): p. 215-241.

103. Peterson, K.A., et al., *On the Spectroscopic and Thermochemical Properties of ClO, BrO, IO, and Their Anions.* Journal of Chemical Physics, 2006(110(51)): p. 13877 -13883.

104. Sadlej, A.J., Theoretica Chimica Acta, 1992(81): p. 339.

105. Davidsson, J., et al., *Structural determination of a transient isomer of CH_2I_2 by picosecond x-ray diffraction.* Physical Review Letters, 2005. **94**(24): p. -.

106. Class, T., R. Kohnle, and K. Ballschmiter, *Chemistry of Organic Traces in Air .7. Bromochloromethanes and Bromochloromethanes in Air over the Atlantic-Ocean.* Chemosphere, 1986. **15**(4): p. 429-436.

107. Cota, G.F. and W.T. Sturges, *Biogenic bromine production in the Arctic.* Marine Chemistry, 1997. **56**(3-4): p. 181-192.

108. Schauffler, S.M., et al., *Measurements of bromine containing organic compounds at the tropical tropopause.* Geophysical Research Letters, 1998. **25**(3): p. 317-320.

109. Sturges, W.T., et al., *Bromoform as a source of stratospheric bromine.* Geophysical Research Letters, 2000. **27**(14): p. 2081-2084.

110. Dvortsov, V.L., et al., *Rethinking reactive halogen budgets in the midlatitude lower stratosphere.* Geophysical Research Letters, 1999. **26**(12): p. 1699-1702.

111. Carpenter, L.J. and P.S. Liss, *On temperate sources of bromoform and other reactive organic bromine gases.* Journal of Geophysical Research-Atmospheres, 2000. **105**(D16): p. 20539-20547.

112. Gschwend, P.M. and J.K. Macfarlane, *Polybromomethanes - Temperate Marine Macroalgal Sources and Aerobic Microbial Sinks.* Abstracts of Papers of the American Chemical Society, 1985. **189**(Apr-): p. 56-Geoc.

113. Quack, B. and D.W.R. Wallace, *Air-sea flux of bromoform: Controls, rates, and implications.* Global Biogeochemical Cycles, 2003. **17**(1): p. -.

114. Bayes, K.D., et al., *Measurements of quantum yields of bromine atoms in the photolysis of bromoform from 266 to 324 nm.* Journal of Geophysical Research-Atmospheres, 2003. **108**(D3): p. -.

115. McGivern, W.S., et al., *Primary and secondary processes in the photodissociation of CHBr3.* Journal of Physical Chemistry A, 2000. **104**(45): p. 10085-10091.

116. Peterson, K.A. and J.S. Francisco, *Should bromoform absorb at wavelengths longer than 300 nm?* Journal of Chemical Physics, 2002. **117**(13): p. 6103-6107.

117. Tang, Y., et al., *Studies on photodissociation of alkyl bromides at 234 and 267 nm.* Chemical Physics Letters, 2004. **392**(4-6): p. 493-497.

118. Zou, P., et al., *Photodissociation of bromoform at 248 nm: Single and multiphoton processes.* Journal of Physical Chemistry A, 2004. **108**(9): p. 1482-1488.

119. Carrier, S.L., et al., *Ultrafast Observation of Isomerization and Complexation in the Photolysis of Bromoform in Solution.* Journal of Physical Chemistry A, 2010. **114**(3): p. 1548-1555.

120. Zhao, C.Y., et al., *Water-catalyzed dehalogenation reactions of the isomer of CBr_4 and its reaction products and a comparison to analogous reactions of the isomers of di- and trihalomethanes.* Chemistry-a European Journal, 2005. **11**(4): p. 1093-1108.

121. Zhang, H., A.S. Dvornikov, and P.M. Rentzepis, *Photolysis of CBr_4 and its transient solvent stabilized (CBr_3^+//Br^-)(Solv) ion pair.* Journal of Physical Chemistry A, 2005. **109**(27): p. 5984-5988.

122. Kong, Q.Y., et al., *Photochemical reaction pathways of carbon tetrabromide in solution probed by picosecond X-ray diffraction.* Journal of the American Chemical Society, 2007. **129**(44): p. 13584-13591.

123. Kong, Q.Y., et al., *Structure of the photodissociation products of CCl_4, CBr_4, and CI_4 in solution studied by DFT and ab initio calculations.* Journal of Physical Chemistry A, 2006. **110**(38): p. 11178-11187.

124. Morken, P.A., et al., *Synthesis of Fluorinated 1,2,3-Butatrienes from Alpha-Halovinyl Organometallic Reagents.* Journal of the American Chemical Society, 1993. **115**(13): p. 5430-5439.

125. Frisch, M.J., et al., *GAUSSIAN 03*, 2003, Gaussian Inc.: Wallingford, CT.

126. El-Khoury, P.Z. and A. Tarnovsky, unpublished results, 2010.

127. Fukui, K., *The Path of Chemical-Reactions - the Irc Approach.* Accounts of Chemical Research, 1981. **14**(12): p. 363-368.

128. George, L., et al., *Matrix isolation and computational study of isodifluorodibromomethane (F_2CBr-Br): A route to Br_2 formation in CF_2Br_2 photolysis.* Journal of Chemical Physics, 2010. **132**(8).

129. Kalume, A., L. George, and S.A. Reid, *Isomerization as a Key Path to Molecular Products in the Gas-Phase Decomposition of Halons.* Journal of Physical Chemistry Letters, 2010. **1**(20): p. 3090-3095.

130. George, L., et al., *Spectroscopic and computational studies of matrix-isolated iso-CHBr3: Structure, properties, and photochemistry of iso-bromoform.* Journal of Chemical Physics, 2011. **135**(12).

131. Zavitsas, A.A., *Quantitative Relationship between Bond-Dissociation Energies, Infrared Stretching Frequencies, and Force-Constants in Polyatomic-Molecules.* Journal of Physical Chemistry, 1987. **91**(22): p. 5573-5577.

132. Maier, G., et al., *Photoisomerization of Tetrachloromethane in an Argon Matrix.* Tetrahedron Letters, 1989. **30**(31): p. 4105-4108.

133. Frisch, M.J., *Gaussian 09 Revision*, 2009, Gaussian Inc.: Wallingford, CT.

134. Glendening, E.D., et al., *NBO*, 2004, Theoretical Chemistry Institute, University of Wisconsin-Madison: Madison, WI.

135. Glendening, E.D., J.K. Badenhoop, and F. Weinhold, *Natural resonance theory: III. Chemical applications.* Journal of Computational Chemistry, 1998. **19**(6): p. 628-646.

136. Glendening, E.D. and F. Weinhold, *Natural Resonance Theory: II. Natural bond order and valency.* Journal of Computational Chemistry, 1998. **19**(6): p. 610-627.

137. Glendening, E.D. and F. Weinhold, *Natural resonance theory: I. General formalism.* Journal of Computational Chemistry, 1998. **19**(6): p. 593-609.

138. Preston, T.J., et al., *Formation and relaxation dynamics of iso-CH_2Cl-I in cryogenic matrices.* Journal of Chemical Physics, 2011. **135**(11).

139. Maier, G. and H.P. Reisenauer, *Photoisomerization of Dihalomethanes.* Angew. Chem.-Int. Ed. Eng., 1986. **25**(9): p. 819-822.

140. Maier, G., et al., *Photoisomerization of Tetrachloromethane in an Argon Matrix.* Tetrahedron Lett., 1989. **30**(31): p. 4105-4108.

141. Maier, G., et al., *Photochemical Isomerization of Dihalomethanes in Argon Matrices.* J. Am. Chem. Soc., 1990. **112**(13): p. 5117-5122.

142. George, L., et al., *Spectroscopic and computational studies of matrix-isolated iso-$CXBr_3$ (X = F, Cl, Br): Structure, properties, and photochemistry of substituted iso-tribromomethanes.* Journal of Molecular Structure, 2012. **1025**: p. 61-68.

143. Western, C., *PGOPHER*, 2010, University of Bristol. p. A Program for Simulating Rotational Structure.

144. Sando, G.M. and K.G. Spears, *Ab initio computation of the Duschinsky mixing of vibrations and nonlinear effects.* Journal of Physical Chemistry A, 2001. **105**(22): p. 5326-5333.

145. Nagy, A., et al., *On the Benzylium/Tropylium Ion Dichotomy: Electronic Absorption Spectra in Neon Matrices.* Angewandte Chemie-International Edition, 2011. **50**(13): p. 3022-3025.

146. Troy, T.P., et al., *On the electronic spectroscopy of closed-shell cations derived from resonance-stabilized radicals: Insights from theory and Franck-Condon analysis.* Astronomy & Astrophysics, 2012. **541**.

147. Sturges, W.T., et al., *Methyl bromide, other brominated methanes, and methyl iodide in polar firn air.* Journal of Geophysical Research-Atmospheres, 2001. **106**(D2): p. 1595-1606.

148. Singh, H.B., et al., *Measurement of Volatile Organic-Chemicals at Selected Sites in California.* Atmospheric Environment Part a-General Topics, 1992. **26**(16): p. 2929-2946.

149. Pankow, J.F., et al., *Determination of a wide range of volatile organic compounds in ambient air using multisorbent adsorption/thermal desorption and gas chromatography mass spectrometry.* Analytical Chemistry, 1998. **70**(24): p. 5213-5221.

150. Bose, P.K., et al., *Experimental and Abinitio Vibrational-Spectra of 1,2-Dibromoethane, Meso-1,2-Dideuterio-1,2-Dibromoethane, and Chiral 1,2-Dideuterio-1,2-Dibromoethane.* Journal of Physical Chemistry, 1989. **93**(13): p. 5070-5078.

151. Christiansen, C.J. and J.S. Francisco, *Atmospheric Oxidation Mechanism of 1,2-Dibromoethane.* Journal of Physical Chemistry A, 2009. **113**(26): p. 7189-7204.

152. Ihee, H., A.H. Zewail, and W.A. Goddard, *Conformations and barriers of haloethyl radicals (CH_2XCH_2, X = F, Cl, Br, I): Ab initio studies 1.* Journal of Physical Chemistry A, 1999. **103**(33): p. 6638-6649.

153. Zheng, X.M. and D.L. Phillips, *Solvation can open the photoisomerization pathway for the direct photodissociation reaction of diiodomethane: Transient resonance Raman observation of the isodiiodomethane photoproduct from ultraviolet excitation of diiodomethane in the solution phase.* Journal of Physical Chemistry A, 2000. **104**(29): p. 6880-6886.

154. Waters, W.A., *Free Radical Reactions*. Organic Series 2. 1975, Butterworths, UK. 375.

155. Frisch, M.J., et al., *GAUSSIAN 09*, 2009, Gaussian Inc.: Wallingford, CT.

156. Guest, M.F., et al., *The GAMESS-UK electronic structure package: algorithms, developments and applications.* Molecular Physics, 2005. **103**(6-8): p. 719-747.

157. Maier, G. and S. Senger, *Bromine complexes of ethylene and cyclopropene: Matrix-IR-spectroscopic identification, photochemical reactions, ab initio studies.* Liebigs Annalen-Recueil, 1997(2): p. 317-326.

158. Legon, A.C. and J.M.A. Thumwood, *A pi-electron donor-acceptor complex $C_2H_4 \cdots Br_2$ characterized by its rotational spectrum 3.* Physical Chemistry Chemical Physics, 2001. **3**(8): p. 1397-1402.

159. Zheng, X.M. and D.L. Phillips, *Initio investigation of XCH_2CH_2 and $XCHCH_3$ radicals (X = F, Cl, Br).* Journal of Physical Chemistry A, 2000. **104**(5): p. 1030-1038.

160. Lee, H.L., et al., *Photodissociation of dibromoethanes at 248 nm: An ignored channel of Br_2 elimination.* Journal of Chemical Physics, 2009. **130**(18).

161. Farmer, C.B., et al., *Stratospheric Trace Gases in the Spring 1986 Antarctic Atmosphere.* Nature, 1987. **329**(6135): p. 126-130.

162. M. J. Molina, F.S.R., in *2nd Int. Conf. Environ. Impact Aerosp. Oper. High Atmos.*1974. p. 99.

163. Pollock, W.H., et al., *On the Age of Stratospheric Air and Ozone Depletion Potentials in Polar-Regions.* Journal of Geophysical Research-Atmospheres, 1992. **97**(D12): p. 12993-12999.

164. Prather, M.J., M.B. Mcelroy, and S.C. Wofsy, *Reductions in Ozone at High-Concentrations of Stratospheric Halogens.* Nature, 1984. **312**(5991): p. 227-231.

165. Solomon, S. and D.L. Albritton, *Time-Dependent Ozone Depletion Potentials for Short-Term and Long-Term Forecasts.* Nature, 1992. **357**(6373): p. 33-37.

166. El-Khoury, P.Z., et al., *Characterization of iso-CF_2I_2 in frequency and ultrafast time domains.* Journal of Chemical Physics, 2010. **132**(12).

167. Raff, J.D., et al., *Chlorine activation indoors and outdoors via surface-mediated reactions of nitrogen oxides with hydrogen chloride.* Proceedings of the National Academy of Sciences of the United States of America, 2009. **106**(33): p. 13647-13654.

168. Kalume, A., et al., *Spectroscopic and Computational Studies of the Laser Photolysis of Matrix Isolated 1,2-Dibromoethanes: Formation and Fate of the Bromoethyl Radicals.* Journal of Physical Chemistry A, 2010. **114**(36): p. 9919-9926.

169. Ji, L., et al., *Photodissociation dynamics of allyl bromide at 234, 265, and 267 nm.* Journal of Chemical Physics, 2006. **125**(16).

170. Lee, Y.R., C.C. Chen, and S.M. Lin, *Photodissociation of CH_2Br_2, 1,1- and 1,2-$C_2H_4Br_2$ at 248 nm: A simple C-Br bond fission versus a concerted three-body formation.* Journal of Chemical Physics, 2003. **118**(23): p. 10494-10501.

171. Nguyen, T. and D.F. Ollis, *Complete Heterogeneously Photocatalyzed Transformation of 1,1-Dibromoethane and 1,2-Dibromoethane to CO_2 and HBr.* Journal of Physical Chemistry, 1984. **88**(16): p. 3386-3388.

172. Andrews, L. and X.F. Wang, *Infrared spectra of the H_3N-HBr complex in solid Ne, Ne/Ar, Ar, Kr, and N-2. Strong matrix effects on a hydrogen-bonded complex.* Journal of Physical Chemistry A, 2001. **105**(26): p. 6420-6429.

173. Legon, A.C. and D.J. Millen, *Hydrogen-Bonding as a Probe of Electron-Densities - Limiting Gas-Phase Nucleophilicities and Electrophilicities of B and Hx.* Journal of the American Chemical Society, 1987. **109**(2): p. 356-358.

174. Fowler, P.W., et al., *Geometry and binding strength of a pi-type hydrogen-bonded complex of ethene and hydrogen bromide determined by rotational spectroscopy.* Coordination Chemistry Reviews, 2000. **197**: p. 231-247.

175. Legon, A.C., P.D. Aldrich, and W.H. Flygare, *The Rotational Spectrum and Molecular-Structure of the Acetylene-Hcl Dimer.* Journal of Chemical Physics, 1981. **75**(2): p. 625-630.

176. Shea, J.A. and W.H. Flygare, *The Rotational Spectrum and Molecular-Structure of the Ethylene-Hf Complex.* Journal of Chemical Physics, 1982. **76**(10): p. 4857-4864.

177. Andrews, L., G.L. Johnson, and B.J. Kelsall, *Fourier-Transform Infrared-Spectra of the C_2H_2-H_x and C_2H_x-H_x Hydrogen-Bonded Complexes in Solid Argon.* Journal of Physical Chemistry, 1982. **86**(17): p. 3374-3380.

178. Andrews, L., G.L. Johnson, and B.J. Kelsall, *Infrared-Spectra of the Hydrogen-Bonded Pi-Complex C_2H_4-HF in Solid Argon.* Journal of Chemical Physics, 1982. **76**(12): p. 5767-5773.

179. Hammes-Schiffer, S., *Introduction: Proton-Coupled Electron Transfer.* Chemical Reviews, 2010. **110**(12): p. 6937-6938.

180. Hammes-Schiffer, S. and A.A. Stuchebrukhov, *Theory of Coupled Electron and Proton Transfer Reactions.* Chemical Reviews, 2010. **110**(12): p. 6939-6960.

181. Sirjoosingh, A. and S. Hammes-Schiffer, *Proton-Coupled Electron Transfer versus Hydrogen Atom Transfer: Generation of Charge-Localized Diabatic States.* Journal of Physical Chemistry A, 2011. **115**(11): p. 2367-2377.

182. Belevich, I., et al., *Proton-coupled electron equilibrium in soluble and membrane-bound cytochrome c oxidase from Paracoccus denitrificans.* Biochemistry, 2006. **45**(12): p. 4000-4006.

183. Belevich, I., M.I. Verkhovsky, and M. Wikstrom, *Proton-coupled electron transfer drives the proton pump of cytochrome c oxidase.* Nature, 2006. **440**(7085): p. 829-832.

184. Kaila, V.R.I., M.I. Verkhovsky, and M. Wikstrom, *Proton-Coupled Electron Transfer in Cytochrome Oxidase.* Chemical Reviews, 2010. **110**(12): p. 7062-7081.

185. Kumar, A. and M.D. Sevilla, *Proton-Coupled Electron Transfer in DNA on Formation of Radiation-Produced Ion Radicals.* Chemical Reviews, 2010. **110**(12): p. 7002-7023.

186. Li, B., et al., *Ultrafast interfacial proton-coupled electron transfer.* Science, 2006. **311**(5766): p. 1436-1440.

187. Masgrau, L., et al., *Atomic description of an enzyme reaction dominated by proton tunneling.* Science, 2006. **312**(5771): p. 237-241.

188. Ribas, X., et al., *Facile C-H Bond Cleavage via a Proton-Coupled Electron Transfer Involving a C-H ···Cu-II Interaction.* Journal of the American Chemical Society, 2010. **132**(35): p. 12299-12306.

189. Lewis, N.S. and D.G. Nocera, *Powering the planet: Chemical challenges in solar energy utilization.* Proceedings of the National Academy of Sciences of the United States of America, 2007. **104**(50): p. 20142-20142.

190. Schrauben, J.N., et al., *Titanium and Zinc Oxide Nanoparticles Are Proton-Coupled Electron Transfer Agents.* Science, 2012. **336**(6086): p. 1298-1301.

191. Zhang, M.T. and L. Hammarstrom, *Proton-Coupled Electron Transfer from Tryptophan: A Concerted Mechanism with Water as Proton Acceptor.* Journal of the American Chemical Society, 2011. **133**(23): p. 8806-8809.

192. Ayed, T., R.H. Lamoneda, and K.C. Janda, *Theoretical study of the potential energy surfaces of the van der Waals H_2O-X_2^+ (X = Cl or Br) complexes.* Journal of Physical Chemistry A, 2008. **112**(4): p. 722-727.

193. Li, R.Y., et al., *Study of pi halogen bonds in complexes C_2H_4-F-n(n)-ClF (n=0-2).* Journal of Physical Chemistry A, 2005. **109**(11): p. 2608-2613.

194. Tachikawa, H. and E. Komatsu, *Structures and electronic states of the electron donor-acceptor complexes NH_3-X_2(X=F and Cl): An ab-initio MO study.* Inorganic Chemistry, 1995. **34**(26): p. 6546-6549.

195. Tachikawa, H. and E. Komatsu, *Structures and electronic states of the electron donor-acceptor (EDA) complexes: trimethylamine-halogen complex $(CH_3)_3N \cdots F_2$.* Inorganica Chimica Acta, 1998. **281**(1): p. 85-89.

196. Cheng, P.Y., D. Zhong, and A.H. Zewail, *Femtosecond real-time probing of reactions .21. Direct observation of transition-state dynamics and structure in charge-transfer reactions.* Journal of Chemical Physics, 1996. **105**(15): p. 6216-6248.

197. Hilinski, E.F. and P.M. Rentzepis, *Picosecond Photochemistry of I_2-Arene Complexes.* Journal of the American Chemical Society, 1985. **107**(21): p. 5907-5910.

198. Raner, K.D., J. Lusztyk, and K.U. Ingold, *Ultraviolet Visible Spectra of Halogen Molecule Arene and Halogen Atom Arene Pi-Molecular Complexes.* Journal of Physical Chemistry, 1989. **93**(2): p. 564-570.

199. Lenderink, E., et al., *Photodissociation dynamics of the iodine-arene charge-transfer complex.* Journal of Physical Chemistry, 1996. **100**(19): p. 7822-7831.

200. Lenderink, E., K. Duppen, and D.A. Wiersma, *Femtochemistry of the Iodine Arene Charge-Transfer Complex.* Chemical Physics Letters, 1993. **211**(6): p. 503-510.

201. Lenoir, D., *The electrophilic substitution of arenes: Is the pi complex a key intermediate and what is its nature?* Angewandte Chemie-International Edition, 2003. **42**(8): p. 854-857.

202. Maric, D., J.P. Burrows, and G.K. Moortgat, *A Study of the Uv-Visible Absorption-Spectra of Br_2 and BrCl.* Journal of Photochemistry and Photobiology a-Chemistry, 1994. **83**(3): p. 179-192.

203. George, L., et al., *Photoinduced Electron Transfer in a Prototypical Mulliken Donor-Acceptor Complex: $C_2H_4 \cdots Br_2$.* Journal of Physical Chemistry Letters, 2010. **1**(17): p. 2618-2620.

204. Davey, J.B. and A.C. Legon, *A gas phase complex of acetylene and bromine: geometry, binding strength and charge transfer from rotational spectroscopy.* Chemical Physics Letters, 2001. **350**(1-2): p. 39-50.

205. Chang, A.H.H., et al., *Ab initio calculations of potential energy surface and rate constants for ethylene photodissociation at 193 and 157 nm.* Chemical Physics Letters, 1998. **287**(3-4): p. 301-306.

206. Hassel, O. and K.O. Stromme, *Crystal structure of the 1:1 addition compounds formed by acetone and bromine.* Acta Chem. Scand., 1959. **13**: p. 275-80.

207. Bennet, A.J., et al., *An Unprecedented Rapid and Direct Br^+ Transfer from the Bromonium Ion of Adamantylideneadamantane to Acceptor Olefins.* Journal of the American Chemical Society, 1991. **113**(22): p. 8532-8534.

208. Brown, R.S., et al., *Stable Bromonium and Iodonium Ions of the Hindered Olefins Adamantylideneadamantane and Bicyclo[3.3.1]Nonylidenebicyclo[3.3.1]Nonane - X-Ray Structure, Transfer of Positive Halogens to Acceptor Olefins, and Ab-Initio Studies.* Journal of the American Chemical Society, 1994. **116**(6): p. 2448-2456.

209. Cossi, M., M. Persico, and J. Tomasi, *Aspects of Electrophilic Bromination of Alkenes in Solution - Theoretical Calculation of Atomic Charges in Bromonium Ions.* Journal of the American Chemical Society, 1994. **116**(12): p. 5373-5378.

210. Galland, B., E.M. Evleth, and M.F. Ruasse, *An Mndo Approach to the Symmetry of Bromine Bridging in Substituted Bromonium Ions.* Journal of the Chemical Society-Chemical Communications, 1990(13): p. 898-900.

211. Hamilton, T.P. and H.F. Schaefer, *Structure and Energetics of $C_2H_4Br^+$ - Ethylenebromonium Ion Vs Bromoethyl Cations.* Journal of the American Chemical Society, 1990. **112**(23): p. 8260-8265.

212. Vancik, H., K. Percac, and D.E. Sunko, *Isolation and the Ir-Spectra of Chloro-Ethyl and Bromo-Ethyl Cations in Cryogenic SbF_5 Matrices.* Journal of the Chemical Society-Chemical Communications, 1991(12): p. 807-809.

213. Teberekidis, V.I. and M.P. Sigalas, *Density functional study of potential energy surfaces and relative stabilities of halonium cations of ethylene and cyclopentenes.* Tetrahedron, 2002. **58**(31): p. 6171-6178.

214. Engels, B., S.D. Peyerimhoff, and P.S. Skell, *Theoretical-Study of the Potential-Energy Surface Governing the Stereochemistry in ClC_2H_4 Reactions.* Journal of Physical Chemistry, 1990. **94**(4): p. 1267-1275.

215. Ihee, H., et al., *CF_2XCF_2X and CF_2XCF_2 • radicals (X = Cl, Br, I): Ab initio and DFT studies and comparison with experiments.* Journal of Physical Chemistry A, 2001. **105**(14): p. 3623-3632.

216. Ihee, H., A.H. Zewail, and W.A. Goddard, *Conformations and barriers of haloethyl radicals (CH_2XCH_2, X = F, Cl, Br, I): Ab initio studies.* Journal of Physical Chemistry A, 1999. **103**(33): p. 6638-6649.

217. Kim, J., et al., *Structural Dynamics of 1,2-Diiodoethane in Cyclohexane Probed by Picosecond X-ray Liquidography.* Journal of Physical Chemistry A, 2012. **116**(11): p. 2713-2722.

218. Lee, J.H., et al., *Analyzing solution-phase time-resolved x-ray diffraction data by isolated-solute models.* Journal of Chemical Physics, 2006. **125**(17).

219. Skell, P.S., chemical Society Reviews, 1965. **19**: p. 131.

220. Skell, P.S. and S.K. J., *Bridged Free Radicals*. II ed. 1973, New York: John Wiley and Sons.

221. Skell, P.S. and R.R. Pavlis, Journal of the American Chemical Society, 1964. **86**: p. 2956.

222. Skell, P.S., D.L. Tuleen, and P.D. Readio, journal of the American Chemical Society, 1963. **85**: p. 2849.

223. Li, Z.H., K.N. Fan, and M.W. Wong, *Stereochemistry of radical halogenation reactions. An ab initio molecular orbital study.* Journal of Physical Chemistry A, 2001. **105**(48): p. 10890-10898.

224. Peterson, K.A. and T.H. Dunning, *Accurate correlation consistent basis sets for molecular core-valence correlation effects: The second row atoms Al-Ar, and the first row atoms B-Ne revisited.* Journal of Chemical Physics, 2002. **117**(23): p. 10548-10560.

225. Wilson, A. K., et al., *Gaussian basis sets for use in correlated molecular calculations. IX. The atoms gallium through krypton.* Journal of Chemical Physics, 1999. **110**(16): p. 7667-7676.

226. Woon, D.E. and T.H. Dunning, *Gaussian-Basis Sets for Use in Correlated Molecular Calculations .3. The Atoms Aluminum through Argon.* Journal of Chemical Physics, 1993. **98**(2): p. 1358-1371.

227. Dreuw, A., J.L. Weisman, and M. Head-Gordon, *Long-range charge-transfer excited states in time-dependent density functional theory require non-local exchange.* Journal of Chemical Physics, 2003. **119**(6): p. 2943-2946.

228. Fredin, L., Chemica Scripta, 1973. **4**: p. 97.

229. Cheng, P.Y., D. Zhong, and A.H. Zewail, *Microscopic Solvation and Femtochemistry of Charge-Transfer Reactions - the Problem of Benzene(S)-Iodine Binary Complexes and Their Solvent Structures.* Chemical Physics Letters, 1995. **242**(4-5): p. 369-379.

230. Liu, H.J., et al., *The vibrational relaxation of I_2 ($X^1\ \sigma^+_g$) in mesitylene.* Journal of Chemical Physics, 1998. **108**(12): p. 4992-5001.

231. Walker, L.A., et al., *On the Structure of Iodine Charge-Transfer Complexes in Solution.* Chemical Physics Letters, 1995. **242**(1-2): p. 177-183.

232. Whitnell, R.M., et al., *Classical-Theory of Ultrafast Pump-Probe Spectroscopy - Applications to I_2 Photodissociation in Ar Solution.* Journal of Molecular Liquids, 1994. **61**(1-3): p. 153-165.

233. DeBoer, G., J.W. Burnett, and M.A. Young, *Molecular product formation from the charge-transfer state of C_6H_6-I_2.* Chemical Physics Letters, 1996. **259**(3-4): p. 368-374.

234. DeBoer, G., et al., *Photodissociation dynamics of the charge-transfer state of the C_6H_6-I_2 complex.* Journal of Physical Chemistry, 1996. **100**(36): p. 14882-14891.

235. Sogoshi, N., et al., *Infrared spectroscopic studies on photolysis of ethyl iodide in solid parahydrogen.* Journal of Physical Chemistry A, 1997. **101**(4): p. 522-527.

236. Pettersson, M. and J. Nieminen, *Spin-orbit transitions ($^2P_{1/2} \leftarrow {}^2P_{3/2}$) of iodine and bromine atoms in solid rare-gases.* Chemical Physics Letters, 1998. **283**(1-2): p. 1-6.

237. Chen, E.C.M. and W.E. Wentworth, *Negative-Ion States of the Halogens.* Journal of Physical Chemistry, 1985. **89**(19): p. 4099-4105.

238. Bilde, M., et al., *Atmospheric chemistry of CF_2BrH: Kinetics and mechanism of reaction with F and Cl atoms and fate of CF_2BrO radicals.* Journal of Physical Chemistry, 1996. **100**(17): p. 7050-7059.

239. Breslow, R., et al., *Pyridine Complexes of Chlorine Atoms.* Journal of the American Chemical Society, 1987. **109**(23): p. 7204-7206.

240. Chateauneuf, J.E., *Kinetic evidence for chlorine atom complexes in "noncomplexing" solvents.* Journal of Organic Chemistry, 1999. **64**(3): p. 1054-1055.

241. McKee, M.L., A. Nicolaides, and L. Radom, *A theoretical study of chlorine atom and methyl radical addition to nitrogen bases: Why do Cl atoms form two-center-three-electron bonds whereas CH_3 radicals form two-center-two-electron bonds?* Journal of the American Chemical Society, 1996. **118**(43): p. 10571-10576.

242. Kolessov, A., et al., *Probing the Cl-HCl complex via bond-specific photodissociation of the HCl dimer.* Abstracts of Papers of the American Chemical Society, 1999. **217**: p. U325-U326.

243. Lorenz, M., et al., *Photodissociation of hydrogen halides in rare gas matrices, and the effect of hydrogen bonding.* Journal of Chemical Physics, 2000. **112**(8): p. 3803-3811.

244. Choi, M.Y., et al., *Infrared spectroscopy of helium nanodroplets: novel methods for physics and chemistry.* International Reviews in Physical Chemistry, 2006. **25**(1-2): p. 15-75.

245. Dneprovskii, A.S., et al., *Free radical chlorinations in halogenated solvents: Are there any solvents which are truly noncomplexing?* Journal of Organic Chemistry, 1998. **63**(24): p. 8860-8864.

246. Shimanouchi, T., *NIST Chemistry WebBook, NIST Standard Reference Database Number 69*, P.J.a.M. Linstrom, W.G., Editor 1972, National Bureau of Standards: Gaithersburg MD.

247. Politzer, P., et al., *An overview of halogen bonding.* Journal of Molecular Modeling, 2007. **13**(2): p. 305-311.

248. Alfassi, Z.B., et al., *Charge-Transfer Complexes of Bromine Atoms with Haloalkanes and Alkanes.* Journal of Physical Chemistry, 1993. **97**(36): p. 9120-9123.

249. Shoute, L.C.T. and P. Neta, *Reactivity of Bromine Atom Complexes with Organic-Compounds.* Journal of Physical Chemistry, 1990. **94**(18): p. 7181-7184.

250. Shoute, L.C.T. and P. Neta, *Bromine Atom Complexes with Bromoalkanes - Their Formation in the Pulse-Radiolysis of Di-Bromomethane, Tri-Bromomethane, and Tetrabromomethane and Their Reactivity with Organic Reductants.* Journal of Physical Chemistry, 1990. **94**(6): p. 2447-2453.

251. Strong, R.L., Journal of Physical Chemistry, 1962. **66**: p. 2423-2426.

252. Buhler, R.E. and M. Ebert, Nature, 1967. **214**: p. 1220.

253. Yamamoto, N., et al., Journal of the American Chemical Society, 1969. **91**: p. 265-267.

254. Buhler, R.E., journal of Physical Chemistry, 1972. **76**: p. 3220-3228.

255. Mulliken, R.S., Journal of the American Chemical Society, 1952. **74**: p. 811.

256. Mulliken, R.S. and W.B. Person, Annual Review of Physical Chemistry, 1962. **13**: p. 107.

257. Mulliken, R.S. and W.B. Person, *Molecular Complexes, A Lecture and Reprint Volume*. 1969, New-York, NY: Wiley-Interscience.

258. Treinin, A. and E. Hayon, Journal of the American Chemical Society, 1975. **97**: p. 1716-1721.

259. *CRC Handbook of Chemistry and Physics*. Vol. 88. 2008, Boca Raton, FL: CRC Press.

260. Grosso, G., L. Martinelli, and G.P. Parravicini, Solid State Communications, 1978. **25**: p. 435-438.

261. Pal, S.K., et al., *Femtosecond photolysis of CH_2Br_2 in acetonitrile: Capturing the bromomethyl radical and bromine-atom charge transfer complex through deep-to-near UV probing.* Chemical Physics Letters, 2011. **507**(1-3): p. 69-73.

262. Mcgimpsey, W.G. and J.C. Scaiano, *Photochemistry of Alpha-Chloro-Acetophenone and Alpha-Bromoacetophenone - Determination of Extinction Coefficients for Halogen Benzene Complexes.* Canadian Journal of Chemistry-Revue Canadienne De Chimie, 1988. **66**(6): p. 1474-1478.

263. Bossy, J.M., R.E. Buhler, and M.J. Ebert, journal of the American Chemical Society, 1970. **92**: p. 1099-1101.

264. Croft, A.K. and H.M. Howard-Jones, *Chlorine-benzene complexes - the reliability of density functionals for non-covalent radical complexes.* Physical Chemistry Chemical Physics, 2007. **9**(42): p. 5649-5655.

265. Prana, B., R. Gomperts, and J.A. Sordo, *A theoretical study on the mechanism of the reaction between Cl atoms and nitrobenzene.* Chemical Physics Letters, 2004. **392**(1-3): p. 236-241.

266. Kohn, W., Y. Meir, and D.E. Makarov, *vanderWaals energies in density functional theory.* Physical Review Letters, 1998. **80**(19): p. 4153-4156.

267. Zhao, Y. and D.G. Truhlar, *Density functionals with broad applicability in chemistry.* Accounts of Chemical Research, 2008. **41**(2): p. 157-167.

268. Jarzeba, W., *Ultrafast electron transfer in arene - Br atom charge transfer complexes.* Journal of Molecular Liquids, 1996. **68**(1): p. 1-11.

269. Schlief, R.E., et al., *Ultrafast Experiments on Intermolecular Electron-Transfer in the Benzene-Bromine Atom Charge-Transfer Complex.* Journal of Molecular Liquids, 1994. **60**(1-3): p. 201-220.

270. Basso, E.A., et al., *Semiempirical and ab initio calculations versus dynamic NMR on conformational analysis of cyclohexyl-N,N-dimethylcarbamate.* Journal of the Brazilian Chemical Society, 2001. **12**(2): p. 215-222.

271. Cameron, M.R., et al., *Photodissociation dynamics of the reaction $CF_2Br_2+h\upsilon\rightarrow CF_2+2Br$. Energetics, threshold and nascent CF_2 energy distributions for lambda=223-260 nm.* Physical Chemistry Chemical Physics, 2000. **2**(11): p. 2539-2547.

272. Hsu, C.Y., H.Y. Huang, and K.C. Lin, *Br_2 elimination in 248-nm photolysis of CF_2Br_2 probed by using cavity ring-down absorption spectroscopy.* Journal of Chemical Physics, 2005. **123**(13).

273. Ji, L., J. Tang, and B. Zhang, *Photodissociation dynamics study of CH_2Br_2 in ultraviolet region by the ion-velocity imaging technique.* Acta Chimica Sinica, 2007. **65**(6): p. 501-508.

274. Ji, L., et al., *Photodissociation dynamics of CH_2Br_2 near 234 and 267 nm.* Spectrochimica Acta Part a-Molecular and Biomolecular Spectroscopy, 2007. **67**(1): p. 273-280.

275. Owens, N.L., et al., *An experimental and theoretical investigation of the triple fragmentation of $CFClBr_2$ by photolysis near 250 nm.* Chemical Physics Letters, 2003. **370**(3-4): p. 469-477.

276. Park, M.S., et al., *Avoided curve crossing between the A1 and B 1 states in CF_2Br_2 photolysis at 234 and 265 nm.* Journal of Physical Chemistry A, 2001. **105**(23): p. 5606-5612.

277. Saini, R.D., S. Dhanya, and T.N. Das, *Laser (248 nm) flash photolysis and pulse radiolysis of CF_2Br_2 in aqueous solution: Atmospheric implications.* Bulletin of the Chemical Society of Japan, 2002. **75**(8): p. 1699-1705.

278. Talukdar, R.K., et al., *UV laser photodissociation of CF_2ClBr and CF_2Br_2 at 298 K: Quantum yields of Cl, Br, and CF_2.* Chemical Physics Letters, 1996. **262**(6): p. 669-674.

279. Vatsa, R.K., et al., *Uv Absorption-Spectrum and Decay Kinetics of CF_2Br in CO_2 Laser-Induced Photodissociation of CF_2Br_2.* Chemical Physics Letters, 1993. **207**(1): p. 75-80.

280. Wei, P.Y., et al., *Br_2 molecular elimination in 248 nm photolysis of $CHBr_2Cl$ by using cavity ring-down absorption spectroscopy.* Journal of Chemical Physics, 2007. **126**(3).

281. Zhang, Q.Q., U. Marvet, and M. Dantus, *Concerted elimination dynamics from highly excited states.* Faraday Discussions, 1997. **108**: p. 63-80.

282. Abboud, J.L.M., et al., *Superacid chemistry in the gas phase: dissociative proton attachment to halomethanes.* International Journal of Mass Spectrometry, 1998. **175**(1-2): p. 35-40.

283. Andrews, L., et al., *The 1st Bands in the Photoelectron-Spectra of the CH_2Br, CD_2Br, $CHBr_2$, and CH_2I Free-Radicals.* Journal of Physical Chemistry, 1984. **88**(10): p. 1950-1954.

284. Cao, C.Z., *Slater-like model for carbon 1s core ionization energies of halomethanes.* Chemphyschem, 2006. **7**(3): p. 658-663.

285. Lago, A.F., et al., *Dissociative photoionization and thermochemistry of dihalomethane compounds studied by threshold photoelectron photoion coincidence spectroscopy.* Journal of Physical Chemistry A, 2005. **109**(9): p. 1802-1809.

286. Rodriquez, C.F., D.K. Bohme, and A.C. Hopkinson, *Theoretical enthalpies of formation of CH_mCl_n: Neutral molecules and cations.* Journal of Physical Chemistry, 1996. **100**(8): p. 2942-2949.

287. Sorrilha, A.E.P.M., et al., *Intrinsic reactivity of gaseous halocarbocations toward model aromatic compounds.* Journal of Physical Chemistry A, 2004. **108**(34): p. 7009-7020.

288. Olah, G.A., et al., *Preparation, NMR spectroscopic, and ab initio DFT GIAO-MP2 studies of halomethyl cations.* Journal of the American Chemical Society, 1996. **118**(15): p. 3580-3583.

289. Taft, R.W., R.H. Martin, and F.W. Lampe, Journal of the American Chemical Society, 1965. **118**.

290. Bernardi, F., A. Bottoni, and A. Venturini, *The Stabilization of Alpha-Substituted Methyl Cations by 1st-Row and 2nd-Row Substituents.* Journal of the American Chemical Society, 1986. **108**(18): p. 5395-5400.

291. Frenking, G., et al., *The pi-donor ability of the halogens in cations and neutral molecules. A theoretical study of AX_3^+, AH_2X^+, YX_3, and YH_2X (A=C, Si, Ge, Sn, Pb; Y=B, Al, Ga, In, Tl; X=F, Cl, Br, I).* Journal of the American Chemical Society, 1997. **119**(28): p. 6648-6655.

292. Kapp, J., et al., *Heavy element pi donation is not less effective.* Angewandte Chemie-International Edition in English, 1996. **35**(19): p. 2236-2238.

293. Tao, C., et al., *Electronic spectroscopy of an isolated halocarbocation: The iodomethyl cation CH_2I^+ and its deuterated isotopomers.* Journal of Physical Chemistry A, 2007. **111**(42): p. 10562-10566.

294. Tao, C., C. Mukarakate, and S.A. Reid, *Laser Spectroscopy of a halocarbocation in the gas phase: CH2I+*. Journal of the American Chemical Society, 2006. **128**(29): p. 9320-9321.

295. Felder, P., et al., *Photofragment Translational Spectroscopy of Fluorinated Halomethanes.* Israel Journal of Chemistry, 1994. **34**(1): p. 33-42.

296. Jacox, M.E., chemical Physics Letters, 1978. **53**: p. 192.

297. Prochaska, F.T. and L. Andrews, Journal of the American Chemical Society, 1978. **100**.

298. Prochaska, F.T. and L. Andrews, Journal of Physical Chemistry, 1978. **82**.

299. Li, Z.J. and J.S. Francisco, *High level ab initio molecular orbital study of the structures and vibrational spectra of CH_2Br and CH_2Br^+*. Journal of Chemical Physics, 1999. **110**(2): p. 817-822.

300. Kable, S.H., S.A. Reid, and T.J. Sears, *The halocarbenes: model systems for understanding the spectroscopy, dynamics and chemistry of carbenes.* International Reviews in Physical Chemistry, 2009. **28**(3): p. 435-480.

301. Andrews, L., et al., *The 1st Band in the He(I) Photoelectron-Spectrum of the CH_2Cl Free-Radical.* Chemical Physics Letters, 1983. **97**(1): p. 89-93.

302. Jacox, M.E., *The spectroscopy of molecular reaction intermediates trapped in the solid rare gases.* Chemical Society Reviews, 2002. **31**(2): p. 108-115.

303. Jacox, M.E., *Vibrational and electronic spectra of neutral and ionic combustion reaction intermediates trapped in rare-gas matrixes.* Accounts of Chemical Research, 2004. **37**(9): p. 727-734.

304. George, L., et al., *Pulsed Jet Discharge Matrix Isolation and Computational Study of Bromine Atom Complexes: $Br \cdots BrXCH_2$ (X = H, Cl, Br).* Journal of Physical Chemistry A, 2011. **115**(35): p. 9820-9827.